

8-2010

# **BENCHMARKING AND IMPLEMENTATION OF A NEW INDEPENDENT MONTE CARLO DOSE CALCULATION QUALITY ASSURANCE AUDIT TOOL FOR CLINICAL TRIALS**

Scott E. Davidson

Follow this and additional works at: [https://digitalcommons.library.tmc.edu/utgsbs\\_dissertations](https://digitalcommons.library.tmc.edu/utgsbs_dissertations)



Part of the [Oncology Commons](#), and the [Other Physics Commons](#)

## **Recommended Citation**

Davidson, Scott E., "BENCHMARKING AND IMPLEMENTATION OF A NEW INDEPENDENT MONTE CARLO DOSE CALCULATION QUALITY ASSURANCE AUDIT TOOL FOR CLINICAL TRIALS" (2010). *The University of Texas MD Anderson Cancer Center UTHealth Graduate School of Biomedical Sciences Dissertations and Theses (Open Access)*. 68.

[https://digitalcommons.library.tmc.edu/utgsbs\\_dissertations/68](https://digitalcommons.library.tmc.edu/utgsbs_dissertations/68)

This Dissertation (PhD) is brought to you for free and open access by the The University of Texas MD Anderson Cancer Center UTHealth Graduate School of Biomedical Sciences at DigitalCommons@TMC. It has been accepted for inclusion in The University of Texas MD Anderson Cancer Center UTHealth Graduate School of Biomedical Sciences Dissertations and Theses (Open Access) by an authorized administrator of DigitalCommons@TMC. For more information, please contact [digitalcommons@library.tmc.edu](mailto:digitalcommons@library.tmc.edu).

BENCHMARKING AND IMPLEMENTATION OF A NEW INDEPENDENT MONTE  
CARLO DOSE CALCULATION QUALITY ASSURANCE AUDIT TOOL FOR CLINICAL  
TRIALS

by

Scott E. Davidson, M.S.

APPROVED:

---

David Followill, Ph.D.  
Supervisory Professor

---

Geoffrey Ibbott, Ph.D.

---

Stephen Kry, Ph.D.

---

Milos Vicic, Ph.D.

---

Allen White, Ph.D.

---

APPROVED:

---

Dean, The University of Texas  
Health Science Center at Houston  
Graduate School of Biomedical Sciences

BENCHMARKING AND IMPLEMENTATION OF A NEW INDEPENDENT DOSE  
CALCULATION QUALITY ASSURANCE AUDIT TOOL FOR CLINICAL TRIALS

A

DISSERTATION

Presented to the Faculty of  
The University of Texas  
Health Science Center at Houston  
and  
The University of Texas  
M. D. Anderson Cancer Center  
Graduate School of Biomedical Sciences  
in Partial Fulfillment

of the Requirements

for the Degree of

DOCTOR OF PHILOSOPHY

by

Scott E. Davidson, M.S.  
Houston, Texas

August, 2010

# **Benchmarking and implementation of a new independent dose calculation quality assurance audit tool for clinical trials**

Publication No. \_\_\_\_\_

Scott E. Davidson, M.S.

Supervisory Professor: David S. Followill, Ph.D.

**Introduction** Commercial treatment planning systems employ a variety of dose calculation algorithms to plan and predict the dose distributions a patient receives during external beam radiation therapy. Traditionally, the Radiological Physics Center has relied on measurements to assure that institutions participating in the National Cancer Institute sponsored clinical trials administer radiation in doses that are clinically comparable to those of other participating institutions. To complement the effort of the RPC, an independent dose calculation tool needs to be developed that will enable a generic method to determine patient dose distributions in three dimensions and to perform retrospective analysis of radiation delivered to patients who enrolled in past clinical trials.

**Methods** A multi-source model representing output for Varian 6 MV and 10 MV photon beams was developed and evaluated. The Monte Carlo algorithm, known as the Dose Planning Method (DPM), was used to perform the dose calculations. The dose calculations were compared to measurements made in a water phantom and in anthropomorphic phantoms. Intensity modulated radiation therapy and stereotactic body radiation therapy techniques were used with the anthropomorphic phantoms. Finally, past patient treatment plans were selected and recalculated using DPM and contrasted against a commercial dose calculation algorithm.

**Results** The multi-source model was validated for the Varian 6 MV and 10 MV photon beams. The benchmark evaluations demonstrated the ability of the model to accurately calculate dose for the Varian 6 MV and the Varian 10 MV source models. The patient calculations proved that the model was reproducible in determining dose under similar conditions described by the benchmark tests.

**Conclusions** The dose calculation tool that relied on a multi-source model approach and used the DPM code to calculate dose was developed, validated, and benchmarked for the Varian 6 MV and 10 MV photon beams. Several patient dose distributions were contrasted against a commercial algorithm to provide a proof of principle to use as an application in monitoring clinical trial activity.



## TABLE OF CONTENTS

|                  |   |           |
|------------------|---|-----------|
| <b>CHAPTER 1</b> | <b>INTRODUCTION.....</b>                                | <b>1</b>  |
| 1.1              | STATEMENT OF PROBLEM .....                              | 1         |
| 1.2              | BENEFITS TO SCIENCE .....                               | 8         |
| 1.3              | HYPOTHESIS AND SPECIFIC AIMS .....                      | 9         |
| 1.4              | DISSERTATION ORGANIZATION.....                          | 10        |
| <b>CHAPTER 2</b> | <b>DEVELOPMENT, VALIDATION, AND BENCHMARK: VARIAN 6</b> |           |
| <b>MV</b>        | <b>11</b>   |           |
| 2.1              | INTRODUCTION .....                                      | 11        |
| 2.2              | MATERIAL AND METHODS .....                              | 13        |
| 2.2.1            | <i>Source model.....</i>                                | <i>13</i> |
| 2.2.1.1          | <i>Hardware .....</i>                                   | <i>13</i> |
| 2.2.1.2          | <i>Source model commissioning.....</i>                  | <i>13</i> |
| 2.2.1.3          | <i>Fluence map.....</i>                                 | <i>16</i> |
| 2.2.1.4          | <i>Primary source size.....</i>                         | <i>17</i> |
| 2.2.1.5          | <i>Machine output correction.....</i>                   | <i>17</i> |
| 2.2.2            | <i>Anthropomorphic phantoms and dosimeters .....</i>    | <i>18</i> |
| 2.2.3            | <i>Validation testing.....</i>                          | <i>19</i> |
| 2.2.4            | <i>Benchmark testing.....</i>                           | <i>21</i> |
| 2.2.4.1          | <i>Point dose comparisons .....</i>                     | <i>21</i> |
| 2.2.4.2          | <i>Dose profile comparisons .....</i>                   | <i>21</i> |
| 2.2.4.3          | <i>Gamma map comparisons.....</i>                       | <i>22</i> |
| 2.2.4.4          | <i>Treatment plans.....</i>                             | <i>24</i> |
| 2.3              | RESULTS AND DISCUSSION .....                            | 27        |
| 2.3.1            | <i>Source model.....</i>                                | <i>27</i> |
| 2.3.1.1          | <i>Source model commissioning parameters.....</i>       | <i>27</i> |

|  |  |    |
|--|--|----|
| 2.3.1.2  | <i>Fluence map, primary source size, and machine output correction .....</i>                                   | 29 |
| 2.3.2  | <i>Validation testing .....</i>  | 31 |
| 2.3.2.1  | <i>Uncertainty.....</i>  | 31 |
| 2.3.2.2  | <i>Percent depth dose .....</i>  | 31 |
| 2.3.2.3  | <i>Dose profiles .....</i>   | 35 |
| 2.3.3  | <i>Benchmark testing.....</i>  | 40 |
| 2.3.3.1  | <i>Uncertainty.....</i>  | 40 |
| 2.3.3.2  | <i>Effect of finite primary source size on benchmark deliveries .....</i>                                      | 40 |
| 2.3.3.3  | <i>Delivery of the IMRT head and neck phantom plan: Point dose comparisons</i><br><i>42</i>                    |    |
| 2.3.3.4  | <i>Delivery of the IMRT head and neck phantom plan: Dose profile and gamma</i><br><i>map comparisons .....</i> | 44 |
| 2.3.3.5  | <i>Delivery of the SBRT thorax phantom plan: Point dose comparisons .....</i>                                  | 49 |
| 2.3.3.6  | <i>Delivery of the SBRT thorax phantom plan: Dose profile and gamma map</i><br><i>comparisons .....</i>        | 52 |
| 2.3.3.7  | <i>Delivery of the IMRT thorax phantom plan: Point dose comparisons.....</i>                                   | 57 |
| 2.3.3.8  | <i>Delivery of the IMRT thorax phantom plan: Dose profile and gamma map</i><br><i>comparisons .....</i>        | 59 |
| 2.3.3.9  | <i>Benchmark summary.....</i>  | 65 |
| 2.4  | <i>CONCLUSION.....</i>   | 66 |
| <br><b>CHAPTER 3 DEVELOPMENT, VALIDATION, AND BENCHMARK: VARIAN 10</b> |  |    |
| <b>MV 68</b>   |  |    |
| 3.1  | <i>INTRODUCTION .....</i>  | 68 |
| 3.2  | <i>MATERIAL AND METHODS .....</i>  | 71 |
| 3.2.1  | <i>Source Model .....</i>  | 71 |
| 3.2.1.1  | <i>Source model overview .....</i>   | 71 |

|         |  |     |
|---------|--|-----|
| 3.2.1.2 | <i>Source model commissioning</i> .....  | 72  |
| 3.2.1.3 | <i>Electron contamination contribution</i> .....   | 73  |
| 3.2.2   | <i>Validation testing</i> .....  | 73  |
| 3.2.3   | <i>Benchmark testing</i> .....   | 74  |
| 3.2.3.1 | <i>Point dose comparisons</i> .....  | 75  |
| 3.2.3.2 | <i>Dose profile comparisons</i> .....  | 76  |
| 3.2.3.3 | <i>Gamma map comparisons</i> .....   | 76  |
| 3.2.3.4 | <i>Treatment plans</i> .....   | 76  |
| 3.3     | <b>RESULTS AND DISCUSSION</b> .....  | 78  |
| 3.3.1   | <i>Source model</i> .....  | 78  |
| 3.3.1.1 | <i>Source model commissioning parameters</i> .....   | 78  |
| 3.3.1.2 | <i>Fluence map, primary source size, and machine output correction</i> .....                             | 80  |
| 3.3.1.3 | <i>Electron contamination contribution versus field size</i> .....                                       | 82  |
| 3.3.2   | <i>Validation testing</i> .....  | 85  |
| 3.3.2.1 | <i>Uncertainty</i> .....   | 85  |
| 3.3.2.2 | <i>Percent depth dose</i> .....  | 85  |
| 3.3.2.3 | <i>Dose profiles</i> .....   | 88  |
| 3.3.3   | <i>Benchmark testing</i> .....   | 92  |
| 3.3.3.1 | <i>Uncertainty</i> .....   | 92  |
| 3.3.3.2 | <i>Effect of finite primary source size on benchmark deliveries</i> .....                                | 93  |
| 3.3.3.3 | <i>Delivery of the IMRT head and neck phantom plan: Point dose comparisons</i><br>95                     |     |
| 3.3.3.4 | <i>Delivery of the IMRT head and neck phantom plan: Dose profile and gamma<br/>map comparisons</i> ..... | 97  |
| 3.3.3.5 | <i>Delivery of the SBRT thorax phantom: Point dose comparisons</i> .....                                 | 103 |

|  |   |            |
|--|---|------------|
| 3.3.3.6  | <i>Delivery of the SBRT thorax phantom plan: Dose profile and gamma map comparisons .....</i> | 105        |
| 3.3.3.7  | <i>Delivery of the IMRT thorax phantom plan: Point dose comparisons.....</i>                  | 110        |
| 3.3.3.8  | <i>Delivery of the IMRT thorax phantom plan: Dose profile and gamma map comparisons .....</i> | 112        |
| 3.3.3.9  | <i>Benchmark summary.....</i>   | 118        |
| 3.4  | CONCLUSION.....   | 120        |
| <b>CHAPTER 4 PATIENT DOSE COMPARISONS: VARIAN 6 MV &amp; 10 MV .....</b> |   | <b>122</b> |
| 4.1  | INTRODUCTION .....  | 122        |
| 4.2  | MATERIAL AND METHODS .....  | 124        |
| 4.2.1  | <i>Recalculations using DPM.....</i>  | 124        |
| 4.2.2  | <i>Patient plan analysis.....</i>   | 125        |
| 4.3  | RESULTS .....   | 126        |
| 4.3.1  | <i>Dose in region of interest.....</i>  | 126        |
| 4.3.2  | <i>Dose distribution analysis.....</i>  | 128        |
| 4.3.2.1  | <i>6 MV IMRT abdomen patient plan.....</i>  | 128        |
| 4.3.2.2  | <i>6 MV SBRT lung patient plan.....</i>   | 130        |
| 4.3.2.3  | <i>10 MV IMRT prostate patient plan .....</i>   | 132        |
| 4.3.2.4  | <i>10 MV IMRT lung patient plan .....</i>   | 134        |
| 4.3.2.5  | <i>6 MV IMRT head and neck phantom plan.....</i>  | 136        |
| 4.3.2.6  | <i>6 MV SBRT lung phantom plan.....</i>   | 139        |
| 4.3.2.7  | <i>6 MV IMRT lung phantom plan .....</i>  | 141        |
| 4.3.2.8  | <i>10 MV IMRT head and neck phantom plan.....</i>   | 142        |
| 4.3.2.9  | <i>10 MV SBRT lung phantom plan.....</i>  | 145        |
| <b>CHAPTER 5 SUMMARY .....</b>   |   | <b>149</b> |

|                  |  |            |
|------------------|--|------------|
| 5.1              | CHAPTER 2 AND CHAPTER 3 SUMMARY FOR VARIAN MACHINE MODELS          | 149        |
| 5.2              | CHAPTER 4 SUMMARY, PATIENT PLANS .....                             | 150        |
| 5.3              | EVALUATION OF THE HYPOTHESIS .....                                 | 151        |
| 5.4              | GENERAL CONCLUSIONS .....  | 152        |
| 5.5              | FUTURE WORK.....   | 152        |
| <b>CHAPTER 6</b> | <b>APPENDIX .....</b>  | <b>154</b> |
| 6.1              | VARIAN 6 MV: PERCENT DEPTH DOSE AND DOSE PROFILES .....            | 154        |
| 6.2              | VARIAN 6 MV: GAMMA MAPS AND DOSE PROFILES.....                     | 164        |
| 6.2.1            | <i>Varian 6 MV: Delivery for the IMRT head and neck plan.....</i>  | <i>164</i> |
| 6.2.2            | <i>Varian 6 MV: Delivery for the SBRT lung plan.....</i>           | <i>167</i> |
| 6.2.3            | <i>Varian 6 MV: Delivery for the IMRT lung plan.....</i>           | <i>173</i> |
| 6.3              | VARIAN 10 MV: GAMMA MAPS AND DOSE PROFILES.....                    | 179        |
| 6.3.1            | <i>Varian 10 MV: Delivery for the IMRT head and neck plan.....</i> | <i>179</i> |
| 6.3.2            | <i>Varian 10 MV: Delivery for the SBRT lung plan.....</i>          | <i>182</i> |
| 6.3.3            | <i>Varian 10 MV: Delivery for the IMRT lung plan.....</i>          | <i>188</i> |
| <b>CHAPTER 7</b> | <b>ACKNOWLEDGEMENT .....</b>                                       | <b>194</b> |
| <b>CHAPTER 8</b> | <b>REFERENCES.....</b>   | <b>195</b> |
| <b>CHAPTER 9</b> | <b>VITA.....</b>   | <b>203</b> |

## LIST OF ILLUSTRATIONS

|  |    |
|--|----|
| Figure 2.1 Step one of the source model commissioning process. ....  | 14 |
| Figure 2.2 Step two of the source model commissioning process .....  | 15 |
| Figure 2.3 MLC offset position, $x_{pen}$ , with relationship to source size, $s_r$ . The position of the<br>MLC leaf, $x_{mlc}$ , is shown for reference.....   | 17 |
| Figure 2.4 (a) The RPC head and neck phantom. (b) The RPC thorax phantom.....  | 18 |
| Figure 2.5 Asterisk (*) indicates the region of the axial cross plane where separation exists<br>between superior portion and inferior portion of sagittal or coronal film .....   | 22 |
| Figure 2.6 Gamma Map. The regions outlined in ‘white’ represent the estimated area that was<br>not included in the gamma index calculation. The left figure is a representative<br>coronal plane and the right figure is a representative sagittal plane from the thorax<br>phantom. Scale: 1 mm = 0.65 mm.....  | 23 |
| Figure 2.7 Gamma Map. The regions outlined in ‘white’ represent the estimated area that was<br>not included in the gamma index calculation. The figure is representative of the<br>sagittal plane from the head and neck phantom. Scale: 1 mm = 1.09 mm .....  | 24 |
| Figure 2.8 Transverse slice through the center of the targets of the head and neck phantom.<br>Contour colors are as follows: red (primary target); aqua (secondary target); violet<br>(critical structure, spinal cord). Note the dark dots are the TLD measurement<br>locations.....   | 25 |
| Figure 2.9 Transverse slice through the center of the target of the thorax phantom. Contour<br>colors are as follows: green (GTV); aqua (critical structure, heart); violet (critical<br>structure, spinal cord). Note the dark dot in each of the three regions is the TLD<br>measurement location. The TLD location for the target is adjacent the center in<br>the posterior-lateral distal direction. .... | 26 |

|  |    |
|--|----|
| Figure 2.10 Varian 6 MV spectrum: Commissioned source model compared to BEAM spectrum <sup>29</sup> .....  | 28 |
| Figure 2.11 Output factor at $d_{\max}$ versus field size for the measured, calculated and corrected output. A hyperbola curve was determined to correct the calculated values. ....   | 30 |
| Figure 2.12 Calculated and measured percent depth dose curves at 6 MV for a 4 cm x 4 cm field. ....  | 32 |
| Figure 2.13 Calculated and measured percent depth dose curves at 6 MV for a 10 cm x 10 cm field. ....  | 33 |
| Figure 2.14 Calculated and measured percent depth dose curves at 6 MV for a 40 cm x cm 40 field. ....  | 34 |
| Figure 2.15 Calculated and measured dose profiles at 6 MV from a 4 cm by 4 cm field at depths of 1.5 cm, 6 cm, 12.5 cm, and 22 cm. ....  | 36 |
| Figure 2.16 Calculated and measured dose profiles at 6 MV from a 10 cm by 10 cm field at depths of 1.5 cm, 6 cm, 12.5 cm, and 22 cm. ....  | 37 |
| Figure 2.17 Calculated and measured dose profiles at 6 MV from a 40 cm by 40 cm field at depths of 1.5 cm, 6 cm, 12.5 cm, and 22 cm. ....  | 38 |
| Figure 2.18 Frequency histogram of the aperture distances of opposing leaf ends from the IMRT head and neck plan, the SBRT lung plan, and the IMRT lung plan. ....   | 42 |
| Figure 2.19 IMRT H&N delivery single irradiation (number 2): Lateral dose profile. ....  | 45 |
| Figure 2.20 IMRT H&N delivery single irradiation (number 2): A-to-P dose profile. ....   | 45 |
| Figure 2.21 IMRT H&N delivery single irradiation (number 2): S-to-I dose profile. ....   | 46 |
| Figure 2.22 IMRT H&N delivery single irradiation (number 2): Axial plane, gamma map tested to 3%/2 mm criteria, where 94% of the data passed. Scale is 1 mm = 0.95 mm. Small circle outline represents the location of the secondary PTV, large crescent shaped outline represents the primary PTV, and the small red circle represents the spinal cord critical structure. .... | 47 |

|   |    |
|---|----|
| Figure 2.23 IMRT H&N delivery single irradiation (number 2): Sagittal plane; gamma map tested to 3%/2 mm criteria, where 91% of the data passed. Scale is 1 mm = 1.3 mm. Rectangle outline represents the location of the primary PTV. The maroon region in the vertical direction is where the film has been cut away to avoid interference with the critical structure region. .... | 47 |
| Figure 2.24 IMRT head and neck: Gamma maps (a and b) and lateral dose profiles (c and d) from the same irradiation, but before (a and c) and after (b and d) changes to the model to improve the penumbra. ....   | 48 |
| Figure 2.25 Gamma map (a through d) and dose profile (e through g) comparisons between the Pinnacle calculation and measurement for the IMRT H&N delivery (single irradiation, number 2) .....  | 49 |
| Figure 2.26 SBRT lung delivery single irradiation (number 1): lateral dose profile. ....  | 52 |
| Figure 2.27 SBRT lung delivery single irradiation (number 1): A-P dose profile.....   | 53 |
| Figure 2.28 SBRT lung delivery single irradiation (number 1): S-I dose profile. ....  | 53 |
| Figure 2.29 SBRT lung delivery single irradiation (number 1): Axial plane, gamma map tested to 3%/2 mm criteria, where 90% of the data passed. Scale is 1 mm = 0.8 mm. Circle outline represents the location of the PTV.....   | 54 |
| Figure 2.30 SBRT lung delivery single irradiation (number 1): Sagittal plane, gamma map tested to 3%/2 mm criteria, where 95% of the data passed. Scale is 1 mm = 0.65 mm. Elongated circle outline represents the location of the PTV. ....  | 55 |
| Figure 2.31 SBRT lung delivery single irradiation (number 1): Coronal plane, gamma map tested to 3%/2 mm criteria, where 93% of the data passed. Scale is 1 mm = 0.65 mm. Elongated circle outline represents the location of the PTV. ....   | 55 |
| Figure 2.32 Gamma map and dose profile comparisons between the Pinnacle calculation and measurement for the SBRT lung delivery (single irradiation, number 1) .....   | 57 |
| Figure 2.33 IMRT lung delivery single irradiation (number 3): lateral dose profile. ....  | 60 |



|  |    |
|--|----|
| Figure 2.34 IMRT lung delivery single irradiation (number 3): A-P dose profile.....  | 60 |
| Figure 2.35 IMRT lung delivery single irradiation (number 3): S-I dose profile. ....   | 61 |
| Figure 2.36 IMRT lung delivery single irradiation (number 3): Axial plane, gamma map tested<br>to 3%/2 mm criteria, where 92% of the data passed. Scale is 1 mm = 0.8 mm.<br>Circle outline represents the location of the PTV.....  | 62 |
| Figure 2.37 IMRT lung delivery single irradiation (number 3): Sagittal plane, gamma map<br>tested to 3%/2 mm criteria, where 91% of the data passed. Scale is 1 mm = 0.65<br>mm. Elongated circle outline represents the location of the PTV. ....   | 62 |
| Figure 2.38 IMRT lung delivery single irradiation (number 3): Coronal plane, gamma map<br>tested to 3%/2 mm criteria, where 84% of the data passed. Scale is 1 mm = 0.65<br>mm. Elongated circle outline represents the location of the PTV. ....  | 63 |
| Figure 2.39 Gamma map and dose profile comparisons between the Pinnacle calculation and<br>measurement for the IMRT lung delivery (single irradiation, number 2) .....   | 64 |
| Figure 3.1 CT images of head and neck plans used for benchmark testing. Left image used<br>with Varian 6 MV model. Right image used for Varian 10 MV image. Viewed I<br>to S.....  | 75 |
| Figure 3.2 Varian 10 MV spectrum: Commissioned source model compared to BEAM<br>spectrum <sup>29</sup> .....   | 79 |
| Figure 3.3 Output factor at $d_{max}$ versus field size for the measured, calculated and corrected<br>output. A hyperbola curve was determined to correct the calculated values.....   | 82 |
| Figure 3.4 Plot of the relative electron contamination as a percentage of the dose relative to the<br>primary source as a function of field size. ....   | 83 |
| Figure 3.5 Percent depth dose of 4 cm x 4 cm field size showing build-up region for the<br>measured and calculated data sets. The plot includes the change in the electron<br>contamination with field size (corrected) versus a constant contribution, regardless<br>of field size (uncorrected)..... | 84 |

|  |    |
|--|----|
| Figure 3.6 Percent depth dose of 40cm x 40 cm field size showing build-up region for the measured and calculated data sets. The plot includes the change in the electron contamination with field size (corrected) versus a constant contribution, regardless of field size (uncorrected).   | 85 |
| Figure 3.7 Calculated and measured percent depth dose curves at 10 MV for a 4 cm x 4 cm field.   | 86 |
| Figure 3.8 Calculated and measured percent depth dose curves at 10 MV for a 10 cm x 10 cm field.   | 87 |
| Figure 3.9 Calculated and measured percent depth dose curves at 10 MV for a 40 cm x 40 cm field.   | 87 |
| Figure 3.10 Calculated and measured dose profiles at 10 MV from a 4 cm by 4 cm field at depths of 2.4 cm, 5 cm, 10 cm, and 20 cm.  | 89 |
| Figure 3.11 Calculated and measured dose profiles at 10 MV from a 10 cm by 10 cm field at depths of 2.4 cm, 5 cm, 10 cm, and 20 cm.  | 90 |
| Figure 3.12 Calculated and measured dose profiles at 10 MV from a 40 cm by 40 cm field at depths of 2.4 cm, 5 cm, 10 cm, and 20 cm.  | 91 |
| Figure 3.13 Dose profile agreement between calculated and measured data. Profiles are from the depths of 2.4 cm, 5 cm, 10 cm, and 20 cm for each field size. Minimum percentage of the data meeting the criteria of 2% of $d_{max}$ or 2 mm DTA and the percent difference is the average of all local percent differences from all of the profiles for a given field. | 92 |
| Figure 3.14 Frequency histogram of the aperture distances of opposing leaf ends from the IMRT head and neck plan, the SBRT lung plan, and the IMRT lung plan.  | 95 |
| Figure 3.15 IMRT H&N delivery single irradiation (number 3): Lateral dose profile.   | 98 |
| Figure 3.16 IMRT H&N delivery single irradiation (number 3): A-to-P dose profile.  | 98 |
| Figure 3.17 IMRT H&N delivery single irradiation (number 3): S-to-I dose profile.  | 99 |

|   |     |
|---|-----|
| Figure 3.18 IMRT H&N delivery single irradiation (number 3): Axial plane, gamma map tested to 3%/2 mm criteria, where 99% of the data passed. Scale is 1 mm = 0.95 mm. Small circle outline represents the location of the secondary PTV, large crescent shaped outline represents the primary PTV, and the small red circle represents the spinal cord critical structure.....       | 100 |
| Figure 3.19 IMRT H&N delivery single irradiation (number 3): Sagittal plane; gamma map tested to 3%/2 mm criteria, where 93% of the data passed. Scale is 1 mm = 1.3 mm. Rectangle outline represents the location of the primary PTV. The maroon region in the vertical direction is where the film has been cut away to avoid interference with the critical structure region. .... | 100 |
| Figure 3.20 IMRT head and neck: Gamma maps (a and b) and lateral dose profiles (c and d) from the same irradiation, but before (a and c) and after (b and d) changes to the model to improve the penumbra. ....   | 101 |
| Figure 3.21 Gamma map (a thru d) and dose profile (e thru g) comparisons between the Pinnacle calculation and measurement for the IMRT H&N delivery (single irradiation, no. 3). The gamma map comparisons show results with differing criteria (3%/2 mm vs. 5%/3 mm). ....   | 102 |
| Figure 3.22 SBRT lung delivery single irradiation (number 1): lateral dose profile. ....  | 105 |
| Figure 3.23 SBRT lung delivery single irradiation (number 1): A-P dose profile.....   | 106 |
| Figure 3.24 SBRT lung delivery single irradiation (number 1): S-I dose profile. ....  | 106 |
| Figure 3.25 SBRT lung delivery single irradiation (number 1): Axial plane, gamma map tested to 3%/2 mm criteria, where 98% of the data passed. Scale is 1 mm = 0.8 mm. Circle outline represents the location of the PTV.....   | 107 |
| Figure 3.26 SBRT lung delivery single irradiation (number 1): Sagittal plane, gamma map tested to 3%/2 mm criteria, where 97% of the data passed. Scale is 1 mm = 0.65 mm. Elongated circle outline represents the location of the PTV. ....  | 108 |

|  |     |
|--|-----|
| Figure 3.27 SBRT lung delivery single irradiation (number 1): Coronal plane, gamma map tested to 3%/2 mm criteria, where 98% of the data passed. Scale is 1 mm = 0.65 mm. Elongated circle outline represents the location of the PTV. ....  | 108 |
| Figure 3.28 Gamma map and dose profile comparisons between the Pinnacle calculation and measurement for the SBRT lung delivery (single irradiation, number 1) .....  | 110 |
| Figure 3.29 IMRT lung delivery single irradiation (number 1): lateral dose profile. ....   | 113 |
| Figure 3.30 IMRT lung delivery single irradiation (number 1): A-P dose profile.....  | 113 |
| Figure 3.31 IMRT lung delivery single irradiation (number 1): S-I dose profile. ....   | 114 |
| Figure 3.32 IMRT lung delivery single irradiation (number 1): Axial plane, gamma map tested to 3%/2 mm criteria, where 92% of the data passed. Scale is 1 mm = 0.8 mm. Circle outline represents the location of the PTV.....                | 115 |
| Figure 3.33 IMRT lung delivery single irradiation (number 1): Sagittal plane, gamma map tested to 3%/2 mm criteria, where 84% of the data passed. Scale is 1 mm = 0.65 mm. Elongated circle outline represents the location of the PTV. .... | 115 |
| Figure 3.34 IMRT lung delivery single irradiation (number 1): Coronal plane, gamma map tested to 3%/2 mm criteria, where 86% of the data passed. Scale is 1 mm = 0.65 mm. Elongated circle outline represents the location of the PTV. ....  | 116 |
| Figure 3.35 Gamma map and dose profile comparisons between the Pinnacle calculation and measurement for the IMRT lung delivery (single irradiation, number 1) .....  | 117 |
| Figure 4.1 DVH of the 6 MV IMRT abdomen patient plan for the PTV and the left (Lt) kidney. ....  | 129 |
| Figure 4.2 Gamma map (5%, 3mm) of the 6 MV IMRT abdomen patient plan and associated axial CT image with DPM calculated dose distribution. The black arrow shows the dose line profile in the CT image for Figure 4.3.....                    | 129 |
| Figure 4.3 Dose (cGy) line profile comparing TPS and DPM calculations. Location of profile is shown in the CT image of Figure 4.2.....   | 130 |

|  |     |
|--|-----|
| Figure 4.4 DVH of the 6 MV SBRT lung patient plan for the GTV, PTV, left (lt) kidney lung, and cord. ....  | 131 |
| Figure 4.5 Gamma map (5%, 3mm) of the 6 MV SBRT lung patient plan and associated axial CT image with DPM calculated dose distribution. The black arrow shows the dose line profile in the CT image for Figure 4.6. ....            | 131 |
| Figure 4.6 Dose (cGy) line profile comparing TPS and DPM calculations. Location of profile is shown in the CT image of Figure 4.5.....   | 132 |
| Figure 4.7 DVH of the 10 MV IMRT prostate patient plan for the PTV, anus-rectum, and the right (R) femoral head. ....  | 133 |
| Figure 4.8 Gamma map (5%, 3mm) of the 10 MV IMRT prostate patient plan and associated axial CT image with DPM calculated dose distribution. The black arrow shows the dose line profile in the CT image for Figure 4.9.....        | 134 |
| Figure 4.9 Dose (cGy) line profile comparing TPS and DPM calculations. Location of profile is shown in the CT image of Figure 4.8.....   | 134 |
| Figure 4.10 DVH of the 10 MV IMRT lung patient plan for the PTV, carina, esophagus, and the lungs.....   | 135 |
| Figure 4.11 Gamma map (5%, 3mm) of the 10 MV IMRT lung patient plan and associated axial CT image with DPM calculated dose distribution. The black arrow shows the dose line profile in the CT image for Figure 4.12. ....         | 136 |
| Figure 4.12 Dose (cGy) line profile comparing TPS and DPM calculations. Location of profile is shown in the CT image of Figure 4.11.....   | 136 |
| Figure 4.13 DVH of the 6 MV IMRT head and neck phantom plan for the primary, secondary, and the cord (CS). ....  | 137 |
| Figure 4.14 Gamma map (5%, 3mm) of the 6 MV IMRT head and neck phantom plan and associated axial CT image with DPM calculated dose distribution. The black arrow shows the dose line profile in the CT image for Figure 4.15. .... | 138 |

|   |     |
|---|-----|
| Figure 4.15 Dose (cGy) line profile comparing TPS and DPM calculations. Location of profile is shown in the CT image of Figure 4.14.....  | 138 |
| Figure 4.16 DVH of the 6 MV SBRT lung phantom plan for the target, PTV, left (LT) lung (net), and the heart. ....   | 139 |
| Figure 4.17 Gamma map (5%, 3mm) of the 6 MV SBRT lung phantom plan and associated axial CT image with DPM calculated dose distribution. The black arrow shows the dose line profile in the CT image for Figure 4.18.....            | 140 |
| Figure 4.18 Dose (cGy) line profile comparing TPS and DPM calculations. Location of profile is shown in the CT image of Figure 4.17.....  | 140 |
| Figure 4.19 DVH of the 6 MV IMRT lung phantom plan for the GTV, PTV, left (LT) lung, and the heart. ....  | 141 |
| Figure 4.20 Gamma map (5%, 3mm) of the 6 MV IMRT lung phantom plan and associated axial CT image with DPM calculated dose distribution. The black arrow shows the dose line profile in the CT image for Figure 4.21.....            | 142 |
| Figure 4.21 Dose (cGy) line profile comparing TPS and DPM calculations. Location of profile is shown in the CT image of Figure 4.20.....  | 142 |
| Figure 4.22 DVH of the 10 MV IMRT head and neck phantom plan for the primary (PTV-66), secondary (PTV-54), and the cord (CS). ....  | 143 |
| Figure 4.23 Gamma map (5%, 3mm) of the 10 MV IMRT head and neck phantom plan and associated axial CT image with DPM calculated dose distribution. The black arrow shows the dose line profile in the CT image for Figure 4.24. .... | 144 |
| Figure 4.24 Dose (cGy) line profile comparing TPS and DPM calculations. Location of profile is shown in the CT image of Figure 4.23.....  | 144 |
| Figure 4.25 DVH of the 10 MV SBRT lung phantom plan for the target, PTV, left (LT) lung (net), and the heart. ....  | 145 |

|   |     |
|---|-----|
| Figure 4.26 Gamma map (5%, 3mm) of the 10 MV SBRT lung phantom plan and associated axial CT image with DPM calculated dose distribution. The black arrow shows the dose line profile in the CT image for Figure 4.27..... | 146 |
| Figure 4.27 Dose (cGy) line profile comparing TPS and DPM calculations. Location of profile is shown in the CT image of Figure 4.26.....  | 146 |
| Figure 4.28 DVH of the 10 MV IMRT lung phantom plan for the target, PTV, left (LT) lung (net), and the heart .....  | 147 |
| Figure 4.29 Gamma map (5%, 3mm) of the 10 MV IMRT lung phantom plan and associated axial CT image with DPM calculated dose distribution. The black arrow shows the dose line profile in the CT image for Figure 4.30..... | 148 |
| Figure 4.30 Dose (cGy) line profile comparing TPS and DPM calculations. Location of profile is shown in the CT image of Figure 4.29.....  | 148 |
| Figure 6.1 Calculated and measured percent depth dose curves at 6 MV from a 4 cm by 4 cm field.....   | 154 |
| Figure 6.2 Calculated and measured dose profiles at 6 MV from a 4 cm by 4 cm field at depths of 1.5 cm, 6 cm, 12.5 cm, and 22 cm.....   | 155 |
| Figure 6.3 Calculated and measured percent depth dose curves at 6 MV from a 5 cm by 5 cm field.....   | 155 |
| Figure 6.4 Calculated and measured dose profiles at 6 MV from a 5 cm by 5 cm field at depths of 1.5 cm, 6 cm, 12.5 cm, and 22 cm.....   | 156 |
| Figure 6.5 Calculated and measured percent depth dose curves at 6 MV from a 6 cm by 6 cm field.....   | 156 |
| Figure 6.6 Calculated and measured dose profiles at 6 MV from a 6 cm by 6 cm field at depths of 1.5 cm, 6 cm, 12.5 cm, and 22 cm.....   | 157 |
| Figure 6.7 Calculated and measured percent depth dose curves at 6 MV from a 8 cm by 8 cm field.....   | 157 |

|   |     |
|---|-----|
| Figure 6.8 Calculated and measured dose profiles at 6 MV from a 8 cm by 8 cm field at depths of 1.5 cm, 6 cm, 12.5 cm, and 22 cm.....     | 158 |
| Figure 6.9 Calculated and measured percent depth dose curves at 6 MV from a 10 cm by 10 cm field.....                                     | 158 |
| Figure 6.10 Calculated and measured dose profiles at 6 MV from a 10 cm by 10 cm field at depths of 1.5 cm, 6 cm, 12.5 cm, and 22 cm. .... | 159 |
| Figure 6.11 Calculated and measured percent depth dose curves at 6 MV from a 15 cm by 15 cm field. ....                                   | 159 |
| Figure 6.12 Calculated and measured dose profiles at 6 MV from a 15 cm by 15 cm field at depths of 1.5 cm, 6 cm, 12.5 cm, and 22 cm. .... | 160 |
| Figure 6.13 Calculated and measured percent depth dose curves at 6 MV from a 20 cm by 20 cm field. ....                                   | 160 |
| Figure 6.14 Calculated and measured dose profiles at 6 MV from a 20 cm by 20 cm field at depths of 1.5 cm, 6 cm, 12.5 cm, and 22 cm. .... | 161 |
| Figure 6.15 Calculated and measured percent depth dose curves at 6 MV from a 25 cm by 25 cm field. ....                                   | 161 |
| Figure 6.16 Calculated and measured dose profiles at 6 MV from a 25 cm by 25 cm field at depths of 1.5 cm, 6 cm, 12.5 cm, and 22 cm. .... | 162 |
| Figure 6.17 Calculated and measured percent depth dose curves at 6 MV from a 40 cm by 40 cm field. ....                                   | 162 |
| Figure 6.18 Calculated and measured dose profiles at 6 MV from a 40 cm by 40 cm field at depths of 1.5 cm, 6 cm, 12.5 cm, and 22 cm. .... | 163 |
| Figure 6.19 Varian 6 MV: IMRT H&N delivery single irradiation (number 1): Gamma maps and dose profiles. ....                              | 164 |
| Figure 6.20 Varian 6 MV: IMRT H&N delivery single irradiation (number 2): Gamma maps and dose profiles. ....                              | 165 |



|   |     |
|---|-----|
| Figure 6.21 Varian 6 MV: IMRT H&N delivery single irradiation (number 3): Gamma maps and dose profiles.....   | 166 |
| Figure 6.22 Varian 6 MV: SBRT lung delivery single irradiation (number 1): Gamma maps and dose profiles.....  | 168 |
| Figure 6.23 Varian 6 MV: SBRT lung delivery single irradiation (number 2): Gamma maps and dose profiles.....  | 170 |
| Figure 6.24 Varian 6 MV: SBRT lung delivery single irradiation (number 3): Gamma maps and dose profiles.....  | 172 |
| Figure 6.25 Varian 6 MV: IMRT lung delivery single irradiation (number 1): Gamma maps and dose profiles.....  | 174 |
| Figure 6.26 Varian 6 MV: IMRT lung delivery single irradiation (number 2): Gamma maps and dose profiles.....  | 176 |
| Figure 6.27 Varian 6 MV: IMRT lung delivery single irradiation (number 3): Gamma maps and dose profiles.....  | 178 |
| Figure 6.28 Varian 10 MV: IMRT H&N delivery single irradiation (number 1): Gamma maps and dose profiles.....  | 179 |
| Figure 6.29 Varian 10 MV: IMRT H&N delivery single irradiation (number 2): Gamma maps and dose profiles.....  | 180 |
| Figure 6.30 Varian 10 MV: IMRT H&N delivery single irradiation (number 3): Gamma maps and dose profiles.....  | 181 |
| Figure 6.31 Varian 10 MV: SBRT lung delivery single irradiation (number 1): Gamma maps and dose profiles..... | 183 |
| Figure 6.32 Varian 10 MV: SBRT lung delivery single irradiation (number 2): Gamma maps and dose profiles..... | 185 |
| Figure 6.33 Varian 10 MV: SBRT lung delivery single irradiation (number 3): Gamma maps and dose profiles..... | 187 |

|  |     |
|--|-----|
| Figure 6.34 Varian 10 MV: IMRT lung delivery single irradiation (number 1): Gamma maps<br>and dose profiles..... | 189 |
| Figure 6.35 Varian 10 MV: IMRT lung delivery single irradiation (number 2): Gamma maps<br>and dose profiles..... | 191 |
| Figure 6.36 Varian 10 MV: IMRT lung delivery single irradiation (number 3): Gamma maps<br>and dose profiles..... | 193 |

## LIST OF TABLES

|   |    |
|---|----|
| Table 1 Parameters of the commissioned source model for spectra, fluence, and profile<br>penumbra measurement effect.....   | 27 |
| Table 2 Coefficients of a piecewise linear function to describe the increase of fluence as the off-axis angle increases (horn-effect) .....   | 29 |
| Table 3 Dose profile agreement between calculated and measured data. Profiles are from the depths of 1.5 cm, 6 cm, 12.5 cm, and 22 cm for each field size. Minimum percentage of the data meeting the criteria of 2% of $d_{max}$ or 2 mm DTA and the percent difference is the average of all local percent differences from all of the profiles for a given field.....  | 39 |
| Table 4 Point dose comparisons of the IMRT head and neck phantom. The measured dose is the average dose from the three repeated irradiations. Calculated results are from DPM. The Pinnacle calculation is provided for reference. Point dose locations are keyed as follows: Pri = primary target; Sec = secondary target; CS = critical structure; S = superior; I = inferior; A = anterior; P = posterior..... | 43 |
| Table 5 IMRT head and neck: The range and average calculation to TLD measurement ratio of the point doses for the primary and secondary targets and critical structure for DPM and Pinnacle. The data is for each TLD location from each repeated irradiations....  | 44 |
| Table 6 Point dose comparisons of the SBRT thoracic phantom. The measured dose is the average dose from the three repeated irradiations. Calculated results are from DPM. The Pinnacle calculation is provided for reference. ....  | 50 |
| Table 7 SBRT lung plan: The range and average calculation to measurement ratio of the point doses for the target, cord, and heart for DPM and Pinnacle. The data is for each TLD location from each repeated irradiations.....  | 51 |

|  |    |
|--|----|
| Table 8 Point dose comparisons of the IMRT thoracic phantom. The measured dose is the average dose from the three repeated irradiations. Calculated results are from DPM. The Pinnacle calculation is provided for reference. ....   | 58 |
| Table 9 IMRT lung: The range and average calculation to measurement ratio of the point doses for the target, cord, and heart for DPM and Pinnacle. The data is for each TLD location from each repeated irradiations.....  | 59 |
| Table 10 Varian 6 MV: The average and range of the percentage of data from meeting criteria from the gamma index of 3%/2 mm for repeated irradiations from each treatment plan. ....   | 65 |
| Table 11 Parameters of the commissioned source model for spectra, fluence, and profile penumbra measurement effect.....  | 78 |
| Table 12 Coefficients of a piecewise linear function to describe the increase of fluence as the off-axis angle increases (horn-effect) .....   | 80 |
| Table 13 Percent differences of the EUD of the MLC offset opening of 0.4 mm (applied to each leaf; applied to each segment for IMRT) with respect to no offset (DICOM file with no change). Table compares the EUD for the PTV structure for the Varian 6 MV and 10 MV source models.....  | 94 |
| Table 14 Point dose comparisons of the IMRT head and neck phantom. The measured dose is the average dose from the three repeated irradiations. Calculated results are from DPM. The Pinnacle calculation is provided for reference. Point dose locations are keyed as follows: Pri = primary target; Sec = secondary target; CS = critical structure; S = superior; I = inferior; A = anterior; P = posterior..... | 96 |
| Table 15 IMRT head and neck: The range and average calculation to TLD measurement ratio of the point doses for the primary and secondary targets and critical structure for DPM and Pinnacle. The data is for each TLD location from each repeated irradiations. ....  | 97 |

|   |     |
|---|-----|
| Table 16 Point dose comparisons of the SBRT thoracic phantom. The measured dose is the average dose from the three repeated irradiations. Calculated results are from DPM. The Pinnacle calculation is provided for reference. ....                             | 103 |
| Table 17 SBRT lung plan: The range and average calculation to measurement ratio of the point doses for the target, cord, and heart for DPM and Pinnacle. The data is for each TLD location from each repeated irradiations.....                                 | 104 |
| Table 18 Point dose comparisons of the IMRT thoracic phantom. The measured dose is the average dose from the three repeated irradiations. Calculated results are from DPM. The Pinnacle calculation is provided for reference. ....                             | 111 |
| Table 19 IMRT lung: The range and average calculation to measurement ratio of the point doses for the target, cord, and heart for DPM and Pinnacle. The data is for each TLD location from each repeated irradiations.....                                      | 112 |
| Table 20 Varian 6 MV and 10 MV: The average and range of the percentage of data from meeting criteria from the gamma index of 3%/2 mm for repeated irradiations from each treatment plan. Values in parenthesis are corresponding numbers for 6 MV results..... | 118 |
| Table 21 Ratio of TPS calculation to DPM calculation for mean dose to GTV, PTV, and critical structure for patient and phantom plans. Performance trends are similar as noted by SBRT plans.....  | 126 |
| Table 22 Comparison of calculation and measurement in GTV for 6 MV IMRT head and neck plan. Benchmark phantom and IMRT QA phantom included.....   | 127 |

# **Chapter 1 Introduction**

## **1.1 STATEMENT OF PROBLEM**

The Radiological Physics Center (RPC) is one of three quality assurance (QA) offices funded by the National Cancer Institute (NCI) that provides quality audit services for institutions participating in NCI cooperative clinical trials. In the past twenty years the number of quality assurance offices has been reduced by half, while the number of participating institutions has more than doubled to nearly 1,700. In response to this increase in demand, the RPC has evolved to develop several programs to efficiently provide improved dosimetric and QA services to the clinical trial community. These programs include on-site audit evaluations and remote audit tools. The on-site evaluation includes interviewing the institution's physics and oncology personnel, performing physical measurements of the therapy machines, and reviewing quality control procedures, basic machine dosimetry data, and patient dose calculations. The remote audit tools include review of patient dose calculations, credentialing institutions for participation in specific protocols utilizing advanced radiotherapy technology, verification of reference beam output with thermoluminescent detectors (TLD), and evaluation of advanced technology treatments with anthropomorphic QA phantoms. The anthropomorphic phantom remote audit tool using TLD and radiochromic film enables comparison between measurement of the actual delivered dose distribution and the institutions' planned treatment which includes the dose calculation algorithm of the patient plan.

Although measurement based comparisons have traditionally provided an acceptable assurance in determining an institution's performance in terms of correct dose delivery, there has been growing concern that today's advances in therapy equipment including multi-leaf collimators and dynamic wedges, and other advances in treatment technique conformality such as three-dimensional stereotactic radiotherapy and intensity-modulated radiation therapy

(IMRT), have pushed the limits of measurement uncertainty.<sup>1</sup> In part, this is due to the common occurrence of steep dose gradients found in today's conformal treatments comprised of multiple segmented fields delivered per gantry angle. In addition to the uncertainties associated with TLD and radiochromic film, the RPC has published the results from their remote anthropomorphic phantom audit program detailing the ability of institutions that participate in clinical trials to conform to prescribed treatment plans. The results also show a varying degree of compliance even for treatment plans from the same treatment planning system (TPS).<sup>2-6</sup> The TPS dose calculation algorithm, the beam model commissioning process, and delivery may contribute to these discrepancies. These differences have caused concern over an institution's ability to consistently deliver IMRT treatments and/or perform consistent heterogeneous dose calculations for patients entered onto clinical trials. The use of a trusted independent dose calculation such as, the Monte Carlo (MC) technique can help to improve the understanding of the dose delivered by bridging the gap between the actual dosimetry and the TPS's predicted dose distributions. Such a tool that is capable of being applied to a majority of patient plans across many institutions and linear accelerator platforms can aid in the reduction of dose uncertainty by providing a centralized dose calculation method for treatment verification and retrospective dose response analysis.

The MC dose calculation method is a statistical method for numerical integration that relies on the probability distributions describing the individual interactions of electrons and photons in a given set of materials. The simulation of the histories is tracked to provide the information about the average quantities, such as dose. Several MC codes, such as EGS4<sup>7</sup>, MCNP<sup>8</sup>, and PENELOPE<sup>9</sup> are widely available and have been extensively benchmarked. The MC method in general is regarded as the most accurate computational method currently available for determining dose, especially in heterogeneous patient tissues such as the lung.<sup>10</sup> Much of the motivation for the need for MC dose calculations comes from the variations found in numerous reports comparing the more accurate MC dose calculation to the conventional

calculation methods, such as the correction based methods<sup>11-16</sup> and the convolution superposition (CS) method.<sup>17-19</sup> It is clear that correction based calculations, which do not account for lateral scatter and electron transport, tend to overestimate dose and underestimate the penumbra broadening in cases involving lung tumors. It is not clear how significant the improvement in accuracy is for the MC method when compared to the CS method. Arnfield et al<sup>19</sup> did report on the improved accuracy of the MC method when compared to the SC method in the application of an 18 MV photon beam, but found little difference for a 6 MV photon beam when irradiating a lung equivalent slab phantom using a 4 x 4 cm<sup>2</sup> field size. Various studies have reported differences between the MC and SC methods when comparing patient plans.<sup>12,13,20,21</sup> The MC method has found growing widespread use in medical physics to complement measurements and traditional analytical based numerical calculations. Even though MC calculations have gained a great deal of attention in the medical physics research community recently, its progress has been slowed due to the enormous amount of computational power necessary to perform the dose calculations with the accuracy that is required in radiation oncology. With time, it is expected that computing power requirements will be met making the MC dose calculation an efficient and common tool in a clinical setting. In the meantime, researchers have reported on alternatives to the pure computationally intensive MC method, e.g., EGS4, MCNP, and PENELOPE, in an effort to increase the speed of computing.<sup>22</sup>

One such MC computational method, and the method of choice for this project, is the Dose Planning Method (DPM).<sup>22</sup> This method was largely chosen because its source code is open to allow for modifications and interfacing. DPM uses the standard condensed history model for electron transport referred to as a mixed class simulation scheme as described by Berger.<sup>23</sup> Here, large energy transfer collisions are handled by direct sampling of the distance to next collision using the total electron interaction cross-section and small collisions are modeled by the continuous slowing down approximation (CSDA). Photon transport for



photoelectric absorption, Compton scatter, and pair production is handled interaction-by-interaction. The transport mechanics have been reformulated to increase the computing speed by enabling large electron transport steps even across heterogeneous boundaries while adhering to the applied multiple scattering distribution theory. DPM has been shown to reproduce electron beam dose distributions calculated with EGS4 and PENELOPE MC codes with differences of less than 1.25% and a statistical uncertainty on the order of 0.2% of the dose maximum using in a variety of different materials.<sup>22</sup> DPM has recently begun to find increased clinical use. The University of Michigan in-house treatment planning system (UMPlan) uses DPM in a variety of photon treatment planning studies.<sup>24</sup> Recently, Fragoso et al<sup>25</sup> have evaluated a preclinical version of an electron beam dose calculation algorithm from Pinnacle (Philips Medical Systems, Andover, MA) that employed DPM based on a parameterized beam model which included a primary electron source and a contaminant photon source. They found differences were, on average, 2% or 2 mm between measurement and calculation. However, differences of 3% to 4% were found in the off-axis profiles for the largest applicator sizes.

The MC dose calculation requires a beam model of the linear accelerator (linac) to describe the photon fluence and energy distributions in the radiation field. Three common beam model approaches<sup>10</sup> include the full MC simulation of the geometry of the linac head including the MLCs, a multiple-source model derived from the original head simulation with or without modifications from measurements, and a multiple-source model whose analytical function parameters are derived by a standard set of measurements. We have chosen to apply the latter, a parameterized multi-source model derived from a standard set of measurements, for its simplicity and generic applicability. Using a parameterized source model approach facilitates the unique representation of a particular linac make. This is not easily done using the traditional MC codes such as EGS4 and MCNP that require detailed drawings defining a particular make of linac in order to describe the treatment head geometry and material composition. Coupling this source model to DPM provides a generic solution for an

independent dose calculation tool. Originally developed by Joseph Deasy and his research group at Washington University in St. Louis, the multiple-source model is comprised of three sources; a primary source, an extra-focal source, and a source for electron contamination.<sup>26</sup> The primary point source represents isotropically distributed primary photons from the target. This distribution is modified by the horn-effect using a piecewise linear function to represent the increase of fluence as the off-axis angle increases due to the flattening filter selectively absorbing a number of lower energy photons near the central axis as a function of the filter thickness. As a result, the average mean energy becomes lower as the off-axis angle increase (off-axis softening). The off-axis softening is accounted for by relating the off-axis half-value layer (HVL) as a function of the off-axis angle.<sup>27</sup> The photon energy spectrum is described by the product of the Fatigue-Life distribution<sup>28</sup> and the Fermi function [Equation 1].

$$f(E) = \left( \frac{\sqrt{\frac{E-\mu}{\beta}} + \sqrt{\frac{\beta}{E-\mu}}}{2\gamma E - \mu} \right) \left( \frac{\exp \left( -\frac{1}{2} \left[ \frac{\sqrt{\frac{E-\mu}{\beta}} - \sqrt{\frac{\beta}{E-\mu}}}{\gamma} \right]^2 \right)}{\sqrt{2\pi}} \right) \left( \frac{1}{1 + \exp \left( \frac{E - E_F}{kT} \right)} \right) \quad (1)$$

where,  $E > \mu$ ;  $\gamma, \beta > 0$

We refer to this combined photon energy spectrum distribution as the Fatigue-Fermi distribution (FFD) where  $E$  is the photon energy,  $E_F$  is the cut-off energy,  $\mu$ ,  $\gamma$ , and  $\beta$  are coefficients that shape the photon energy spectra. Note that within the FFD function, the

probability density function in the form of,  $\frac{\exp \left( -\frac{x^2}{2} \right)}{\sqrt{2\pi}}$ , of the standard normal distribution is

expressed. This fitting function was selected from among an array of possible statistical distribution functions for its ability to fit the nine different photon spectra from various linac manufacturers based on simulations using the general purpose Monte Carlo code, BEAM, performed by Sheikh-Bagheri and Rogers.<sup>26,29</sup> The extra-focal disk source, located at a distance consistent with the location of the flattening filter, represents exponentially distributed photons consistent with the filter radius and are generated or scattered within the head (primary collimator, flattening filter, jaws, etc) of the modern Varian linac<sup>30</sup> (not necessarily specific for the modern Elekta or Siemens machines). The extra-focal source applies the same FFD function as shown in equation 1 to describe its photon spectrum, however the FFD is scaled down to represent the reduction in energy due to the scattered and secondary photons. The electron contamination source, located at a plane consistent with the bottom of the flattening filter, comprises a circular disk of uniformly distributed electrons created within the head. The electrons from the third source have an exponential energy distribution as described by Fippel et al<sup>31</sup> for Elekta and Siemens linacs, but presently is being applied to the Varian linac for this project.

The source model commissioning, a two-step optimization process, is performed one time for each modern linac make and energy. The justification for this is the fact that the vast majority of modern accelerators of the same make, model and energy have very similar dosimetry parameters. The first step in commissioning the source model is based on a 10 x 10 cm<sup>2</sup> field size and the second step is based on a 40 x 40 cm<sup>2</sup> field size. In the first step, differences between the MC calculated dose and the measured dose using the data from the percent depth dose (PDD) and profiles at several depths in water for a 10 x 10 cm<sup>2</sup> field size are minimized by adjusting model parameters. The model parameters include: the FFD parameters, the scaled extra focal FFD factor, a global dose scale factor,<sup>32</sup> the electron contamination relative fluence factor, and a blurring parameter to account for the smearing of dose from ion chamber volume effects that are apparent in profile measurements.<sup>33</sup> In the second step,

differences between the MC calculated dose and the measured dose using the data from the profile at  $d_{\max}$  in water for a 40 x 40 cm<sup>2</sup> field size are minimized by adjusting the model parameters for a piecewise linear function that represents the increase in fluence as the off-axis angle increases (the horn-effect). A fluence map is generated from the MLC positions that are imported from the DICOM plan file. The map considers leaf transmission, interleaf leakage, and the effect of transmission from the rounded leaf ends. To compensate for the assumption that the primary source is a point source, the MLC positions are retracted by an amount consistent with a finite sized source. The completed fluence map is divided into beamlets based on areas of similar monitor unit weighting. Corrections for photon fluence changes from the extra-focal source and fluence changes in electron contamination relative to changes in the field size are taken into consideration.

Built around the source model and the DPM dose calculation is a graphical user interface (GUI). The GUI was designed in the software application Matlab (MathWorks Inc., Natick, MA) and runs off the Computational Environment for Radiotherapy Research (CERR) software platform developed at Washington University.<sup>34</sup> CERR was developed so that researchers in the radiotherapy community could share results in treatment planning. The platform provides a common data structure for the creation of multi-institutional treatment plan databases for various types of research studies, including dose-volume-outcome analysis and IMRT treatment planning comparisons. For instance, Pinnacle treatment plans are imported directly into CERR so that all of the necessary information about the plan can be is available for the DPM dose calculation.

The basis for this project was established by a desire to generate an independent dose calculation tool built within CERR using the DPM code for which the initial version of the source model code was for the modern Varian linac (6 MV photon beam commissioned to 10 x 10 cm<sup>2</sup> only). This project as described here completes the development, validation, and benchmarking of the Varian 6 MV photon beam and extends the DPM source model calculation

tool to provide a generic solution for both the Varian 6 MV and 10 MV photon beams as an independent dose calculation tool capable of computing dose accurately for a variety of homogeneous and heterogeneous treatment plans.

Because of the source model's flexibility in simulating the output of a linear accelerator by the optimization of analytical parameters, the source model can be developed for other machines and other energies. Although not within the scope of this project, future work would be to continue development of source models to provide models for the Elekta and Siemens linacs at 6 MV and 10 MV photon energies. Other energies, such as 18 MV, can also be included.

## **1.2 BENEFITS TO SCIENCE**

The goal of this project, using DPM and the multiple-source model approach, as a generic dose calculation tool, is to provide a solution for the RPC to address past, current, and future clinical trial quality assurance issues. Further development beyond the Varian accelerators would enable the RPC to apply this tool as part of their standard quality audit procedures when reporting to the treatment community the outcome of clinical trial quality assurance studies. Specifically, the development of an independent dose calculation audit tool, receiving input plan information from a treatment planning system via CERR, will:

- i) Provide the framework to perform retrospective clinical outcome analysis by recomputing patient doses using a common independent dose calculation algorithm.
- ii) Complement the measurement-based anthropomorphic phantom remote audit program by providing an additional data set to compare to the TPS calculated dose
- iii) Supplement the overall quality assurance program by providing direct comparison of patient plans entered into current or retrospective clinical trials. This eliminates any potential errors associated with the remaining steps of the treatment plan, such as record

and verify. And, in the case of phantoms, it also eliminates the phantom set-up uncertainty. Here, the performance of the TPS dose calculation, dependent on the institution's beam model, is isolated.

iv) Facilitate the determination of treatment planning system performance that is unknown today. Reports by the RPC<sup>2-6</sup> show that the variation in TPS calculations as compared to measurements from the RPC's QA anthropomorphic phantom can be large due to improper beam modeling, planning errors, and phantom set up mistakes. This variation in TPS performance is difficult to understand because each analysis from each institution is unique and independent. A single treatment plan planned on a specific TPS could be imported at any institution with the same TPS and recalculated. The resulting dose distribution could then be compared against the dose distribution calculated by the baseline DPM/source model tool. Given this scenario, TPS dose calculation performance and the dependency of the institution's beam model could be delineated.

### **1.3 HYPOTHESIS AND SPECIFIC AIMS**

#### **Hypothesis:**

A quality assurance tool based on the Monte Carlo Dose Planning Method (DPM) and coupled to a measurement-based source model can be developed to predict dose within 3%/2mm of measurement for IMRT and stereotactic treatments planned on the Varian linear accelerator at the photon energies of 6 MV and 10 MV.

**Specific Aim 1:** Complete the development of the Varian 6 MV photon beam source model. Modify the developed 6 MV source model to include a source model for the Varian 10 MV photon beam. Validate the Varian 6 MV and 10 MV photon beam source models. The

accuracy of calculated data consisting of percent depth dose and profiles up to a field size of 20 x 20 cm<sup>2</sup> is to be within 2%/2mm of measurement in at least 90% of the data tested.

**Specific Aim 2:** Benchmark the validated source models in specific aim 1 against measurement using anthropomorphic phantoms planned as IMRT homogeneous head and neck, stereotactic lung, and IMRT lung treatments. The accuracy of the algorithm is to be within 3%/2mm of measurement in at least 85% of the data tested.

**Specific Aim 3:** Benchmark the Pinnacle TPS calculation against the validated and benchmarked source models for the Varian 6 MV and 10 MV photon beams using the patient plans. Dose volume histograms and dose profiles will be presented and compared.

## **1.4 DISSERTATION ORGANIZATION**

Chapters 2 through 4 are each self-contained studies, including an introduction, material and methods, results and discussion, and conclusion. These chapters describe the steps of work required to address the specific aims and complete the project. Chapter 2 answers specific aim 1 and 2 with respect to the Varian 6 MV photon beam. Within Chapter 2, the development, validation, and benchmark are presented. Chapter 3 is similar to Chapter 2 but the validation and benchmarking of the Varian 10 MV model is presented. In addition, chapter 3 discusses an extension of the electron contamination model which was not presented in Chapter 2 because of its negligible contribution to the Varian 6 MV model. Chapter 4 addresses specific aim 3 by performing patient dose calculations on a number of treatment sites planned with the Varian 6 MV and the Varian 10 MV photon beams. Within Chapter 4 a commercial calculation algorithm is used to compare against the MC dose calculation. Chapter 6 is a summary of the research project as a whole, and an evaluation of the hypothesis. Chapter 7 is the Appendix for the supporting data not presented in the aforementioned chapters.

## **Chapter 2 Development, Validation, and Benchmark: Varian 6 MV**

### **2.1 INTRODUCTION**

Motivated by its high degree of accuracy, the use of the Monte Carlo (MC) method in dose calculations has been extensively reported.<sup>22,35-38</sup> By applying known probability distributions that govern the interactions of electrons and photons, the individual particle histories can be tracked with a high degree of certainty. In general, today's analytical dose calculation algorithms such as the convolution superposition algorithm found in commercially available treatment planning systems (TPSs) are very good at determining dose accurately. However, there are situations, such as patient heterogeneities (within the lung) and complicated deliveries of small fields or steep dose gradients, in which dose differences between the convolution superposition (CS) algorithm and the MC method exist.<sup>17-19</sup> The ability to measure these complicated dose distributions in anthropomorphic phantom simulations is also a challenge. The MC method is uniquely positioned to bridge the gap between dosimetry and the TPS's predicted dose distributions as an independent method for determining dose.

The traditional approach to applying the MC method requires a detailed knowledge of the treatment head geometry. Depending on the quantities of interest and desire for accuracy, the extent to which the treatment head geometry is defined is a key component of the simulation. For instance, in-field dose distributions can be accurately modeled by only defining the beam-line components such as target, flattening filter, jaws, MLC, and ion chamber. However, if the out-of-field dose needs to be studied, additional modeling of the primary and secondary collimators, and the shielding and structural components of the accelerator need to



be defined. This can become a tedious and tenuous effort due to the level of detail and access to this information, as it is not always readily available from the manufacturer.

Additionally the MC method has been slow to be implemented into the clinic because it has been historically very time consuming due to its computationally intensive nature. Speed considerations are becoming less of an issue due to faster computers. As a result, alternate approaches using MC have been studied and developed.<sup>22,35-38</sup> The American Association of Physicists in Medicine's Task Group Report No. 105 (TG-105) has described general schemes that outline three approaches.<sup>10</sup> The first approach is the simulation of the accelerator treatment head resulting in phase-space information of the physical interactions. The second involves the use of a multiple-source model with parameters derived from the initial simulation and stored phase-space information. And finally the third relies on the use of measurements to derive parameters of analytical functions that describe a multiple-source model.

We have reported on a versatile source model using the Dose Planning Method (DPM) Monte Carlo dose calculation algorithm for the Varian 2100 series linear accelerators (Varian Medical Systems, Inc., Palo Alto, CA) for the 6 MV photon beam.<sup>26</sup> This conference series paper described the model, presented an analytical function used to describe the energy spectrums of many different linear accelerators and energies, and presented initial benchmark test results. Briefly, the measurement-driven source model consists of three sources: one, the primary photon isotropic point source; two, an extra-focal disk source<sup>30</sup>; and three, an electron contamination uniform disk source<sup>31</sup>. Since lower energy photon beams contain low amounts of electron contamination, this source is sometimes not considered. The model also accounts for fluence and off-axis energy<sup>27</sup> effects due to the flattening filter.

Modifications to the model were necessary to complete the validation of the 6 MV photon beam for the field sizes between 4 cm x 4 cm and 40 cm x 40 cm and to improve the benchmark evaluations in order to achieve better agreement. This work details those modifications and reports the results of the validation and benchmarking testing of the Varian 6

MV photon beam source model with DPM dose calculation engine, hereafter referred to as the source model. The validation testing compared ion chamber measurements of dose profiles and percent depth doses (PDDs) to the source model calculation for square field sizes. The benchmark testing used the Radiological Physics Center's (RPC's) anthropomorphic phantoms that house thermo-luminescent detectors (TLDs) and radiochromic film (Figure 2.4). Under this testing, the entire model, including the multi-leaf collimator (MLC), was evaluated using realistic treatment plans. These treatment plans were designed so that homogeneous and heterogeneous media were considered using highly modulated fields and small fields.

## **2.2 MATERIAL AND METHODS**

### **2.2.1 Source model**

#### **2.2.1.1 Hardware**

The dose calculations were performed using a Hewlett Packard ProLiant DL585 G5 3.2-GHz Server with 16 AMD Opteron™ processors and 32GB of RAM (Hewlett-Packard Company, Palo Alto, CA). The computation time was decreased by dedicating each beam defined in a treatment plan to a processor. Each simulation used 10 million particles per square centimeter beamlet. The calculations applied low energy electron and photon cutoffs of 200 and 50 keV, respectively.

#### **2.2.1.2 Source model commissioning**

The source model commissioning process as described by Davidson, et al<sup>26</sup> consisted of two main steps shown in Figure 2.1 and Figure 2.2. The first step was based on a 10 cm x 10 cm open field. The process consisted of separate dose calculations that were performed for the primary and extra-focal sources using energy bins of 0.25 MeV increments over the range of

energies that make up the energy spectrum for the nominal accelerating voltage of the linear accelerator.

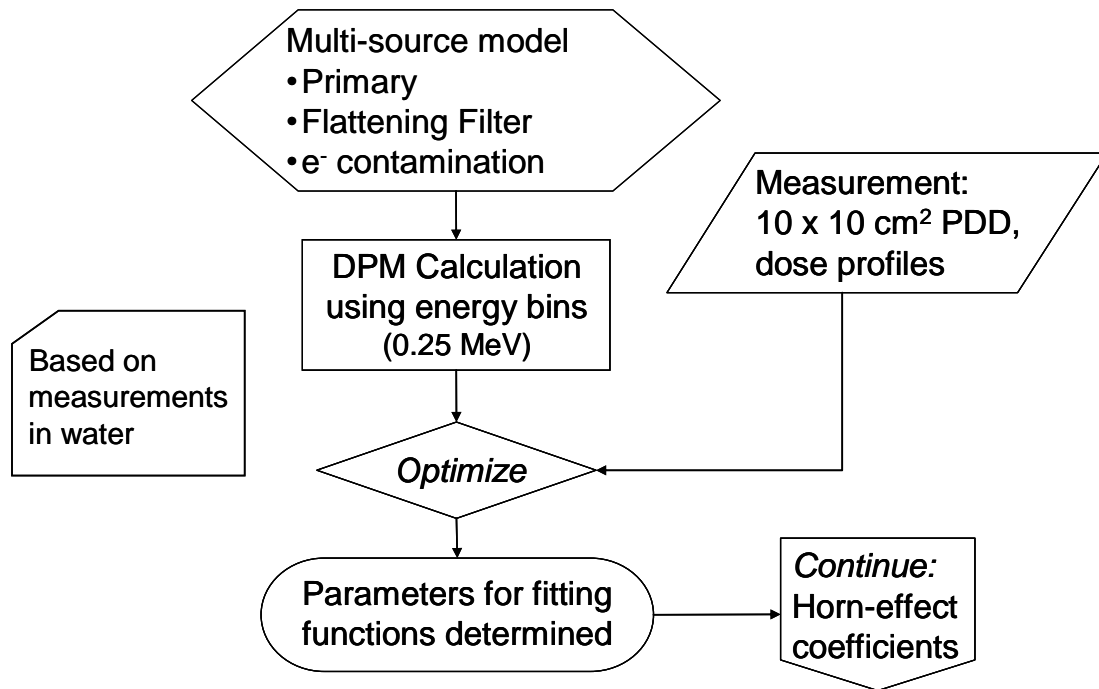


Figure 2.1 Step one of the source model commissioning process.

The energy bins were varied within boundary constraints until the difference between the DPM calculation and the measurement was minimized. Lower energy photon beams contain low amounts of electron contamination. For the 6 MV photon beam, published work indicates that the contribution from electron contamination is less than one-half percent.<sup>29</sup> Therefore, it was decided not to include the electron contamination source for the Varian 6 MV photon beam. Seven parameters used to describe the source model were determined during the first step of commissioning. These parameters describe the primary and secondary energy spectrums, the relative fluence contributions from the extra-focal source and the electron contamination source, and a parameter that is used to describe the penumbra effects from the use of an ion chamber in the open field profile measurements.

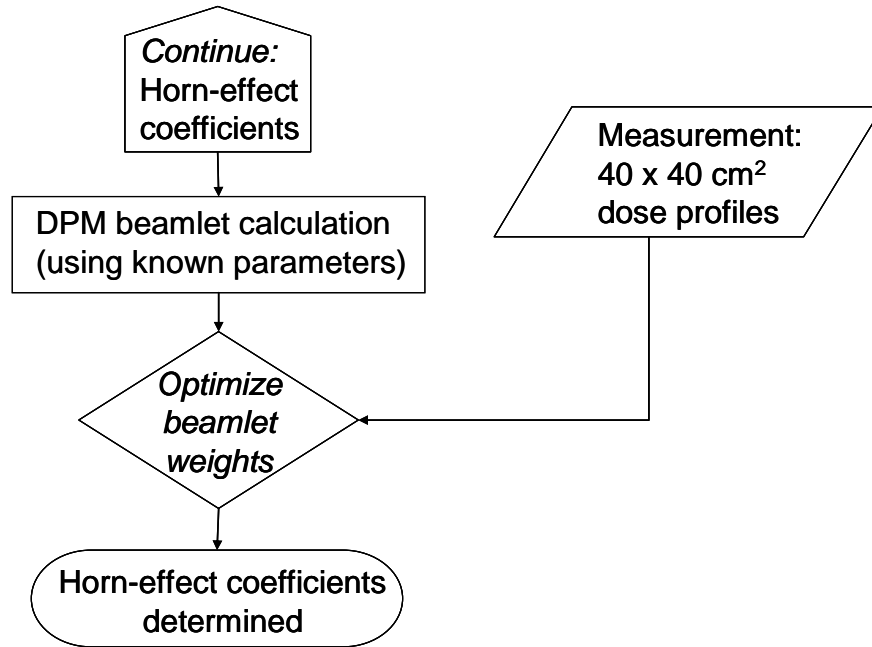


Figure 2.2 Step two of the source model commissioning process

In the second step of the commissioning process, the horn-effect model was represented by a piecewise linear function whose coefficients were determined by an optimization process. A large field size of 40 cm x 40 cm was used to model the increase in fluence as a function of the off-axis angle. For this step, the calculation was divided into 1 cm x 1 cm beamlets. Each beamlet contribution was adjusted via the optimization routine until the difference between the calculated profile and the measured profile was minimized.

The primary source and extra-focal source spectra were represented by a fatigue life distribution function combined with a Fermi function [Equation 1] and were described in Chapter 1. The analytical functions that describe the spatial distributions of the secondary sources<sup>30</sup> as well as the off-axis softening<sup>27</sup> were implemented directly and without change. A final conversion factor was applied to convert energy per photon to dose. To avoid the statistical uncertainties of a single normalization point, the conversion factor was determined by normalizing to an integral dose defined by the area under the curve from the measured PDD between the depths of 5 cm to 15 cm for the 10 cm x 10 cm open field.<sup>32</sup>

### 2.2.1.3 *Fluence map*

A fluence map, or monitor unit map, was formed at the distance to isocenter from the field size defined by the jaw settings. The map was dependent on the position of the MLC leaves that comprised each segment, the transmission through the leaves, the effect of the transmission through the rounded leaf ends, and the leakage between adjacent leaves (interleaf leakage). Specifically, the fluence map was divided into 1 mm by 1 mm regions. The monitor units assigned to a given segment were recorded into each region that was exposed to the primary source. Transmission through the MLC was defined as a percentage of the monitor units given for the segment. This amount was recorded into the 1 mm by 1 mm regions that were unexposed to the primary source. The transmission through the MLC leaves varies and increases as the thickness decreases near the leaf tip. A piecewise linear function was used to model the rounded leaf ends. The coefficients of the function were used to scale the monitor units in the region represented under the rounded leaf tip. Essentially, this region was 5 mm by 5 mm, which coincided with the width of the center leaves and the ‘length’ of the leaf tip. In this way, the dose was blurred to improve the effect of the penumbra due to MLC rounded leaf ends. The interleaf leakage was defined as a percentage of the monitor units designated for a given segment. This amount was recorded alongside the location of one of the two leaves that comprised a 1 mm wide region of varying interleaf length. The monitor units from all 1 mm by 1 mm regions from all segments for the beam were summed together and a final composite fluence map was constructed. While the resolution of the fluence map was 1 mm by 1 mm, a finer resolution of 0.5 mm by 0.5 mm could be used requiring more beamlet calculations and therefore more computation time. The DPM calculation was performed by segmenting the fluence map into calculation beamlets of similar monitor units.

#### 2.2.1.4 Primary source size

As stated earlier, the primary source was modeled as a point source. However, the primary source in reality was known to have a finite dimension of about 1 mm in full width half maximum (FWHM).<sup>39-42</sup> The effect of the finite source was seen in the penumbra regions of the film measurements from the benchmark evaluations. Currently, the model accounts for this penumbra effect by applying an offset of the MLC leaf positions. The offset was a fixed amount defined by the source radius and the distance from the source to the MLC (Figure 2.3).

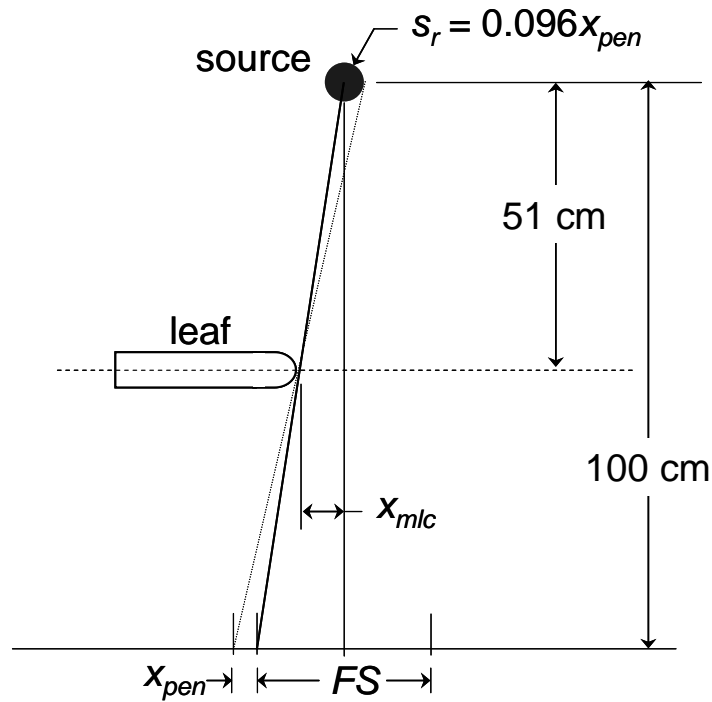


Figure 2.3 MLC offset position,  $x_{pen}$ , with relationship to source size,  $s_r$ . The position of the MLC leaf,  $x_{mlc}$ , is shown for reference.

#### 2.2.1.5 Machine output correction

The model incorporated a hyperbolic equation that corrected for the machine output versus field size.<sup>43</sup> Similar in concept to that described in the Pinnacle Physics Reference Guide<sup>44</sup> (Philips Medical Systems, Andover, MA), a second-order hyperbolic equation with three constants sought to correct for the machine output as the ratio between the measured

output factor and the calculated output factor for a given field size. The correction was applied to the three-dimensional (3D) dose matrix following the dose calculation.

### 2.2.2 *Anthropomorphic phantoms and dosimeters*

The homogeneous head and neck phantom of Figure 2.4(a) was made of acrylic and included an insert made of polystyrene. Within the insert was solid water material that represented the primary target and the secondary target (node or parotid gland), and acrylic was used to represent the critical structure (spinal cord). The heterogeneous thorax phantom seen in Figure 2.4(b) consisted of a high density polyvinyl chloride (PVC) housing, a nylon heart, a polybutylene terephthalate polyester (PBT) spinal cord, CIRS exhale lung material (Computerized Imaging Reference Systems, Inc., Norfolk, VA), a nylon target located in the medial-anterior direction of the left lung, and water used to fill the remaining volume.

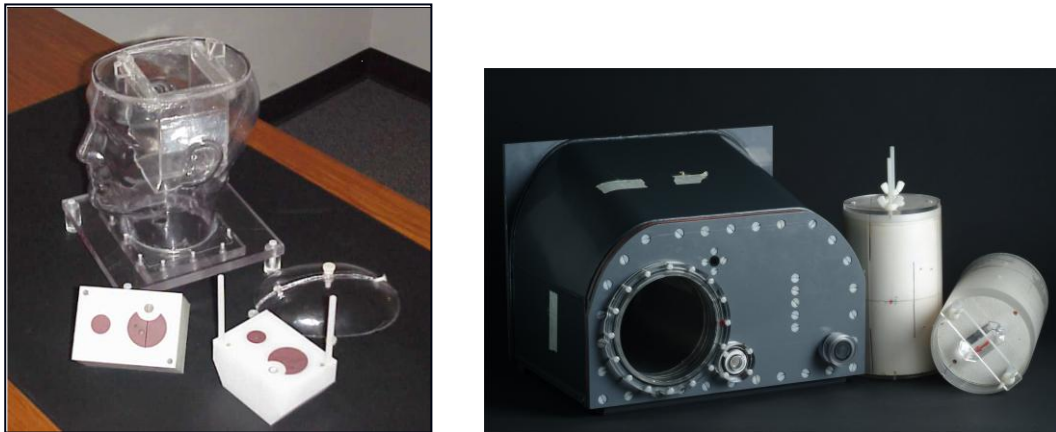


Figure 2.4 (a) The RPC head and neck phantom. (b) The RPC thorax phantom

The details of the design and use of these phantoms can be found elsewhere in the literature.<sup>45,46</sup> Presently, the DPM code allows up to five material definitions. The material properties defined in the DPM code originated from user input of the elemental composition, atomic number, and density of a specific material. The code extracts the raw physics data from a library of constants, and produces the cross-sectional information. Air, polystyrene, water,

solid water, and acrylic were defined for the head and neck phantom while air, CIRS lung, water, nylon, and PVC were defined for the thorax phantom.

The head and neck phantom and thorax phantom housed TLD capsules and radiochromic film. The TLD capsules (TLD-100 capsules, Radiation Detection Company, Gilroy, CA) were located at the center of the target(s) and within the critical structure(s) to collect near-point absolute dose information. For the head and neck phantom, four capsules were used for the primary target, two capsules were used for the secondary target, and two capsules were used for the critical structure. For the thorax phantom, two capsules were used for the target and two capsules were used in each critical structure (heart and spinal cord). The films were strategically located in close proximity to the primary target TLD capsules so that the films' intersection coincided with the center of the primary target and the films were normalized to the TLD values. The normalization was defined as the average of the ratio of each target TLD dose value to the dose value of the adjacent film region.

All three major planes were represented by the films for the thorax phantom while the films for the head and neck phantom were positioned only in the axial and sagittal planes. EBT radiochromic film was used for the deliveries of the IMRT head and neck plan and SBRT lung plan. MD-55 was used for the delivery of the IMRT lung plan (EBT and MD-55 radiochromic film, International Specialty Products, Wayne, NJ). All films were read using a densitometer with a CCD camera and light source (Photoelectron Corporation (defunct), Lexington, MA). For each batch of film, a sensitometric curve was established to relate the film optical density (OD) to dose.

### **2.2.3 Validation testing**

The validation of the Varian 6 MV photon beam was performed by comparing calculated values to the measured values of the basic beam data. These data consisted of the



percent depth dose and the dose profiles at several depths from several field sizes. The depths of the dose profile comparisons were 1.5 cm, 6 cm, 12.5 cm, and 22 cm in a water phantom. The field sizes included 4 cm x 4 cm, 5 cm x 5 cm, 6 cm x 6 cm, 8 cm x 8 cm, 10 cm x 10 cm, 15 cm x 15 cm, 20 cm x 20 cm, 25 cm x 25 cm, and 40 cm x 40 cm. The simulated water phantom had dimensions of 50 cm x 50 cm x 50 cm.

The calculated data were extracted from the 3D dose matrix relative to the location of the surface of the water phantom. This location was the region of interest defined by the skin contour. The resolution of the calculated data was 0.2 cm in the depth direction. This direction was defined in the CT data set as the y-direction. The x-direction, or lateral direction, was also 0.2 cm and the z-direction, or in-plane direction, was the slice thickness of 0.3 cm. The measured data was the same data used for the beam model commissioning of the clinical treatment planning system (TPS).

The measured values were made using a small volume ion chamber (0.04 cm<sup>3</sup> internal volume). To account for the volume effects of the ion chamber which tend to smear the dose and exaggerate the dose penumbra, a Gaussian convolution was applied to the calculated dose data for all profile comparisons.<sup>33</sup> The standard deviation of the Gaussian kernel was one of the seven parameters determined in the model optimization process described above.

The accuracy of the calculated data compared to the measured data (PDDs and dose profiles) for field sizes from 4 x 4 cm<sup>2</sup> to 40 x 40 cm<sup>2</sup> was tested to a gamma criterion of 2% of the maximum dose and 2 mm distance to agreement. In addition, local dose differences were studied at depths beyond  $d_{\max}$  and in the high dose regions of the dose profiles. The high dose region within a dose profile at a specific depth was defined by the dose greater than or equal to 80% of the dose at the central axis.<sup>47</sup> Quantifying the distance-to-agreement for the location of the calculated  $d_{\max}$  relative to the measured  $d_{\max}$  was also evaluated.

#### **2.2.4 Benchmark testing**

The validated source model was benchmarked under a variety of conditions. Designed to be progressively more difficult, treatment plans were evaluated for homogeneity, heterogeneity, small fields, and highly modulated fields. The RPC's anthropomorphic IMRT head and neck phantom was used to test a highly modulated delivery of nine coplanar beams which comprised of 72 segments to a homogeneous medium (Figure 2.1(a)). The RPC's anthropomorphic thorax phantom was used to test a nine beam SBRT plan and a five beam, 63 segment non-coplanar IMRT plan (Figure 2.1(b)). The IMRT head and neck plan and SBRT lung plan were designed using the credentialing guidelines and irradiation instructions employed by the Radiation Therapy Oncology Group (RTOG) to credential institutions for participation in specific advance technology protocols. Each plan was delivered three times to evaluate the repeatability.

The resolution of the DPM calculation was governed by the size of the CT voxel. For this work, the voxel size was 0.195 cm by 0.195 cm by 0.25 cm for all treatment plans studied. The accuracy of the DPM calculation was determined by comparing point doses, dose profiles, and 2D gamma maps to the measured data.

##### **2.2.4.1 Point dose comparisons**

Point dose comparisons were made between the calculated values and measured TLD values of the target and critical structure locations. The measured point doses were defined by the small volume of TLD powder inside the capsule while the respective calculated point doses were derived from the small regions of interest contoured from the CT scan.

##### **2.2.4.2 Dose profile comparisons**

Dose profiles along the major planes intersecting the center of the targets were qualitatively evaluated between the calculated and measured film values. The superior-inferior profiles were extracted from the sagittal film plane for the head and neck planned deliveries and

from the coronal film plane for the lung planned deliveries. Since the sagittal and coronal film planes are composed of a separate superior portion and a separate inferior portion due to the intersecting axial film plane, the plotted profiles showed a discontinuity of the measured dose within the center of the target. The profile plot was meant to be interpreted qualitatively, although quantitative information existed, the reader should ignore the measured data in this limited central region as demonstrated in Figure 2.5.

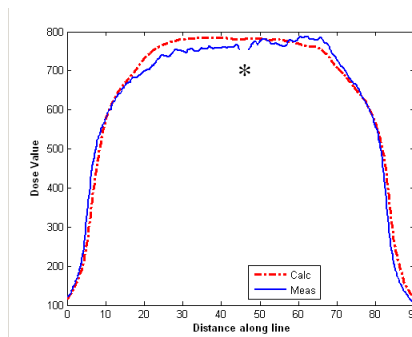


Figure 2.5 Asterisk (\*) indicates the region of the axial cross plane where separation exists between superior portion and inferior portion of sagittal or coronal film

#### 2.2.4.3 Gamma map comparisons

2D dose distributions were evaluated using the gamma index method<sup>48</sup> where quantitative results were recorded and used to test the hypothesis. The accuracy of the calculated data compared to the measured film data from the major planes intersecting the targets was tested to a gamma criterion of 3% of the target TLD dose and 2 mm distance to agreement.

Some regions of the gamma map have no measured dose because the test region encompassed more area than the film. Typically, larger regions that were maroon in color and that were fairly rigid and defined were most likely regions outside of where the film was located. For instance, the sagittal and coronal films of the thorax phantom had these regions along the central A-P and lateral directions, respectively, and in the S-I direction to provide

clearance from one another to coincide with the axis they shared (Figure 2.6). The sagittal film for the head and neck phantom also had a region that was cut away to accommodate the spinal cord critical structure (Figure 2.7). The axial film for the head and neck phantom had a small region in the posterior, right lateral corner that was cut away to allow proper assembly of the target insert. These regions were included in the initial gamma analysis, but a subsequent estimate of the data in those regions allowed for a correction to be made to the final results.

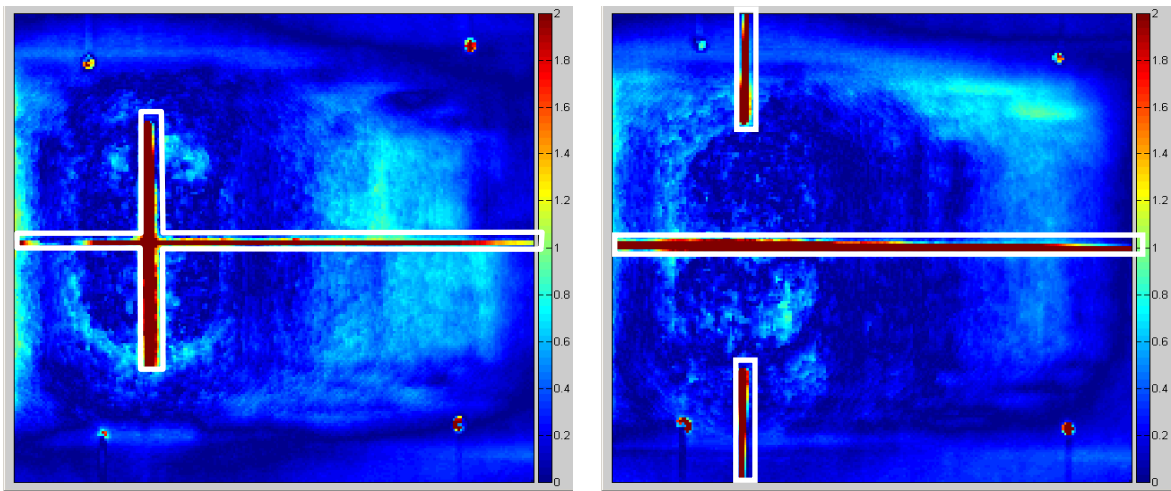


Figure 2.6 Gamma Map. The regions outlined in ‘white’ represent the estimated area that was not included in the gamma index calculation. The left figure is a representative coronal plane and the right figure is a representative sagittal plane from the thorax phantom. Scale: 1 mm = 0.65 mm

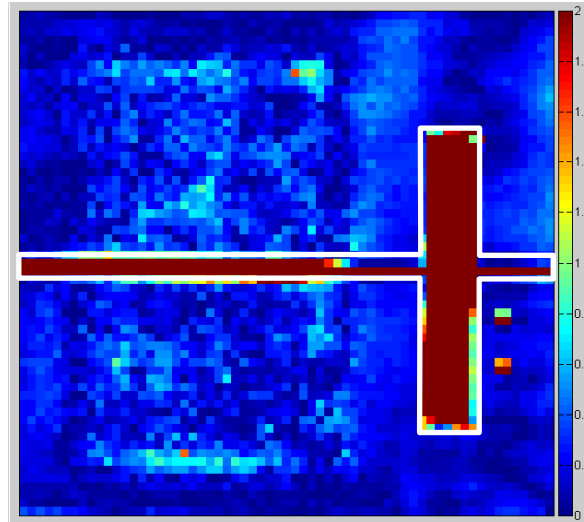


Figure 2.7 Gamma Map. The regions outlined in ‘white’ represent the estimated area that was not included in the gamma index calculation. The figure is representative of the sagittal plane from the head and neck phantom. Scale: 1 mm = 1.09 mm

#### 2.2.4.4 *Treatment plans*

All treatment plans were planned using the Pinnacle treatment planning system (version 7.6c or higher) (Philips Medical Systems, Andover, MA). The dose prescription and dose constraints were met based on the calculated dose using Pinnacle’s collapsed cone convolution algorithm.

For the head and neck plan, at least 95% of the primary planning target volume (PTV) received 6.6 Gy and less than 1% of the primary PTV received less than 93% of the prescribed dose. At least 95% of the secondary PTV received 5.4 Gy and less than 1% of the secondary PTV received less than 93% of the prescribed dose. The PTV was constrained to the gross tumor volume (GTV). The organ at risk received less than 4.5 Gy. The dose to the normal tissue received no more than 7.26 Gy. The targets and the organ at risk (critical structure of the spinal cord) are shown in Figure 2.8.



Figure 2.8 Transverse slice through the center of the targets of the head and neck phantom. Contour colors are as follows: red (primary target); aqua (secondary target); violet (critical structure, spinal cord). Note the dark dots are the TLD measurement locations.

The PTV for the SBRT lung plan was the GTV plus 0.5 cm in the axial plane and plus 1 cm in the longitudinal plane. At least 95% of the PTV received 6 Gy and at least 99% of the PTV received 5.4 Gy. The maximum dose received at 2 cm and beyond from the PTV was no more than 3.5 Gy. The dose to the PTV was within 60% and 90% of the maximum dose. The prescription isodose volume to PTV ratio was less than 1.2 and the ratio of 50% of the prescribed isodose volume to PTV was less than 3.6. Figure 2.9 is a transverse CT slice through the center of the target showing the GTV and critical structures within the anatomy of the thorax phantom.

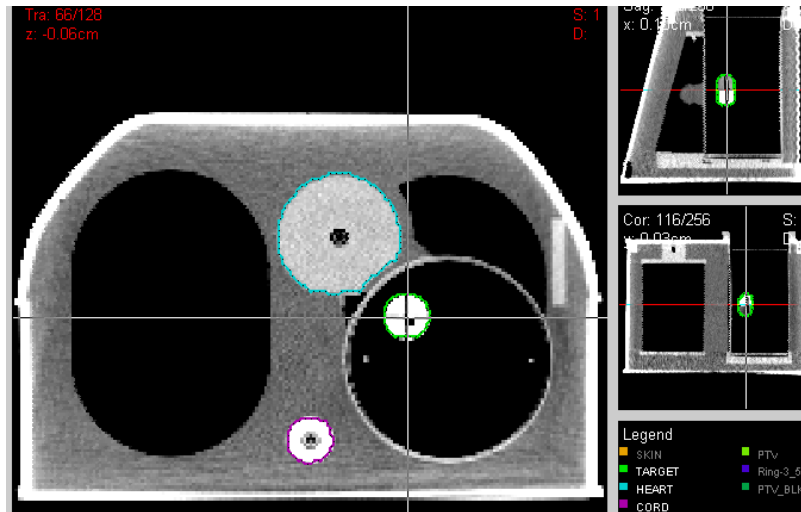


Figure 2.9 Transverse slice through the center of the target of the thorax phantom. Contour colors are as follows: green (GTV); aqua (critical structure, heart); violet (critical structure, spinal cord). Note the dark dot in each of the three regions is the TLD measurement location. The TLD location for the target is adjacent the center in the posterior-lateral distal direction.

For the IMRT lung plan, the PTV was the GTV plus a 1 cm margin. The prescription was to deliver 66 Gy to at least 95% of the PTV in 33 fractions. The maximum dose prescribed to the spinal cord was 45 Gy. No more than 40% of the total lung was to receive more than 20 Gy. The dose to the entire heart was not to exceed 40 Gy or no more than 50% of the heart was to receive more than 50 Gy. MD-55 radiochromic film is sensitive in the range of 20 Gy, therefore an equivalent of 10 fractions was delivered from this plan and the prescription dose was adjusted accordingly. Figure 2.9 shows the location of the PTV within in the lung and the heart and spinal cord critical structures.

## 2.3 RESULTS AND DISCUSSION

### 2.3.1 Source model

#### 2.3.1.1 Source model commissioning parameters

The seven model parameters that describe the photon energy spectra, fluence contributions, and the penumbra measurement effect for the first step of the commissioning process for the Varian 6 MV photon beam are shown in Table 1. The first three parameters,  $\gamma$ ,  $\mu$ , and  $\beta$ , defined the spectrum shape, relative peak energy location, and relative scale, respectively, of the fatigue life distribution function.

| Parameter  | Value   |
|--|---------|
| Fatigue-Life distribution shape parameter, $\gamma$  | 1.75    |
| Fatigue-Life distribution location parameter, $\mu$  | -0.0165 |
| Fatigue-Life distribution scale parameter, $\beta$   | 3.50    |
| Primary spectrum to extra-focal spectrum reduction scale factor  | 1.7     |
| Extra-focal fluence relative to the primary fluence  | 0.13    |
| Electron contamination contribution (relative to the primary photon contribution)  | 0.002   |
| Standard deviation of Gaussian used to convolve the MC dose profile to match the measured dose profile during the validation process | 1.2     |

Table 1 Parameters of the commissioned source model for spectra, fluence, and profile penumbra measurement effect.

A plot of the energy spectrum compared to the energy spectrum computed using the widely accepted BEAM code<sup>29</sup> for simulating radiation transport in accelerators is shown in Figure 2.10. Clearly, the commissioned source model spectrum was not ideal compared to the BEAM code, but provided an adequate representation of the photon beam based on the validation. The extra-focal energy spectrum was scaled in energy by a factor of 1.7. The



relative fluence of the extra-focal source was 13% of the primary source fluence for the 10 cm x 10 cm open field. The dose contribution from the electron contamination source was less than one-half percent (0.2%) of the primary dose and was not included in the model because of its minor contribution. The standard deviation of the Gaussian function used for the dose smearing convolution was 1.2 mm.

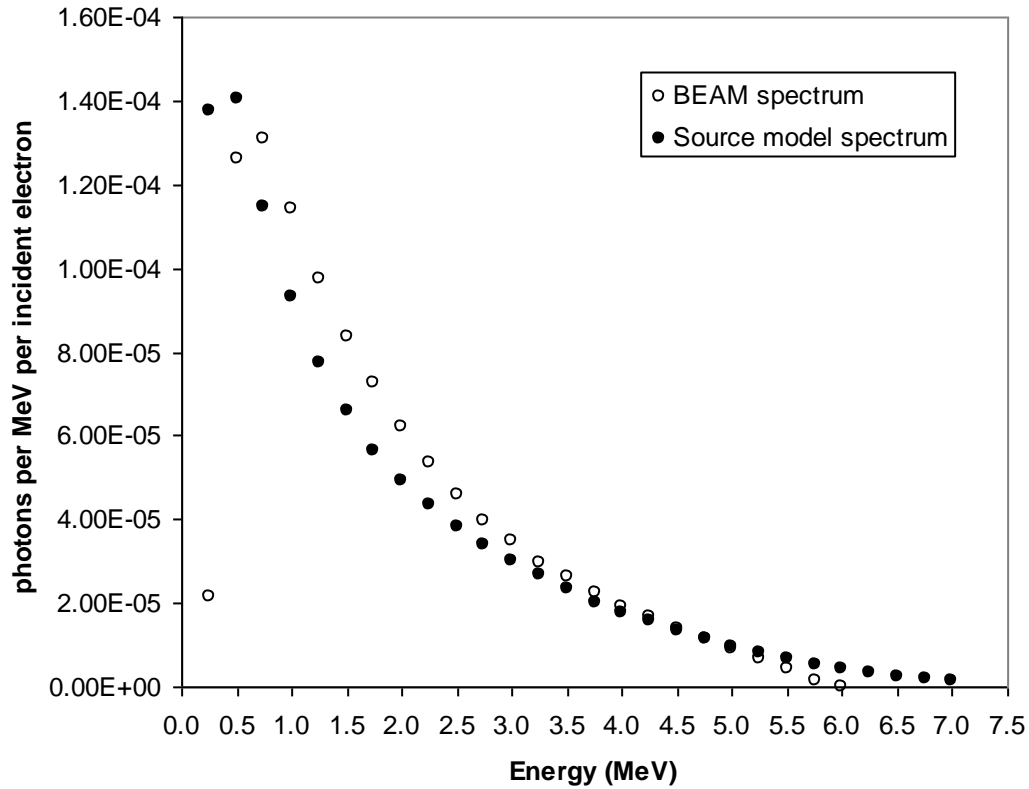


Figure 2.10 Varian 6 MV spectrum: Commissioned source model compared to BEAM spectrum<sup>29</sup>

The results of the second step of the commissioning process are shown in Table 2. The horn-effect coefficients of the piecewise linear function are shown as increases in the fluence weighting as a function of the cosine of the off-axis angle.

| Cosine(off-axis angle) | Fluence weight increase |
|------------------------|-------------------------|
| 1.00000                | 1                       |
| 0.99970                | 1.0135                  |
| 0.99879                | 1.048                   |
| 0.99728                | 1.099                   |
| 0.99518                | 1.13                    |
| 0.99250                | 1.17                    |
| 0.98926                | 1.22                    |
| 0.98546                | 1.24                    |
| 0.98113                | 1.26                    |
| 0.97630                | 1.28                    |
| 0.97098                | 1.30                    |
| 0.96277                | 1.32                    |

Table 2 Coefficients of a piecewise linear function to describe the increase of fluence as the off-axis angle increases (horn-effect)

Following the completion of the two-step commissioning process, the final conversion factor that was applied to convert energy per photon to dose in cGy was 0.24442. This factor was applied to every dose calculation performed for the Varian 6 MV source model.

#### 2.3.1.2 Fluence map, primary source size, and machine output correction

In terms of transmission, the fluence map generation was unique to the beam energy and the MLC configuration characterized by the patient or phantom treatment plan. For the Varian 6 MV photon beam, the transmission through the bulk of the MLC leaves was 1% while, the interleaf leakage was an additional 1% of the monitor units given for the particular segment.

The offset of the MLC leaf positions,  $x_{pen}$ , which was necessary to compensate for the absence of a finite primary source size, was 0.4 mm. The offset amount was fixed for the Varian accelerator as it has been reported that the source size was nearly the same regardless of energy.<sup>39-42</sup> Based on the relationship of the source-to-MLC distance and the source-to-axis distance, the source diameter,  $s_r$ , was 0.84 mm FWHM.

Figure 2.11 shows the relationship between the output factor and the field size for the calculated and measured data. A hyperbolic equation was determined to correct the calculated output factors. This equation,  $y = 1.12 - \frac{3.95}{22.81 + x}$ , where  $y$  is the output correction and  $x$  is the field size was necessary to maintain the proper predicted machine output and which had been a deficiency of the model to completely describe the scatter conditions that change as a function of field size.

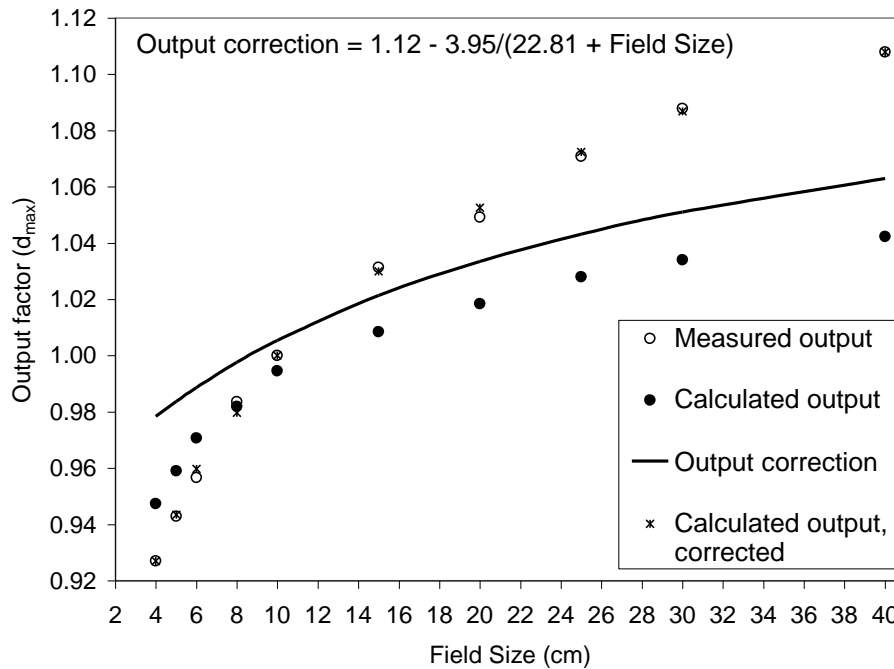


Figure 2.11 Output factor at  $d_{max}$  versus field size for the measured, calculated and corrected output. A hyperbola curve was determined to correct the calculated values.

### **2.3.2 Validation testing**

#### **2.3.2.1 Uncertainty**

The uncertainty of the dose determined for the ion chamber measurements was estimated to be 1.5% at one standard deviation.<sup>49</sup> The estimate of uncertainty, or the standard error of the mean, for the simulation was 1% using 10 million particles per square centimeter.<sup>10</sup>

#### **2.3.2.2 Percent depth dose**

Comparisons of the measured percent depth dose (PDD) and the source model calculated PDD data for the Varian 6 MV photon beam were made for the field sizes between 4 cm x 4 cm and 40 cm x 40 cm. While all of the PDD comparisons are presented in the appendix (Chapter 6), three fields that represent the range of field sizes are presented here. Those fields are 4 cm x 4cm, 10 cm x 10 cm, and 40 cm x 40 cm and their data are shown in Figure 2.12, Figure 2.13 and Figure 2.14, respectively.

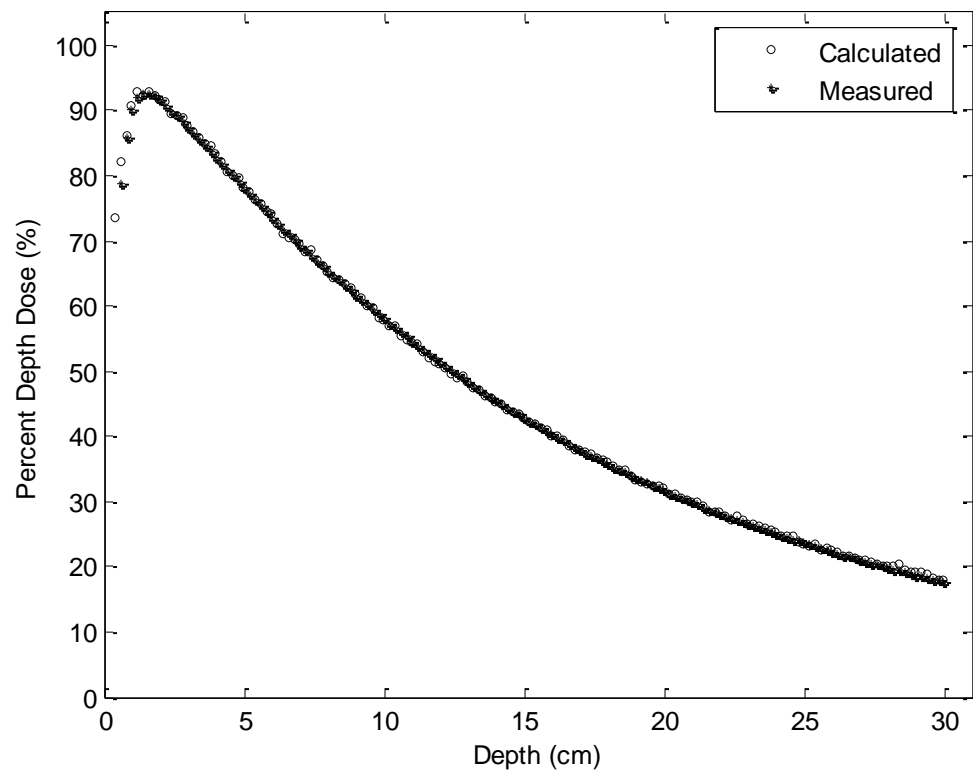


Figure 2.12 Calculated and measured percent depth dose curves at 6 MV for a 4 cm x 4 cm field.

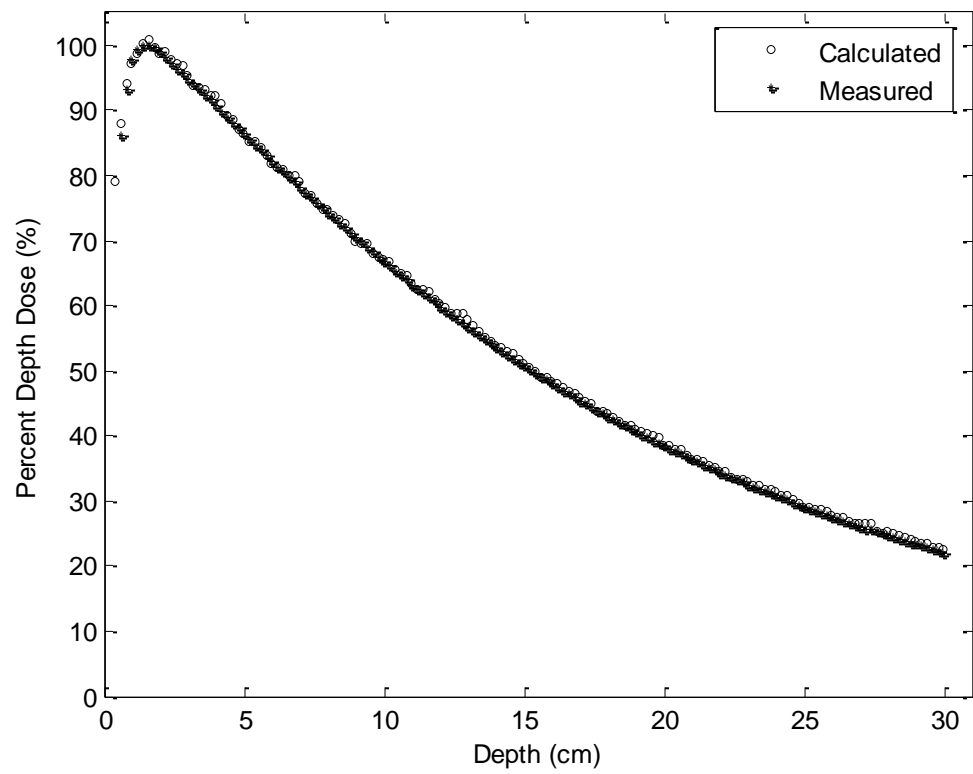


Figure 2.13 Calculated and measured percent depth dose curves at 6 MV for a 10 cm x 10 cm field.

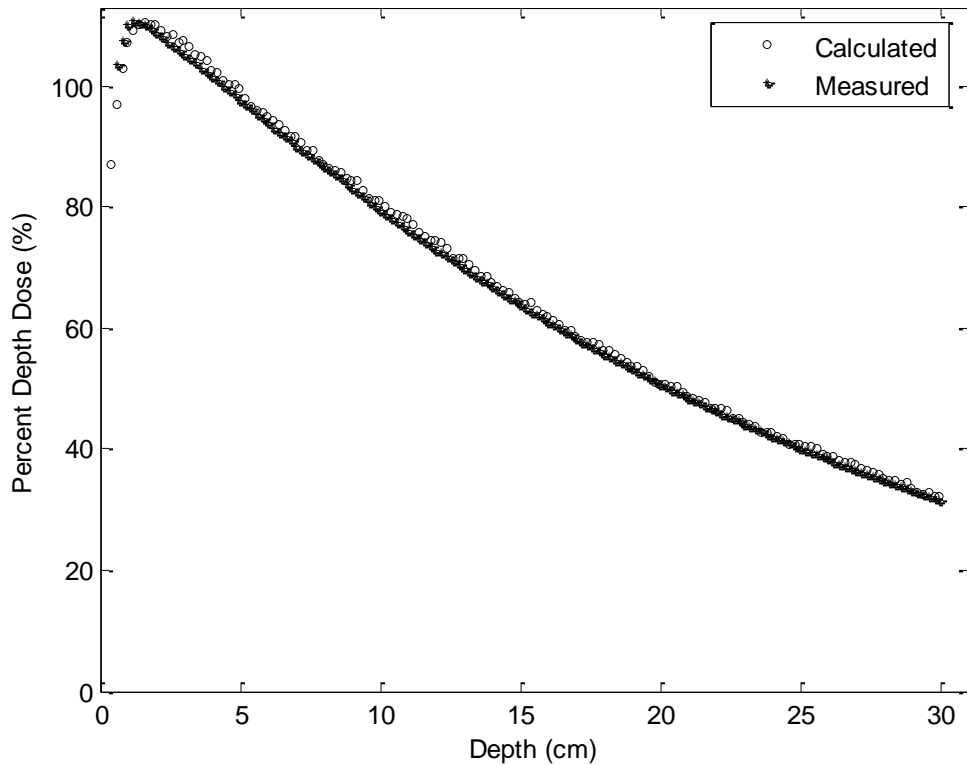


Figure 2.14 Calculated and measured percent depth dose curves at 6 MV for a 40 cm x cm 40 field.

Overall, for the open field tests along the central axis, good agreement existed between the calculated data set and the measured data set. Beyond  $d_{\max}$ , the mean of the local percent difference was within 1.0% for the fields from 4 cm x 4 cm (see Figure 2.12) to 15 cm x 15 cm. 100% of all data tested for these fields were within the 2%/2 mm criteria. Otherwise, for the larger field sizes from 20 cm x 20 cm to 40 cm x 40 cm (see Figure 2.14) the mean local percent difference was between 1.2% and 2.0% beyond  $d_{\max}$ . The minimum percentage of the all the data tested for these larger field sizes that met the criteria of 2%/2 mm, was 96%; and on average 97% of the data met the criteria.

For the 4 cm by 4 cm field (Figure 2.12), the calculated  $d_{\max}$  was 1.6 cm, while the measured  $d_{\max}$  was 1.5 cm. The 40 cm x 40 cm field (Figure 2.14) showed the least agreement, where  $d_{\max}$  was 1.6 cm for the calculated point versus 1.2 cm for the measured point. The 10 cm x 10 cm field (Figure 2.13), which was the field that was used to commission the source

model,  $d_{\max}$  was 1.6 cm for the calculated point and 1.5 cm for the measured point. For the larger fields, the few data points that fell outside the stated criteria tended to occur in the build-up region where the calculation reported dose was less than the measured dose. The model did not predict the shift in  $d_{\max}$  to shallower depths and underestimated the dose in the build-up region as the field size increased. This is a limitation in the model and is mainly due to the increased collimator scatter that occurred with an increase in field size and could be improved by including the small contribution from the electron contamination.<sup>50</sup> Recall that the model was commissioned based on the conditions of the 10 cm x 10 cm field size and does not explicitly model the relative fluence and energy as a function of field size for the extra-focal source and also assumes that the primary source originates as a point. Although a small contribution, the dose from electron contamination was not included in the commissioning of the 6 MV source model. Another contribution to the disagreement between the calculation and measurement for the larger field sizes may be how the calculated data is extracted from the 3D dose matrix. The percent depth dose calculated data relied on the resolution of the CT scan (0.2 cm) and the accurate placement of the contoured region of interest which defined the water surface. Since a steeper dose gradient exists as the build-up region and  $d_{\max}$  shift toward the surface to shallower depths as the field size increases due to the increase in collimator scatter, agreement between the calculation and the measurement becomes more sensitive to an accurate registration of the surface location within the calculation algorithm.

#### 2.3.2.3 *Dose profiles*

The dose profile data for the 6 MV photon beam are shown in Figure 2.15, Figure 2.16, and Figure 2.17 for field sizes of 4 cm x 4, 10 cm x 10 cm, and 40 cm x 40 cm, respectively. The dose profile comparisons for the remaining fields are presented in the appendix (Chapter 6).



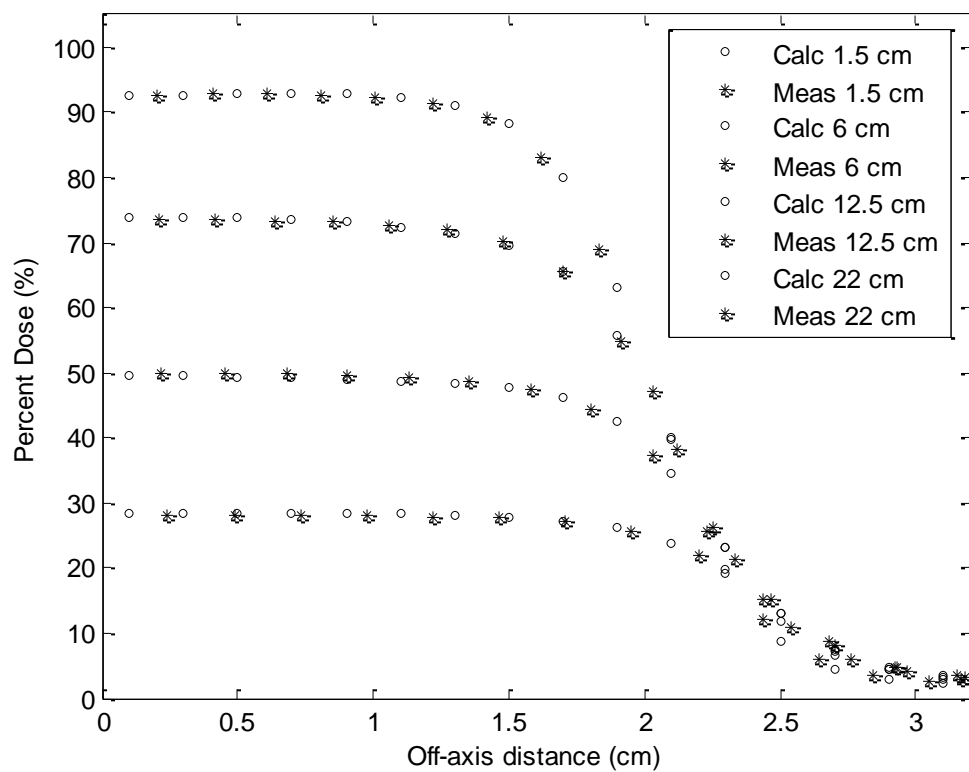


Figure 2.15 Calculated and measured dose profiles at 6 MV from a 4 cm by 4 cm field at depths of 1.5 cm, 6 cm, 12.5 cm, and 22 cm.

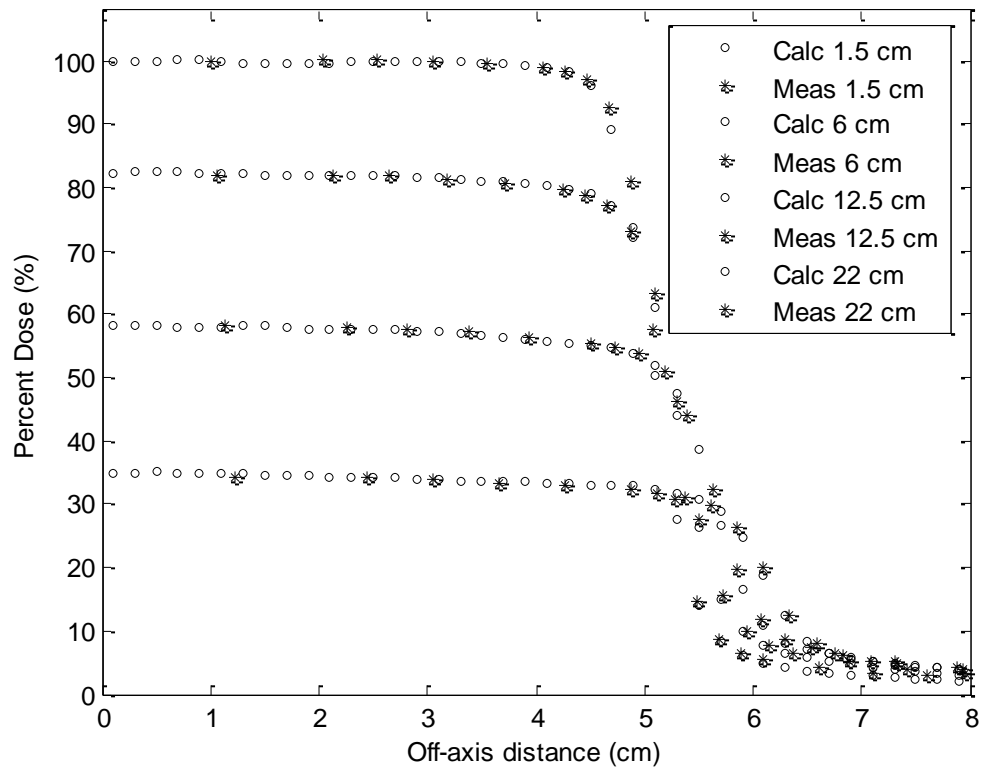


Figure 2.16 Calculated and measured dose profiles at 6 MV from a 10 cm by 10 cm field at depths of 1.5 cm, 6 cm, 12.5 cm, and 22 cm.

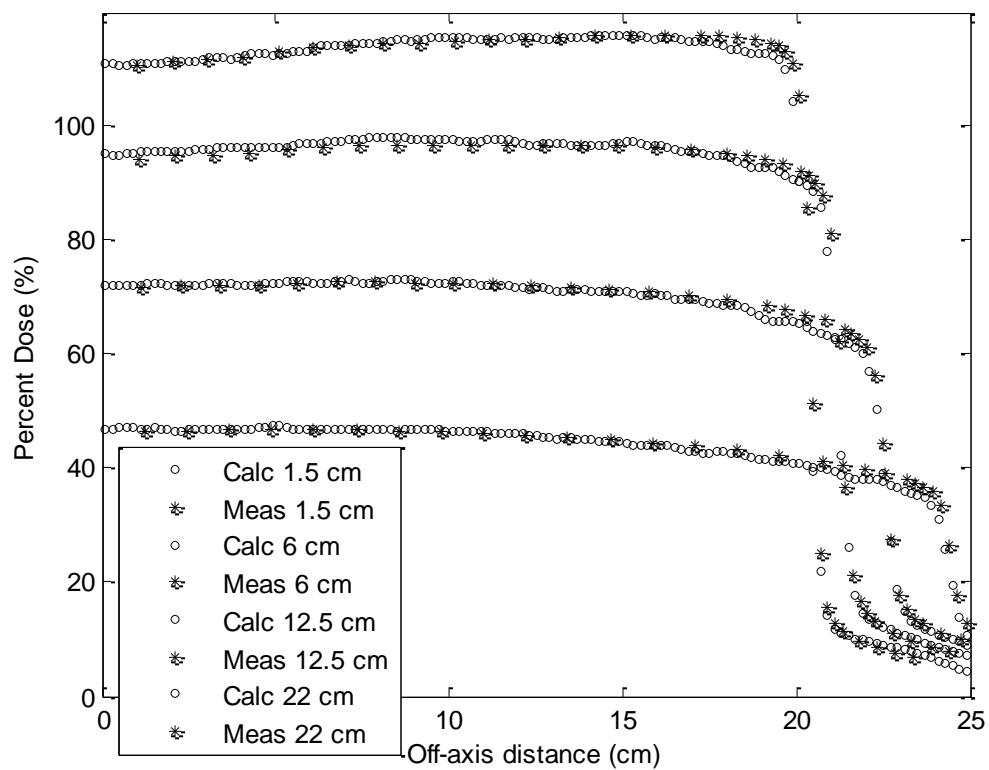


Figure 2.17 Calculated and measured dose profiles at 6 MV from a 40 cm by 40 cm field at depths of 1.5 cm, 6 cm, 12.5 cm, and 22 cm.

Good agreement existed between the calculation and measurement for all field sizes at all depths. As was the case for the percent depth dose comparisons, the dose profiles for the field sizes from 4 cm x 4 cm to 15 cm x 15 cm met the criteria of 2%/2 mm completely (Table 3). For the larger fields, the minimum percentage that met the criteria of 2%/2 mm, was 95%; and on average 98% of the data met the criteria.

| Field size<br>(cm <sup>2</sup> ) | Minimum percentage of data meeting the<br>criteria of 2% of $d_{\max}$ or 2 mm DTA<br>(%) | Average percent<br>difference (local dose)<br>(%) |
|----------------------------------|---|---|
| 4 × 4                            | 100   | 0.8   |
| 5 × 5                            | 100   | 0.6   |
| 6 × 6                            | 100   | 0.7   |
| 8 × 8                            | 100   | 0.6   |
| 10 × 10                          | 100   | 0.5   |
| 15 × 15                          | 100   | 0.8   |
| 20 × 20                          | 97  | 1.3   |
| 25 × 25                          | 99  | 0.9   |
| 40 × 40                          | 95  | 1.0   |

Table 3 Dose profile agreement between calculated and measured data. Profiles are from the depths of 1.5 cm, 6 cm, 12.5 cm, and 22 cm for each field size. Minimum percentage of the data meeting the criteria of 2% of  $d_{\max}$  or 2 mm DTA and the percent difference is the average of all local percent differences from all of the profiles for a given field.

The average local percent difference in the high dose region defined by the measured dose values greater than or equal to 80% of the dose at the central axis was between 0.5% and 1.3%. Generally, the average differences were consistent regardless of the field size, although the larger fields did exhibit slightly less agreement. The results of the gamma criteria and local dose comparisons of the high dose regions showed that the occasional disagreement was limited to the penumbra and low dose regions of the larger fields (see Figure 2.17) where scatter conditions offered their greatest contribution. The dose profiles comparisons, like the

percent depth dose comparisons, suggested the extra-focal model, while very robust, was likely the single biggest contributor to the small inaccuracies of the model.

### **2.3.3 Benchmark testing**

#### **2.3.3.1 Uncertainty**

The uncertainty of the dose distribution as determined by the EBT film and TLD at one standard deviation was between 2.6% and 3.5%. This is consistent with a previously published report using the same methodology.<sup>51</sup> TLD used as an absolute dosimeter helped to reduce the variation that can occur between the film calibration process and the actual film used in the phantom at the time of irradiation. The estimate included the uncertainty of the TLD dose,<sup>52</sup> the film uniformity, the film-to-film variation, and the fit of the sensitometric curve.<sup>53</sup> The TLD uncertainty was included because the film was normalized to the adjacent target TLD housed within the phantom. The estimate of uncertainty, or the standard error of the mean, for the simulation was 1% using 10 million particles per square centimeter.<sup>10</sup>

#### **2.3.3.2 Effect of finite primary source size on benchmark deliveries**

Prior to presenting the results of the benchmark evaluation, the effect of the MLC offset is presented. As described in Section 2.3.1.2 and in Figure 2.3, an MLC offset was applied to open each leaf position by 0.4 mm to compensate for the finite dimension of the primary source. Rangel and Dunscombe performed a study where they looked at the dosimetric impact of MLC position errors in dynamic IMRT deliveries.<sup>54</sup> They applied the equivalent uniform dose (EUD) metric to the dose volumes of targets and structures whose plans were compared with and without an MLC offset as a way to quantify MLC positional changes. They chose this metric for its applicability to treatment dosimetry since it is sensitive to both dose and volume. The EUD describes the dose from a nonuniform dose distribution producing the same radiobiological effect as if it was the dose from a uniform dose distribution. As expected,

an MLC offset in which the leaves are opened resulted in an increase in the EUD of an irradiated volume due to an increase in head and phantom scatter. They found that for more highly modulated treatments, such as head and neck plans versus prostate plans, the increase in the EUD of the clinical target volume was an average of 2.8% versus 1.0% higher, respectively, given an MLC offset of an additional 0.5 mm opening for every modulated leaf. Figure 2.18 shows the frequency histogram of the aperture distances. The aperture distance is defined as the distance between opposing leaf ends. The histogram is the grouping of aperture distances used to form each static segment for each beam and was determined for each treatment plan. In our studies, we found the EUD of the primary PTV in the head and neck plan was 2.4% higher, the EUD of the PTV in the SBRT lung plan was 1.7% higher, and the EUD of the PTV in the IMRT lung plan essentially unchanged when an MLC offset of 0.4 mm was applied. While the IMRT head and neck plan was similar to their results and the SBRT lung plan was less affected, most likely due to less modulation, it is not completely clear why the IMRT lung plan remained unchanged. With the additional opening from the MLC offset a higher output existed due to an increase in treatment head and phantom scatter. Therefore, it may be reasonable to conclude the relationship between the MLC positional changes and the EUD of the PTV for low density phantom media is less sensitive due to a reduction in phantom scatter.

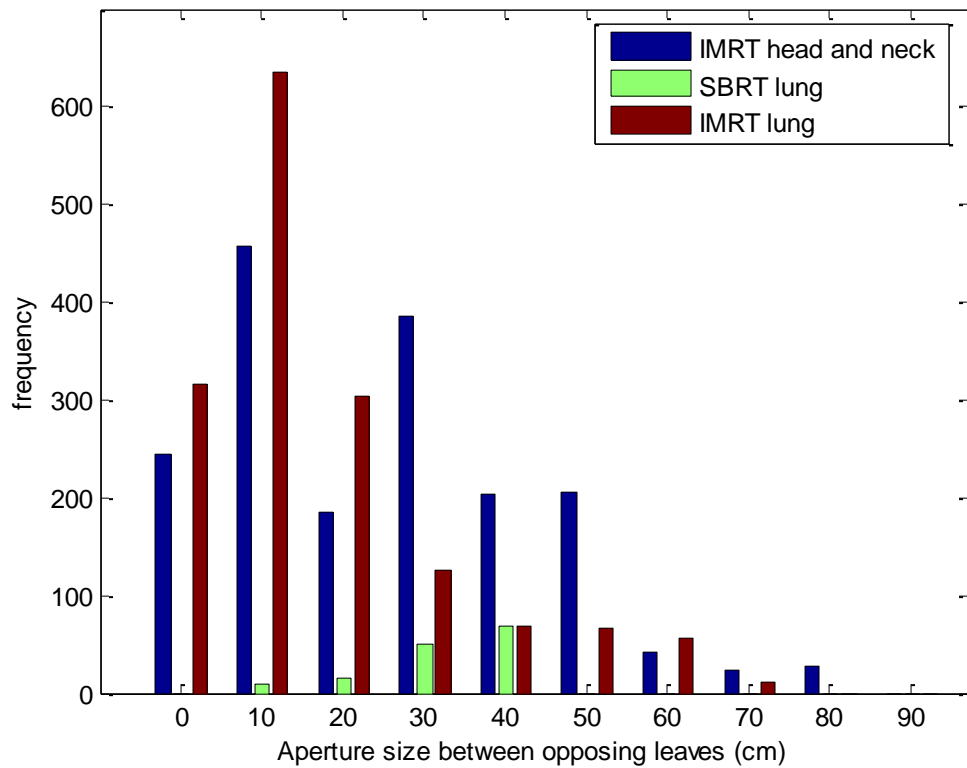


Figure 2.18 Frequency histogram of the aperture distances of opposing leaf ends from the IMRT head and neck plan, the SBRT lung plan, and the IMRT lung plan.

### 2.3.3.3 Delivery of the IMRT head and neck phantom plan: Point dose comparisons

The results of the point dose comparisons are shown for each TLD measurement location in Table 4. Four TLD capsules were located within the center of the primary target, two TLD capsules within the center of the secondary target and two TLD capsules within the spinal cord critical structure. Included in the table are the average dose measurements and the percent standard deviations from the three repeated irradiations. The comparisons of the primary target, the secondary target, and the critical structure between the DPM calculation and measurement and between the Pinnacle calculation and measurement were expressed as a ratio.

| Point<br>dose<br>local | TLD measurement |                | DPM calculation |                |                    | Pinnacle calculation<br>(reference) |                |                    |
|------------------------|-----------------|----------------|-----------------|----------------|--------------------|-------------------------------------|----------------|--------------------|
|                        | Avg.<br>(cGy)   | % std.<br>dev. | Avg.<br>(cGy)   | % std.<br>dev. | Ratio<br>calc/meas | Avg<br>(cGy)                        | % std.<br>dev. | Ratio<br>calc/meas |
| Pri S-A                | 648             | 0.4            | 638             | 1.8            | 0.984              | 677                                 | 1.0            | 1.045              |
| Pri S-P                | 650             | 0.8            | 635             | 0.8            | 0.977              | 674                                 | 0.6            | 1.037              |
| Pri I-A                | 638             | 1.1            | 637             | 1.4            | 0.998              | 678                                 | 0.9            | 1.062              |
| Pri I-P                | 665             | 0.9            | 646             | 1.6            | 0.971              | 683                                 | 1.0            | 1.027              |
| Pri Avg                |                 |                |                 |                | 0.983              |                                     |                | 1.043              |
| Sec S                  | 536             | 0.3            | 531             | 2.0            | 0.991              | 552                                 | 1.4            | 1.030              |
| Sec I                  | 529             | 0.5            | 525             | 2.3            | 0.992              | 546                                 | 1.5            | 1.032              |
| SecAvg                 |                 |                |                 |                | 0.991              |                                     |                | 1.031              |
| CS S                   | 199             | 1.6            | 195             | 7.6            | 0.982              | 235                                 | 9.8            | 1.183              |
| CS I                   | 201             | 1.2            | 176             | 6.7            | 0.877              | 206                                 | 6.2            | 1.026              |
| CS Avg                 |                 |                |                 |                | 0.929              |                                     |                | 1.105              |

Table 4 Point dose comparisons of the IMRT head and neck phantom. The measured dose is the average dose from the three repeated irradiations. Calculated results are from DPM. The Pinnacle calculation is provided for reference. Point dose locations are keyed as follows: Pri = primary target; Sec = secondary target; CS = critical structure; S = superior; I = inferior; A = anterior; P = posterior.

The agreement between the DPM calculation and measurement for the primary target on average was 0.983. The range of this averaged value was from 0.971 to 0.998. For the secondary target, both TLD locations showed that on average the calculation was slightly lower than the measurement by about 1%. The critical structure showed the greatest deviation where the calculation for the superior TLD location underestimated the dose by 2% and for the inferior TLD location underestimated the dose by about 12%. The larger differences between the calculated and measured dose were seen in their larger standard deviations. This, in large part, was due to the high dose gradient region that existed between the critical structure and target. It is also possible that the operation of the MLCs were in error. Given the close proximity of the superior and inferior TLDs to one another, it is possible that the MLC leaf in line with the superior TLD was not the correct position. In general, it is noted that the Pinnacle



calculation overestimated the dose in the targets so that the ratio between the calculation and measurement on average was 1.031 to 1.043.

The results in Table 5 present the overall range and average of the ratios between the source model calculation and the measurement, and between the Pinnacle calculation and the measurement for the primary and secondary targets and critical structure for all TLD locations and all repeated irradiations and not as an average of the repeated irradiations as was the data contained in Table 4.

|      | DPM calculation to measurement |                  |                    | Pinnacle calculation to measurement |                  |                    |
|------|--------------------------------|------------------|--------------------|-------------------------------------|------------------|--------------------|
|      | Primary target                 | Secondary target | Critical structure | Primary target                      | Secondary target | Critical structure |
| high | 1.006                          | 0.997            | 0.997              | 1.071                               | 1.037            | 1.202              |
| low  | 0.966                          | 0.988            | 0.865              | 1.021                               | 1.026            | 1.013              |
| avg  | 0.983                          | 0.991            | 0.929              | 1.043                               | 1.031            | 1.105              |

Table 5 IMRT head and neck: The range and average calculation to TLD measurement ratio of the point doses for the primary and secondary targets and critical structure for DPM and Pinnacle. The data is for each TLD location from each repeated irradiations.

The benchmark evaluation was strictly between the validated source model and measurement. The Pinnacle comparison with the measurement is shown only for reference and is representative of the comparison one might find between the source model calculation and a state of the art planning system.

#### 2.3.3.4 *Delivery of the IMRT head and neck phantom plan: Dose profile and gamma map comparisons*

Dose profiles along all three major planes are shown in Figure 2.19, Figure 2.20, and Figure 2.21. The dose profiles show the qualitative agreement between the source model DPM calculation and the measured dose and indicate the tendency of the calculation to slightly

underestimate the dose. Good agreement is seen across all dose profiles. The DPM calculation responded to the subtle changes in dose delivery across the primary PTV as noted in the lateral profile of Figure 2.19.

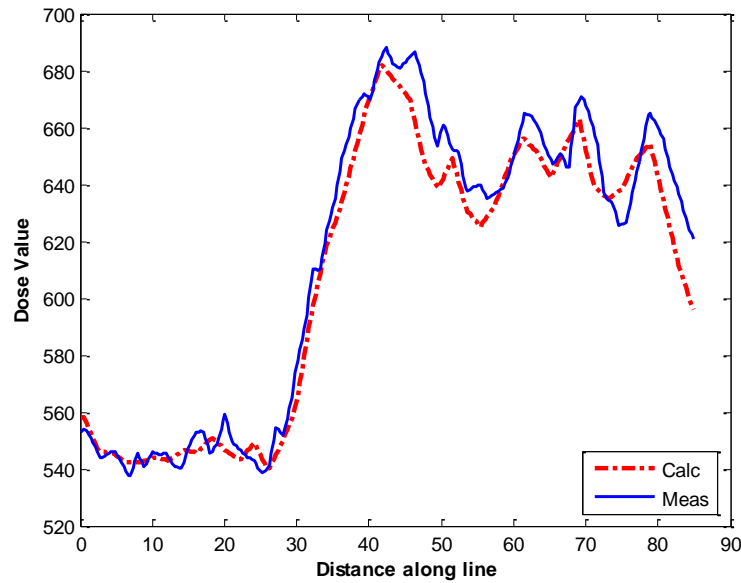


Figure 2.19 IMRT H&N delivery single irradiation (number 2): Lateral dose profile.

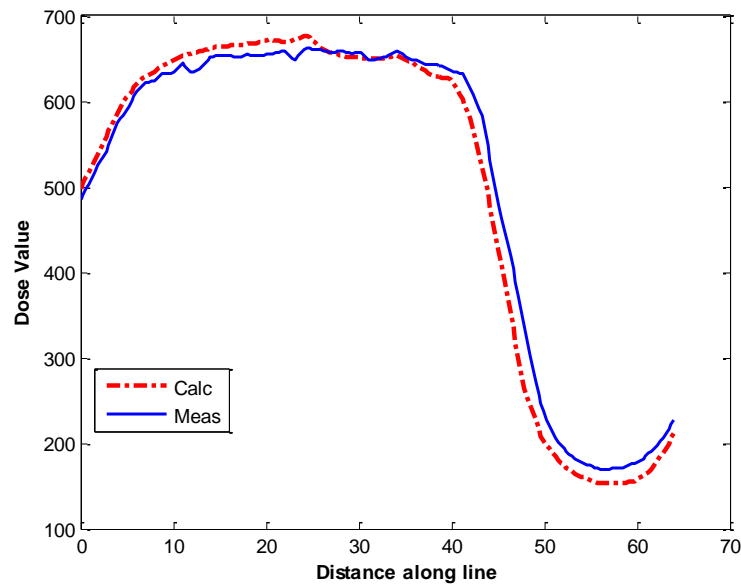


Figure 2.20 IMRT H&N delivery single irradiation (number 2): A-to-P dose profile.

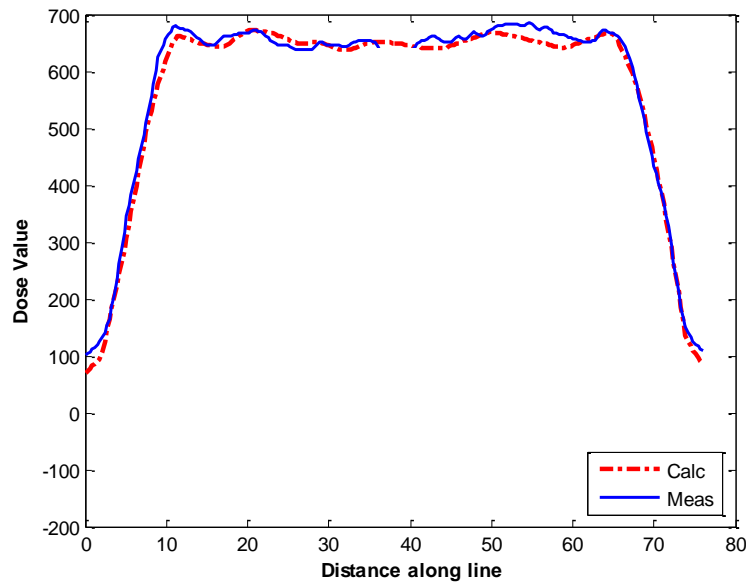


Figure 2.21 IMRT H&N delivery single irradiation (number 2): S-to-I dose profile.

In conjunction with the dose profiles, the gamma maps at a test criterion of 3%/2 mm are shown in Figure 2.22 and Figure 2.23. These figures report the results from a single irradiation. Gamma maps at the criteria levels of 3%/2 mm and 5%/3 mm and dose profiles for all three repeated irradiations are presented in the Chapter 6 Appendix. For the IMRT head and neck plan, the percentage of the data meeting the criterion of 3% or 2 mm for the gamma maps from the axial and sagittal dose planes intersecting the center of the primary target from all three repeated irradiations averaged 93% and ranged from 90% to 98%. The gamma maps, which consider dose differences as a relative percentage and dose differences as a distance to agreement, showed that in general the calculation predicted the dose within the criteria in the high dose, high gradient, and low dose regions that lied along the axial and sagittal planes. The dose profiles in conjunction with the gamma maps indicated that the modeling to describe the penumbra which applied an MLC offset, interleaf leakage, rounded leaf and leaf transmission factors in the highly modulated fields of the head and neck plan was correct.

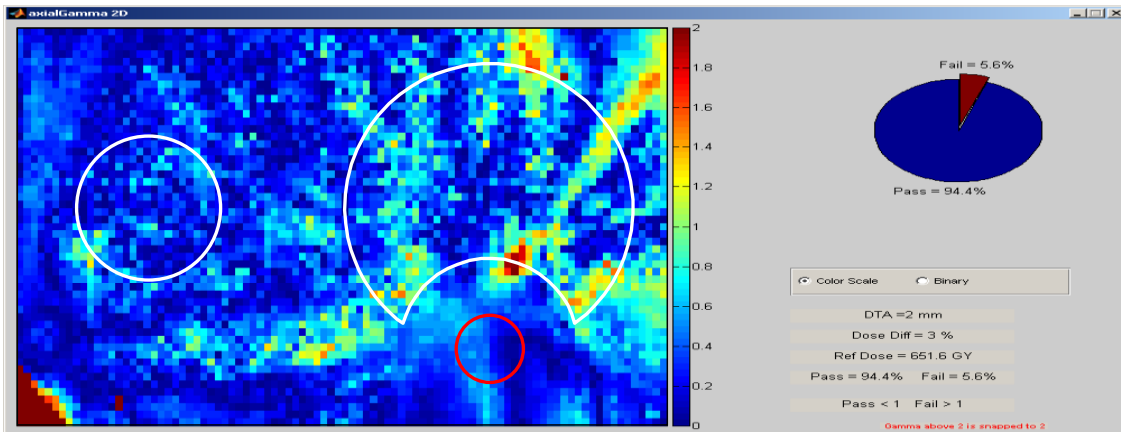


Figure 2.22 IMRT H&N delivery single irradiation (number 2): Axial plane, gamma map tested to 3%/2 mm criteria, where 94% of the data passed. Scale is 1 mm = 0.95 mm. Small circle outline represents the location of the secondary PTV, large crescent shaped outline represents the primary PTV, and the small red circle represents the spinal cord critical structure.

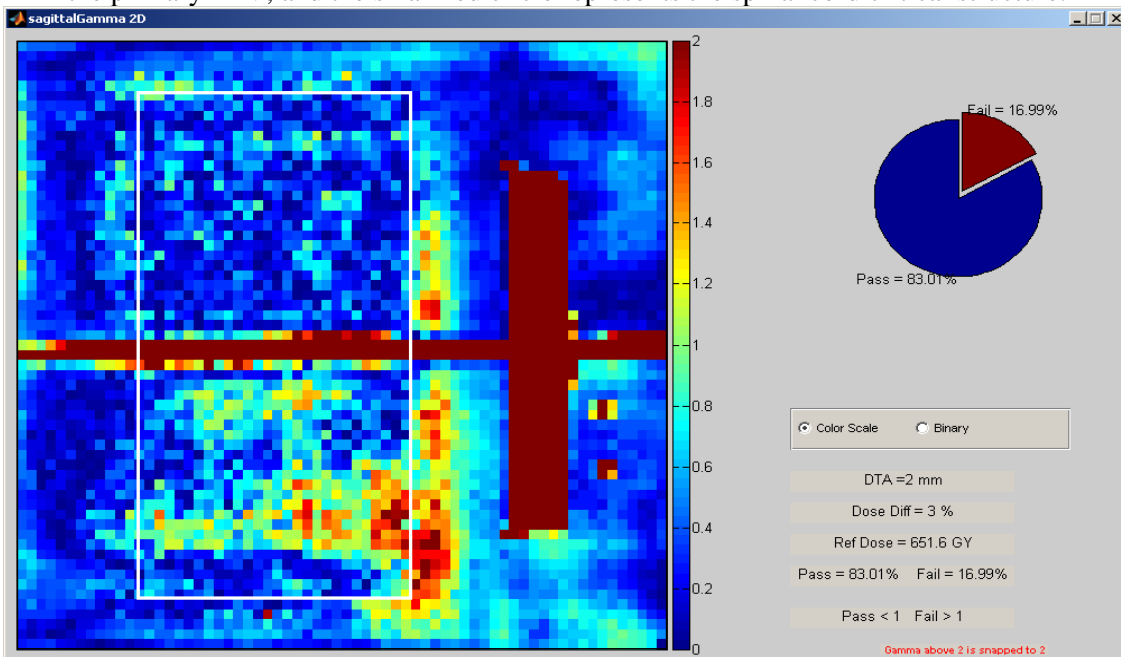


Figure 2.23 IMRT H&N delivery single irradiation (number 2): Sagittal plane; gamma map tested to 3%/2 mm criteria, where 91% of the data passed. Scale is 1 mm = 1.3 mm. Rectangle outline represents the location of the primary PTV. The maroon region in the vertical direction is where the film has been cut away to avoid interference with the critical structure region.

Figure 2.24 shows the performance with and without consideration for the primary finite source, interleaf leakage, and the effect of the rounded leaf ends on transmission. Note that in addition to an increase in the calculated dose to the primary and secondary targets, there was an improvement in the widening and shape of the penumbra.

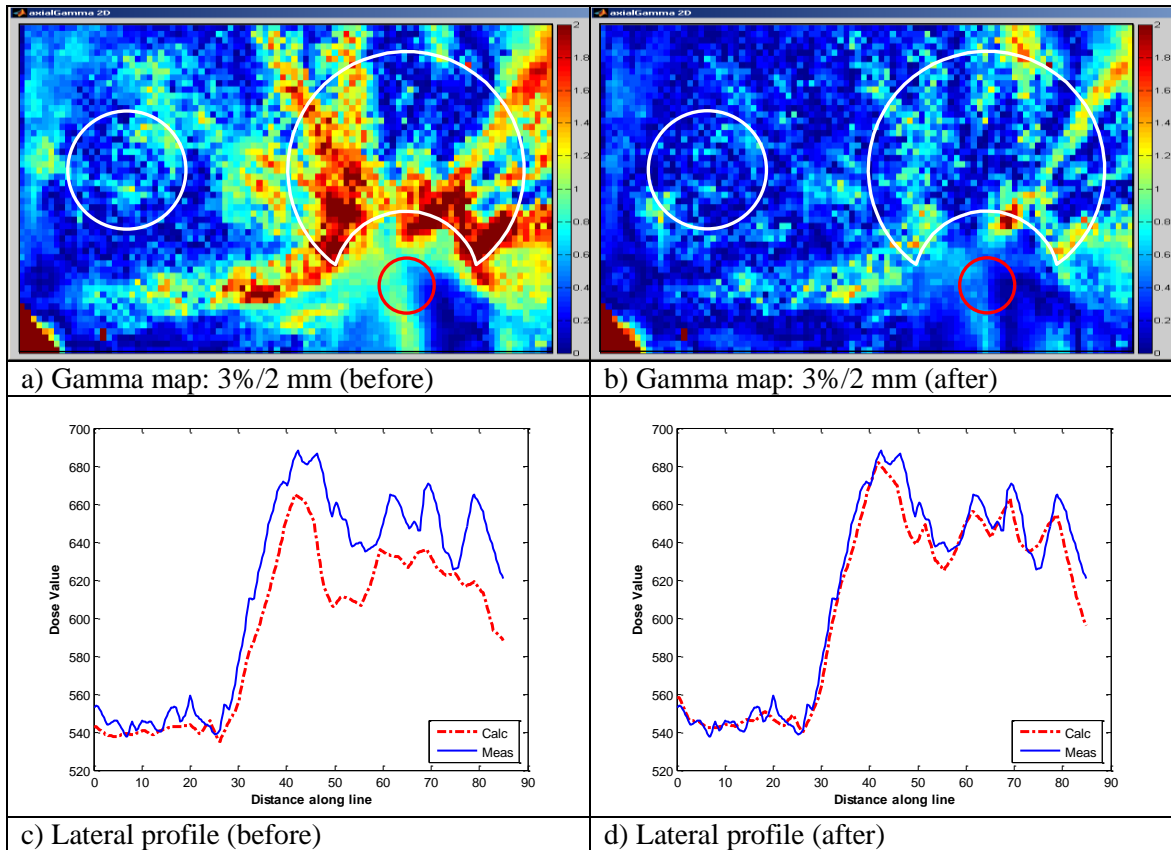


Figure 2.24 IMRT head and neck: Gamma maps (a and b) and lateral dose profiles (c and d) from the same irradiation, but before (a and c) and after (b and d) changes to the model to improve the penumbra.

For reference, the Pinnacle calculation was compared to the same measured data and is shown in Figure 2.25. The results were somewhat surprising given that the delivery was made in a homogeneous phantom. However, the results at 5%/3 mm show a marked improvement in agreement over the results at 3%/2 mm. The lateral dose profile (Figure 2.25) shows somewhat steep gradients occurring frequently. The dose grid calculation for Pinnacle plan was studied at 0.4 cm and 0.2 cm. No improvement was gained given the finer resolution. The Pinnacle calculation commonly includes a post processed smoothing function which may account for the lack of the dose gradient changes in the Pinnacle calculation. The dose profiles show that Pinnacle is overpredicting the dose in the primary and secondary targets when compared to the film measurement.

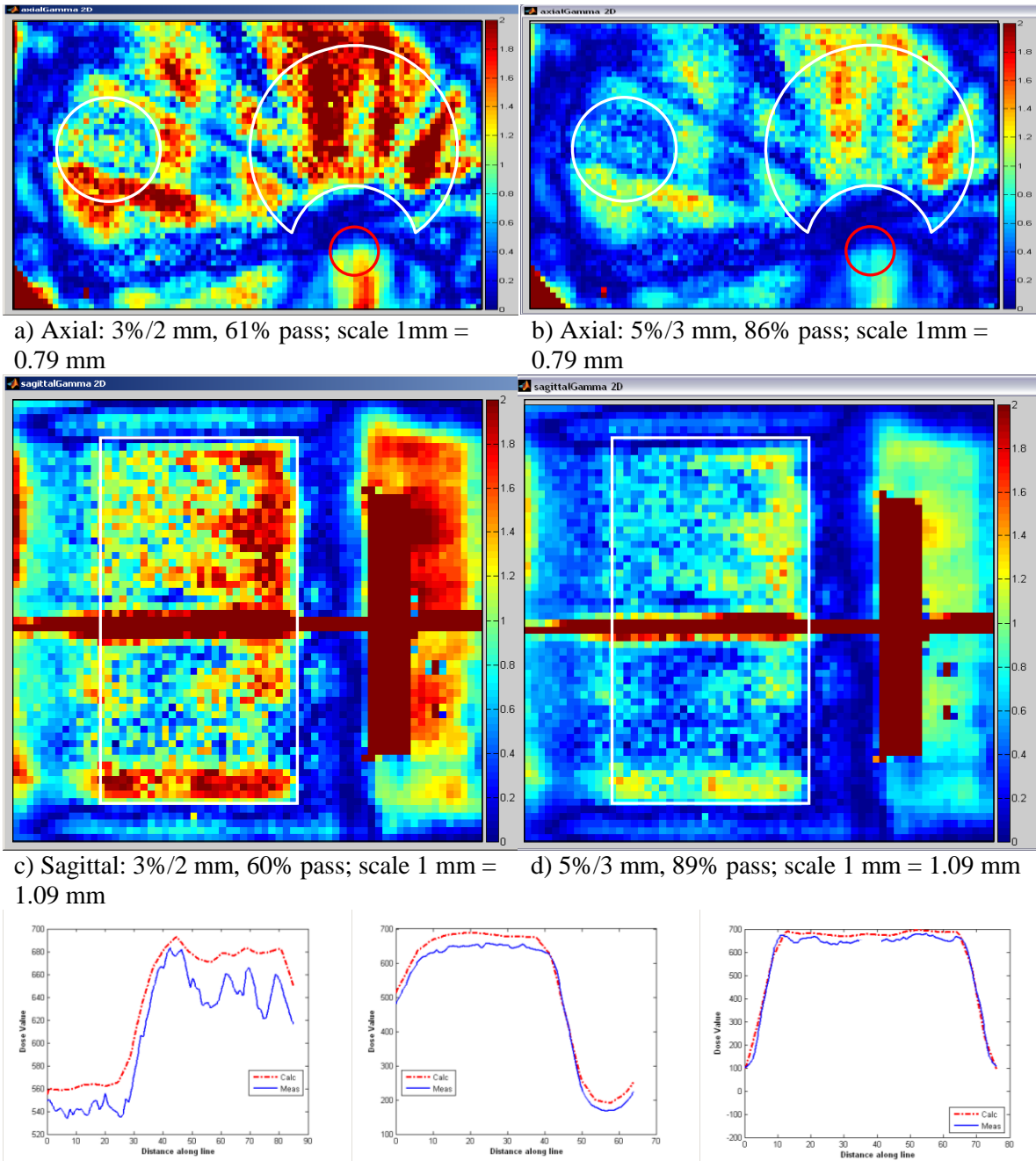


Figure 2.25 Gamma map (a through d) and dose profile (e through g) comparisons between the Pinnacle calculation and measurement for the IMRT H&N delivery (single irradiation, number 2)

### 2.3.3.5 Delivery of the SBRT thorax phantom plan: Point dose comparisons

The results of the point dose comparisons are shown for each TLD measurement location in Table 6. Two TLD capsules were located within the center of the target, two TLD

capsules within the heart and two TLD capsules within the spinal cord critical structures. Included in the table are the average dose measurements and the percent standard deviations from the three repeated irradiations. The comparisons of the target and the critical structures between the DPM calculation and measurement and between the Pinnacle calculation and measurement were expressed as a ratio.

| Point dose local | TLD measurement |             | DPM calculation |             |                 | Pinnacle calculation (reference) |             |                 |
|------------------|-----------------|-------------|-----------------|-------------|-----------------|----------------------------------|-------------|-----------------|
|                  | Avg. (cGy)      | % std. dev. | Avg. (cGy)      | % std. dev. | Ratio calc/meas | Avg (cGy)                        | % std. dev. | Ratio calc/meas |
| Target Sup       | 774             | 0.6         | 783             | 0.3         | 1.012           | 784                              | 0.1         | 1.013           |
| Target Inf       | 769             | 0.4         | 780             | 0.5         | 1.014           | 781                              | 0.1         | 1.015           |
| Target Average   |                 |             |                 |             | 1.013           |                                  |             | 1.014           |
| Cord             | 71              | 0.5         | 78              | 1.4         | 1.089           | 75                               | 0.1         | 1.046           |
| Heart            | 134             | 0.7         | 137             | 1.7         | 1.022           | 132                              | 2.0         | 0.988           |

Table 6 Point dose comparisons of the SBRT thoracic phantom. The measured dose is the average dose from the three repeated irradiations. Calculated results are from DPM. The Pinnacle calculation is provided for reference.

The agreement between the DPM calculation and measurement for the target on average was 1.013. It is noted that the Pinnacle calculation estimated the point dose to the target similar to the DPM calculation so that the ratio between the calculation and measurement was 1.014. While the DPM calculated dose for the heart agreed with measurement (1.022), the ratio of the calculated dose to the measured dose to the spinal cord was 1.089. The cord dose was very low. While the repeatability of the dose was less than 1%, the uncertainty in the dose is not known at these low levels. It was no less than the known uncertainty of 3% for the calibration standard dose. The calibration standard dose was more than four times the

benchmark cord dose. Included in the measurement uncertainty was the phantom setup. Any translational error in the setup would be compounded with the radial distance from the isocenter. The spinal cord was distal to the target at isocenter and would suffer the greatest error given such a setup error. For the calculation, the estimate of uncertainty for the standard error of the mean in the voxels that circumscribe the location of the TLD in the spinal cord was 2.6%. This was higher than the reported uncertainty because of the fewer number of histories reported in the low dose region. Although this uncertainty does not completely justify the overestimation of the DPM calculation, other sources for error include the uncertainty of the scatter dose from the extra-focal model as discussed in section 2.3.2.3, the penumbra effect from the finite primary source, and the MLC model that defined the leaf transmission factor, interleaf leakage, and rounded leaf end.

The results in Table 7 present the range and average of the ratios between the source model and Pinnacle calculations and the measurement for the target and critical structures for all TLD locations and all repeated irradiations and not as an average of the repeated irradiations as was the data contained in Table 6. The calculation was 1.0% to 1.8% higher than the measurement standard for the target when all TLD locations are compared to the calculation locations individually.

|      | DPM calculation to measurement |       |       | Pinnacle calculation to measurement |       |       |
|------|--------------------------------|-------|-------|-------------------------------------|-------|-------|
|      | Target                         | Heart | Cord  | Target                              | Heart | Cord  |
| high | 1.019                          | 1.030 | 1.095 | 1.019                               | 0.996 | 1.051 |
| low  | 1.008                          | 1.016 | 1.084 | 1.009                               | 0.981 | 1.041 |
| avg  | 1.013                          | 1.022 | 1.089 | 1.014                               | 0.988 | 1.046 |

Table 7 SBRT lung plan: The range and average calculation to measurement ratio of the point doses for the target, cord, and heart for DPM and Pinnacle. The data is for each TLD location from each repeated irradiations.



The benchmark evaluation was strictly between the validated source model and measurement. The Pinnacle comparison with the measurement is shown only for reference and is representative of the comparison one might find between the source model calculation and a state of the art planning system.

#### 2.3.3.6 *Delivery of the SBRT thorax phantom plan: Dose profile and gamma map comparisons*

Dose profiles along all three major planes are shown in Figure 2.26, Figure 2.27, and Figure 2.28. The figures reported the results from a single irradiation. As were the results of the comparison between the calculation and measurement of the homogeneous, highly modulated head and neck plan, the results for the SBRT lung plan were very good. The calculated and measured dose from the lateral, anterior-posterior, and superior-inferior profiles agreed in the PTV and penumbra regions, but the lower dose regions showed the calculation was slightly overestimating as quantified by the gamma map results.

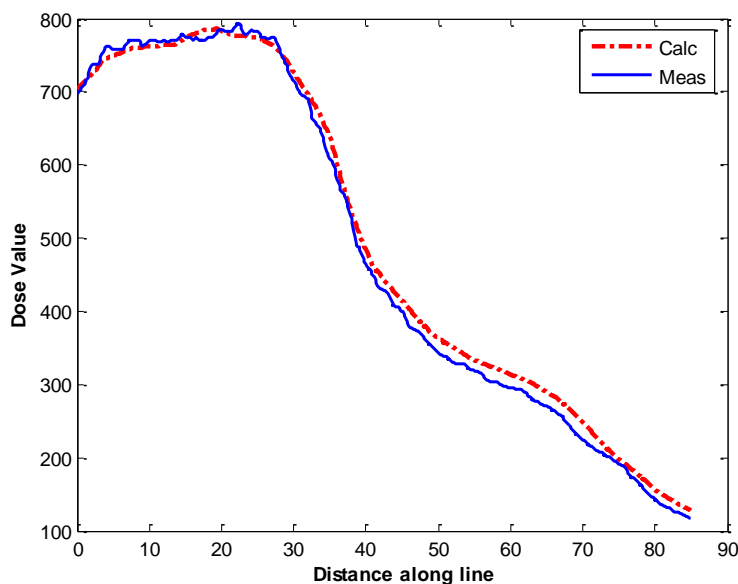


Figure 2.26 SBRT lung delivery single irradiation (number 1): lateral dose profile.

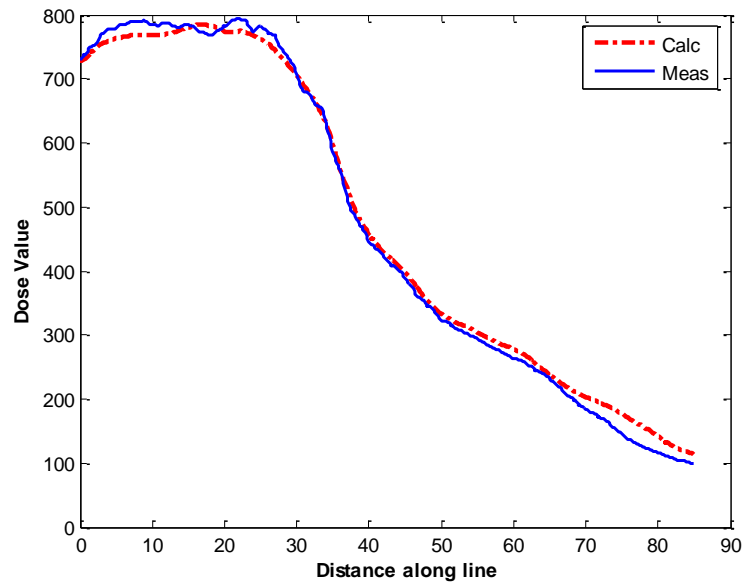


Figure 2.27 SBRT lung delivery single irradiation (number 1): A-P dose profile.

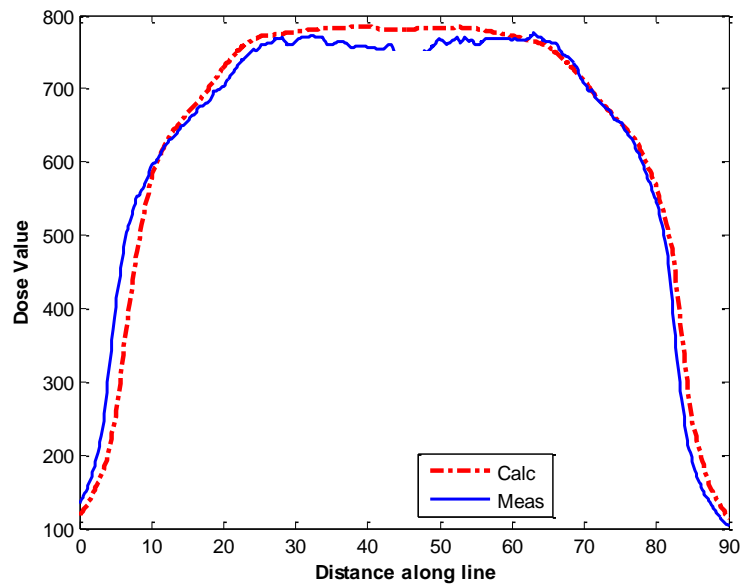


Figure 2.28 SBRT lung delivery single irradiation (number 1): S-I dose profile.

The gamma maps at a test criterion of 3%/2 mm are shown in Figure 2.29, Figure 2.30, and Figure 2.31. The maps reported the results from a single irradiation. The gamma map of the axial plane shows a small disagreement in the entrance dose from one of the beams positioned left lateral and posterior of the target,. Another region of a different beam's entrance dose and an opposing beam's exit dose, another small disagreement existed. Regardless, the SBRT lung plan had good agreement overall where 94% of the calculated data met the criterion of 3%/2 mm. The DPM dose calculation was able to accurately predict the dose from small fields in a low density anthropomorphic phantom. Gamma maps at the criteria levels of 3%/2 mm and 5%/3 mm and dose profiles for all three repeated irradiations are presented in the Appendix, Chapter 6.

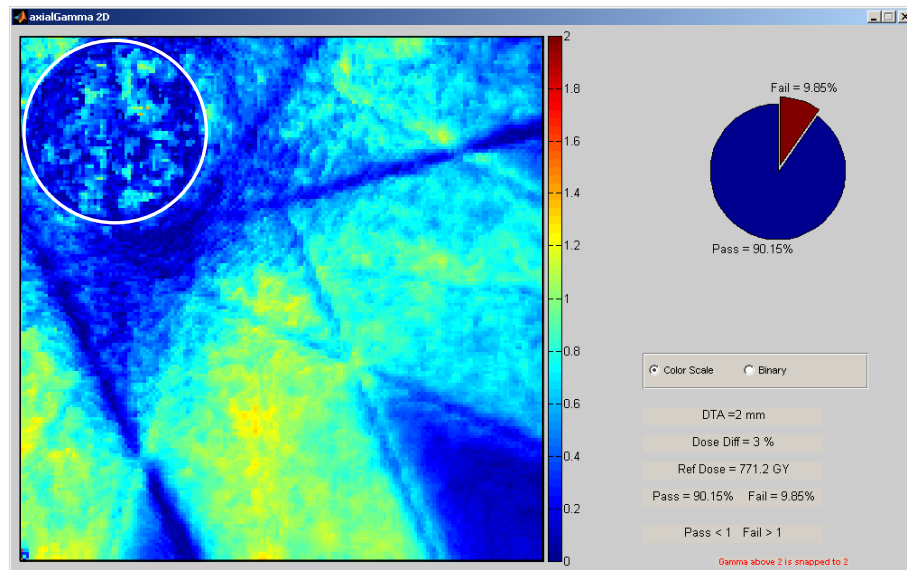


Figure 2.29 SBRT lung delivery single irradiation (number 1): Axial plane, gamma map tested to 3%/2 mm criteria, where 90% of the data passed. Scale is 1 mm = 0.8 mm. Circle outline represents the location of the PTV.

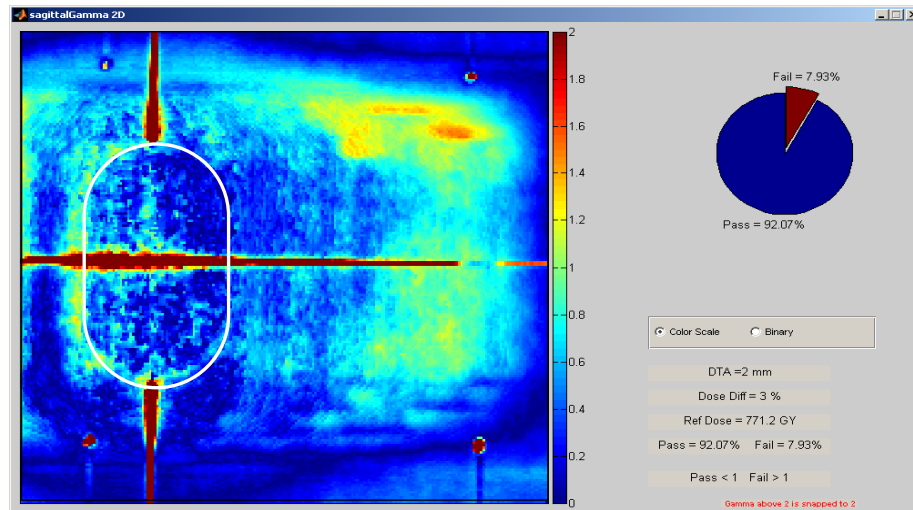


Figure 2.30 SBRT lung delivery single irradiation (number 1): Sagittal plane, gamma map tested to 3%/2 mm criteria, where 95% of the data passed. Scale is 1 mm = 0.65 mm. Elongated circle outline represents the location of the PTV.

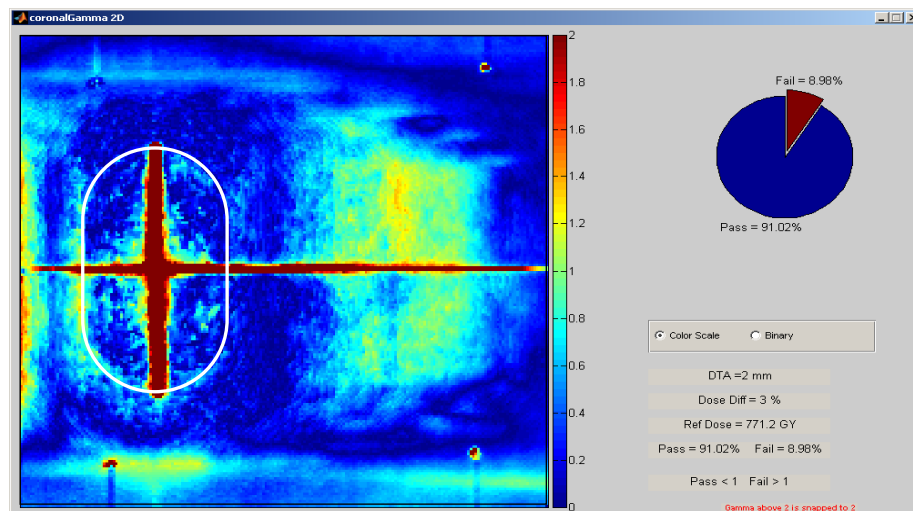
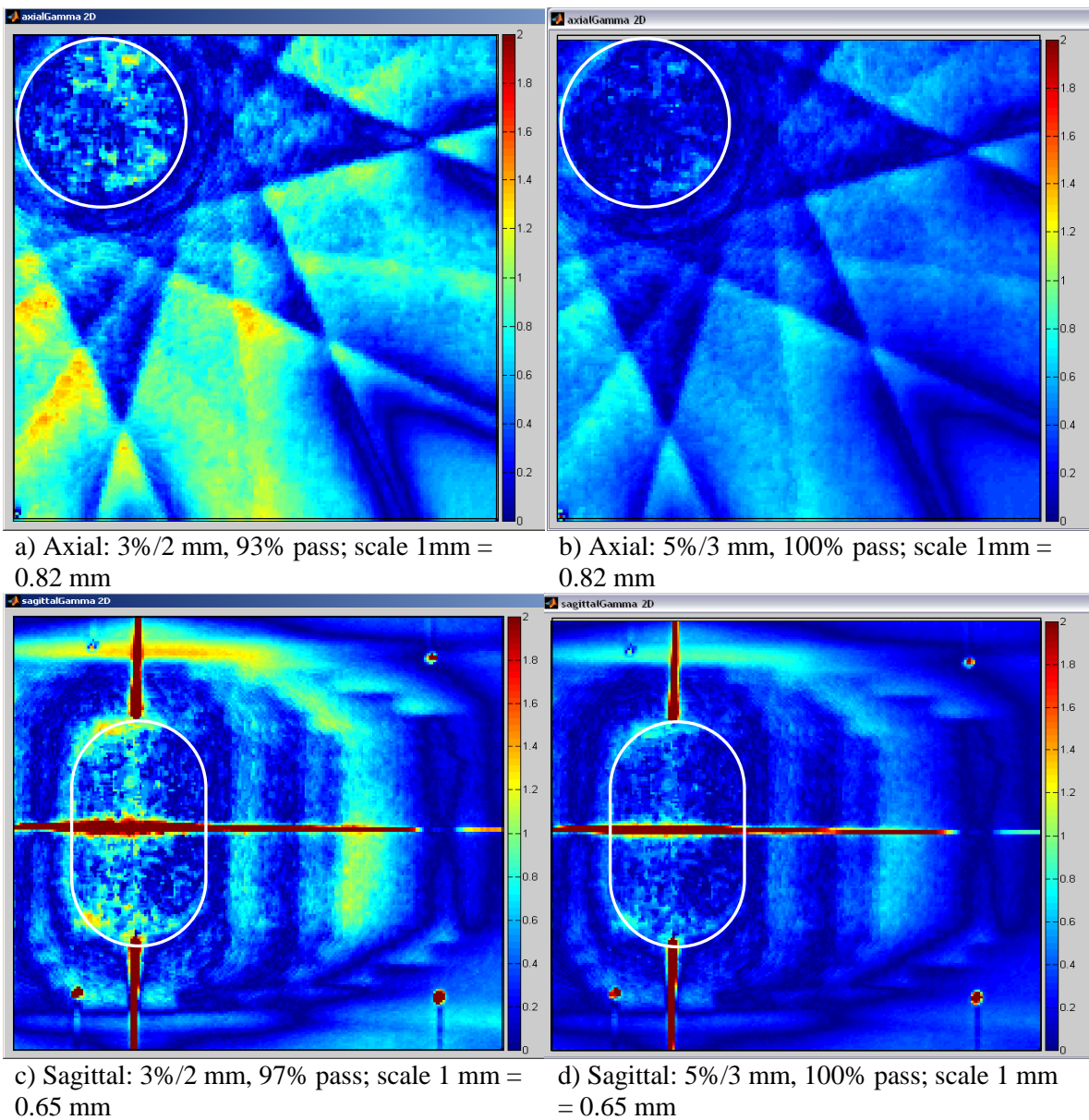
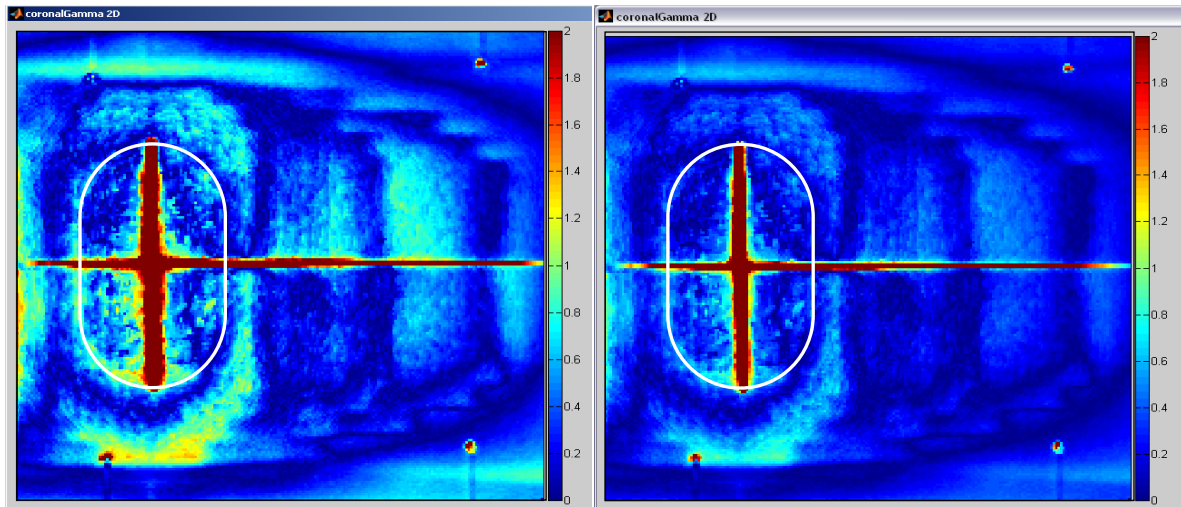


Figure 2.31 SBRT lung delivery single irradiation (number 1): Coronal plane, gamma map tested to 3%/2 mm criteria, where 93% of the data passed. Scale is 1 mm = 0.65 mm. Elongated circle outline represents the location of the PTV.

For reference, the Pinnacle calculation was compared to the same measured data and is shown in Figure 2.32. The results were exceptional throughout the all major planes, including

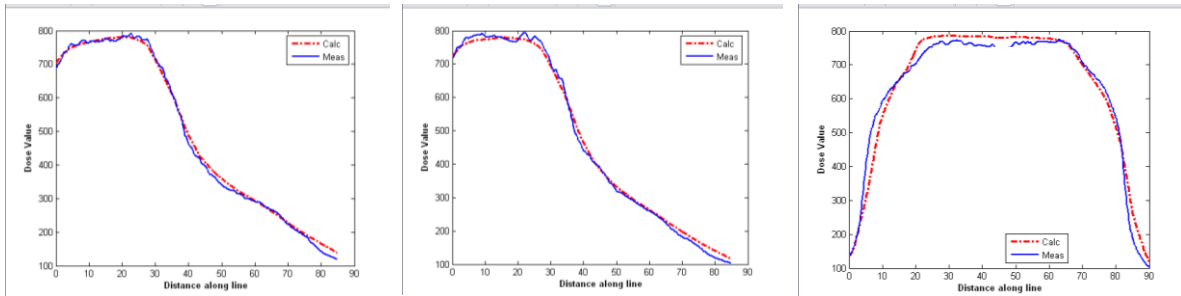
the low dose regions where the DPM calculation was slightly higher. Note the more abrupt field edges from the open beams and the dose pattern created in the regions of intersecting beams. This may be due to the larger dose grid used to perform the Pinnacle calculation (0.4 cm versus 0.2 cm for DPM). Or, this may be a result of applying dose kernels or a smoothing function across a homogeneous region in contrast to Monte Carlo where the particle history was tracked explicitly.





e) Coronal: 3%/2 mm, 96% pass; scale 1 mm = 0.65 mm

f) Coronal: 5%/3 mm, 99% pass; scale 1 mm = 0.65 mm



e) Lateral profile

f) Anterior to posterior profile

g) Superior to inferior profile

Figure 2.32 Gamma map and dose profile comparisons between the Pinnacle calculation and measurement for the SBRT lung delivery (single irradiation, number 1)

### 2.3.3.7 Delivery of the IMRT thorax phantom plan: Point dose comparisons

The results of the point dose comparisons are shown for each TLD measurement location in Table 8. As in the SBRT lung case, two TLD capsules were located within the center of the target, two TLD capsules within the heart and two TLD capsules within the spinal cord critical structures. Included in the table are the average dose measurements and the percent standard deviations from the three repeated irradiations. The comparisons of the target and the critical structures between the DPM calculation and measurement, and between the Pinnacle calculation and measurement were expressed as a ratio.

| Point dose local | TLD measurement |             | DPM calculation |             |                 | Pinnacle calculation (reference) |             |                 |
|------------------|-----------------|-------------|-----------------|-------------|-----------------|----------------------------------|-------------|-----------------|
|                  | Avg. (cGy)      | % std. dev. | Avg. (cGy)      | % std. dev. | Ratio calc/meas | Avg (cGy)                        | % std. dev. | Ratio calc/meas |
| Target Sup       | 6523            | 0.4         | 6697            | 1.1         | 1.024           | 6656                             | 0.2         | 1.027           |
| Target Inf       | 6556            | 0.4         | 6721            | 0.7         | 1.025           | 6671                             | 0.2         | 1.018           |
| Target Average   |                 |             |                 |             | 1.025           |                                  |             | 1.019           |
| Cord             | 808             | 0.2         | 809             | 1.1         | 1.001           | 800                              | 1.2         | 0.990           |
| Heart            | 1097            | 1.8         | 1178            | 2.0         | 1.074           | 1153                             | 1.4         | 1.052           |

Table 8 Point dose comparisons of the IMRT thoracic phantom. The measured dose is the average dose from the three repeated irradiations. Calculated results are from DPM. The Pinnacle calculation is provided for reference.

The DPM calculation overestimated the point dose to the target center by 2.6%. The Pinnacle calculation overestimated the point dose to the target by 1.9%. The DPM and Pinnacle calculation tended to agree for estimates of dose to the critical structures. The DPM calculation correctly predicted the dose to the cord and Pinnacle underestimated the dose by 1.0%. While both calculations overestimated the dose to the heart, The DPM calculation dose estimate overestimated by more than 7% and the Pinnacle calculation overestimated by more than 5%. The repeatability in the measurement of 1.8% and the standard deviation of the DPM calculation of 2.0% could account for some of the discrepancy as the TLD heart location was within a dose gradient region that changed by more than 30%/cm, Also the phantom set-up is more sensitive in measurement locations where high dose gradients exist. While the scatter dose was a contributor to uncertainty in the source model based approach, the TLD's close proximity to the target was not believed to be a large contributor to the disagreement in the TLD location of the heart.

The results in Table 9 present the range and average of the ratios between the source model and Pinnacle calculations and the measurement for the target and critical structures for all TLD locations and all repeated irradiations and not as an average of the repeated irradiations as was the data contained in Table 8. The calculation was 1.9% to 2.9% higher than the measurement standard for the target when all TLD locations are compared to the calculation locations individually.

|      | DPM calculation to measurement |       |       | Pinnacle calculation to measurement |       |       |
|------|--------------------------------|-------|-------|-------------------------------------|-------|-------|
|      | Target                         | Heart | Cord  | Target                              | Heart | Cord  |
| high | 1.029                          | 1.092 | 1.004 | 1.023                               | 1.070 | 0.992 |
| low  | 1.019                          | 1.055 | 1.000 | 1.015                               | 1.033 | 0.988 |
| avg  | 1.025                          | 1.074 | 1.001 | 1.019                               | 1.052 | 0.990 |

Table 9 IMRT lung: The range and average calculation to measurement ratio of the point doses for the target, cord, and heart for DPM and Pinnacle. The data is for each TLD location from each repeated irradiations.

The benchmark evaluation was strictly between the validated source model and measurement. The Pinnacle comparison with the measurement is shown only for reference and is representative of the comparison one might find between the source model calculation and a state of the art planning system.

#### 2.3.3.8 *Delivery of the IMRT thorax phantom plan: Dose profile and gamma map comparisons*

Dose profiles along all three major planes are shown in Figure 2.33, Figure 2.34, and Figure 2.35. The gamma maps at a test criterion of 3%/2 mm are shown in Figure 2.36, Figure 2.37, and Figure 2.38. These figures reported the results from a single irradiation. Gamma maps at the criteria levels of 3%/2 mm and 5%/3 mm and dose profiles for all three repeated irradiations are presented in the Appendix, Chapter 6. The calculated and measured dose from the lateral, anterior-posterior, and superior-inferior profiles generally agreed. However, the



dose profile showed in the posterior penumbra region some local dose differences in the range of 3% to 5%.

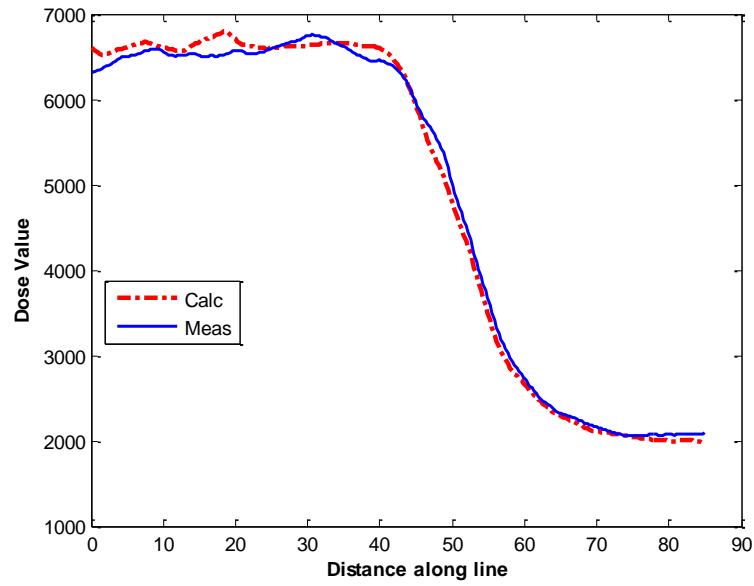


Figure 2.33 IMRT lung delivery single irradiation (number 3): lateral dose profile.

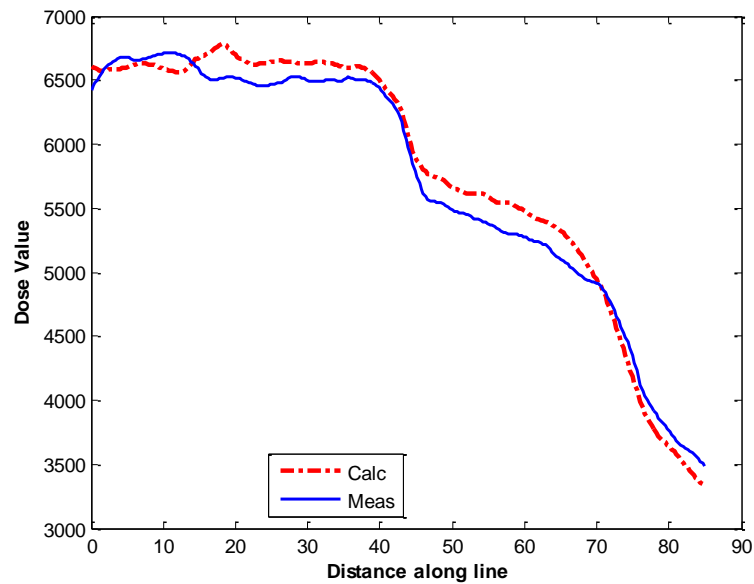


Figure 2.34 IMRT lung delivery single irradiation (number 3): A-P dose profile.

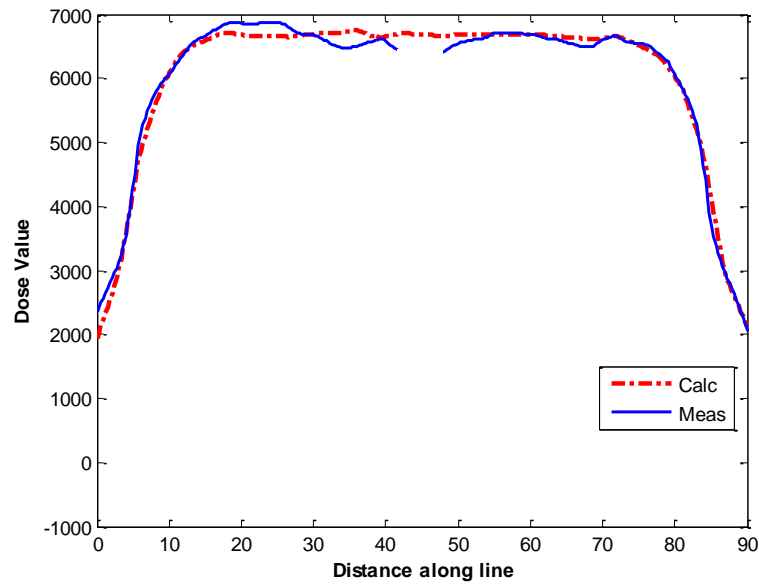


Figure 2.35 IMRT lung delivery single irradiation (number 3): S-I dose profile.

The gamma maps also showed small regions of disagreement which typically occurred in the penumbra regions. The penumbra region represented not only the change in the high dose region to low dose region, but also the change from the target tissue-like density to the low density region of the lung where electronic disequilibrium occurred. Disagreement may also be more likely to occur near the lung and the chest wall for the same reason. This may explain some of the differences between the calculation and measurement seen on the coronal gamma map.

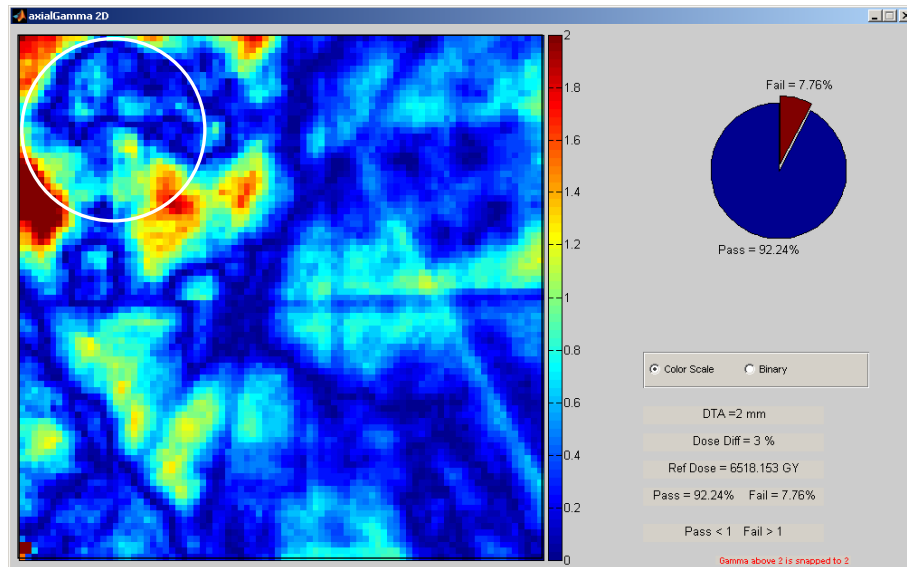


Figure 2.36 IMRT lung delivery single irradiation (number 3): Axial plane, gamma map tested to 3%/2 mm criteria, where 92% of the data passed. Scale is 1 mm = 0.8 mm. Circle outline represents the location of the PTV.

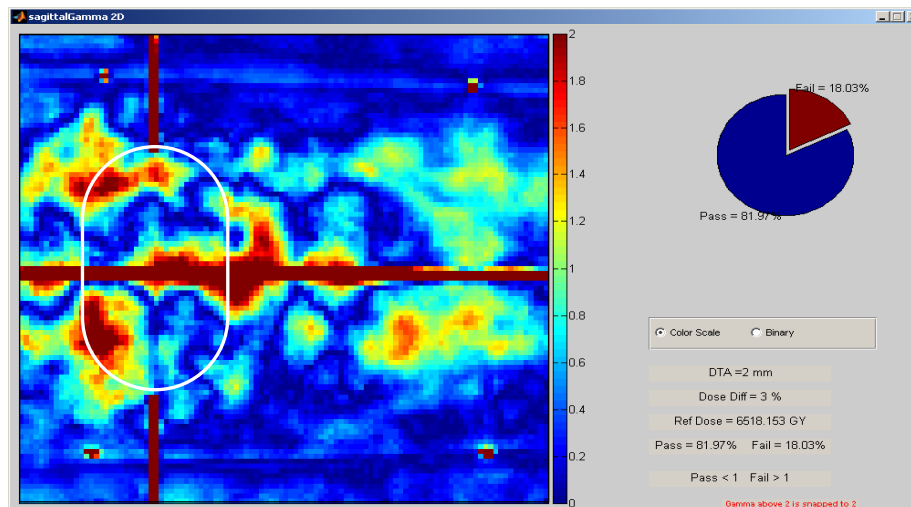


Figure 2.37 IMRT lung delivery single irradiation (number 3): Sagittal plane, gamma map tested to 3%/2 mm criteria, where 91% of the data passed. Scale is 1 mm = 0.65 mm. Elongated circle outline represents the location of the PTV.

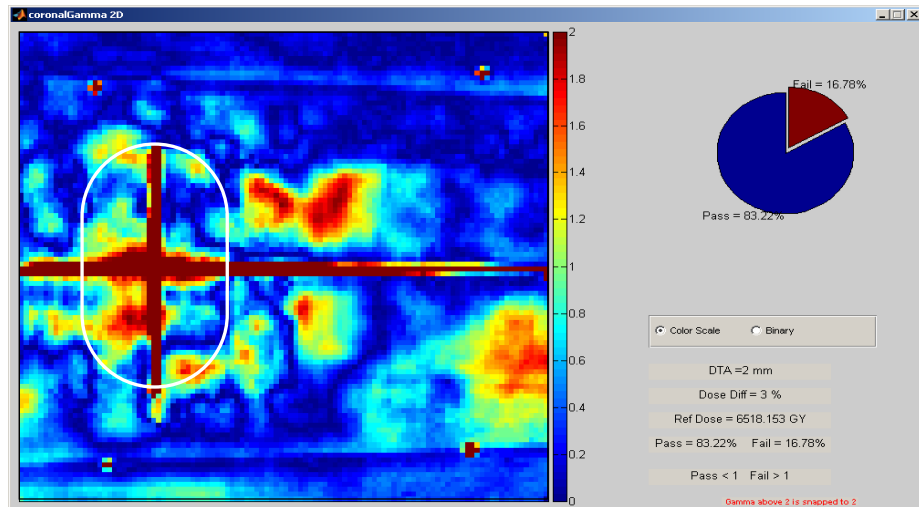
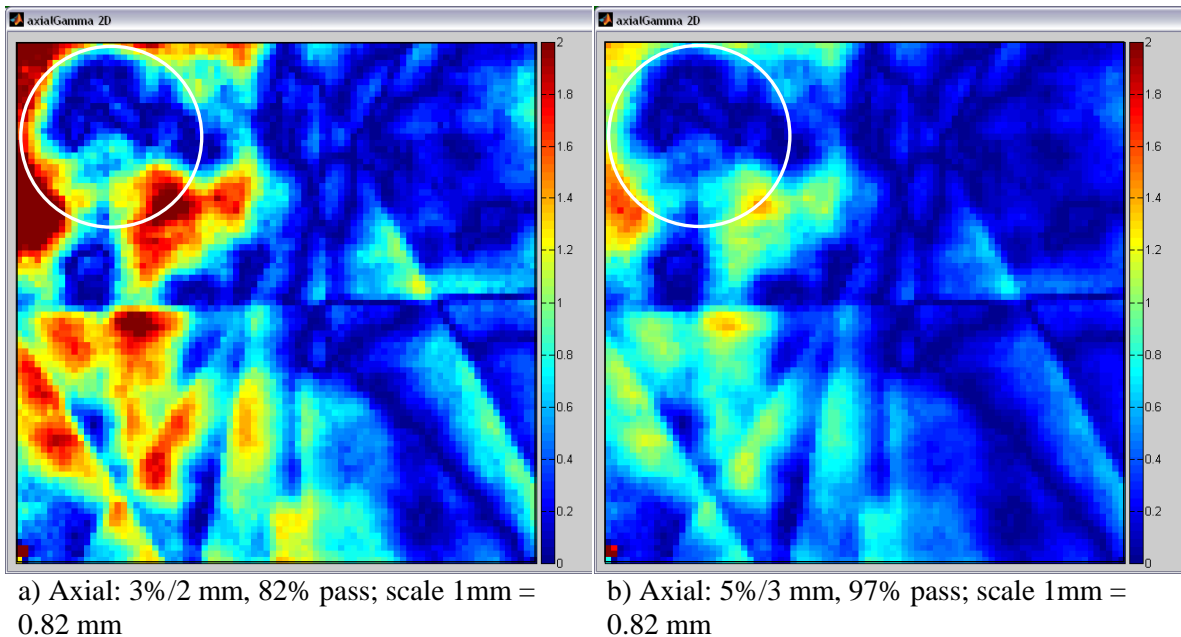
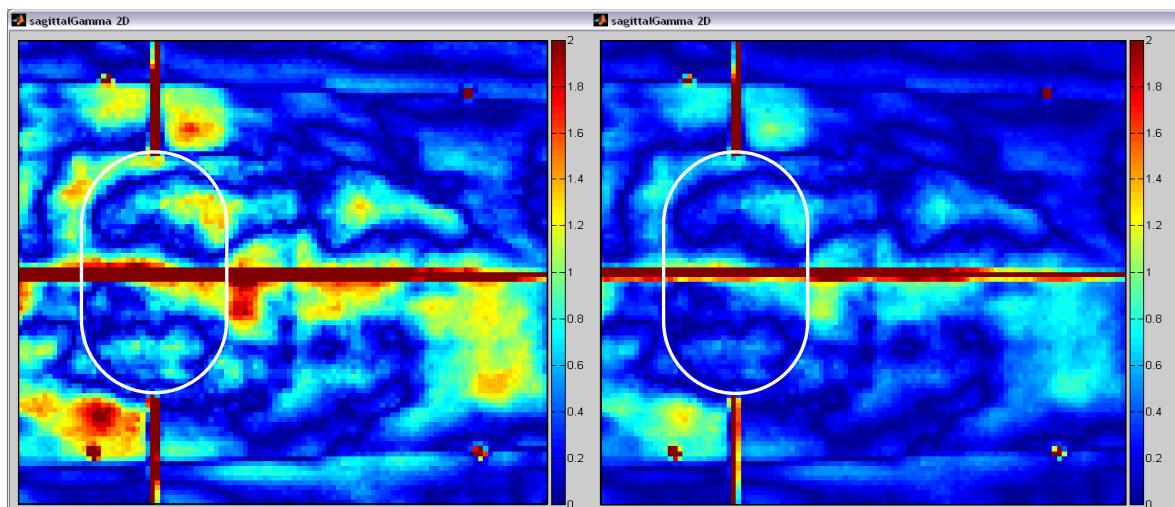


Figure 2.38 IMRT lung delivery single irradiation (number 3): Coronal plane, gamma map tested to 3%/2 mm criteria, where 84% of the data passed. Scale is 1 mm = 0.65 mm. Elongated circle outline represents the location of the PTV.

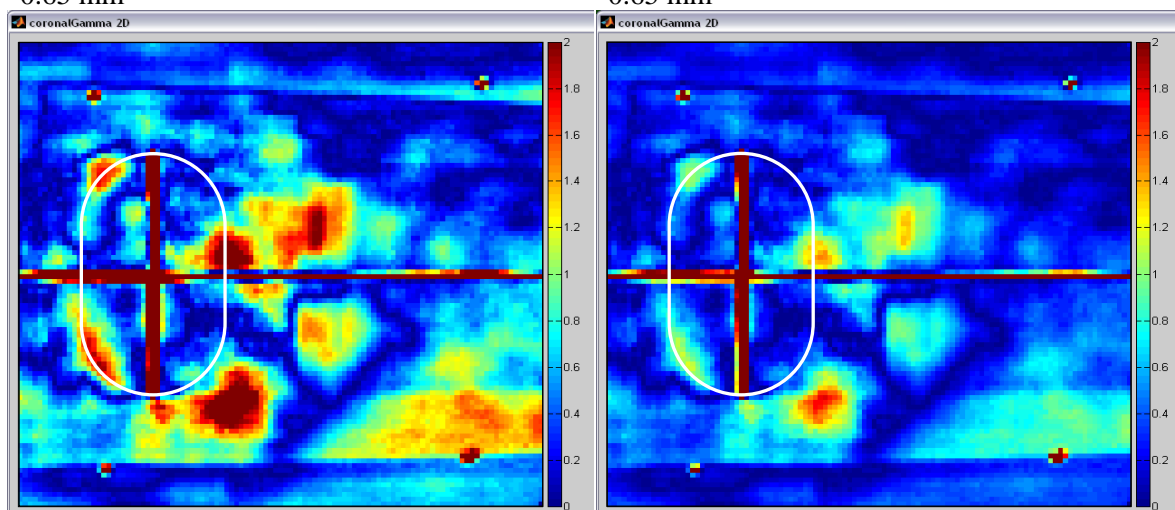
Figure 2.39 shows the comparison of the Pinnacle calculation and the same measured data used in the DPM evaluation. The results were very similar to the results from the DPM Monte Carlo calculation for each dose profile and each gamma map.





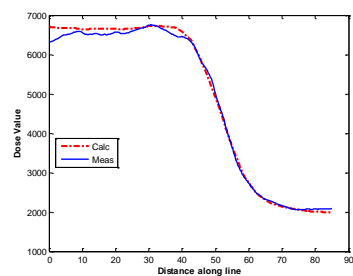
c) Sagittal: 3%/2 mm, 86% pass; scale 1 mm = 0.65 mm

d) Sagittal: 5%/3 mm, 98% pass; scale 1 mm = 0.65 mm

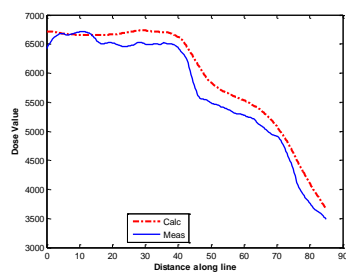


e) Coronal: 3%/2 mm, 83% pass; scale 1 mm = 0.65 mm

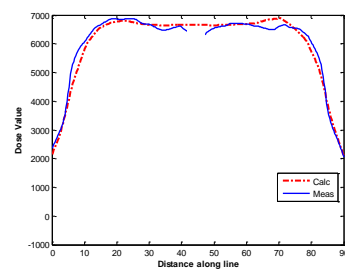
f) Coronal: 5%/3 mm, 97% pass; scale 1 mm = 0.65 mm



e) Lateral profile



f) Anterior to posterior profile



g) Superior to inferior profile

Figure 2.39 Gamma map and dose profile comparisons between the Pinnacle calculation and measurement for the IMRT lung delivery (single irradiation, number 2)

#### 2.3.3.9 Benchmark summary

Table 10 shows the overall results of the percentage of the data that met the gamma index criteria of 3% of the normalized PTV dose and 2 mm distance to agreement for the comparison between the DPM calculation and measurement. The table shows the average and range from the repeated irradiations for each treatment plan.

|         | IMRT H&N | SBRT Lung | IMRT Lung |
|---------|----------|-----------|-----------|
| average | 93       | 94        | 87        |
| range   | 90-98    | 90-97     | 81-92     |

Table 10 Varian 6 MV: The average and range of the percentage of data from meeting criteria from the gamma index of 3%/2 mm for repeated irradiations from each treatment plan.

A series of progressively more difficult benchmark tests were designed using IMRT and SBRT techniques delivered to homogeneous and heterogeneous phantoms. An IMRT head and neck plan was designed and delivered to the RPC homogeneous head and neck phantom using 9 coplanar beams and 72 segments. The results of this first benchmark test showed that on average 93% of the data tested met the criteria of 3% or 2 mm. The range from the axial and sagittal dose planes from all three repeated irradiations was 90% to 98%. In general, disagreement was limited to small regions near the primary target edge and was due to the beam penumbra that existed in this particular IMRT plan. Some disagreement also occurred was in posterior and inferior region of the primary target. This region is adjacent to the spinal cord critical structure. The DPM calculation tended to underestimate the high dose gradient.

A small field irradiation using 9 coplanar beams was designed and delivered to a low density heterogeneous medium using the RPC thorax phantom. The field was defined by a static MLC field with an equivalent square of approximately 5 cm<sup>2</sup>. The results of this second

benchmark test showed that on average 94% of the data tested met the criteria of 3% or 2 mm. The range from the axial, coronal, and sagittal dose planes from all three repeated irradiations was 90% to 97%. While nearly all data from all of the three major planes intersecting the center of the target met the criteria, the point dose measurement in the target showed the calculation to overestimate the dose by 1%. The DPM calculation accurately predicted the dose in the penumbra region of the target and tended to slightly overestimate the dose in the low dose regions of the lung.

Combining the more difficult treatment technique of IMRT with the low-density heterogeneous media of the thorax phantom, and IMRT lung plan was designed and delivered to the same thorax phantom used for the SBRT test. In this plan four coplanar beams plus one non-coplanar beam consisting of 63 segments were used. The results of this third benchmark test showed that on average 87% of the data tested met the criteria of 3% or 2 mm. The range from the axial, coronal, and sagittal dose planes from all three repeated irradiations was 81% to 92%. As expected, combining the low density lung material with IMRT provided the greater challenge as greater differences between the calculation and measurement were observed. The DPM calculation overestimated the dose by 2.5% in the center of the target. Disagreement tended to occur in the penumbra regions and in the anterior-medial narrowed lung region in between the boundary between the target and the water equivalent tissue where the calculation overestimated the dose.

## **2.4 CONCLUSION**

The analytical source model using the Dose Planning Method (DPM) Monte Carlo code, was developed and validated within 2% of the maximum dose and 2 mm distance to agreement of measurement for the open field sizes between 4 cm x 4 cm and 40 cm x 40 cm. The average local percent differences for the central axis and for the off axis at several depths

were found to range from 0.2% to 2.0%. For field sizes 15 cm x 15 cm and below this range was 0.2% to 1.4%.

The first step of the two-step automated commissioning process that relied on the PDD and dose profile measured data from the 10 cm x 10 cm field size was able to optimize the energy spectrum for the primary isotropic point source and secondary (extra-focal) photon sources, the relative fluence from the extra-focal source, and the relative dose contribution from the electron contamination source. The second step of the commissioning process optimized the horn-effect so that the calculation could accurately predict the increase in fluence as the off angle axis increased. For this step, the commissioning process used the dose profile measured data from the 40 cm x 40 cm field size. In addition, the extra-focal source model's energy distribution as described by Liu, et al<sup>30</sup> was implemented without modification. A correction to the output factor for a given field size was designed in response to the change in the fluence contribution that occurs with the change in field size from the extra-focal source. By combining these model attributes, an accurate model for the Varian 6 MV photon beam using the DPM Monte Carlo method was able to faithfully calculate the basic beam data that comprised of open fields from 4 cm x 4 cm to 40 cm x 40 cm.

The validated source model with the DPM calculation was found to be accurate within 3% of the normalization dose and 2 mm distance to agreement of measurement under increasingly more difficult benchmark conditions of IMRT and SBRT treatment techniques delivered to anthropomorphic phantoms where TLD and radiochromic film measurements were made. The accuracy of the source model calculation for the benchmark tests of an IMRT treatment delivered to the homogeneous head and neck phantom, a SBRT treatment delivered to the heterogeneous thorax phantom, and an IMRT treatment delivered to the heterogeneous thorax phantom ranged from 87% to 94% of the data tested at the gamma index of 3%/2mm.

To achieve the level of accuracy for the benchmark evaluations, an MLC model was developed to account for leaf transmission, interleaf leakage, and the rounded leaf ends. In



addition, the implementation of an MLC offset of 0.4 mm to compensate for the finite size of the primary source and reproduce the measured penumbra was necessary for the model to meet the conditions of the accuracy defined. In this work we have demonstrated that with the use of the DPM Monte Carlo code, an accurate straightforward multiple-source model was developed for the Varian 6 MV photon beam using basic beam data.

## **Chapter 3 Development, Validation, and Benchmark: Varian 10 MV**

### **3.1 INTRODUCTION**

The detailed Monte Carlo simulation of an accelerator head including the target, primary and secondary collimators, flattening filter, ion chamber, jaws, MLC, and even the head shielding and structural components provides a high level of accuracy in describing the photon and the contaminate electron distributions. However, the simulation must be repeated for every machine type and energy. Once the simulation is complete, the fluence generated can be transported through the patient using the Monte Carlo method. As an intermediate step, the fluence distribution generated from the initial simulation can then be stored in a phase space file. The phase space file contains the energy, position, and momentum of the photons and electrons and is located in a plane perpendicular to the central axis downstream from the exit of the treatment head. An advantage to storing the information in the phase space file is that the Monte Carlo transport can be sped up since the transport from the head to the phase space file does not need to be repeated. Further, an analytical model can be used to describe the fluence information, thereby replacing the phase space file and eliminating the need to maintain the information contained in the file.

An alternative to the full simulation method or to the analytical model representation of the fluence distribution contained within the simulated phase space file is the use of a virtual source model. The aim of this work was to develop a virtual source model using a multi-source model approach to represent the fluence distribution of electrons and photons coming from the accelerator head. The fluence engine is then used to start the Monte Carlo transport of the particle histories through the patient. Multi-source models have long been used in the development of early dose calculation algorithms commonly referred to as the pencil beam and convolution algorithms.<sup>30,55-60</sup> One distinct advantage of this approach is the versatility to adapt the model to other linear accelerators and other energies, which was the ultimate goal of this project.

The multi-source model developed in this work comprised of a primary source, extra-focal source, and a source for electron contamination.<sup>26</sup> The model relied on the Dose Planning Method (DPM) Monte Carlo code as the dose calculation algorithm. The primary source described the photons generated at the target. The extra-focal source was a ‘lumped’ source used to describe the remaining photons in the treatment head. Therefore, the extra-focal photons were predominantly generated and scattered photons from the flattening filter, but also included photons from the primary collimator, jaws, monitor chamber, etc.<sup>30</sup> An electron contamination source was used to describe electrons that were generated within the treatment head from high energy interactions with photons.<sup>31</sup>

As mentioned above, an advantage of the parameterized source model approach used to describe a beam delivery system was its adaptability to characterize other machines and other energies. As an extension of the Varian 6 MV photon beam source model described in Chapter 2, the Varian 10 MV photon beam source model was reoptimized for the higher energy since the components of the Varian accelerator head remained largely the same. The design of the flattening filter for the 10 MV photon beam was different from the Varian 6 MV photon beam. This difference was represented by unique parameters that were used to describe the

exponential nature of the distribution of photons emanating from a disk at the physical location of the flattening filter along the central axis beam line.<sup>30</sup> While the Varian 6 MV photon beam did not include a source for electron contamination because of its small contribution that fell below a predetermined limit of 0.5%, electron contamination was modeled for the Varian 10 MV photon beam. In addition, the model also accounts for fluence and off-axis energy<sup>27</sup> effects due to the decreasing thickness of the flattening filter from the center to the outer edge. Known as the horn-effect, the fluence increases as the off-axis angle increases; and in conjunction, known as off-axis softening, the average energy decreases.

Modifications to the model that were made to the Varian 6 MV photon beam were included in the Varian 10 MV in order to maintain consistency and versatility. These modifications were detailed in Chapter 2 and include an output correction as a function of the field size, an MLC offset based on the finite size of the primary source, and the application of a blurring function to spread the dose under each MLC leaf tip. This work presents those modifications, details the development effort to modify the fluence from the electron contamination source, and reports the results of the validation and benchmark testing of the Varian 10 MV photon beam source model with the DPM dose calculation engine. The validation testing compared the DPM source model calculation to the measurement of the percent depth dose (PDD) and the dose profiles for open fields. The benchmark testing compared the calculation to measurement using IMRT and SBRT techniques in homogeneous and heterogeneous media.

## 3.2 MATERIAL AND METHODS

### 3.2.1 *Source Model*

#### 3.2.1.1 *Source model overview*

Because the source model is generic, much of the methodology remained the same as detailed in Section 2.2. While every aspect and component of the model will be discussed herein, the details of the methodology need not be repeated. One feature unique to the Varian 10 MV photon beam and source models whose energy is greater than 6 MV was the inclusion of the electron contamination model. Therefore, the electron contamination model will be described in detail.

The dose calculations were performed on the Hewlett Packard ProLiant DL585 G5 Server with 16 AMD Opteron™ processors and 32GB of RAM. Each simulation used 10 million particles per square centimeter beamlet. The calculations applied low energy electron and photon cutoffs of 200 and 50 keV, respectively. As discussed in the introduction, the source model approach facilitated the extension of the model to include other energies. This was achieved, in part, by determining a new set of optimized parameters using the same two-step automated commissioning process that was described in Section 2.2.1.2. The remaining parts of the model necessary for the validation of the basic beam data were developed for the Varian 10 MV photon beam by determining the relationship between the change in photon fluence from the extra-focal source and the change in electron fluence from the electron contamination source with respect to changes in the field size. The correction methodology for the change in photon fluence was the same as that described in Section 2.2.1.5 where a hyperbolic function was fit to the calculated output factor in order to account for the effect of head and phantom scatter changes with field size. The correction for the change in electron contamination is detailed in Section 3.2.1.3, below. The analytical functions from the literature

that describe the off-axis softening<sup>27</sup>, the extra-focal fluence distribution<sup>30</sup>, and the electron contamination source<sup>31</sup> were implemented directly and without change.

For the benchmark testing, the size of the primary source was compensated for by applying the same 0.4 mm MLC leaf offset that was modeled for the Varian 6 MV photon beam. The literature has shown the source size is essentially the same regardless of energy.<sup>39-42</sup> The amount of leaf transmission, interleaf leakage, and transmission through the round leaf ends was determined for MLC model.

#### *3.2.1.2 Source model commissioning*

For the first step of the two-step commissioning process, energy bins of 0.25 MeV were defined from which the DPM dose calculation algorithm calculated dose for each bin using the primary source from 0.25 MeV to 12 MeV and using the extra-focal source from 0.25 MeV to 6 MeV. For these calculations a 10 cm x 10 cm field was used. The simulated water phantom had dimensions of 50 cm x 50 cm x 50 cm. The energy spectrum bin weightings, relative photon fluence from the extra-focal source, relative fluence from the electron contamination source, and the chamber volume effect from the use of an ion chamber used to measure the dose profile were optimized until the calculated and measured PDD and dose profiles were in agreement. Seven parameters were determined in order to satisfy the first step of the commissioning process.

For the second step of the commissioning process, the horn-effect influence was modeled for the 10 MV photon beam. Coefficients from a piecewise linear function which was used to represent the increase in fluence as a function of an increase in the off-axis angle were optimized until the calculated dose profile was in agreement with the measured dose profile of a 40 cm x 40 cm open field where the profiles were taken at the depth of maximum dose.

A final conversion factor was determined by normalizing to an integral dose defined by the area under the curve from the measured PDD between the depths of 5 cm to 15 cm for the

10 cm x 10 cm open field.<sup>32</sup> The final conversion factor that was applied to the commissioned source model to convert energy per photon to dose. The factor was applied to all dose calculations which included the validation testing, benchmark testing, and any patient calculations.

#### *3.2.1.3 Electron contamination contribution*

Similar in concept to that described in Section 2.2.1.5 for the correction for the machine output due to changes in the photon fluence with the field size, a second-order hyperbolic equation with three constants described the change in the electron contamination contribution<sup>61,62</sup> as a function of field size to better model the effect that head scatter had on the build-up region and depth of maximum dose. The correction was applied to the three-dimensional (3D) dose matrix following the dose calculation.

#### *3.2.2 Validation testing*

The validation of the Varian 10 MV photon beam was performed by comparing calculated values to the measured values of the basic beam data. The basic beam data consisted of the percent depth dose and the dose profiles at several depths from several field sizes. Validation testing used the Varian ‘Gold’ data. This dataset was chosen over the institution’s dataset because it was more complete. The depths of the dose profile comparisons were 2.4 cm, 5 cm, 10 cm, and 20 cm in a water phantom. The field sizes included 4 cm x 4 cm, 6 cm x 6 cm, 10 cm x 10 cm, 15 cm x 15 cm, 20 cm x 20 cm, 30 cm x 30 cm, and 40 cm x 40 cm.

The measured values were made using an ion chamber, but it was not clear what type. Since it was an ion chamber, it did suffer from volume effects which cause some degree of artificially producing a wider penumbra when the dose profile would have been measured. A Gaussian convolution was applied to the calculated dose data for all profile comparisons in order to perform a realistic comparison to the measured data.<sup>33</sup>

The calculated data for the Varian 10 MV photon beam was extracted in the same manner as the data for the Varian 6 MV photon beam (Section 2.2.3). Namely, the resolution of the calculated data was 0.2 cm (cross-plane) x 0.3 cm (in-plane) x 0.2 cm (depth). The depth of 0 cm was defined along the central axis of the beam where the contoured region that defined the surface of the simulated water phantom existed. The simulated water phantom had dimensions of 50 cm x 50 cm x 50 cm.

The validation test conditions remained unchanged for the 10 MV beam. The accuracy of the calculated data compared to the measured data (PDDs and dose profiles) for field sizes from 4 x 4 cm<sup>2</sup> to 40 x 40 cm<sup>2</sup> was tested to a gamma criterion of 2% of the maximum dose and 2 mm distance to agreement. In addition, local dose differences were studied at depths beyond  $d_{\max}$  and in the high dose regions of the dose profiles. The high dose region within a dose profile at a specific depth was defined by the dose greater than or equal to 80% of the dose at the central axis.<sup>47</sup> The distance-to-agreement for the location of the calculated  $d_{\max}$  relative to the measured  $d_{\max}$  was also evaluated.

### **3.2.3 Benchmark testing**

The same type of RPC anthropomorphic phantoms were used in the benchmarking of the validated Varian 10 MV photon beam source model. The approach was the same in terms of increased difficulty of the treatment within the media. Therefore, a combination of IMRT and SBRT techniques were used with the homogeneous head and neck phantom (Figure 2.4(a)) and the thorax phantom (Figure 2.4(b)). The head and neck phantom for this study was of the same design except the locations for the primary target with critical structure and the secondary target were switched as shown in the images in Figure 3.1. The same thorax phantom was used in all studies.

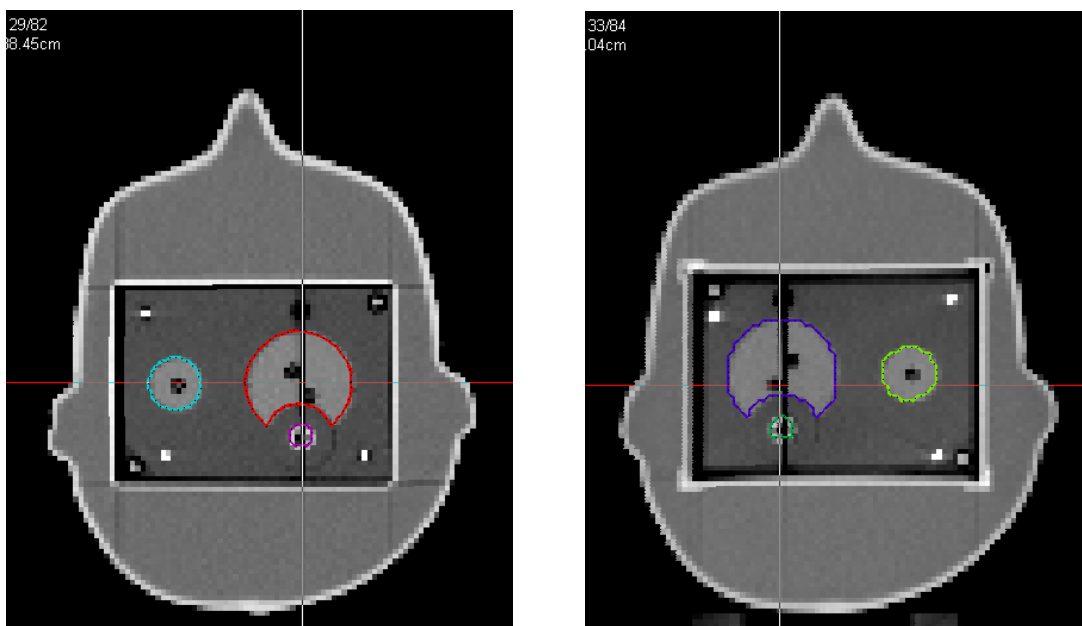


Figure 3.1 CT images of head and neck plans used for benchmark testing. Left image used with Varian 6 MV model. Right image used for Varian 10 MV image. Viewed I to S.

The RPC's anthropomorphic IMRT head and neck phantom was used to test a highly modulated delivery of nine coplanar beams which comprised of 72 segments. The RPC's anthropomorphic thorax phantom was used to test a nine beam SBRT plan and a five beam, 39-segment non-coplanar IMRT plan. The IMRT head and neck plan and SBRT lung plan were designed using the credentialing guidelines and irradiation instructions employed by the Radiation Therapy Oncology Group (RTOG) to credential institutions for participation in specific advanced technology protocols. Each plan was delivered three times to evaluate the repeatability.

The resolution of the DPM calculation was based on the size of the CT voxel (0.195 cm by 0.195 cm by 0.25 cm). The accuracy of the DPM calculation was determined by comparing point doses, dose profiles, and 2D gamma maps to the measured data.

### 3.2.3.1 Point dose comparisons

Point dose comparisons were made between the calculated data and measured TLD data. The TLDs were located in the target and critical structure locations from each phantom.



The measured point doses were defined by the small volume of TLD powder inside the capsule while the respective calculated point doses were derived from the small regions of interest contoured from the CT scan.

#### *3.2.3.2 Dose profile comparisons*

Dose profiles along the major planes intersecting the center of the targets were evaluated between the calculated and measured film values. The profiles were used in conjunction with the more quantitative point dose comparisons and gamma maps to discuss how well the calculation predicted the dose.

#### *3.2.3.3 Gamma map comparisons*

2D dose distributions between the calculation and measurement were evaluated using the gamma index method<sup>48</sup> where quantitative results were recorded and used to test the hypothesis. The gamma criterion remained the same for the Varian 10 MV photon beam as it was for the Varian 6 MV photon beam. The gamma criterion was 3% of the target TLD dose and 2 mm distance to agreement. The regions where the gamma maps have no measured dose because of the non-rectangular shape of the film were included in the initial gamma analysis, but a subsequent estimate of the data in those regions allowed for a correction to be made to the final results.

#### *3.2.3.4 Treatment plans*

All treatment plans were planned using the Pinnacle treatment planning system (version 7.6c or higher) (Philips Medical Systems, Andover, MA). The dose prescription and dose constraints were met based on the calculated dose using Pinnacle's collapsed cone convolution algorithm.

The summary of the prescription and constraints for each treatment plan is listed below. The IMRT head and neck plan:

- The PTV was constrained to the gross tumor volume (GTV).
- At least 95% of the primary planning target volume (PTV) received 6.6Gy (prescribed primary dose).
- Less than 1% of the primary PTV received less than 93% of the prescribed dose.
- At least 95% of the secondary PTV received 5.4 Gy (prescribed secondary dose).
- Less than 1% of the secondary PTV received less than 93% of the prescribed dose.
- The organ at risk received less than 4.5 Gy.
- The dose to the normal tissue received no more than 7.3 Gy.

The SBRT lung plan:

- The PTV was the GTV plus 0.5 cm in the axial plane and plus 1 cm in the longitudinal plane.
- At least 95% of the PTV received 6 Gy
- At least 99% of the PTV received 5.4 Gy.
- The maximum dose received at 2 cm and beyond from the PTV was no more than 3.5 Gy.
- The dose to the PTV was within 60% and 90% of the maximum dose.
- The prescription isodose volume to PTV ratio was less than 1.2
- The ratio of 50% of the prescribed isodose volume to PTV was less than 3.6.

The IMRT lung plan:

- The PTV was the GTV plus a 1 cm margin.
- At least 95% of the PTV received 66 Gy.
- The maximum dose prescribed to the spinal cord was 45 Gy.
- No more than 40% of the total lung was to receive more than 20 Gy.
- The dose to the entire heart was not to exceed 40 Gy
- No more than 50% of the heart was to receive more than 50 Gy.

- Note: EBT radiochromic film is sensitive in the range of 6 Gy, therefore the delivery was limited to 1 fraction and the prescription dose was adjusted accordingly.

### 3.3 RESULTS AND DISCUSSION

#### 3.3.1 Source model

##### 3.3.1.1 Source model commissioning parameters

The seven model parameters that described the photon energy spectra, fluence contributions, and the penumbra measurement effect from the ion chamber for the first step of the commissioning process for the Varian 10 MV photon beam are shown in Table 1. The first three parameters,  $\gamma$ ,  $\mu$ , and  $\beta$ , defined the spectrum shape, relative peak energy location, and relative scale, respectively, of the fatigue life distribution function.

| Parameter  | Value   |
|--|---------|
| Fatigue-Life distribution shape parameter, $\gamma$  | 0.8897  |
| Fatigue-Life distribution location parameter, $\mu$  | -0.0160 |
| Fatigue-Life distribution scale parameter, $\beta$   | 3.92    |
| Primary spectrum to extra-focal spectrum reduction scale factor  | 2.8     |
| Extra-focal fluence relative to the primary fluence  | 0.23    |
| Electron contamination contribution (relative to the primary photon contribution)  | 0.005   |
| Standard deviation of Gaussian used to convolve the MC dose profile to match the measured dose profile during the validation process | 1.2     |

Table 11 Parameters of the commissioned source model for spectra, fluence, and profile penumbra measurement effect.

A plot of the energy spectrum compared to the energy spectrum computed using the commonly used BEAM code<sup>29</sup> for simulating radiation transport in accelerators is shown in Figure 3.2. The commissioned source model spectrum appears representative of the BEAM spectrum. The source model spectrum has more low energy photons and more high energy

photons, but this spectrum proved to be an adequate representation of the photon beam based on the validation results. The extra-focal energy spectrum was scaled in energy by a factor of 2.8. The relative fluence of the extra-focal source was 23% of the primary source fluence. This is in comparison to 13% for the Varian 6 MV photon beam. Liu, et al reported the relative fluence contribution to be just over 18% of which nearly 1% was attributed to the jaws from an open field size of 40 cm x 40 cm. The dose contribution from the electron contamination source was one-half percent (0.5%) of the primary dose. The standard deviation of the Gaussian function used for the dose smearing convolution was 1.2 mm. This was the same value determined in the Varian 6 MV optimization process where the ion chamber was known to have an internal volume of 0.04 cm<sup>3</sup>.

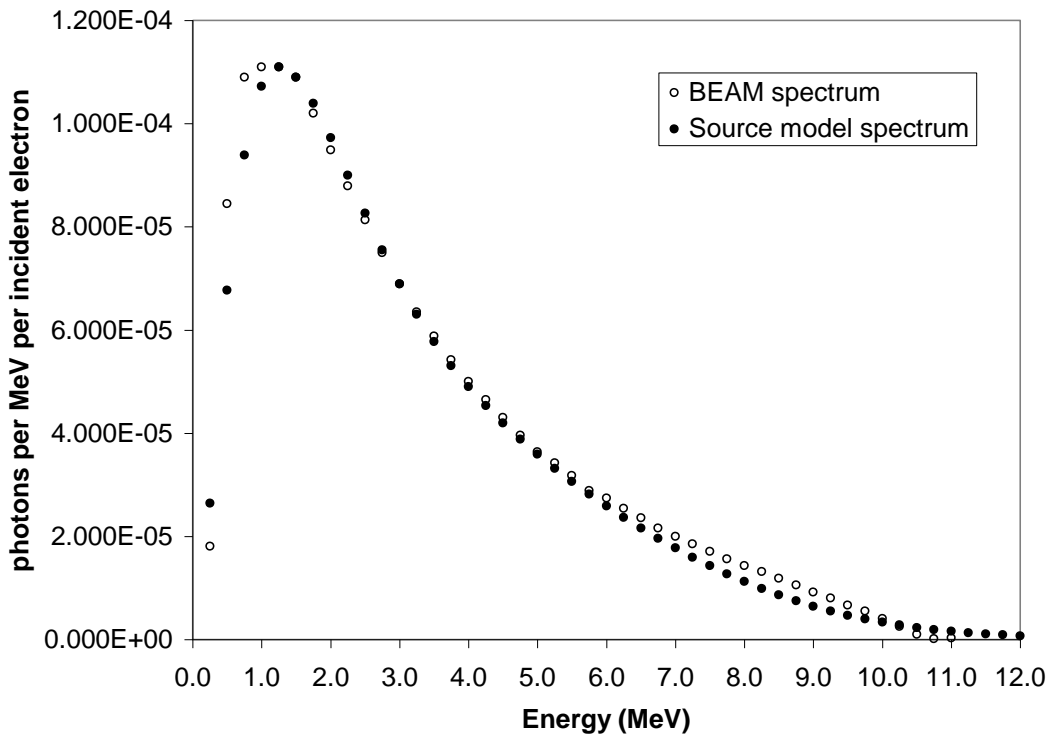


Figure 3.2 Varian 10 MV spectrum: Commissioned source model compared to BEAM spectrum<sup>29</sup>

The results of the second step of the commissioning process are shown in Table 12. The horn-effect coefficients of the piecewise linear function are shown as increases in the

fluence weighting as a function of the cosine of the off-axis angle. The horn-effect coefficients for the Varian 10 MV model were similar to those reported for the Varian 6 MV model in Section Table 2.

| Cosine(off-axis angle) | Fluence weight increase |
|------------------------|-------------------------|
| 1.00000                | 1                       |
| 0.99970                | 1.310                   |
| 0.99879                | 1.062                   |
| 0.99728                | 1.098                   |
| 0.99518                | 1.13                    |
| 0.99250                | 1.17                    |
| 0.98926                | 1.20                    |
| 0.98546                | 1.24                    |
| 0.98113                | 1.26                    |
| 0.97630                | 1.28                    |
| 0.97098                | 1.30                    |
| 0.96277                | 1.31                    |

Table 12 Coefficients of a piecewise linear function to describe the increase of fluence as the off-axis angle increases (horn-effect)

Following the completion of the two-step commissioning process, the final conversion factor that was applied to convert energy per photon to dose in centigray was 0.142368. This factor was applied to every dose calculation performed for the Varian 10 MV source model.

### 3.3.1.2 Fluence map, primary source size, and machine output correction

The Varian 10 MV photon beam applied a transmission of 1% through the bulk thickness of the MLC leaves. This was the same amount of transmission as that applied to the Varian 6 MV MLC model. Even with the higher average energy, the MLC transmission factor did not change. It is worth noting that the Pinnacle model at M.D. Anderson Cancer center uses

nearly the same value for the transmission factor for the 6 MV model (1.6%) versus the 18 MV model (1.8%). The interleaf leakage was an additional 1% of the monitor units given for the particular segment. The interleaf leakage was also the same for the 10 MV model as it was for the 6 MV model. The resolution of the fluence map was 1 mm by 1 mm.

The offset of the MLC leaf positions,  $x_{pen}$ , which compensated for the absence of a finite primary source size, was fixed at 0.4 mm and considered independent of energy based on published reports.<sup>39-42</sup> The offset amount resulted in a source diameter of 0.84 mm FWHM based on the relationship of the source-to-MLC distance and the source-to-axis distance.

Figure 3.3 shows the relationship between the output factor and the field size for the calculated and measured data. A hyperbolic equation was determined to correct the calculated output factors. This equation,  $y = 1.10 - \frac{1.85}{8.89 + x}$ , where  $y$  is the output correction and  $x$  is the field size was necessary to maintain the proper predicted machine output which had been a deficiency of the model to completely describe the scatter conditions that change as a function of field size.

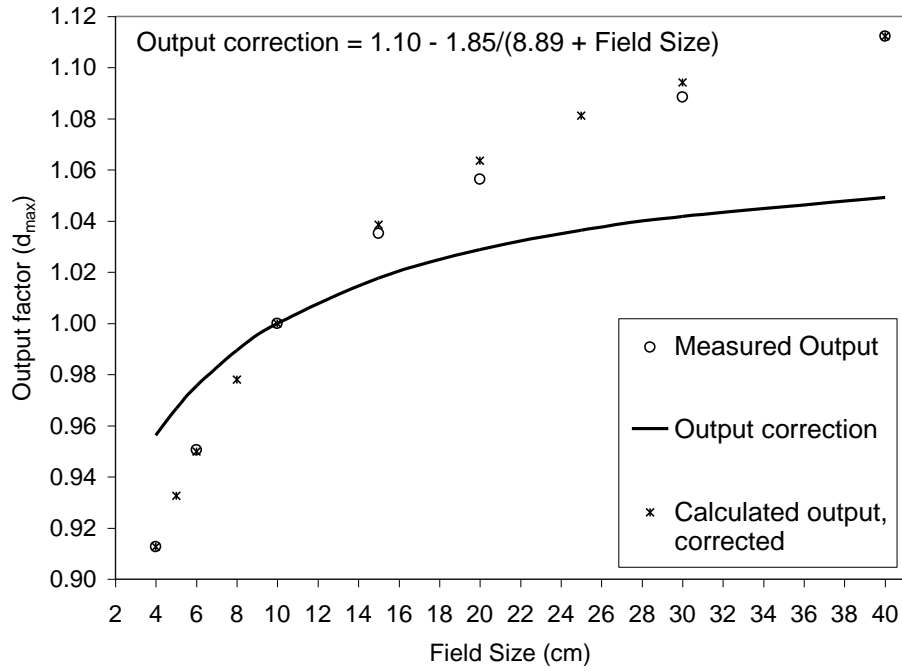


Figure 3.3 Output factor at  $d_{\max}$  versus field size for the measured, calculated and corrected output. A hyperbola curve was determined to correct the calculated values.

### 3.3.1.3 Electron contamination contribution versus field size

Figure 3.4 shows the relationship between the electron contamination dose relative to the dose from the primary source and the field size. A hyperbolic equation,

$$y = 0.025 - \frac{1.008}{40 + x}, \text{ where } y \text{ is the electron contamination and } x \text{ is the field size was}$$

determined empirically from the build-up region of the percent depth dose curve for the field sizes 4 cm x 4 cm and 40 cm x 40 cm. Recall, that the contribution of electron contamination for the 10 cm x 10 cm field size (0.50%) was determined during the first step of the automated commissioning process (Table 11).

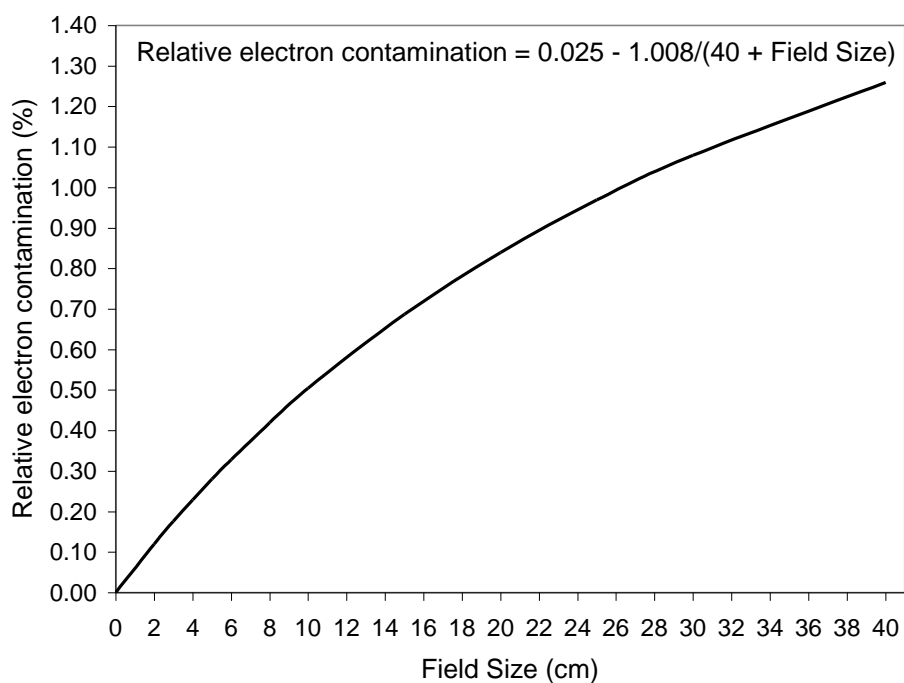


Figure 3.4 Plot of the relative electron contamination as a percentage of the dose relative to the primary source as a function of field size.

Figure 3.5 and Figure 3.6 show the improvement in the build-up region for the field sizes of 4 cm x 4 cm and 40 cm x 40 cm, respectively, due to the correction applied from the hyperbolic function. The improvement in the accuracy of the build-up region for the 4 cm x 4 cm field size (Figure 3.5 ) was less than for the 40 cm x 40 cm field size (Figure 3.6). This was constrained by the hyperbolic equation, which required no electron contamination contribution with the collimator jaws fully closed. While an improvement in the build-up region for smaller field sizes was possible given a different hyperbolic correction equation, an erroneous negative electron contamination contribution based on the 0.50% contribution from the commissioned 10 cm x 10 cm field would have occurred for the fields below the 4 cm x 4 cm field size. The corrected contribution for the 40 cm x 40 cm (Figure 3.6) resulted in a more accurate prediction of the build-up region. Further, the calculation also predicted the correct shift in the dose at



maximum depth,  $d_{\max}$ , to more shallow depths as the field size increased. This was expected due to the increase in the head scatter with field size.<sup>61</sup>

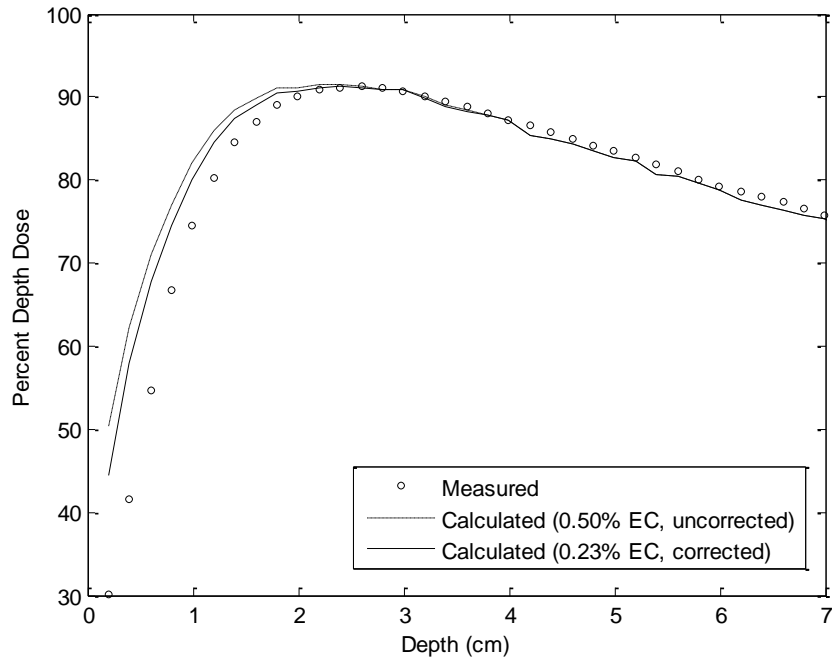


Figure 3.5 Percent depth dose of 4 cm x 4 cm field size showing build-up region for the measured and calculated data sets. The plot includes the change in the electron contamination with field size (corrected) versus a constant contribution, regardless of field size (uncorrected).

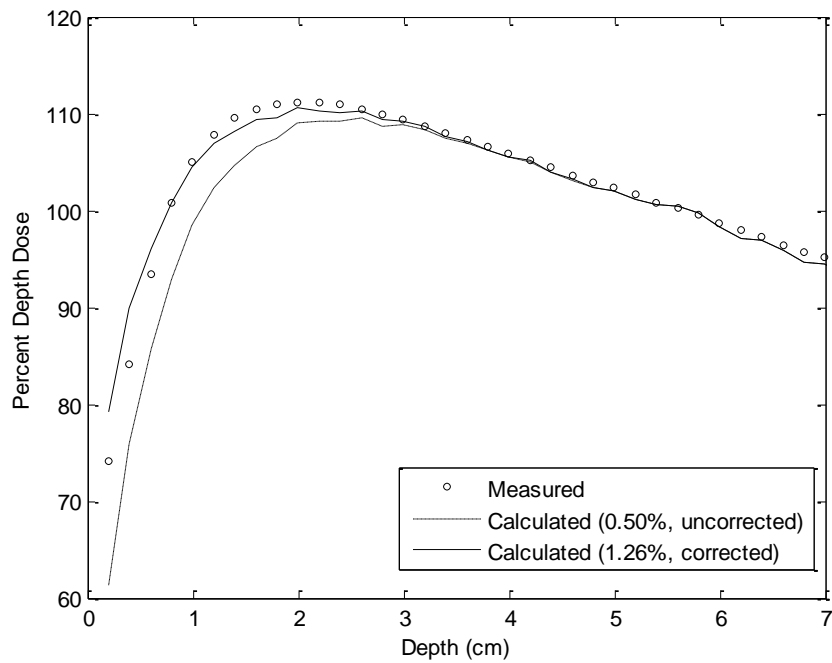


Figure 3.6 Percent depth dose of 40cm x 40 cm field size showing build-up region for the measured and calculated data sets. The plot includes the change in the electron contamination with field size (corrected) versus a constant contribution, regardless of field size (uncorrected).

### 3.3.2 Validation testing

#### 3.3.2.1 Uncertainty

The uncertainty of the dose determined from the measurements using an ion chamber was estimated to be 1.5% at one standard deviation.<sup>49</sup> The standard error of the mean for the Monte Carlo simulations was 1% using 10 million particles per square centimeter.<sup>10</sup>

#### 3.3.2.2 Percent depth dose

The percent depth dose (PDD) data was compared between the measured data and the source model calculated for the field sizes between 4 cm x 4 cm and 40 cm x 40 cm. While all of the PDD comparisons are presented in the appendix (Chapter 6), three fields that represent the range of field sizes are presented here. Those fields are 4 cm x 4cm, 10 cm x 10 cm, and 40 cm x 40 cm and their data are shown in Figure 3.7, Figure 3.8 and Figure 3.9, respectively.

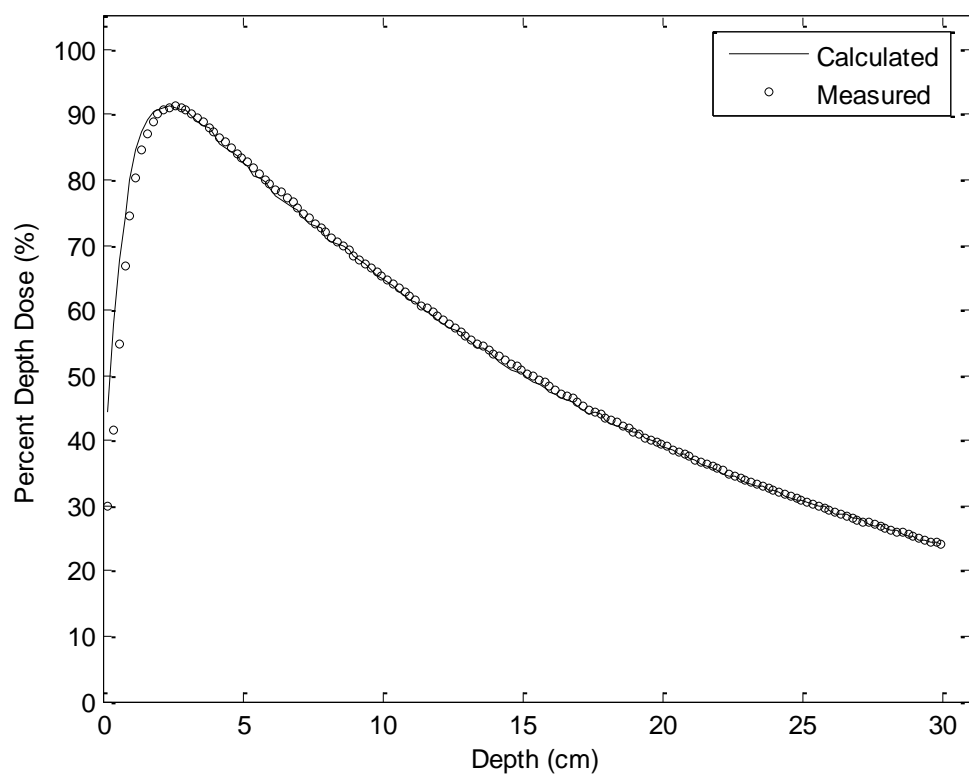


Figure 3.7 Calculated and measured percent depth dose curves at 10 MV for a 4 cm x 4 cm field.

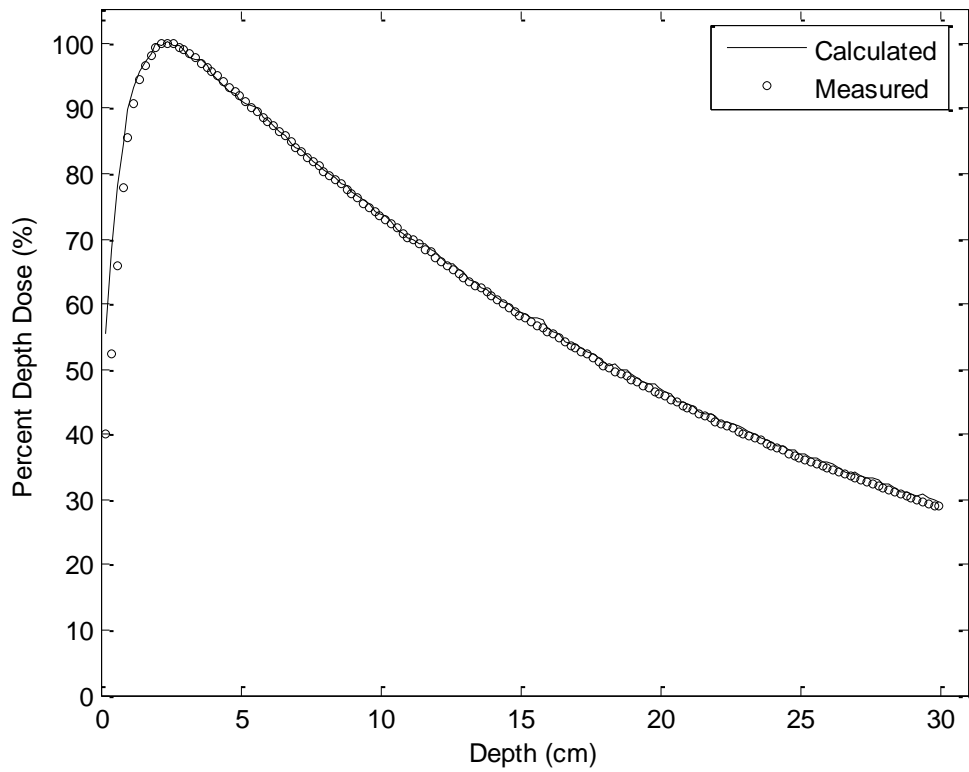


Figure 3.8 Calculated and measured percent depth dose curves at 10 MV for a 10 cm x 10 cm field.

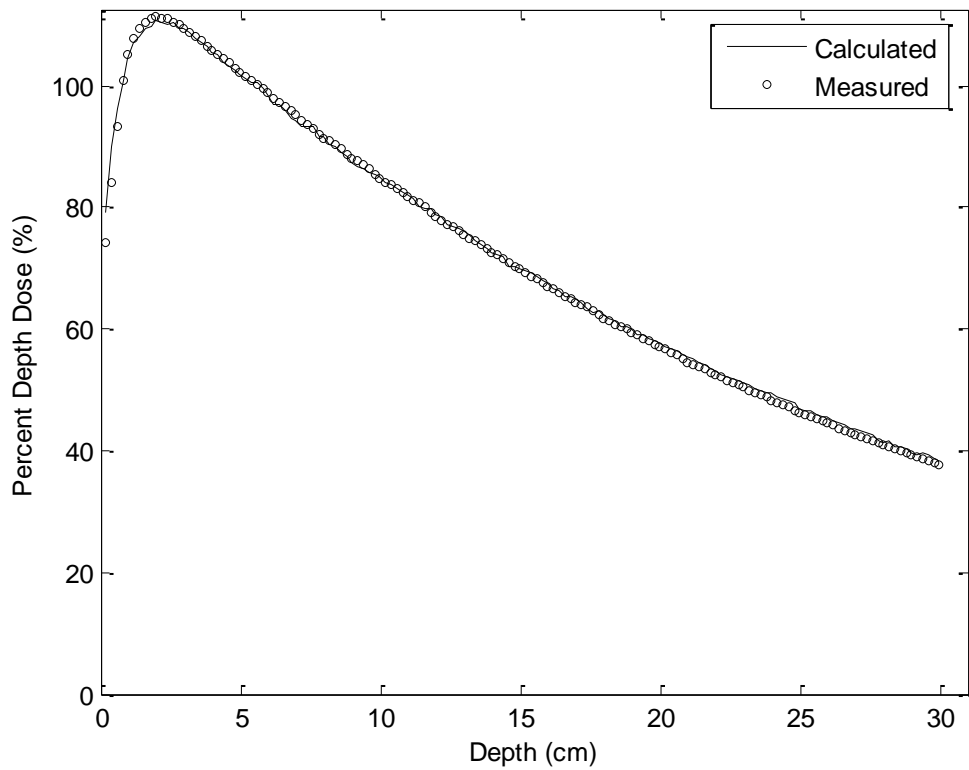


Figure 3.9 Calculated and measured percent depth dose curves at 10 MV for a 40 cm x 40 cm field.

Good agreement existed between the calculated data set and the measured data set along the central axis for all of the field sizes tested between 4 cm x 4 cm and 40 cm x 40 cm. Beyond  $d_{\max}$ , the mean of the local percent difference was within 1.5% for the fields from 4 cm x 4 cm (see Figure 3.7) to 40 cm x 40 cm. The average percentage of those fields tested that were within the 2%/2 mm criteria was 98.8%. The lowest percentage of data meeting the criteria occurred within the build-up region of the 6 cm x 6 cm field. For this field, an average of 96.6% met the criterion.

For the 4 cm x 4 cm field (Figure 3.7), the calculated  $d_{\max}$  was 2.5 cm, while the measured  $d_{\max}$  was 2.6 cm. The calculation did predict the shift of  $d_{\max}$  toward shallower depths as the field size increased due to the fact of increased scatter with field size from the lower energy extra-focal source and the electron contamination source whose dose contribution occurs in the build-up region. The range of the depths for  $d_{\max}$  for the field sizes from 4 cm x 4 cm to 40 cm x 40 cm was 2.5 cm to 2.0 cm for the calculated data and 2.6 cm to 2.0 cm for the measured data. The 10 cm x 10 cm field (Figure 3.8), which was the field that was used to commission the source model, the  $d_{\max}$  was 2.4 cm for the calculated dose and for the measured dose.

### 3.3.2.3 Dose profiles

The dose profile data for the 10 MV photon beam are shown in Figure 3.10, Figure 3.11, and Figure 3.12 for field sizes of 4 cm x 4, 10 cm x 10 cm, and 40 cm x 40 cm, respectively. The dose profile comparisons for the remaining fields are presented in the appendix (Chapter 6).

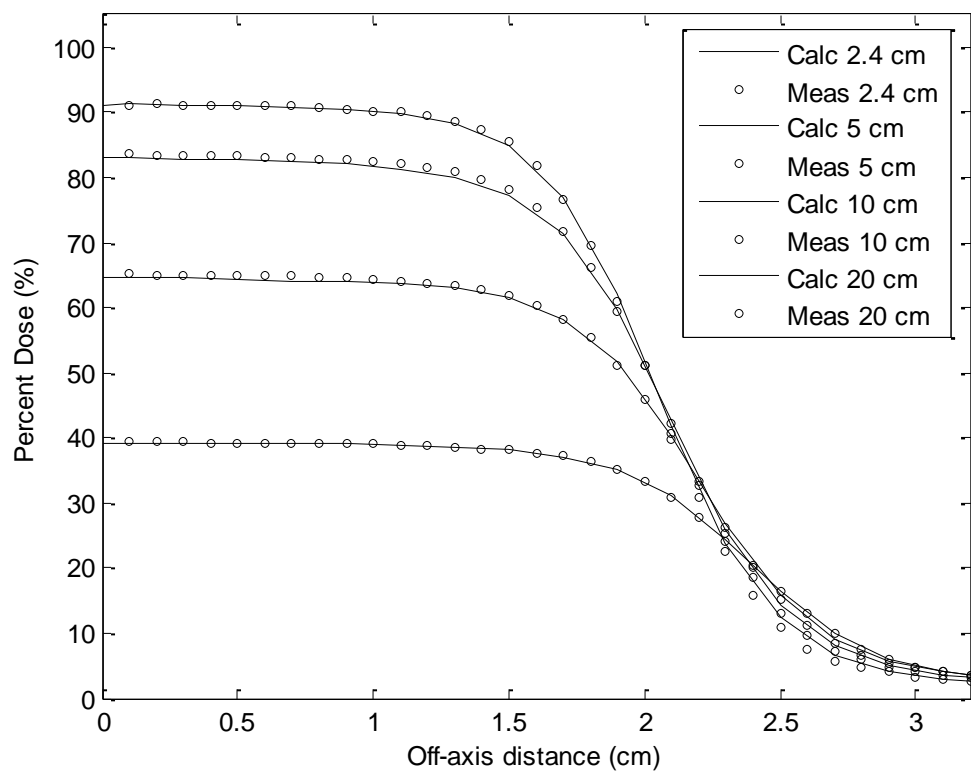


Figure 3.10 Calculated and measured dose profiles at 10 MV from a 4 cm by 4 cm field at depths of 2.4 cm, 5 cm, 10 cm, and 20 cm.

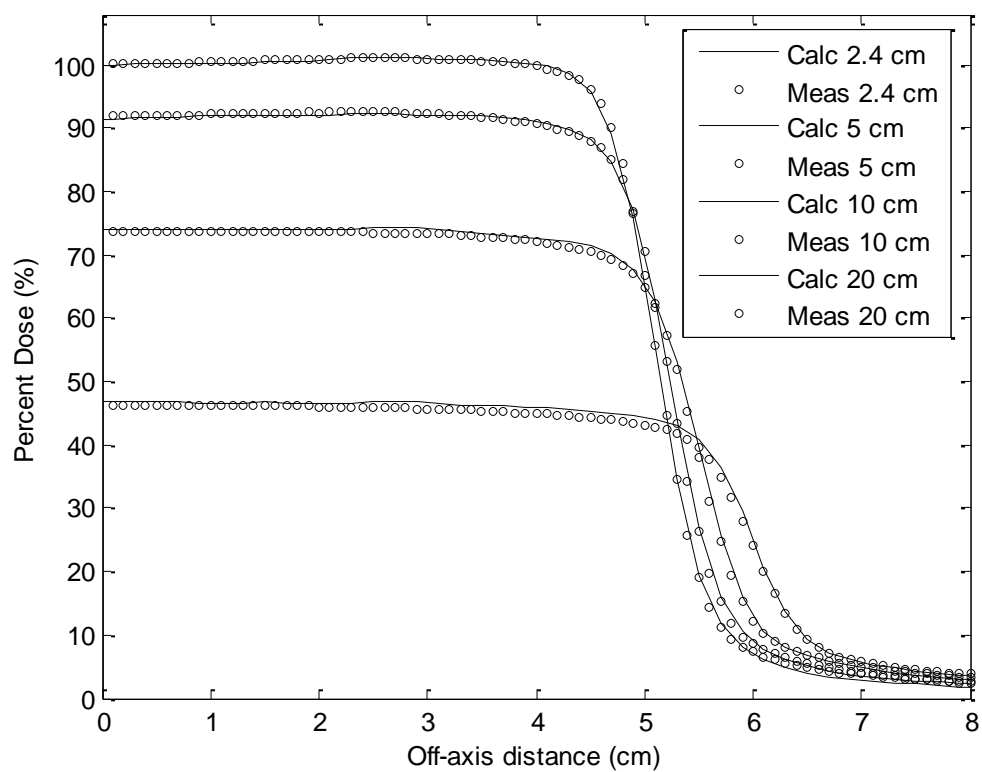


Figure 3.11 Calculated and measured dose profiles at 10 MV from a 10 cm by 10 cm field at depths of 2.4 cm, 5 cm, 10 cm, and 20 cm.

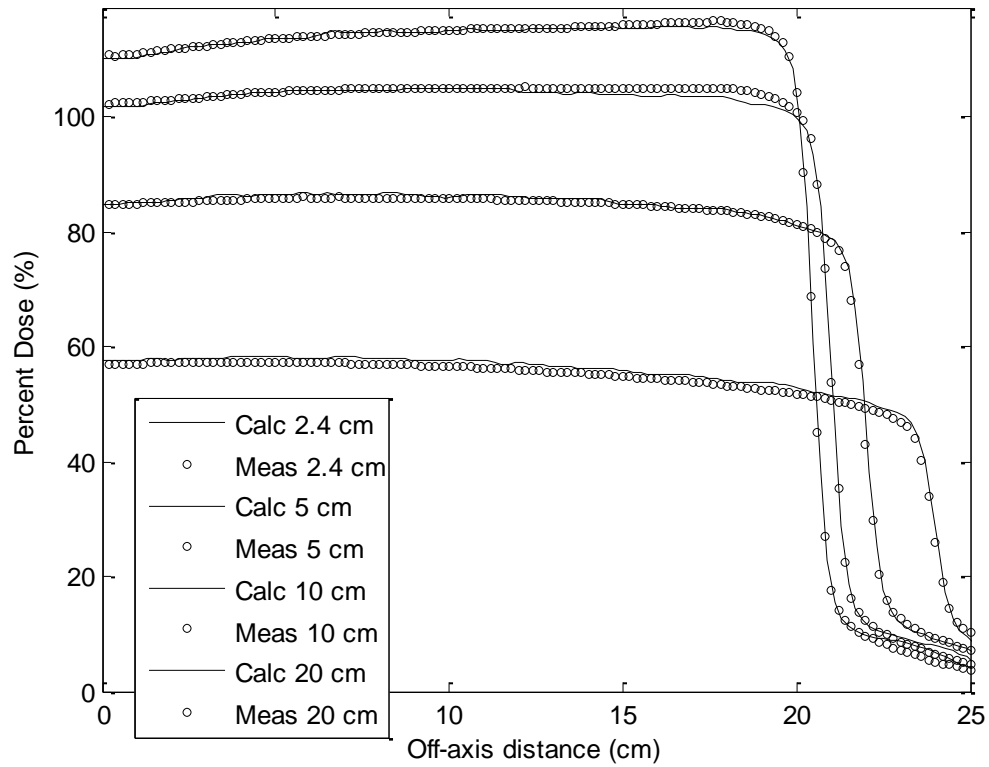


Figure 3.12 Calculated and measured dose profiles at 10 MV from a 40 cm by 40 cm field at depths of 2.4 cm, 5 cm, 10 cm, and 20 cm.

Good agreement existed between the calculation and measurement for all field sizes at all depths. The dose profiles for the field sizes from 4 cm x 4 cm to 15 cm x 15 cm and the 40 cm x 40 cm field size met the criteria of 2%/2 mm completely (Table 3). The remaining two field sizes of 20 cm x 20 cm and 30 cm x 30 cm met the 2% or 2 mm criteria at 98%.



| Field size<br>(cm <sup>2</sup> ) | Minimum percentage of data meeting the<br>criteria of 2% of d <sub>max</sub> or 2 mm DTA<br>(%) | Average percent<br>difference (local dose)<br>(%) |
|----------------------------------|---|---|
| 4 × 4                            | 100   | 0.5   |
| 6 × 6                            | 100   | 0.5   |
| 10 × 10                          | 100   | 0.8   |
| 15 × 15                          | 100   | 1.1   |
| 20 × 20                          | 98  | 1.2   |
| 30 × 30                          | 98  | 1.2   |
| 40 × 40                          | 100   | 0.8   |

Figure 3.13 Dose profile agreement between calculated and measured data. Profiles are from the depths of 2.4 cm, 5 cm, 10 cm, and 20 cm for each field size. Minimum percentage of the data meeting the criteria of 2% of d<sub>max</sub> or 2 mm DTA and the percent difference is the average of all local percent differences from all of the profiles for a given field.

The average local percent difference in the high dose region defined by the measured dose values greater than or equal to 80% of the dose at the central axis<sup>47</sup> was between 0.5% and 1.2%. These results are similar to those found for the Varian 6 MV dose profiles. Some disagreement was occurred in the penumbra and low dose regions of the larger fields where scatter conditions exhibit their greatest contribution.

### 3.3.3 Benchmark testing

#### 3.3.3.1 Uncertainty

The uncertainty of the dose distribution as determined by the EBT film and TLD at one standard deviation was between 2.6% and 3.5%. This was consistent with a previously published report using the same the methodology.<sup>51</sup> TLD used as an absolute dosimeter helped to reduce the variation that can occur between the film calibration process and the actual film

used in the phantom at the time of irradiation. The estimate included the uncertainty of the TLD dose,<sup>52</sup> the film uniformity, the film-to-film variation, and the fit of the sensitometric curve.<sup>53</sup> The TLD uncertainty was included because the film was normalized to the adjacent target TLD housed within the phantom. The estimate of uncertainty, or the standard error of the mean, for the simulation was 1% using 10 million particles per square centimeter.<sup>10</sup>

#### 3.3.3.2 *Effect of finite primary source size on benchmark deliveries*

The MLC offset was described in detail in Section 2.3.1.2 and in Figure 2.3. The MLC offset was applied to open each leaf position by 0.4 mm in response to the finite dimension of the primary source. In the study by Rangel and Dunscombe,<sup>54</sup> they looked at the dosimetric impact of MLC position errors in dynamic IMRT deliveries by comparing the equivalent uniform dose (EUD) metric to the dose volumes of targets and structures with and without an MLC offset. They chose this metric as a way to relate MLC position changes to the changes in dose within a volume. The EUD describes the dose from a nonuniform dose distribution producing the same radiobiological effect as if it was the dose from a uniform dose distribution. The increased opening due to the MLC offset resulted in increased head and phantom scatter. As expected, an MLC offset in which the leaves are opened resulted in an increase in the EUD of an irradiated volume. In our studies, we found the EUD of the primary PTV in the head and neck plan was 3.7% higher, the EUD of the PTV in the SBRT lung plan was 1.1% higher, and the EUD of the PTV in the IMRT lung plan was less than 1% higher with an MLC offset of 0.4 mm. When compared to the Rangel and Dunscombe results, the IMRT head and neck plan was similar. They reported an average increase of 2.81% in the EUD based on a systematic error of a 0.5 mm offset. The EUD difference with the 0.4 mm offset for the 10 MV IMRT head and neck plan was also similar to the 2.4% EUD difference reported in the 6 MV IMRT head and neck plan (Section 2.3.3.2). The differences in the EUD for the unmodulated SBRT lung plan and IMRT lung plan were similar to the differences found for the 6 MV lung plans. These

differences, along with the EUD differences for the IMRT head and neck plan, for the Varian 6 MV and 10 MV source models are shown in Table 13.

| Varian source model | PTV (%)               |           |           |
|---------------------|-----------------------|-----------|-----------|
|                     | IMRT<br>head and neck | SBRT lung | IMRT lung |
| 6 MV                | 2.4                   | 1.7       | 0.0       |
| 10 MV               | 3.7                   | 1.1       | 0.8       |

Table 13 Percent differences of the EUD of the MLC offset opening of 0.4 mm (applied to each leaf; applied to each segment for IMRT) with respect to no offset (DICOM file with no change). Table compares the EUD for the PTV structure for the Varian 6 MV and 10 MV source models.

Figure 3.14 shows the frequency histogram of the aperture distances from all three benchmark treatment plans. The aperture distance was defined as the distance between opposing leaf ends. The aperture distances were binned into 10 cm bins. The histogram attempted to explain the differences between treatment plans in terms of the amount of modulation and the aperture size. The IMRT lung plan was not substantially affected by the 0.4 mm offset. Consistent with the observation made by Rangel and Dunscombe,<sup>54</sup> the SBRT and IMRT plans had relatively fewer narrow aperture openings compared to the IMRT head and neck plan. In addition, it is clear that an offset of larger proportions would have to increase the EUD value because of the increase in machine output given a larger equivalent square field. However, since phantom scatter is reduced in the thorax phantom compared to the head and neck phantom it is reasonable that the difference in EUD for a small MLC offset for a lung plan would be less.

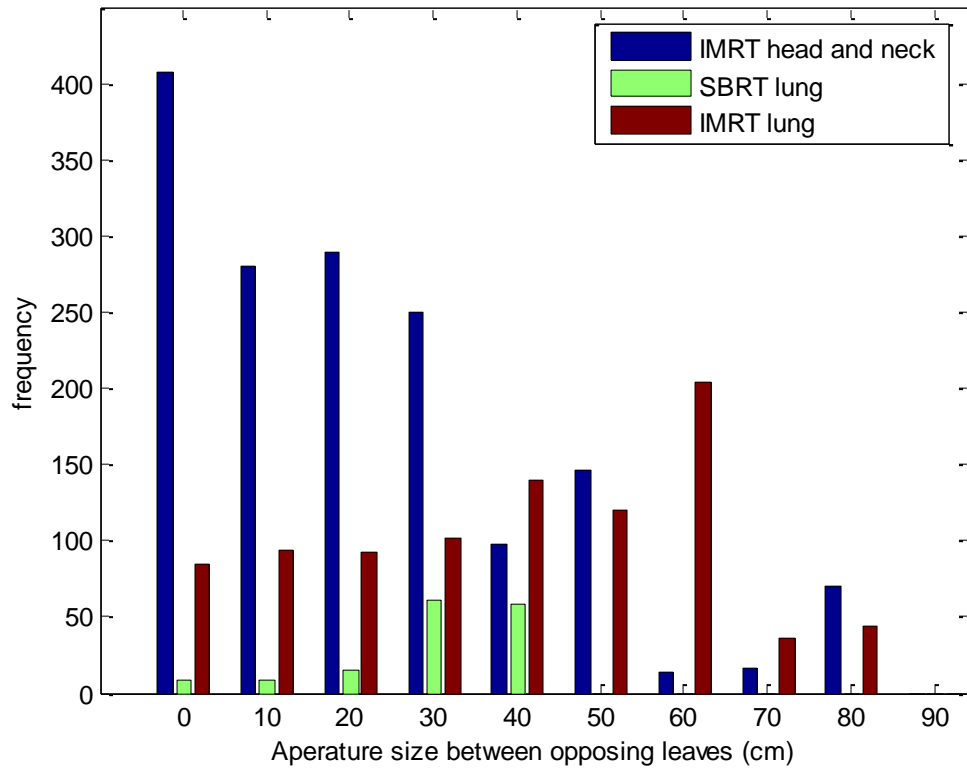


Figure 3.14 Frequency histogram of the aperture distances of opposing leaf ends from the IMRT head and neck plan, the SBRT lung plan, and the IMRT lung plan.

### 3.3.3.3 Delivery of the IMRT head and neck phantom plan: Point dose comparisons

The results of the point dose comparisons are shown in Table 14 for each TLD measurement location. Four TLD capsules were located within the center of the primary target, two TLD capsules within the center of the secondary target and two TLD capsules within the spinal cord critical structure. Included in the table are the average dose measurements and the percent standard deviations from the three repeated irradiations. The comparisons between the DPM calculation and measurement and between the Pinnacle calculation and measurement were expressed as a ratio for the primary target, the secondary target, and the critical structure.

| Point dose local | TLD measurement |             | DPM calculation |             |                 | Pinnacle calculation (reference) |             |                 |
|------------------|-----------------|-------------|-----------------|-------------|-----------------|----------------------------------|-------------|-----------------|
|                  | Avg. (cGy)      | % std. dev. | Avg. (cGy)      | % std. dev. | Ratio calc/meas | Avg (cGy)                        | % std. dev. | Ratio calc/meas |
| Pri S-A          | 696             | 0.2         | 675             | 0.7         | 0.970           | 684                              | 0.2         | 0.983           |
| Pri S-P          | 688             | 0.7         | 695             | 0.7         | 1.010           | 686                              | 0.2         | 0.996           |
| Pri I-A          | 700             | 0.1         | 680             | 0.7         | 0.972           | 686                              | 0.4         | 0.981           |
| Pri I-P          | 696             | 0.8         | 692             | 1.0         | 0.995           | 684                              | 0.3         | 0.983           |
| Pri Avg          |                 |             |                 |             | 0.987           |                                  |             | 0.986           |
| Sec S            | 547             | 0.4         | 537             | 0.9         | 0.982           | 553                              | 0.6         | 1.011           |
| Sec I            | 543             | 0.3         | 532             | 1.5         | 0.980           | 552                              | 0.3         | 1.017           |
| SecAvg           |                 |             |                 |             | 0.981           |                                  |             | 1.014           |
| CS S             | 185             | 2.3         | 163             | 4.2         | 0.881           | 215                              | 4.9         | 1.166           |
| CS I             | 187             | 2.0         | 166             | 4.6         | 0.889           | 214                              | 4.9         | 1.145           |
| CS Avg           |                 |             |                 |             | 0.885           |                                  |             | 1.156           |

Table 14 Point dose comparisons of the IMRT head and neck phantom. The measured dose is the average dose from the three repeated irradiations. Calculated results are from DPM. The Pinnacle calculation is provided for reference. Point dose locations are keyed as follows: Pri = primary target; Sec = secondary target; CS = critical structure; S = superior; I = inferior; A = anterior; P = posterior.

The ratios of the calculated value to the measured value from the four TLD locations in the primary target were averaged so that the over all agreement for the primary target 0.987. The range of this averaged value was from 0.970 to 1.010. For reference, the Pinnacle calculation to measurement ratio averaged was 0.986. For the secondary target, both TLD locations showed that on average the calculation was lower than the measurement in the same manner as the primary target. The average of the ratios of the calculated value to the measured value was 0.981. For Pinnacle, the secondary target average of the ratios between the Pinnacle calculation and the measurement was 1.014. The critical structure showed the greatest deviation where the average of the ratios of the calculated dose to the measured dose was 0.885. In stark contrast, the Pinnacle calculated dose to the measured dose for the critical structure was

1.156. The larger differences between the calculated and measured dose were seen in their larger standard deviations (>4%). This, in large part, was due to the high dose gradient region that existed between the critical structure and target.

The results in Table 15 present the overall range and average of the ratios between the source model calculation and the measurement, and between the Pinnacle calculations and the measurement for the primary and secondary targets and critical structure for all TLD locations and all repeated irradiations and not as an average of the repeated irradiations as was the data contained in Table 4.

|      | DPM calculation to measurement |                  |                    | Pinnacle calculation to measurement |                  |                    |
|------|--------------------------------|------------------|--------------------|-------------------------------------|------------------|--------------------|
|      | Primary target                 | Secondary target | Critical structure | Primary target                      | Secondary target | Critical structure |
| high | 1.018                          | 0.985            | 0.908              | 1.003                               | 1.020            | 1.197              |
| low  | 0.967                          | 0.977            | 0.868              | 0.976                               | 1.008            | 1.125              |
| avg  | 0.987                          | 0.981            | 0.885              | 0.986                               | 1.014            | 1.156              |

Table 15 IMRT head and neck: The range and average calculation to TLD measurement ratio of the point doses for the primary and secondary targets and critical structure for DPM and Pinnacle. The data is for each TLD location from each repeated irradiations.

The benchmark evaluation was strictly between the validated source model and measurement. The Pinnacle comparison with the measurement is shown only for reference and is representative of the comparison one might find between the source model calculation and a state of the art planning system.

#### 3.3.3.4 *Delivery of the IMRT head and neck phantom plan: Dose profile and gamma map comparisons*

The dose profiles along all three major planes are shown in Figure 3.15, Figure 3.16, and Figure 3.17. The dose profiles show the qualitative agreement between the source model DPM calculation and the measured dose and demonstrate the ability of the calculation to

predict dose with even small changes in the range of 20 cGy that occurred across short distances of about 5 mm. Good agreement was seen across all dose profiles.

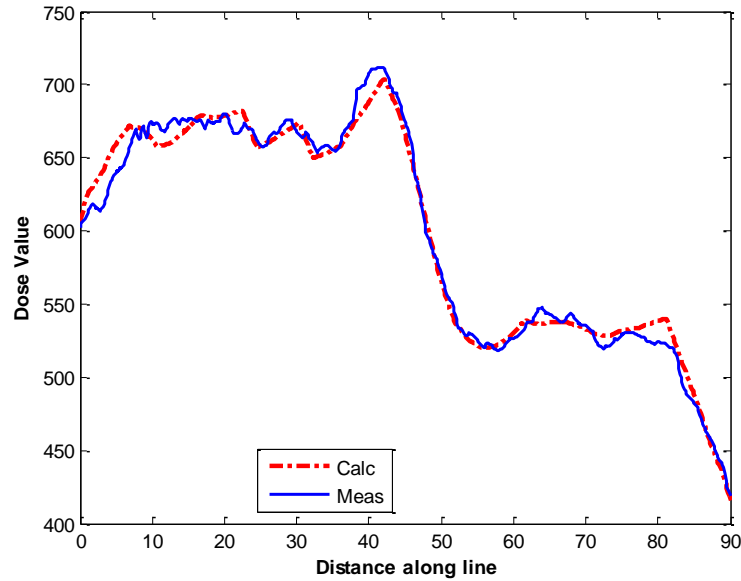


Figure 3.15 IMRT H&N delivery single irradiation (number 3): Lateral dose profile.

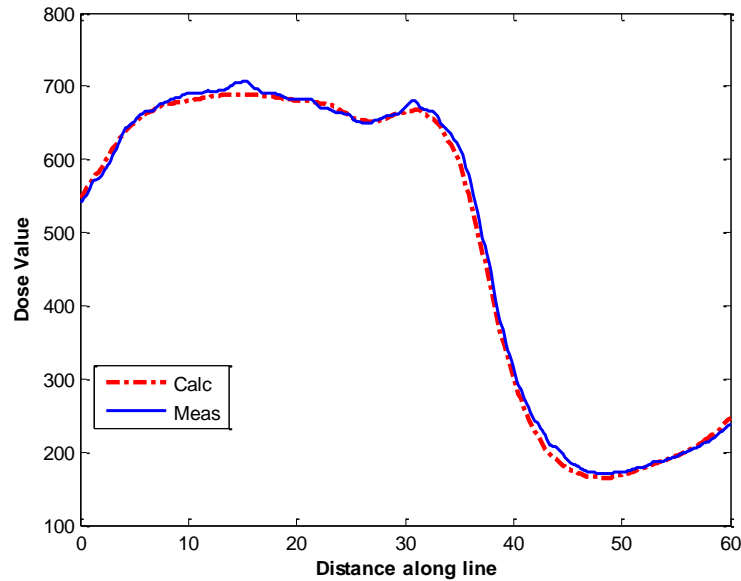


Figure 3.16 IMRT H&N delivery single irradiation (number 3): A-to-P dose profile.

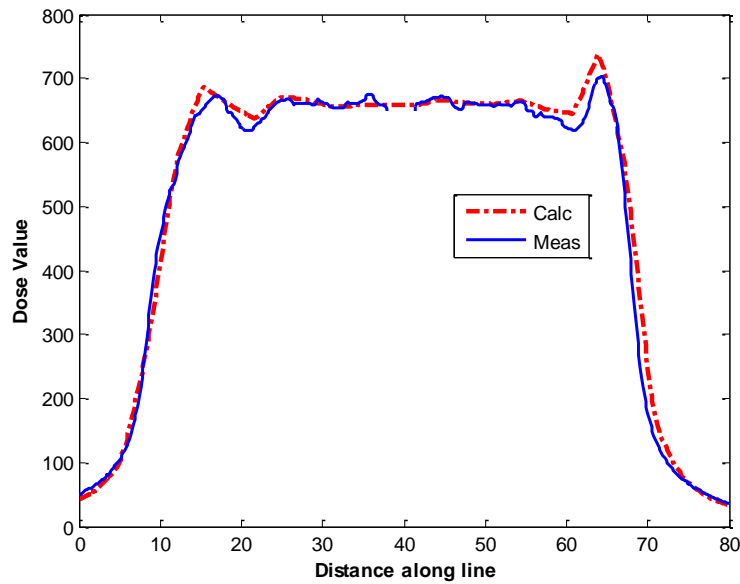


Figure 3.17 IMRT H&N delivery single irradiation (number 3): S-to-I dose profile.

Where the dose profiles quantify the amount of dose that was overpredicted or underpredicted by the source model calculation along a one dimensional direction, the gamma maps quantify the percentage of dose that met the criterion defined by a normalized percentage and a distance to agreement. The calculation and measurement axial and sagittal 2D dose planes were tested at a criterion of 3%/2 mm. The results of these tests are shown as the gamma maps in Figure 3.18 and Figure 3.19. Shown in the figures are the results from a single irradiation. Gamma maps at the criteria levels of 3%/2 mm and 5%/3 mm and dose profiles for all three repeated irradiations are presented in the Chapter 6, Appendix. For the IMRT head and neck plan, the percentage of the data meeting the criterion of 3% or 2 mm for the gamma maps from the axial and sagittal dose planes intersecting the center of the primary target from all three repeated irradiations averaged 94% and ranged from 90% to 97%. The gamma maps showed that in general the calculation predicted the dose within the criteria in the high dose, high gradient, and low dose regions within the axial and sagittal planes. The dose profiles and the gamma maps demonstrated that the modeling to describe the penumbra which applied an



MLC offset, interleaf leakage, rounded leaf and leaf transmission factors in the highly modulated fields of the head and neck plan was correct.

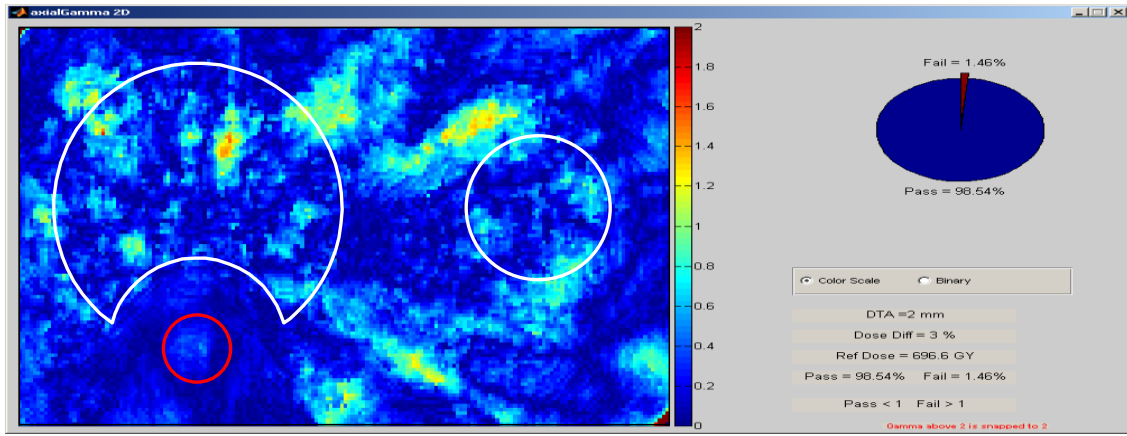


Figure 3.18 IMRT H&N delivery single irradiation (number 3): Axial plane, gamma map tested to 3%/2 mm criteria, where 99% of the data passed. Scale is 1 mm = 0.95 mm. Small circle outline represents the location of the secondary PTV, large crescent shaped outline represents the primary PTV, and the small red circle represents the spinal cord critical structure.

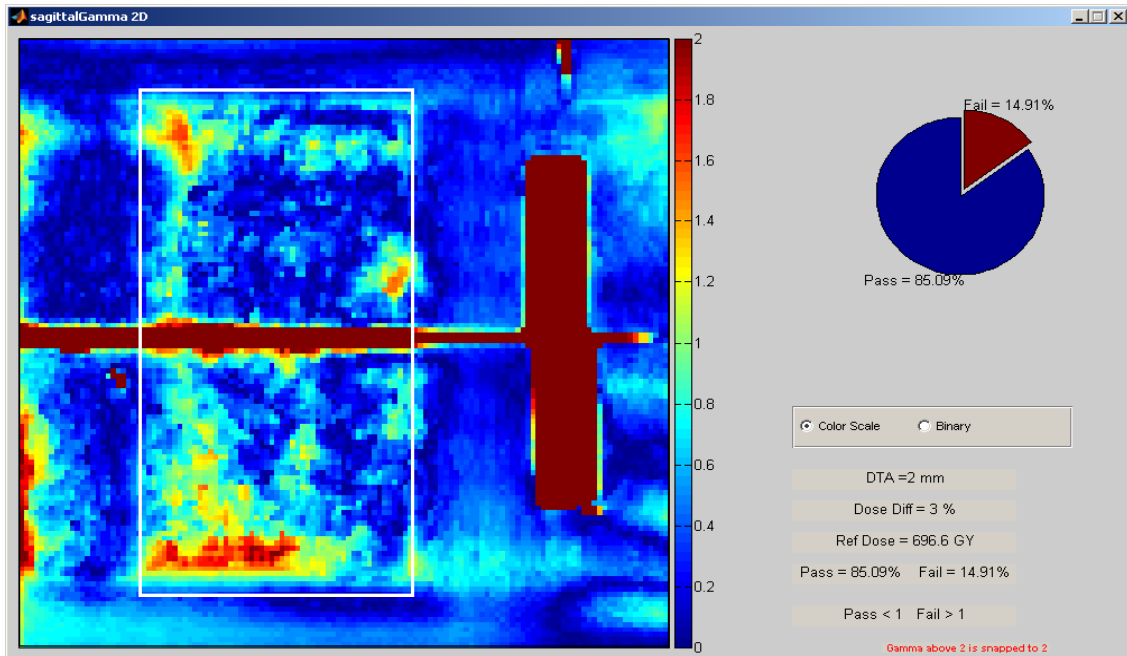


Figure 3.19 IMRT H&N delivery single irradiation (number 3): Sagittal plane; gamma map tested to 3%/2 mm criteria, where 93% of the data passed. Scale is 1 mm = 1.3 mm. Rectangle outline represents the location of the primary PTV. The maroon region in the vertical direction is where the film has been cut away to avoid interference with the critical structure region.

Figure 3.20 shows the performance of the source model calculation with and without the modeling the primary finite source, interleaf leakage, and the effect of the rounded leaf ends on transmission. Note that in addition to an increase in the calculated dose to the primary targets, there was an improvement in the shape of the penumbra.

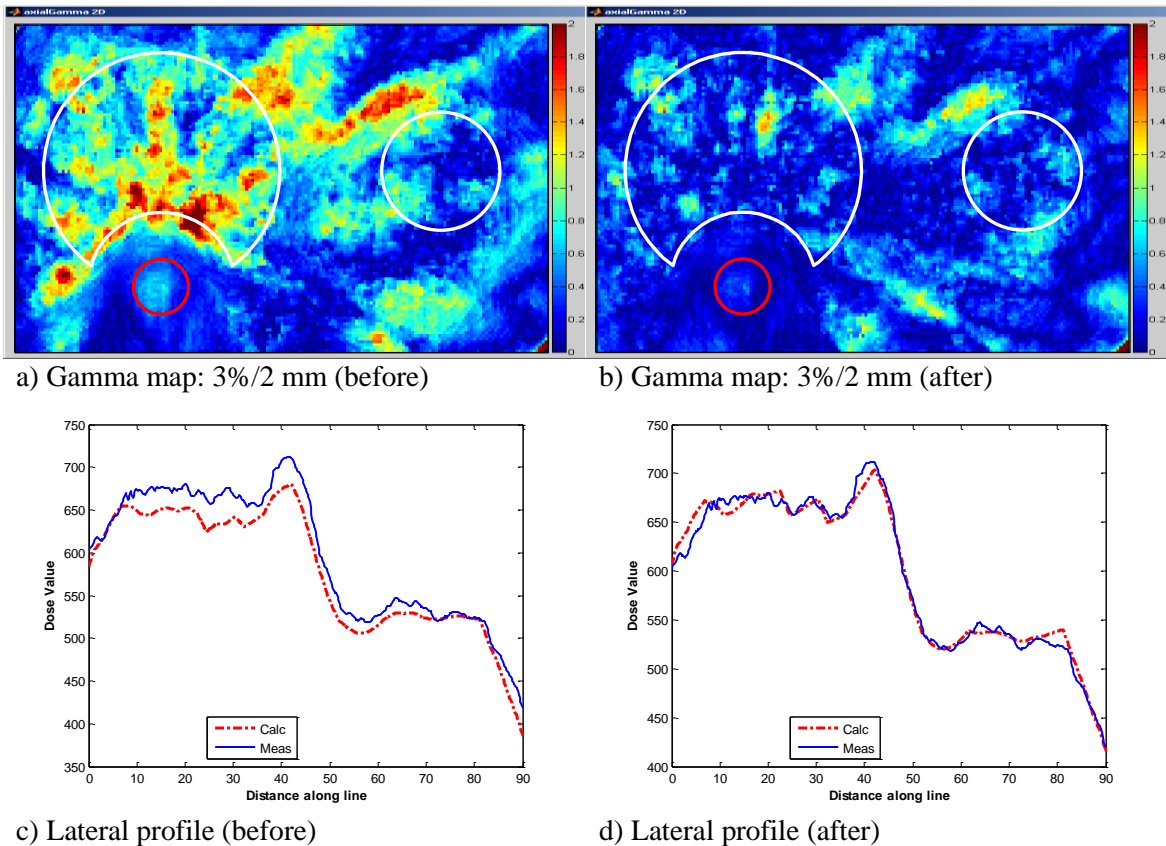
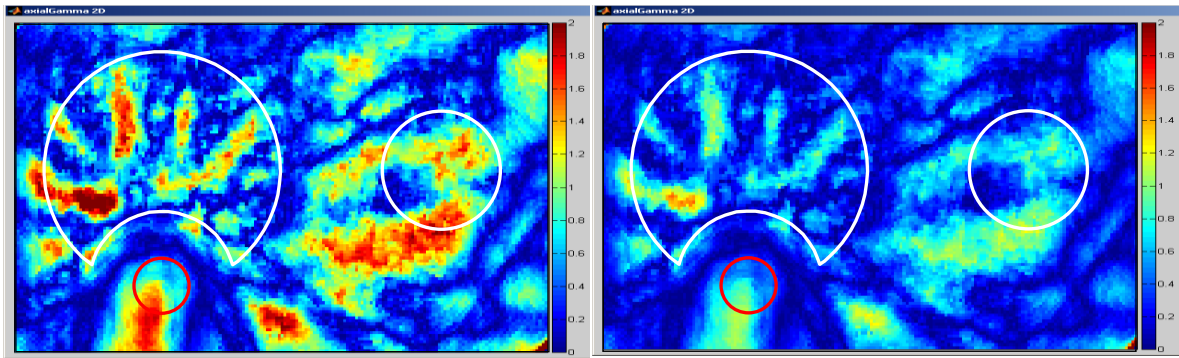


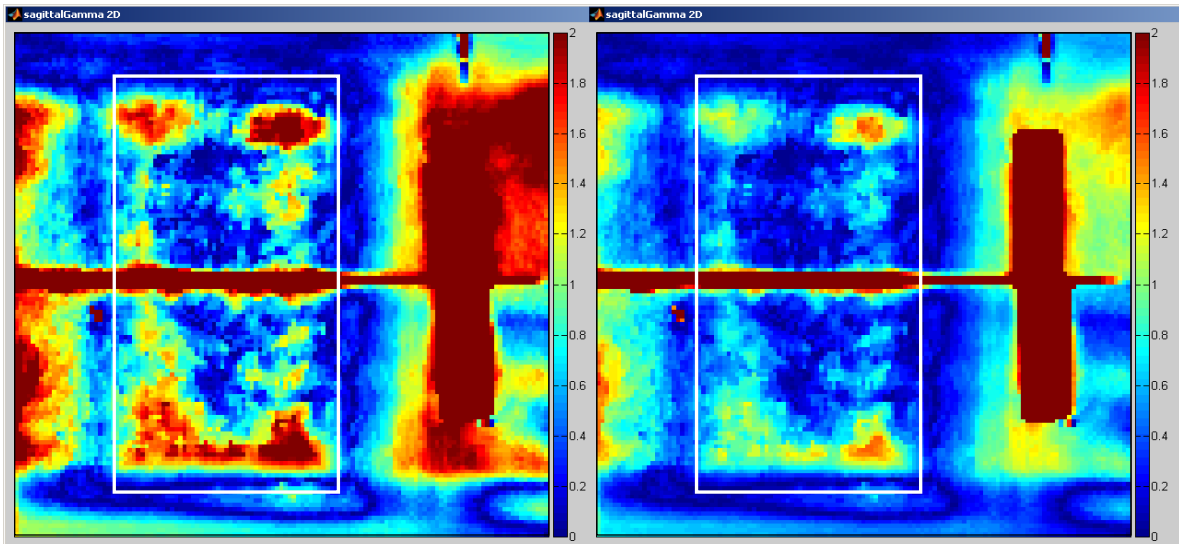
Figure 3.20 IMRT head and neck: Gamma maps (a and b) and lateral dose profiles (c and d) from the same irradiation, but before (a and c) and after (b and d) changes to the model to improve the penumbra.

For reference, the Pinnacle calculation was compared to the same measured data and is shown in Figure 3.21. The Pinnacle calculation tended to overpredict and smooth out some of the small dose gradients within the primary target. The small dose gradients were greater than the nonuniformity of the film measurement.



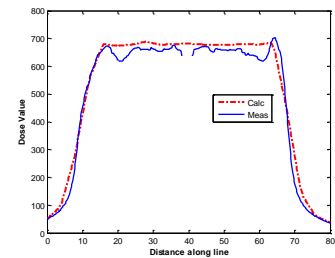
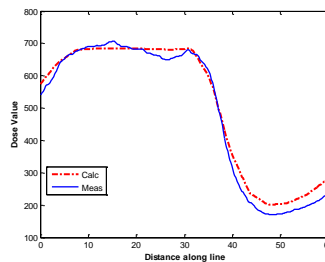
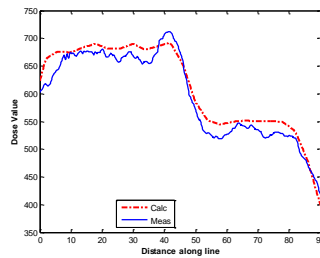
a) Axial: 3%/2 mm, 82% pass; scale 1mm = 0.79 mm

b) Axial: 5%/3 mm, 97% pass; scale 1mm = 0.79 mm



c) Sagittal: 3%/2 mm, 79% pass; scale 1 mm = 1.09 mm

d) 5%/3 mm, 87% pass; scale 1 mm = 1.09 mm



e) Lateral profile

f) Anterior to posterior profile

g) Superior to inferior profile

Figure 3.21 Gamma map (a thru d) and dose profile (e thru g) comparisons between the Pinnacle calculation and measurement for the IMRT H&N delivery (single irradiation, no. 3). The gamma map comparisons show results with differing criteria (3%/2 mm vs. 5%/3 mm).

### 3.3.3.5 Delivery of the SBRT thorax phantom: Point dose comparisons

The center of the target, the center of the heart, and center of the spinal cord proximal to the target each contained two TLD capsules. The results of the point dose comparisons are shown for each TLD measurement location in Table 16. Included in the table are the average dose measurements and the percent standard deviations from the three repeated irradiations. The comparisons of the target and the critical structures between the calculations and measurement were expressed as a ratio. The comparisons included both the DPM calculation the Pinnacle calculation.

| Point dose local | TLD measurement |             | DPM calculation |             |                 | Pinnacle calculation (reference) |             |                 |
|------------------|-----------------|-------------|-----------------|-------------|-----------------|----------------------------------|-------------|-----------------|
|                  | Avg. (cGy)      | % std. dev. | Avg. (cGy)      | % std. dev. | Ratio calc/meas | Avg (cGy)                        | % std. dev. | Ratio calc/meas |
| Target Sup       | 690             | 1.1         | 696             | 0.2         | 1.008           | 684                              | 0.1         | 0.990           |
| Target Inf       | 686             | 1.9         | 695             | 0.3         | 1.013           | 682                              | 0.1         | 0.994           |
| Target Average   |                 |             |                 |             | 1.011           |                                  |             | 0.992           |
| Cord             | 68              | 1.5         | 70              | 0.5         | 1.038           | 70                               | 0.1         | 1.028           |
| Heart            | 118             | 0.3         | 118             | 1.4         | 1.005           | 115                              | 2.4         | 0.973           |

Table 16 Point dose comparisons of the SBRT thoracic phantom. The measured dose is the average dose from the three repeated irradiations. Calculated results are from DPM. The Pinnacle calculation is provided for reference.

The agreement, expressed as a ratio between the DPM calculation and measurement for the target, was on average 1.011. Similar to the DPM calculation, the Pinnacle calculation estimated the point dose to the target within the uncertainty of measurement so that the ratio between the Pinnacle calculation and measurement was 0.992 on average. While the calculated dose for the heart agreed well with measurement. The DPM calculation to measurement ratio

for the heart was 1.005. A greater deviation occurred in the TLD location of the cord where the dose was very low and the uncertainty in TLD measurement is greater as the nonlinearity of the TLD dose is about four times less than the calibrated standard dose so that the ratio between the DPM calculation and measurement was 1.038. In addition the TLD location was distal to the isocenter and would suffer the greatest translational error that would have been due to the phantom setup on the treatment couch.

The results in Table 17 present the range and average of the ratios between the source model calculation and the measurement for the target and critical structures for all TLD locations and all repeated irradiations, and not as an average of the repeated irradiations as was the data contained in Table 16. The Pinnacle calculation to measurement ratio is also included in Table 17. The source model calculation to measurement ratio for the target when all TLD locations are considered was 1.011 with a range from 0.997 to 1.036. The narrow range of the calculation to measurement ratios for the TLD locations for the each structure showed the consistency of the repeated irradiations.

|      | DPM calculation to measurement |       |       | Pinnacle calculation to measurement |       |       |
|------|--------------------------------|-------|-------|-------------------------------------|-------|-------|
|      | Target                         | Heart | Cord  | Target                              | Heart | Cord  |
| high | 1.036                          | 1.008 | 1.049 | 1.016                               | 0.976 | 1.039 |
| low  | 0.997                          | 1.002 | 1.027 | 0.980                               | 0.970 | 1.017 |
| avg  | 1.011                          | 1.005 | 1.038 | 0.992                               | 0.973 | 1.028 |

Table 17 SBRT lung plan: The range and average calculation to measurement ratio of the point doses for the target, cord, and heart for DPM and Pinnacle. The data is for each TLD location from each repeated irradiations.

The benchmark evaluation was strictly between the validated source model and measurement. The Pinnacle comparison with the measurement is shown only for reference and is representative of the comparison one might find between the source model calculation and a state of the art planning system.

### 3.3.3.6 Delivery of the SBRT thorax phantom plan: Dose profile and gamma map comparisons

Dose profiles along all three major planes are shown in Figure 3.22, Figure 3.23, and Figure 3.24. The figures reported the results from a single irradiation. As were the results of the comparison between the calculation and measurement of the homogeneous, highly modulated head and neck plan, the results for the SBRT lung plan were very good. The calculated and measured dose from the lateral, anterior-posterior, and superior-inferior profiles agreed in the PTV and penumbra regions. Some small differences up to about 3% were found within the PTV. The variation of the measurement in this region may be, in part, due to the film uncertainty as the SBRT plan was not modulated beyond the same static open field with nine symmetric beams, therefore a fairly flat dose profile was expected. The location of the target in the medial-lateral direction from the center of the lung may have accounted from some of nonuniformity of the dose distribution within the PTV.

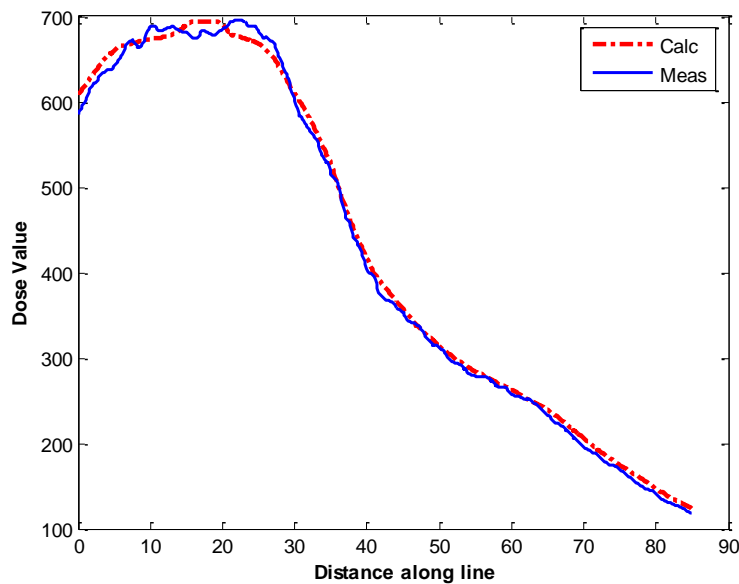


Figure 3.22 SBRT lung delivery single irradiation (number 1): lateral dose profile.

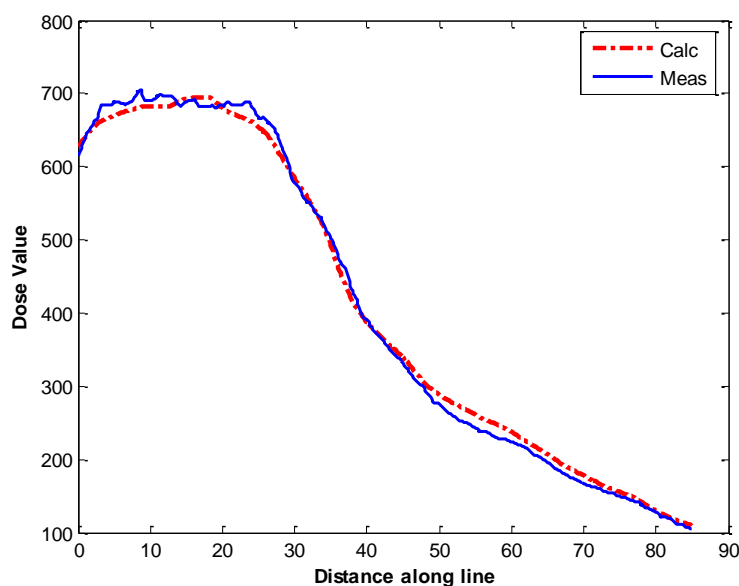


Figure 3.23 SBRT lung delivery single irradiation (number 1): A-P dose profile.

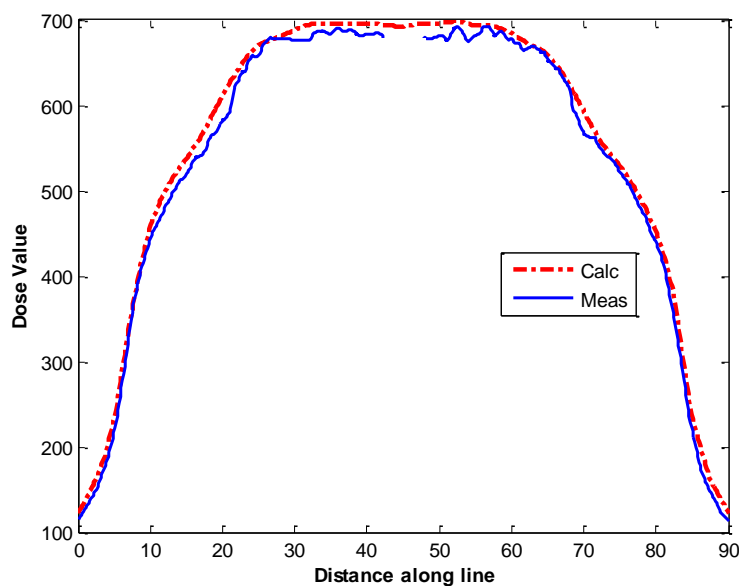


Figure 3.24 SBRT lung delivery single irradiation (number 1): S-I dose profile.

The gamma maps at a test criterion of 3%/2 mm are shown in Figure 3.25, Figure 3.26, and Figure 3.27. The maps were based on a single irradiation. The gamma maps in all three major planes showed that agreement was very good and met the criterion except for the region adjacent in the medial and lateral directions of the target. This region was near the boundary

interface between the lung and chest wall where electronic disequilibrium occurs and requires some distance to re-establish equilibrium. Not accounting for all the scatter conditions within the extra-focal source may be the most sensitive to this condition where the boundary condition existed at the lung interface. The SBRT lung plan had good agreement overall where 96% of the calculated data met the criterion of 3%/2 mm. The DPM dose calculation was able to accurately predict the dose from small fields in a low density anthropomorphic phantom for the Varian 10 MV photon beam. Gamma maps at the criteria levels of 3%/2 mm and 5%/3 mm and dose profiles for all three repeated irradiations are presented in the Appendix, Chapter 6.

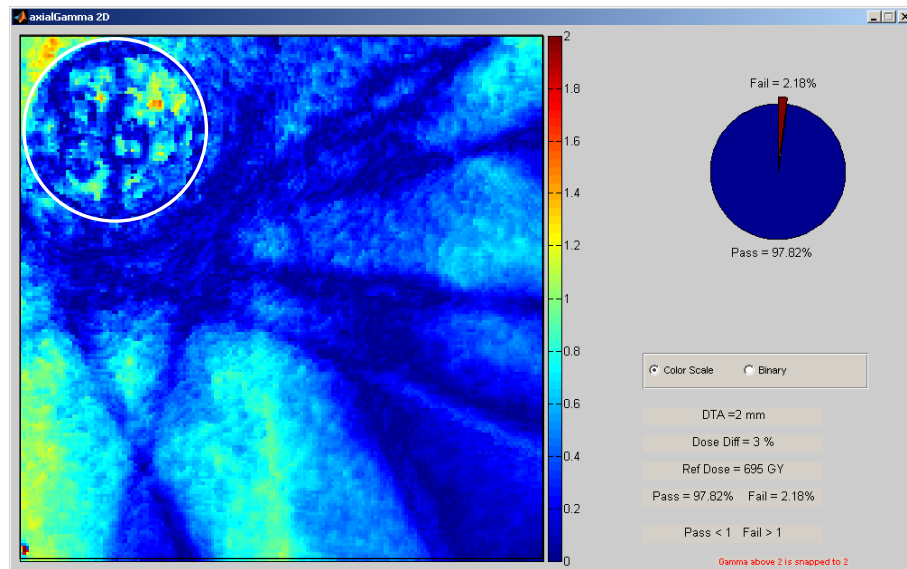


Figure 3.25 SBRT lung delivery single irradiation (number 1): Axial plane, gamma map tested to 3%/2 mm criteria, where 98% of the data passed. Scale is 1 mm = 0.8 mm. Circle outline represents the location of the PTV.



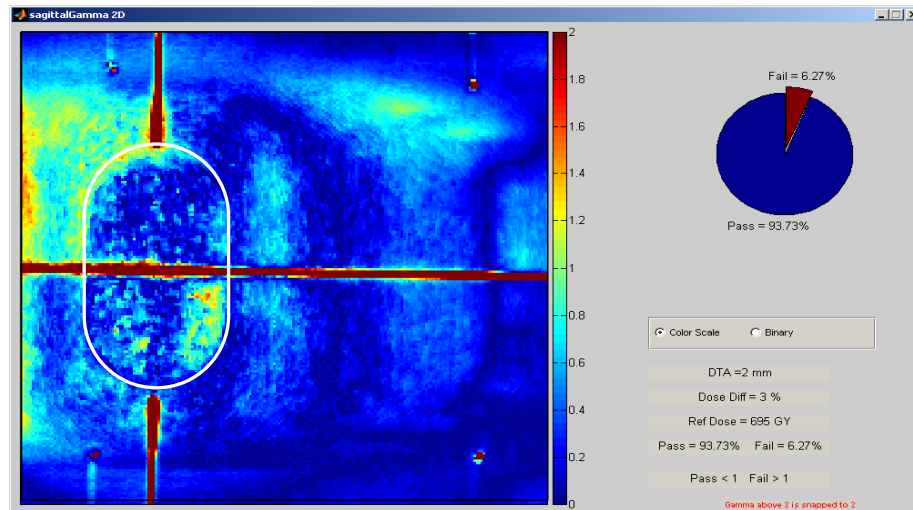


Figure 3.26 SBRT lung delivery single irradiation (number 1): Sagittal plane, gamma map tested to 3%/2 mm criteria, where 97% of the data passed. Scale is 1 mm = 0.65 mm. Elongated circle outline represents the location of the PTV.

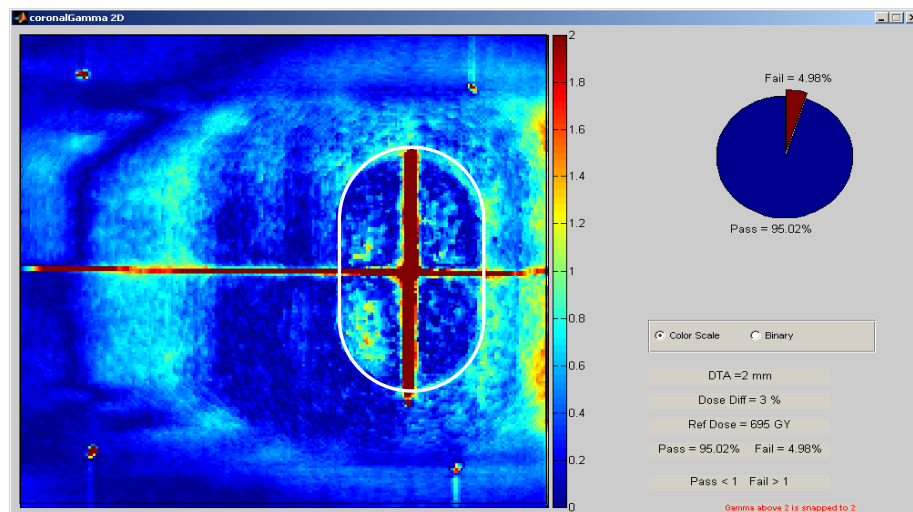
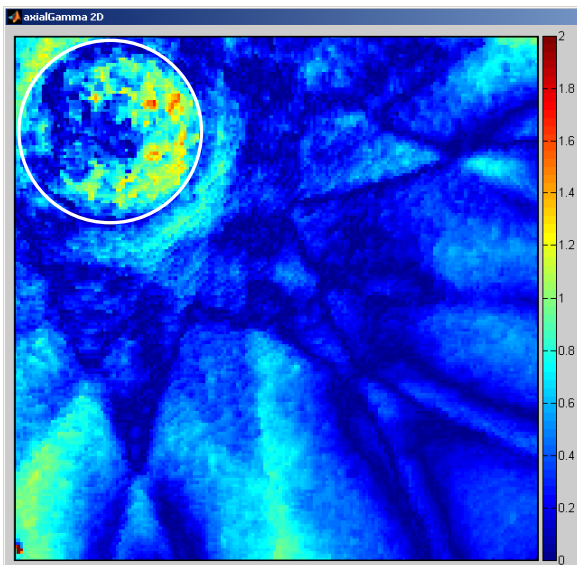
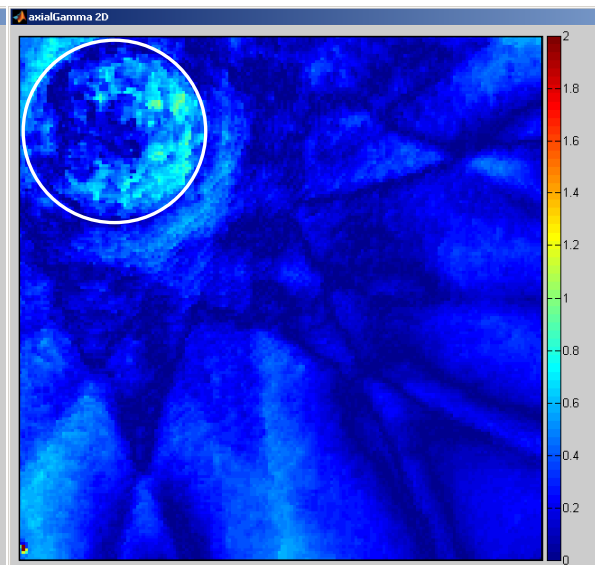


Figure 3.27 SBRT lung delivery single irradiation (number 1): Coronal plane, gamma map tested to 3%/2 mm criteria, where 98% of the data passed. Scale is 1 mm = 0.65 mm. Elongated circle outline represents the location of the PTV.

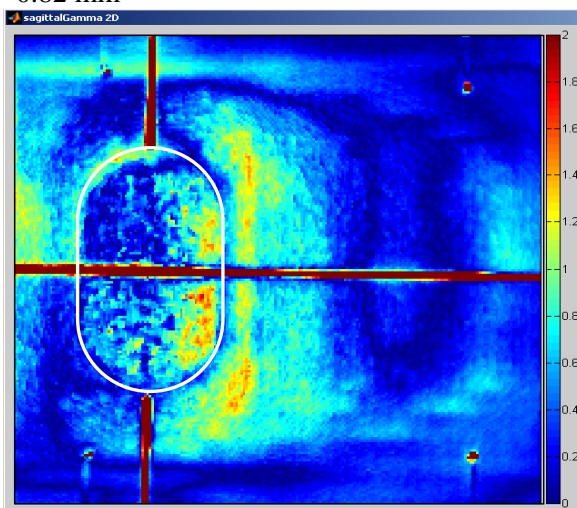
For reference, the Pinnacle calculation was compared to the same measured data and is shown in Figure 3.28. The results were similar to the DPM calculation. The small amount of disagreement tended to occur near the target edge and into the penumbra region of the lung material.



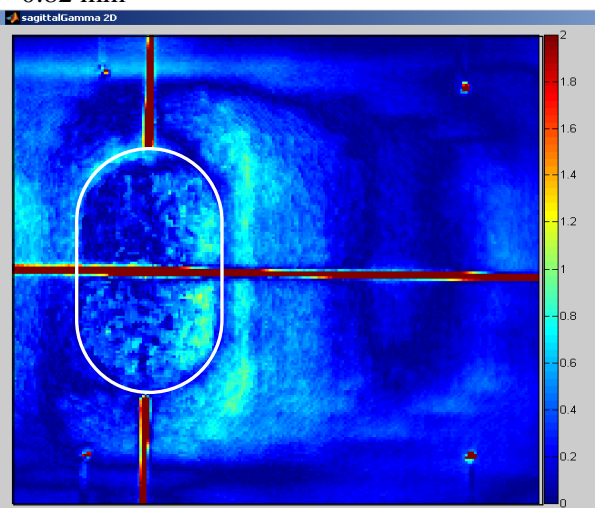
a) Axial: 3%/2 mm, 98% pass; scale 1mm = 0.82 mm



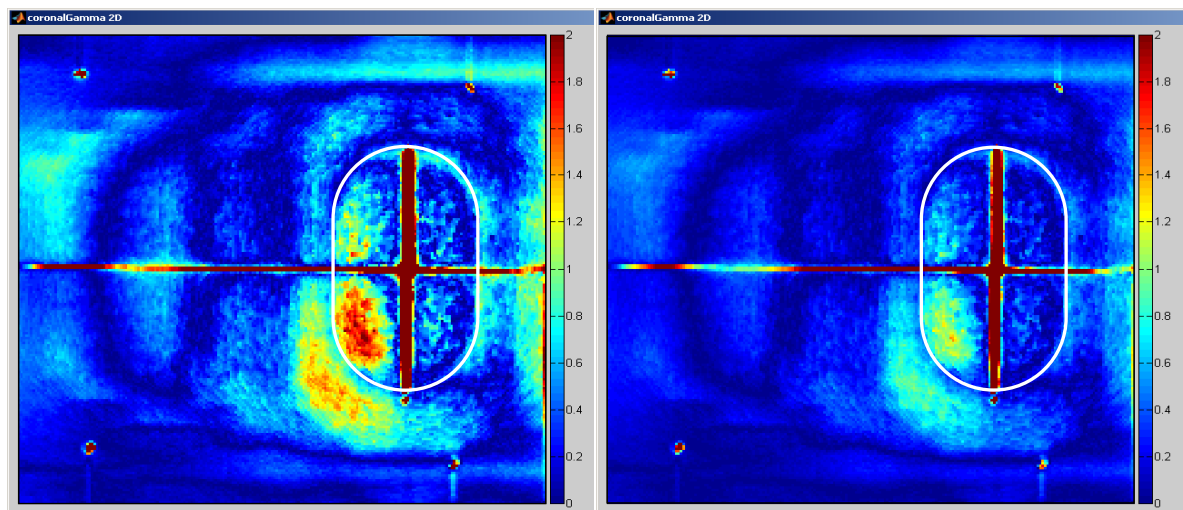
b) Axial: 5%/3 mm, 100% pass; scale 1mm = 0.82 mm



c) Sagittal: 3%/2 mm, 95% pass; scale 1 mm = 0.65 mm

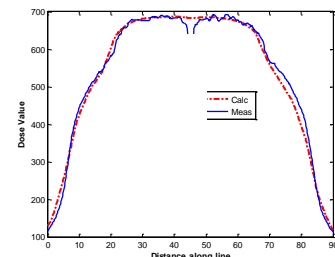
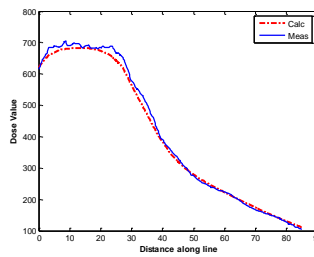
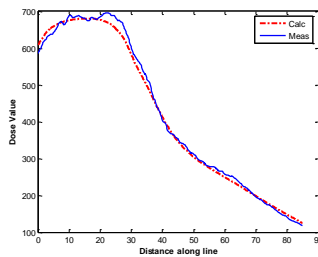


d) Sagittal: 5%/3 mm, 100% pass; scale 1 mm = 0.65 mm



e) Coronal: 3%/2 mm, 96% pass; scale 1 mm = 0.65 mm

f) Coronal: 5%/3 mm, 99% pass; scale 1 mm = 0.65 mm



e) Lateral profile

f) Anterior to posterior profile

g) Superior to inferior profile

Figure 3.28 Gamma map and dose profile comparisons between the Pinnacle calculation and measurement for the SBRT lung delivery (single irradiation, number 1)

### 3.3.3.7 Delivery of the IMRT thorax phantom plan: Point dose comparisons

The results of the point dose comparisons are shown for each TLD measurement location in Table 18. Using the same thorax phantom as that used for the SBRT lung plan, the same TLD locations were used. Namely, two TLD capsules were located within the center of the target, two TLD capsules within the heart and two TLD capsules within the spinal cord critical structures. The average dose measurements and the percent standard deviations from the three repeated irradiations are also given. The comparisons of the target and the critical structures between the DPM calculation and measurement and comparisons between the Pinnacle calculation and measurement were expressed as a ratio.

| Point dose local | TLD measurement |             | DPM calculation |             |                 | Pinnacle calculation (reference) |             |                 |
|------------------|-----------------|-------------|-----------------|-------------|-----------------|----------------------------------|-------------|-----------------|
|                  | Avg. (cGy)      | % std. dev. | Avg. (cGy)      | % std. dev. | Ratio calc/meas | Avg (cGy)                        | % std. dev. | Ratio calc/meas |
| Target Sup       | 608             | 1.9         | 623             | 0.6         | 1.025           | 624                              | 0.4         | 1.027           |
| Target Inf       | 620             | 0.6         | 632             | 1.0         | 1.019           | 628                              | 0.1         | 1.014           |
| Target Average   |                 |             |                 |             | 1.022           |                                  |             | 1.020           |
| Cord             | 53              | 0.5         | 51              | 7.0         | 0.962           | 53                               | 4.1         | 0.994           |
| Heart            | 81              | 0.9         | 86              | 5.2         | 1.062           | 91                               | 4.8         | 1.127           |

Table 18 Point dose comparisons of the IMRT thoracic phantom. The measured dose is the average dose from the three repeated irradiations. Calculated results are from DPM. The Pinnacle calculation is provided for reference.

The DPM calculation overestimated the point dose to the target center by an average of 2.2%. The Pinnacle calculation overestimated the point dose to the target by an average of 2.0%. The standard deviation of the DPM calculation for the critical structures was large from 5.2% to 7.0%, which was enough to account for the variation in the dose estimations of the spinal cord (0.962, calculation to measurement ratio) and heart (1.062, calculation to measurement ratio). The Pinnacle calculation also reported standard deviations to account for some of the variation for the ratio of the calculation to measurement of 1.127 for the heart. Since both the DPM and Pinnacle reported high standard deviations for the small regions of interest of the TLD within the cord and heart, most likely this was due to the dose gradients that existed in these regions. Other sources for error would include the smaller number of histories recorded in the voxels distal to the PTV where most of the energy was deposited. The distal regions of cord and heart where the dose is much lower are influenced more by the second and third order scatter kernels of the convolution algorithm, which are less accurate.

The range and average of the ratios between the source model calculation and the measurement, and between the Pinnacle calculation and the measurement for the target and critical structures for all TLD locations and all repeated irradiations are shown in Table 19. The ratio of the source model calculation to measurement ranged from 1.003 to 1.037 for all the TLD locations from all of the repeated irradiations evaluated within the target.

|      | DPM calculation to measurement |       |       | Pinnacle calculation to measurement |       |       |
|------|--------------------------------|-------|-------|-------------------------------------|-------|-------|
|      | Target                         | Heart | Cord  | Target                              | Heart | Cord  |
| high | 1.037                          | 1.072 | 0.965 | 1.038                               | 1.139 | 0.997 |
| low  | 1.003                          | 1.055 | 0.956 | 1.004                               | 1.120 | 0.988 |
| avg  | 1.022                          | 1.062 | 0.962 | 1.020                               | 1.127 | 0.994 |

Table 19 IMRT lung: The range and average calculation to measurement ratio of the point doses for the target, cord, and heart for DPM and Pinnacle. The data is for each TLD location from each repeated irradiations.

The benchmark evaluation was strictly between the validated source model and measurement. The Pinnacle comparison with the measurement is shown only for reference and is representative of the comparison one might find between the source model calculation and a state of the art planning system.

### 3.3.3.8 *Delivery of the IMRT thorax phantom plan: Dose profile and gamma map comparisons*

Dose profiles along all three major planes are shown in Figure 2.33, Figure 2.34, and Figure 2.35. The gamma maps at a test criterion of 3%/2 mm are shown in Figure 2.36, Figure 2.37, and Figure 2.38. These figures reported the results from a single irradiation. Gamma maps at the criteria levels of 3%/2 mm and 5%/3 mm and dose profiles for all three repeated irradiations are presented in the Appendix Chapter 6. The calculated and measured dose from the lateral, anterior-posterior, and superior-inferior profiles generally agreed. However, the

dose profile showed in the posterior penumbra region some local dose differences in the range of 3% to 5%.

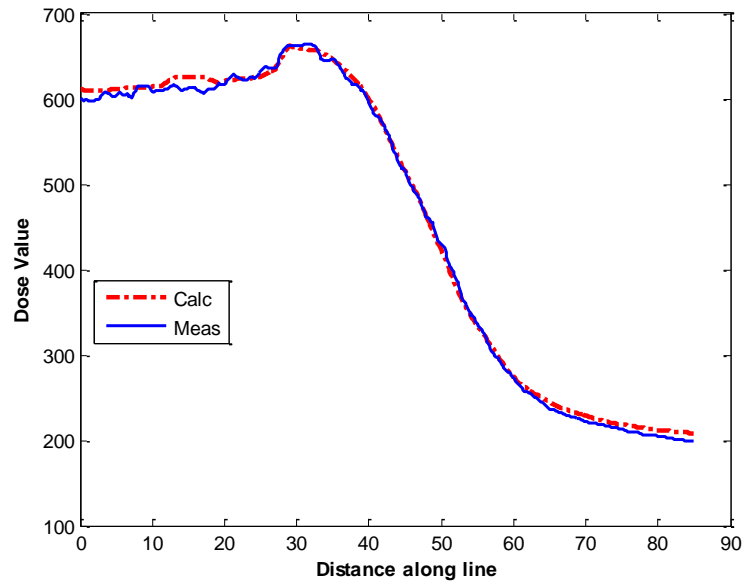


Figure 3.29 IMRT lung delivery single irradiation (number 1): lateral dose profile.

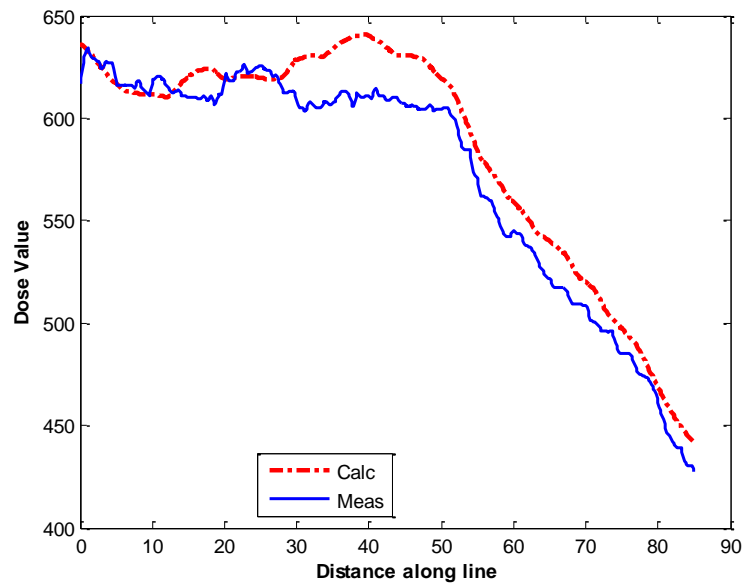


Figure 3.30 IMRT lung delivery single irradiation (number 1): A-P dose profile.

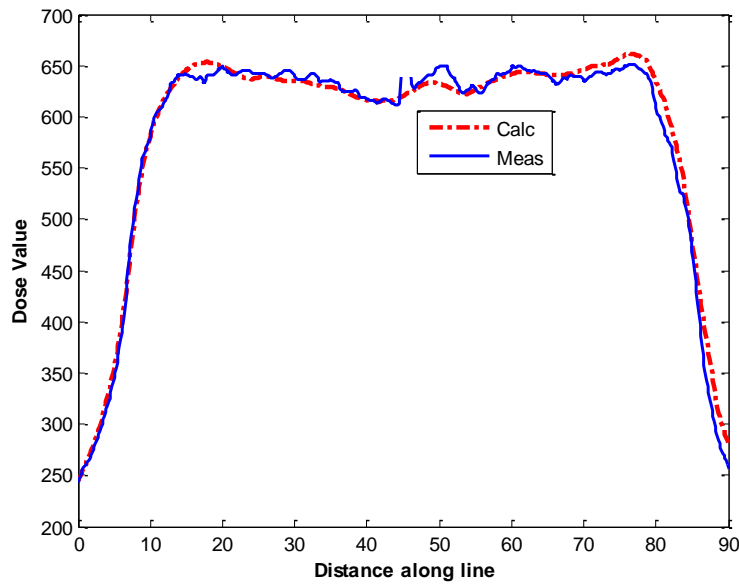


Figure 3.31 IMRT lung delivery single irradiation (number 1): S-I dose profile.

The gamma maps also showed small regions of disagreement which typically occurred in the penumbra regions. The penumbra region represented not only the change in the high dose region to low dose region, but also the change from the target tissue-like density to the low density region of the lung where electronic disequilibrium occurred. Disagreement may also be more likely to occur near the lung and the chest wall for the same reason. This may explain some of the differences between the calculation and measurement seen on the coronal gamma map.

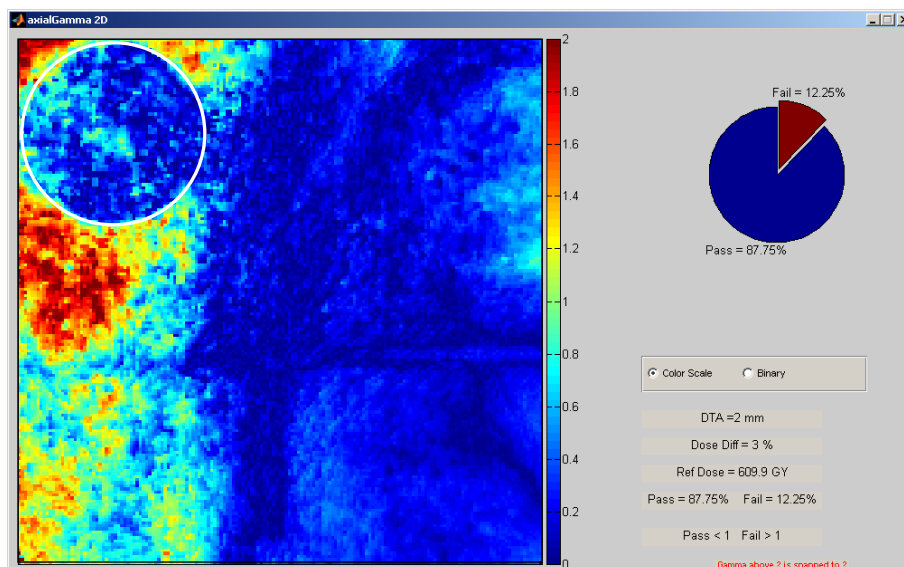


Figure 3.32 IMRT lung delivery single irradiation (number 1): Axial plane, gamma map tested to 3%/2 mm criteria, where 92% of the data passed. Scale is 1 mm = 0.8 mm. Circle outline represents the location of the PTV.

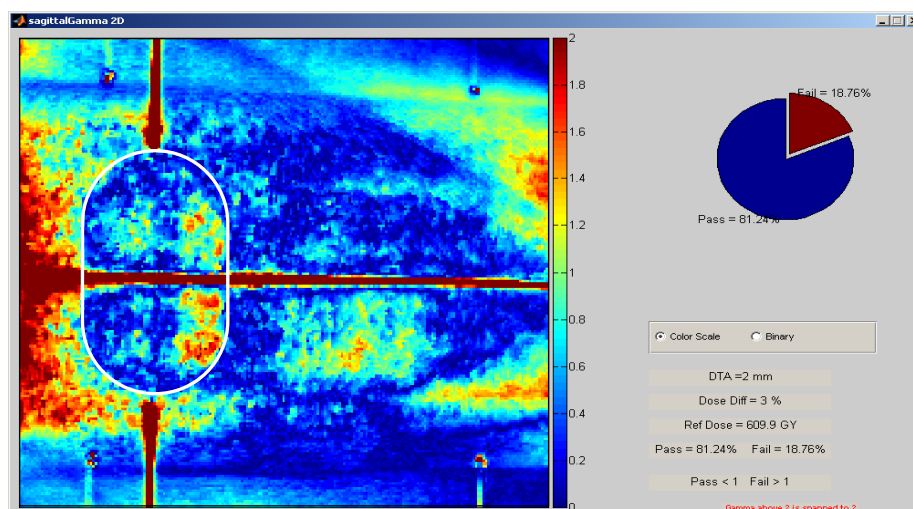


Figure 3.33 IMRT lung delivery single irradiation (number 1): Sagittal plane, gamma map tested to 3%/2 mm criteria, where 84% of the data passed. Scale is 1 mm = 0.65 mm. Elongated circle outline represents the location of the PTV.



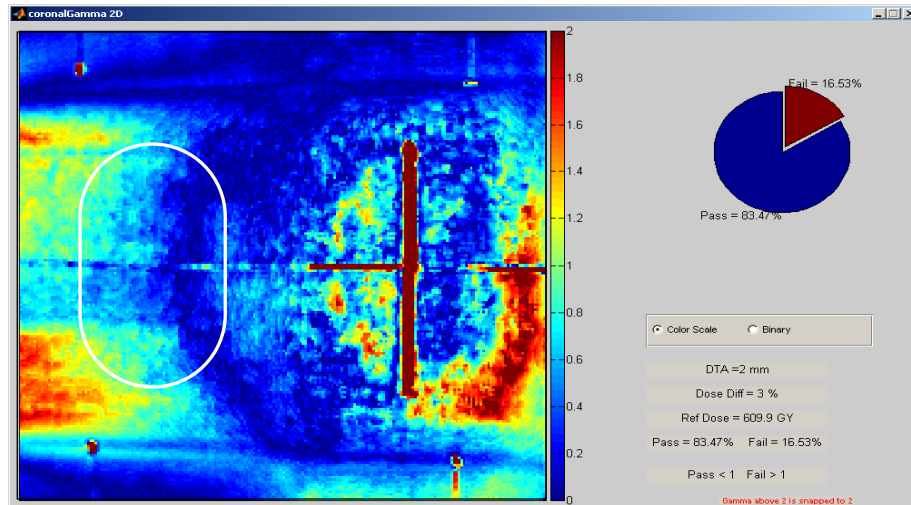
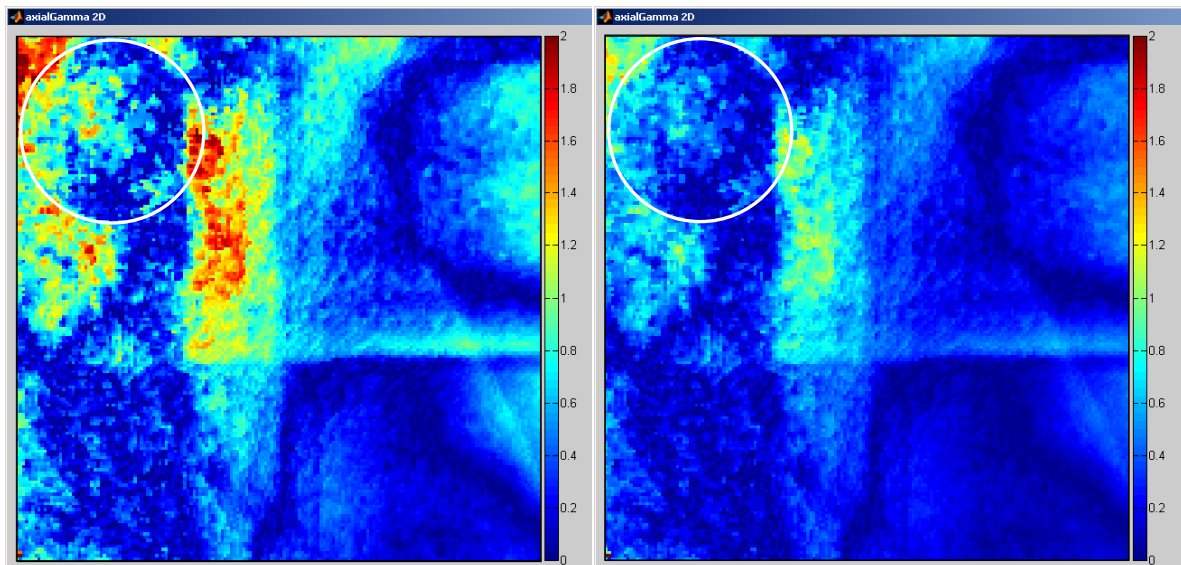


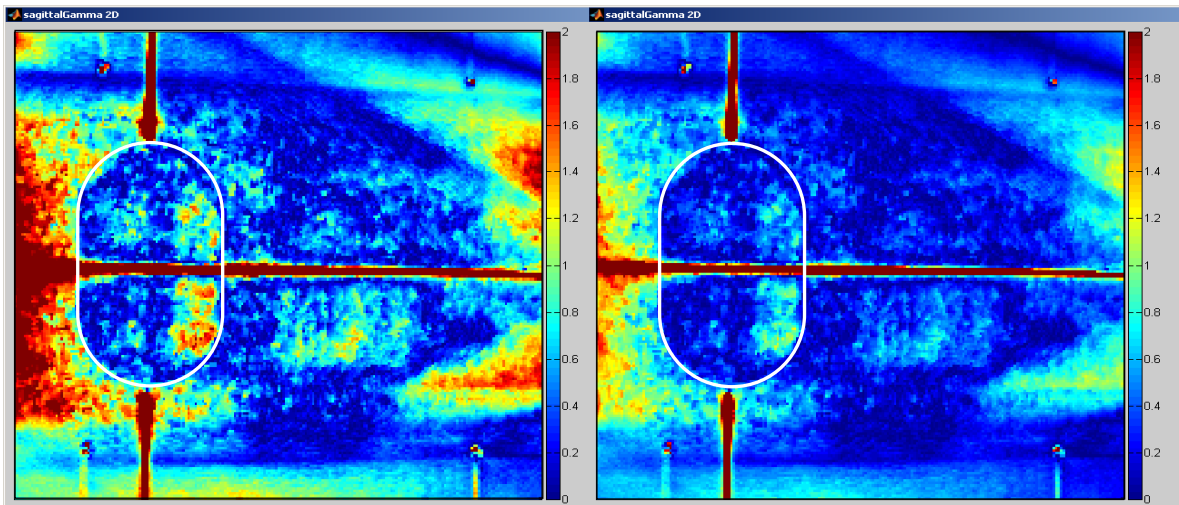
Figure 3.34 IMRT lung delivery single irradiation (number 1): Coronal plane, gamma map tested to 3%/2 mm criteria, where 86% of the data passed. Scale is 1 mm = 0.65 mm. Elongated circle outline represents the location of the PTV.

The comparison of the Pinnacle calculation and the same measured data used in the DPM evaluation above is shown in Figure 3.35. The results were similar to the results from the DPM Monte Carlo calculation in terms of disagreement occurring in the penumbra region. However, where the DPM calculation overpredicted dose in the penumbra, the Pinnacle calculation underpredicted the dose and tended to overestimate the broadening of the penumbra.



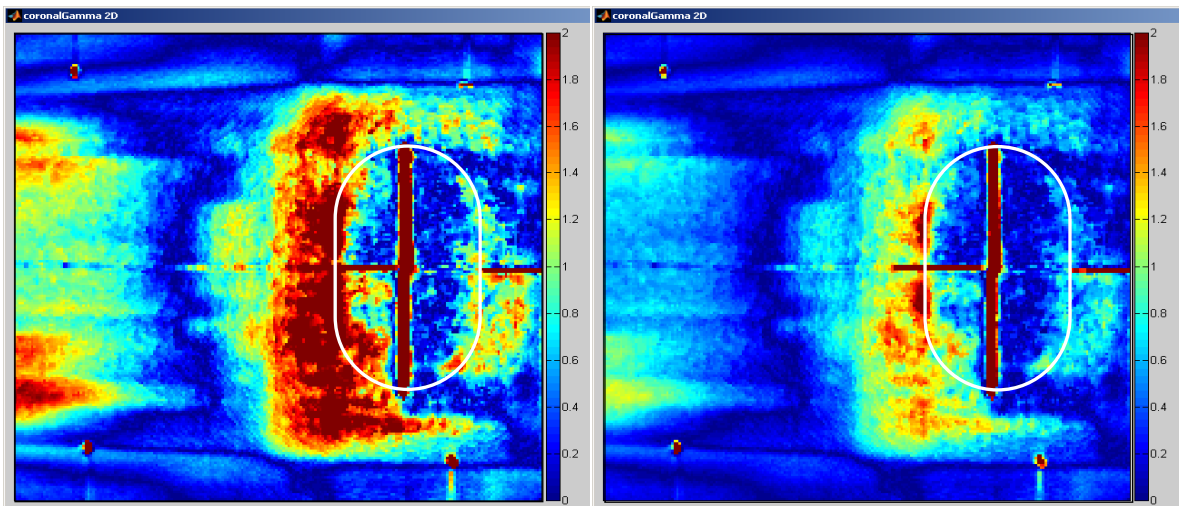
a) Axial: 3%/2 mm, 90% pass; scale 1mm = 0.82 mm

b) Axial: 5%/3 mm, 99% pass; scale 1mm = 0.82 mm



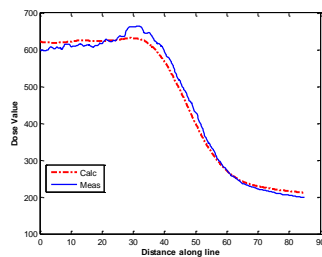
c) Sagittal: 3%/2 mm, 86% pass; scale 1 mm = 0.65 mm

d) Sagittal: 5%/3 mm, 98% pass; scale 1 mm = 0.65 mm

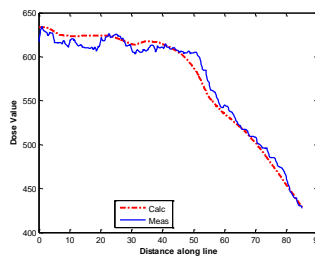


e) Coronal: 3%/2 mm, 72% pass; scale 1 mm = 0.65 mm

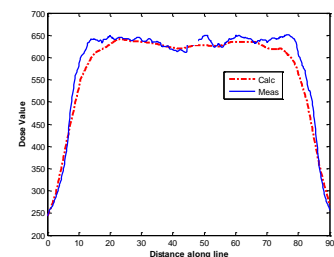
f) Coronal: 5%/3 mm, 92% pass; scale 1 mm = 0.65 mm



e) Lateral profile



f) Anterior to posterior profile



g) Superior to inferior profile

Figure 3.35 Gamma map and dose profile comparisons between the Pinnacle calculation and measurement for the IMRT lung delivery (single irradiation, number 1)

### 3.3.3.9 Benchmark summary

The overall results of the percentage of the data that met the gamma index criteria of 3% of the normalized PTV dose or 2 mm distance to agreement for the comparison between the DPM calculation and measurement is shown in Table 20. The average and range from the repeated irradiations for each treatment plan are included in the data. The percentage of data that met the gamma index criteria for the Varian 6 MV source model are shown in parenthesis in Table 20.

|         | IMRT H&N      | SBRT Lung     | IMRT Lung     |
|---------|---------------|---------------|---------------|
| average | 94 (93)       | 96 (94)       | 85 (87)       |
| range   | 90-97 (90-98) | 91-98 (90-97) | 79-90 (81-92) |

Table 20 Varian 6 MV and 10 MV: The average and range of the percentage of data from meeting criteria from the gamma index of 3%/2 mm for repeated irradiations from each treatment plan. Values in parenthesis are corresponding numbers for 6 MV results.

The methodology for evaluation of source model energies was designed to be consistent. The plan prescription, constraints, and beam gantry angles were the same for the IMRT head and neck plan, SBRT lung plan, and IMRT lung plan. In addition, the MLC field conformed to the same PTV for both energies. The trend for the percentage of data meeting the criteria was the same for the Varian 6 MV and 10 MV source models. In addition, the range of the percentage of data meeting criteria was also similar indicating consistent methodology. Benchmark treatment plans were designed at three different levels of difficulty so that the source model with the DPM Monte Carlo calculation was thoroughly tested. The first test was an IMRT head and neck plan with a primary and secondary PTV, but delivered to a homogeneous phantom. Next, an SBRT lung plan using a small field with an equivalent square of approximately 5 cm<sup>2</sup> was delivered to a heterogeneous phantom where the target was positioned near the anterior medial edge of the low-density lung material. The final test used

the same heterogeneous thorax phantom that was used in the SBRT deliveries, but instead an IMRT lung plan was designed including one non-coplanar beam.

The results of this first benchmark test showed that an average of 94% of the data tested met the criteria of 3% or 2 mm. The range from the axial and sagittal dose planes from all three repeated irradiations was 90% to 97%. In general, disagreement was limited to small regions within the primary target edge and was due to the beam penumbra that existed within the primary PTV in this IMRT plan. Even in the steep dose gradient region between the adjacent structures of the primary PTV and the spinal cord the agreement was within the criteria.

The results of SBRT lung plan, the second benchmark test, showed that an average of 96% of the data tested met the criteria of 3% or 2 mm. The range from the axial, coronal, and sagittal dose planes from all three repeated irradiations was 91% to 98. Nearly all data from all of the three major planes intersecting the center of the target met the criteria. The point dose measurement in the target showed the calculation to overestimate the dose by 1%.

The final benchmark test was the IMRT lung plan. The results showed that an average of 85% of the data tested met the criteria of 3% or 2 mm. The range from the axial, coronal, and sagittal dose planes from all three repeated irradiations was 79% to 90%. As expected, combining the low density lung material with IMRT provided the greater challenge as greater differences between the calculation and measurement were observed. The DPM calculation overestimated the dose by 2.2% in the center of the target. Disagreement occurred in the penumbra regions posterior and medial-lateral/anterior of the target. Since agreement was typical in the distal-lateral direction, the regions of disagreement may be due to electronic disequilibrium crossing at a boundary and into low-density heterogeneous regions. In these regions, the DPM calculation overestimated the dose. Another region of disagreement occurred in the low dose regions. Disagreement here may also be due to the heterogeneous boundary condition as the DPM calculation overestimated the dose at the lung and chest wall interface.

### 3.4 CONCLUSION

The analytical source model using the Dose Planning Method (DPM) Monte Carlo calculation was developed and validated within 2% of the maximum dose and 2 mm distance to agreement of measurement for the open field sizes between 4 cm x 4 cm and 40 cm x 40 cm. The average local percent difference for the central axis dose beyond  $d_{\max}$  was 1.0% and the range was 0.5% to 1.5%. The average local percent difference for the off-axis dose at several different depths and whose dose was greater than or equal to 80% of the dose at the central axis dose at depth<sup>47</sup> was 0.5% to 1.2%.

The first step of the two-step automated commissioning process that relied on the PDD and dose profile measured data from the 10 cm x 10 cm field size was able to optimize the energy spectrum for the primary isotropic point source and secondary (extra-focal) photon sources, the relative fluence from the extra-focal source, and the relative dose contribution from the electron contamination source. The second step of the commissioning process optimized the horn-effect so that the calculation could accurately predict the increase in fluence as the off angle axis increased. For this step, the commissioning process used the dose profile measured data from the 40 cm x 40 cm field size. In addition, the extra-focal source model's energy distribution as described by Liu, et al<sup>30</sup> was implemented without modification. A correction to the output factor for a given field size was designed in response to the change in the fluence contribution that occurs with the change in field size from the extra-focal source. Similarly, a correction to account for the change in electron contamination with a change in the field size was designed to improve the build-up region and the depth of maximum dose. By combining these model attributes to represent the output of the linear accelerator, an accurate model for the Varian 10 MV photon beam using the DPM Monte Carlo method was able to faithfully calculate the basic beam data that comprised of open fields from 4 cm x 4 cm to 40 cm x 40 cm.

The validated source model with the DPM calculation was found to be accurate within 3% of the normalization dose and 2 mm distance to agreement of measurement under progressively more difficult benchmark conditions of IMRT and SBRT treatment techniques delivered to anthropomorphic phantoms where TLD and radiochromic film measurements were made. The accuracy of the source model calculation for the benchmark tests of an IMRT treatment delivered to the homogeneous head and neck phantom, a SBRT treatment delivered to the heterogeneous thorax phantom, and an IMRT treatment delivered to the heterogeneous thorax phantom ranged from 85% to 96% of the data tested at the gamma index of 3%/2mm.

To achieve the level of accuracy for the benchmark evaluations, an MLC model was developed to account for leaf transmission, interleaf leakage, and the rounded leaf ends. In addition, the implementation of an MLC offset of 0.4 mm to compensate for the finite size of the primary source and reproduce the measured penumbra was necessary for the model to meet the conditions of the accuracy defined. In this work we have demonstrated that with the use of the DPM Monte Carlo code, an accurate straightforward multiple-source model was developed for the Varian 10 MV photon beam using basic beam data.

## **Chapter 4 Patient Dose Comparisons: Varian 6 MV & 10 MV**

### **4.1 INTRODUCTION**

An obviously important quality assurance aspect of a clinical trial in radiotherapy is the ability to analyze the results of the advanced treatment being studied. The analysis is a difficult task because of the complexity of disease and the need to organize and track the information about a patient's treatment and follow-up evaluations over a period of time. A coordinated and efficient approach is required to provide a timely response to the treatment outcomes analysis. Steady progress of new technologies introduced into the clinic with the emphasis for their justification make it critical to ascertain if the patient is benefiting from the proposed advances. The Radiation Therapy Oncology Group (RTOG), intimately involved with clinical trials, is chartered with the task of evaluating the new methods of delivery with the ultimate goal of improving local and regional control, and survival.

Recent publications have focused on improving the outcome analysis process.<sup>34,63,64</sup> In these publications, the patients are from a single institution and rely on a single dose calculation algorithm, thus these variables are already minimized. Centralizing the patient data is an important first step to minimize and control the number of input variables used in the biological model. As part of the outcomes analysis process in clinical trials, dose distributions from the enrolled patients are from a multitude of participating institutions via the institution's dose calculation algorithm embedded within their treatment planning system. When all of the patient data from all of the institutions are combined, an outcome analysis assumes the dose data are correct. Participating institutions may use any number of different commercially available dose calculation algorithms to predict the patient's dose distribution. Additionally, each institution is responsible for creating an accurate beam model based on the algorithm.

Finally, institutions utilize linear accelerators from several manufactures and when combined with the different dose calculation algorithms, another layer of complexity is added.

One way to eliminate these variables and unify the patient dose distributions is to use a single independent dose calculation algorithm, such as the Monte Carlo (MC) method. Generally considered the most accurate method to determine dose, it has yet to see widespread use in the clinic for photon dose calculations mainly because of the intense amount of computational power necessary to perform the calculations. A drawback for the purposes of an independent method for use in clinical trials is that the MC method traditionally relies on detailed modeling of the treatment head. This process would have to be repeated for every linear accelerator type and energy and is dependent on the detail of the machine specification. Instead, a measurement-driven source model approach, such as the one described in Chapter 2 and Chapter 3, that applies parameterized analytical functions to describe the energy spectrum and distribution of primary and secondary photons and contaminant electrons provides a generic standard dose calculation methodology for any source and its resulting output, regardless of the type of accelerator. To date, this source model has been developed, validated, and benchmarked for the Varian 6 MV and 10 MV photon beams using the Dose Planning Method (DPM) Monte Carlo code as the dose calculation engine.

The mission of the Radiological Physics Center is to assure the NCI and the Cooperative Groups, such as the RTOG, that institutions participating in clinical trials deliver prescribed radiation doses that are clinically comparable and consistent. The RPC assists the study groups in developing protocols and QA procedures. Implementing the independent and generic source model DPM dose calculation algorithm for use by the RPC will enhance the way the clinical trial community performs retrospective dose calculations and outcomes analysis by assuring the dose data are correct.



## 4.2 MATERIAL AND METHODS

### 4.2.1 *Recalculations using DPM*

Source models were developed and validated for the Varian 6 MV and Varian 10 MV photon beams. The DPM code was used to perform the Monte Carlo dose calculations. The details of the source model development and validation were described in Chapter 2 (Varian 6 MV) and Chapter 3 (Varian 10 MV). The source model DPM calculation was applied to several patient cases. The purpose was to benchmark a commercial treatment planning system's dose calculation algorithm against the validated and benchmarked independent dose calculation tool in an effort to establish a baseline of what might be expected from a retrospective calculation study as part of the clinical trial outcomes analysis. The cases were selected from a database of past patient treatments that were previously planned on the Pinnacle treatment planning system (TPS) (version 7.6c, or higher) (Philips Medical Systems, Andover, MA). Common treatments that applied IMRT and SBRT to disease sites in water-like and low density tissue anatomy were studied. The test cases included treatments of the prostate, abdomen, and lung. Specifically, the recalculated treatments using the source model DPM calculation were:

- IMRT abdomen, 6 MV, 9 beams, 134 segments
- IMRT prostate, 10 MV, 9 beams, 93 segments
- SBRT lung, 6 MV, 7 beams, equivalent field size from 5.2 cm<sup>2</sup> to 5.8 cm<sup>2</sup>
- IMRT lung, 10 MV, 6 beams, 82 segments

Additionally, a useful exercise was performed to bridge the benchmarking of the independent dose calculation tool using the anthropomorphic phantoms to the recalculation of the patient plans. This exercise compared the DPM calculation to the TPS calculation of the phantom plans in the same way the comparisons were made from the patient plans. These analyses are described below.

The RTOG CT images and DICOM RT plan were exported from the Pinnacle treatment planning system and imported into CERR, the Computational Environment for Radiotherapy Research software platform (Washington University, St. Louis, MO), where the source model DPM calculations were performed on a Hewlett Packard ProLiant DL585 G5 Server with 16 AMD Opteron™ processors and 32GB of RAM. Each plan was simulated with 10 million photons per square centimeter defined at the isocenter plane so that the standard error of the mean was 1% for those voxels whose dose value was at least 50% of the maximum dose. The simulation applied low energy electron and photon cutoffs of 200 and 50 keV, respectively.

#### **4.2.2 Patient plan analysis**

The comparisons for each plan included quantifying the dose in the regions of interest, dose volume histograms, and 2D dose distributions that were evaluated using the gamma index method.<sup>48</sup> In addition, the same analysis was performed between Pinnacle and the source model DPM calculation for the measurement benchmark cases described in Chapter 2 and Chapter 3 that used the RPC head and neck and thorax phantoms. For the 2D dose distribution evaluation, the gamma criteria was 5% of the maximum dose and 3 mm distance to agreement to match the criteria applied by the RPC in their QA protocols. Presently, the gamma analysis erroneously considers the data outside the skin contour of the patient and artificially inflates the percentage of pixels meeting the criteria. Therefore, the gamma analysis was only meant to show where the regions of agreement and disagreement existed.

The procedure used to perform the patient IMRT quality assurance (QA) at MD Anderson was used on the IMRT head and neck 6 MV anthropomorphic phantom plan. The IMRT QA procedure used an ion chamber (IC) placed into a standard phantom (IMRT QA phantom, IBA Dosimetry America, Bartlett, TN) and located in the GTV where the standard deviation of the predicted dose within the volume of the IC was less than one percent as

reported by the TPS calculation. In addition, this procedure was repeated a second time with a second location selected for placement of the IC. The plan was also calculated for the second location. A comparison of the average ratios between the TPS calculation and the IC measurement and between the DPM calculation and IC measurement was made. To perform the DPM calculation, the QA phantom material (98% polystyrene, 2% titanium dioxide) was specified within the DPM code in order to obtain the material probability cross section data.

### 4.3 RESULTS

#### 4.3.1 Dose in region of interest

Table 21 shows the mean dose from several regions of interest for the patient treatment plans studied (prostate, abdomen, and lung), as well as the for the treatment plans delivered (head and neck and lung) to the anthropomorphic phantoms.

| Plan    | Treatment      | Energy | GTV   | PTV   | Critical Structure |
|---------|----------------|--------|-------|-------|--------------------|
| patient | IMRT abdomen   | 6      | 1.016 | 1.008 | 1.033 (kidney)     |
|         | SBRT lung      |        | 1.000 | 0.984 | 0.979 (cord)       |
|         | IMRT prostate  | 10     | 1.000 | 0.996 | 0.998 (femur)      |
|         | IMRT lung      |        | N/A   | 1.008 | 1.034 (carina)     |
| phantom | IMRT head/neck | 6      | 1.049 | N/A   | 1.198 (cord)       |
|         | SBRT lung      |        | 1.002 | 0.987 | 0.977 (heart)      |
|         | IMRT lung      |        | 1.015 | 1.010 | 1.014 (heart)      |
|         | IMRT head/neck | 10     | 1.019 | N/A   | 1.253 (cord)       |
|         | SBRT lung      |        | 0.990 | 0.974 | 0.999 (heart)      |
|         | IMRT lung      |        | 1.008 | 0.984 | 1.010 (heart)      |

Table 21 Ratio of TPS calculation to DPM calculation for mean dose to GTV, PTV, and critical structure for patient and phantom plans. Performance trends are similar as noted by SBRT plans

In all cases the difference in the mean dose to the gross target volume (GTV) and to planning target volume (PTV) between the calculations was within 2.6% except for the 6 MV

IMRT head and neck benchmark phantom plan. In this case the ratio of TPS calculation to DPM calculation was 1.049. Table 4 presented the results from the benchmark testing of this plan which showed the TPS calculation overestimated the dose to the TLD in the center of the GTV by 1.043 on average. In contrast, the DPM calculation underestimated the dose to the TLD by 0.983 on average. To understand the differences between the two calculations, the results of the IMRT QA procedure and the selected benchmark results from Table 4 are shown in Table 22.

| Comparison ratio | Phantom | Region    | Ratio |
|------------------|---------|-----------|-------|
| TPS/DPM          | H&N     | mean GTV  | 1.049 |
| TPS/TLD          | H&N     | point GTV | 1.043 |
| DPM/TLD          |         |           | 0.983 |
| TPS/IC           | QA      |           | 1.016 |
| DPM/IC           |         |           | 0.987 |

Table 22 Comparison of calculation and measurement in GTV for 6 MV IMRT head and neck plan. Benchmark phantom and IMRT QA phantom included.

It is clear from Table 22 the DPM calculation consistently underpredicted the dose for the 6 MV IMRT head and neck plan by a small amount (ratios of 0.983 and 0.987) regardless of the phantom used. While the TPS calculation slightly overpredicted the dose in the QA phantom (1.016), the overestimation to the benchmark anthropomorphic phantom was much greater (1.043). Relative to the TLD value, it was inferred that the ratio of the TPS to DPM was 1.061. This ratio was reasonable for the mean GTV when compared to the ratio between the TPS calculation and the DPM calculation of 1.049. The discrepancy between the anthropomorphic phantom and QA phantom used with the TPS calculation could reside within the specific plan as the other benchmark testing and patient studies did not exhibit this level of disagreement. While the 10 MV IMRT head and neck phantom plan revealed similar discrepancies, the disagreement was not the same magnitude. For this plan, the use of the DPM calculation would have provided a better correlation between the phantom plan and the QA plan and may be due

to the superior MC physics which included the detailed material specification of both phantoms. The independent dose calculation tool demonstrates the benefit of the MC calculation to accurately calculate the dose regardless of the heterogeneities involved.

#### ***4.3.2 Dose distribution analysis***

Dose volume histograms (DVHs), gamma maps, and dose profiles were generated for the patient treatment plans studied (prostate, abdomen, and lung), as well as the for the treatment plans delivered (head and neck and lung) to the anthropomorphic phantoms. The gamma map analysis method was applied to the patient treatment plans (prostate, abdomen, and lung), as well as for the anthropomorphic phantom treatment plans (head and neck and lung) for the axial plane in the center of the target for each plan evaluated. The gamma criteria were 5% of the maximum DPM dose and 3 mm distance-to-agreement. An associated CT scan image is provided for each gamma map. An arbitrary dose profile taken from the transverse slice is shown for each plan evaluated.

##### ***4.3.2.1 6 MV IMRT abdomen patient plan***

In Figure 4.1, the DVHs from the TPS and DPM calculations of a 6 MV IMRT abdomen patient case are shown for the PTV and the ipsilateral kidney. In general, The TPS calculation was similar to the DPM calculation, but tended to overestimate the dose similar to what was observed in Table 21. At the dose volume of 90% ( $D_{90}$ ) for the PTV, the TPS calculation reported a dose that was 2.4% greater than the DPM calculation. At  $D_{50}$  for the kidney, the TPS calculation reported a dose that was 3.4% greater than the DPM calculation.

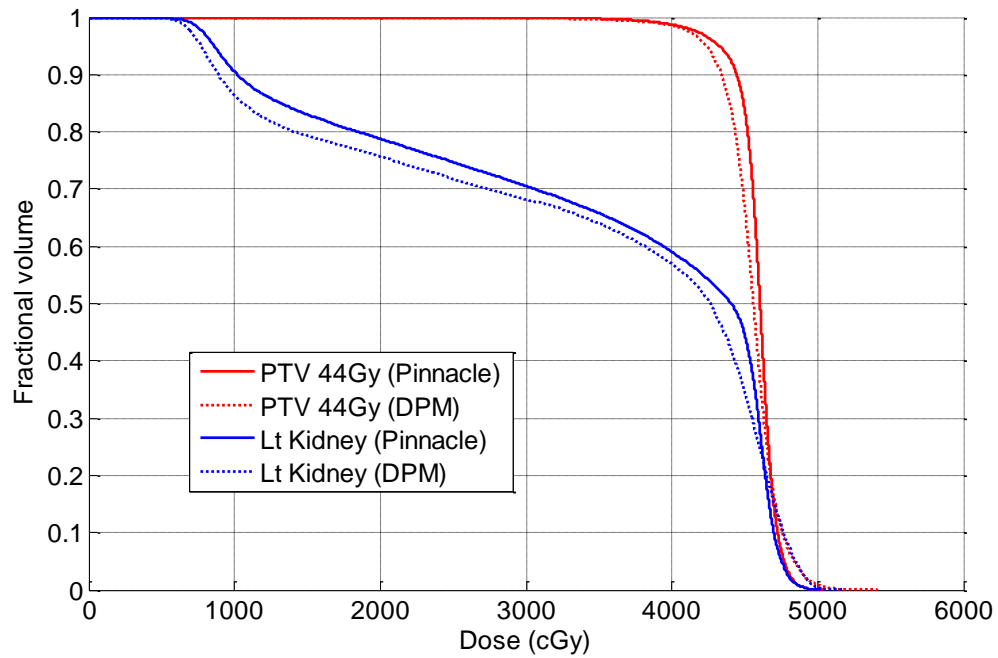


Figure 4.1 DVH of the 6 MV IMRT abdomen patient plan for the PTV and the left (Lt) kidney.

Figure 4.2 shows the gamma map of the axial CT image in the center of the PTV for the abdomen patient case between the TPS and DPM calculations. Disagreement occurred in some penumbra regions. The dose profile in Figure 4.3 showed the discrepancy in the dose calculations was random in the flat dose region.

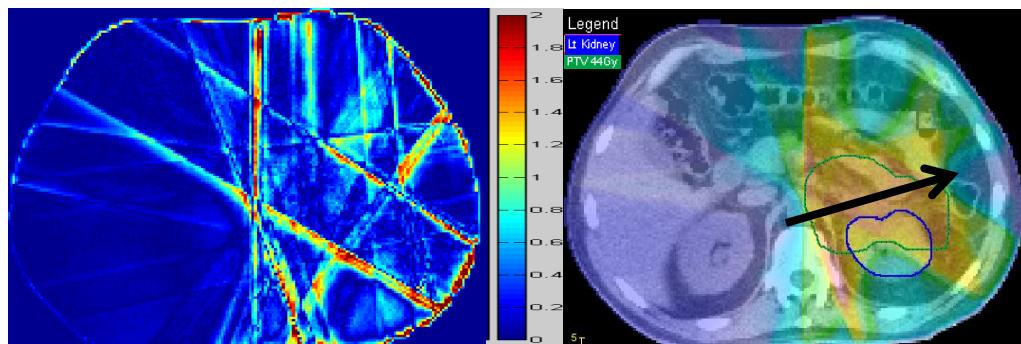


Figure 4.2 Gamma map (5%, 3mm) of the 6 MV IMRT abdomen patient plan and associated axial CT image with DPM calculated dose distribution. The black arrow shows the dose line profile in the CT image for Figure 4.3.

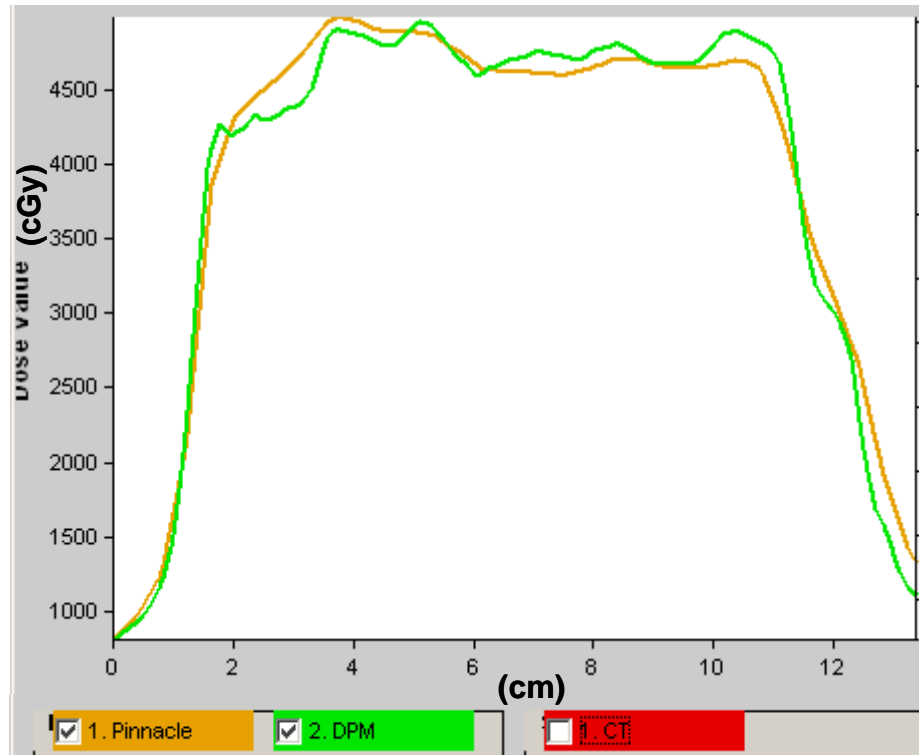


Figure 4.3 Dose (cGy) line profile comparing TPS and DPM calculations. Location of profile is shown in the CT image of Figure 4.2.

#### 4.3.2.2 6 MV SBRT lung patient plan

In Figure 4.4, the DVHs from the TPS and DPM calculations of a 6 MV SBRT lung patient case are shown for the GTV, PTV, ipsilateral lung, and the heart. The DVH comparisons of the GTV, lung, and heart were nearly the same. However, at  $D_{90}$  for the PTV, the TPS calculation reported a dose that was 2.6% less than the DPM calculation. This was consistent with the SBRT thorax phantom results shown below in Figure 4.16 and Figure 4.25.

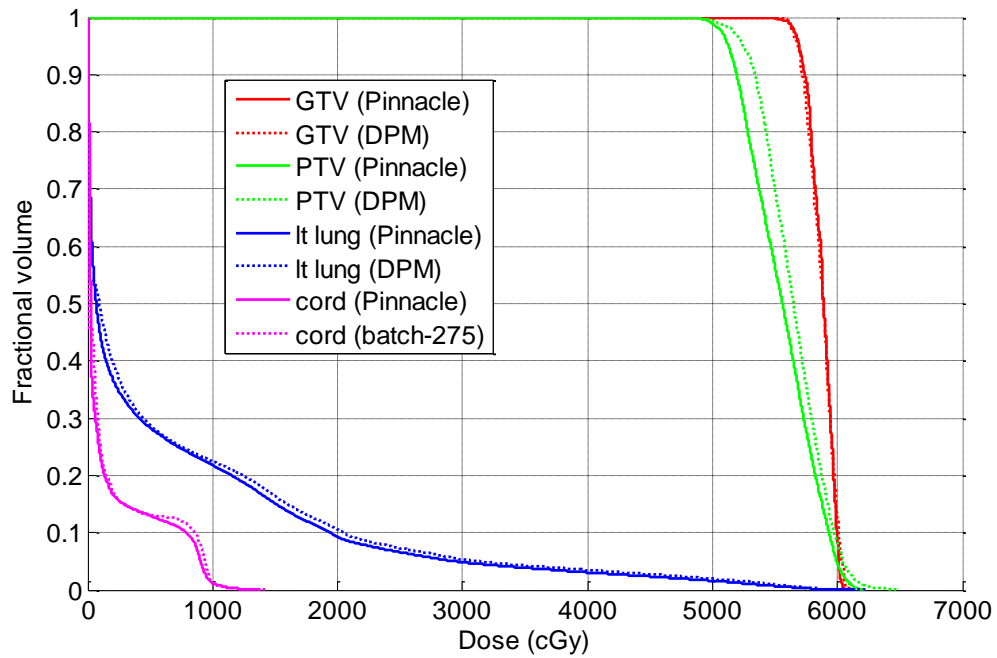


Figure 4.4 DVH of the 6 MV SBRT lung patient plan for the GTV, PTV, left (lt) kidney lung, and cord.

Figure 4.5 shows the gamma map of the axial CT image in the center of the PTV for the lung patient case between the TPS and DPM calculations. Disagreement occurred in some penumbra regions and at the skin surface. There was small disagreement in the low density lung region adjacent to the tumor which the dose profile in Figure 4.6 showed the DPM calculation predicted a wider penumbra.

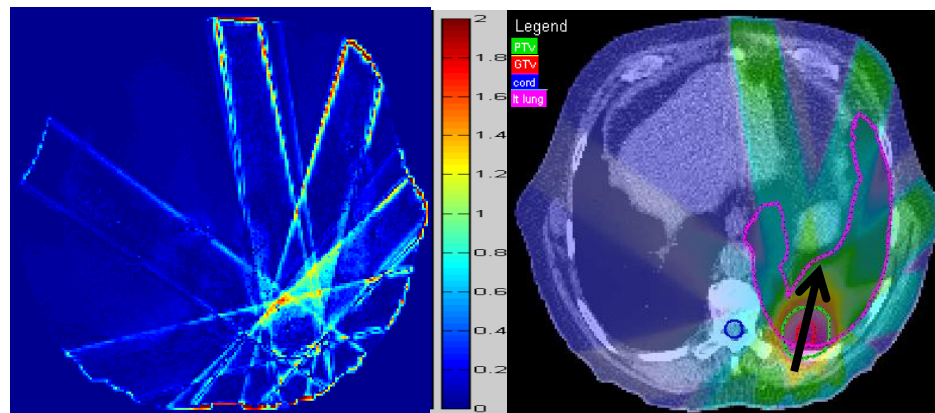


Figure 4.5 Gamma map (5%, 3mm) of the 6 MV SBRT lung patient plan and associated axial CT image with DPM calculated dose distribution. The black arrow shows the dose line profile in the CT image for Figure 4.6.



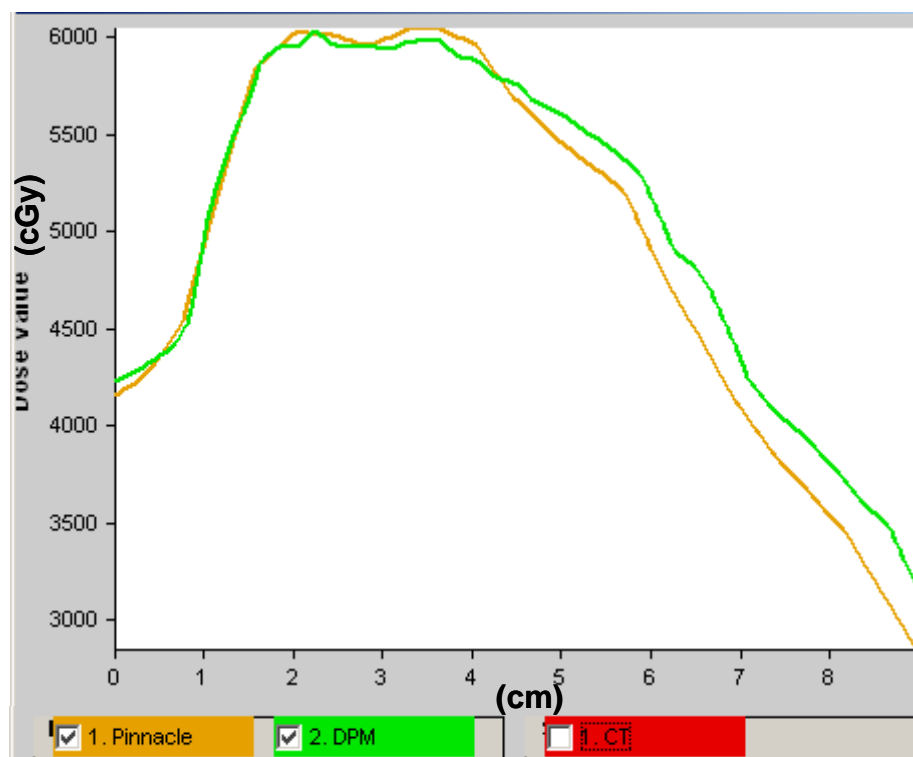


Figure 4.6 Dose (cGy) line profile comparing TPS and DPM calculations. Location of profile is shown in the CT image of Figure 4.5.

#### 4.3.2.3 10 MV IMRT prostate patient plan

In Figure 4.7, the DVHs from the TPS and DPM calculations of a 10 MV IMRT prostate patient case are shown for the PTV, the anus-rectum, and the right femoral head. The DVH comparisons were nearly the same. However, the maximum dose for the DPM calculation was 2.7% greater than for the TPS calculation. The dose difference to the PTV at  $D_5$  was 1.1%.

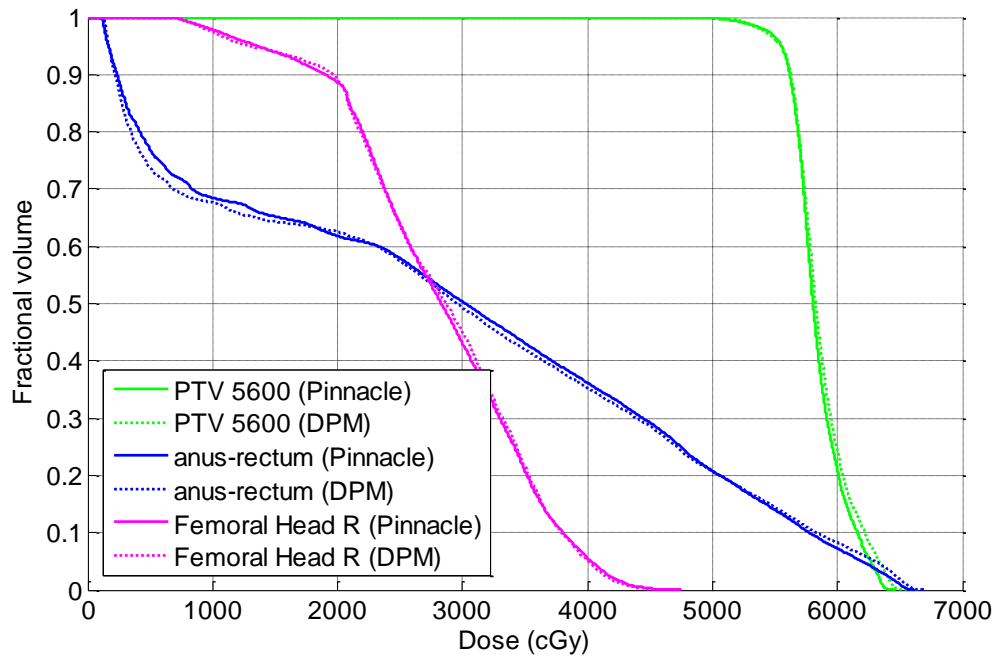


Figure 4.7 DVH of the 10 MV IMRT prostate patient plan for the PTV, anus-rectum, and the right (R) femoral head.

Figure 4.8 shows the gamma map of the axial CT image in the center of the PTV for the prostate patient case between the TPS and DPM calculations. Disagreement occurred in some penumbra regions and at the heterogeneous interfaces, but within the 5%/3 mm criterion. Otherwise, the disagreement occurred in the build-up region at the skin surface. The dose profile in Figure 4.9 showed the DPM calculation predicted sharper dose gradients at the bone/tissue interfaces as noted by the change in the CT value at this interface and about 2% less dose to the anus-rectum critical structure than the TPS calculation.

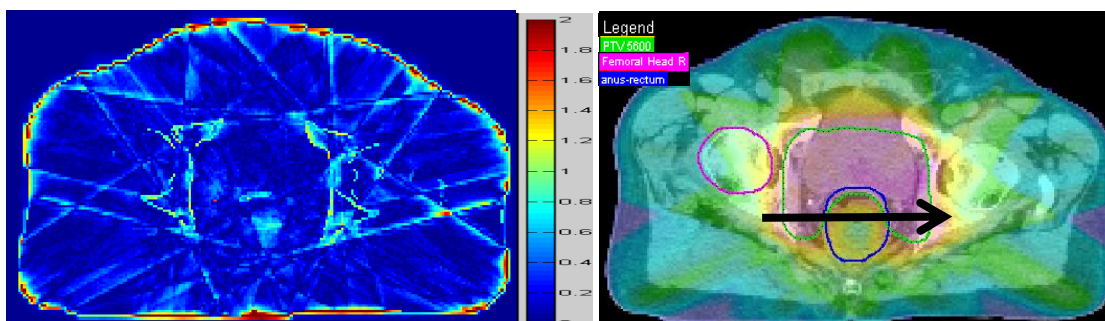


Figure 4.8 Gamma map (5%, 3mm) of the 10 MV IMRT prostate patient plan and associated axial CT image with DPM calculated dose distribution. The black arrow shows the dose line profile in the CT image for Figure 4.9.

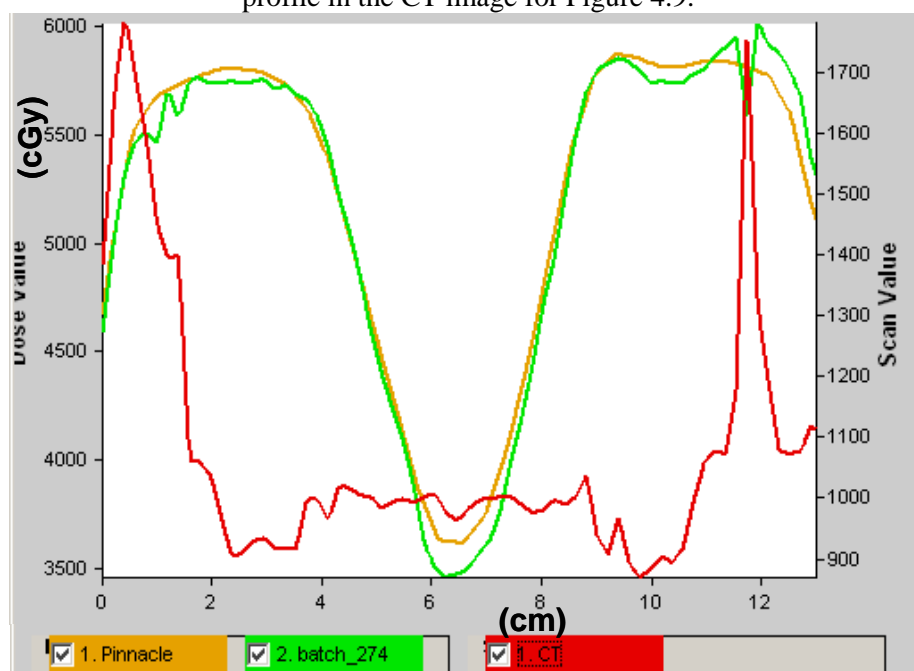


Figure 4.9 Dose (cGy) line profile comparing TPS and DPM calculations. Location of profile is shown in the CT image of Figure 4.8.

#### 4.3.2.4 10 MV IMRT lung patient plan

In Figure 4.10, the DVHs from the TPS and DPM calculations of a 10 MV IMRT lung patient case are shown for the PTV, carina, esophagus, and lungs. In general, the TPS calculation tended to estimate the dose higher than the DPM calculation. However, at  $D_{95}$  the DPM calculation was 3.0% higher and at  $D_{90}$  they were negligibly different. The largest difference in the DVH comparison of the PTV was between at  $D_{30}$  and  $D_{80}$ , and ranged from 1.1% to 1.3%. The  $D_{30}$  to  $D_{80}$  dose difference for the carina ranged from 3.6% to 7.0%. For the

esophagus, the largest dose differences ranged from 7.0% to 9.8% for the dose volumes between  $D_{10}$  and  $D_{40}$ . The dose to the lungs was consistently the same throughout the lung volume.

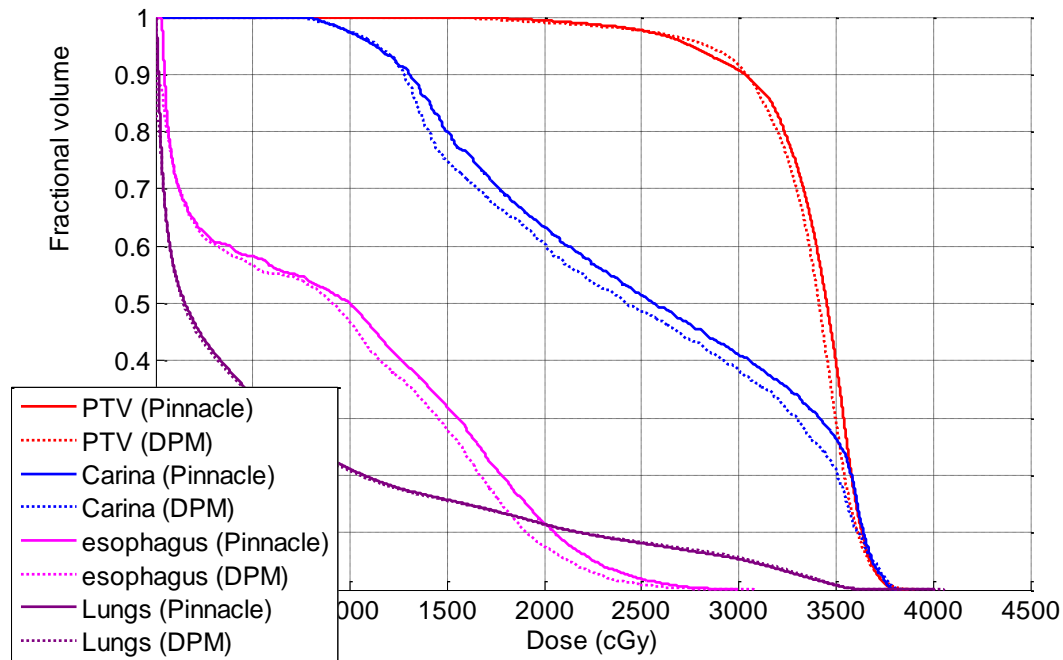


Figure 4.10 DVH of the 10 MV IMRT lung patient plan for the PTV, carina, esophagus, and the lungs.

Figure 4.11 shows the gamma map of the axial CT image in the center of the PTV for the lung patient case between the TPS and DPM calculations. Similar to the results of all of the treatment plans, disagreement occurred at the skin surface as well in the beam penumbra regions. The shape of the tumor was irregular so that a small volume of lung tissue was nearly surrounded by the tumor. In this region, differences between the two calculations existed. The dose profile in Figure 4.12 showed that only the DPM calculation predicted the build-down in dose within the small volume of lung that was circumscribed by the tumor. The CT values reported this small region to be that of air and accordingly, the Monte Carlo code used the

stopping power values of dry air in computing the dose. This would explain the large difference in this region.

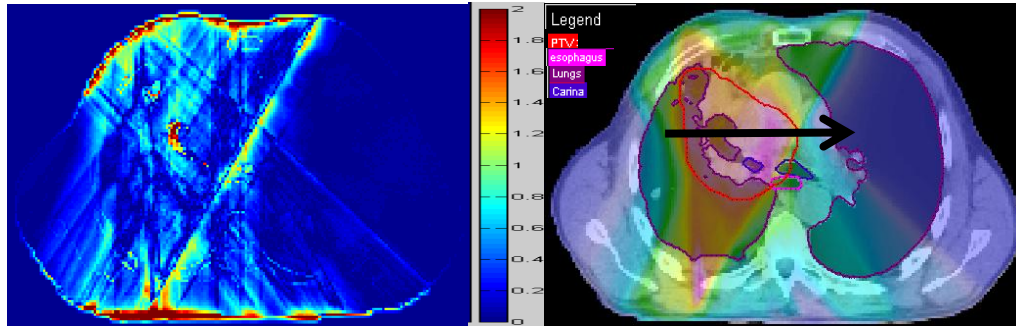


Figure 4.11 Gamma map (5%, 3mm) of the 10 MV IMRT lung patient plan and associated axial CT image with DPM calculated dose distribution. The black arrow shows the dose line profile in the CT image for Figure 4.12.

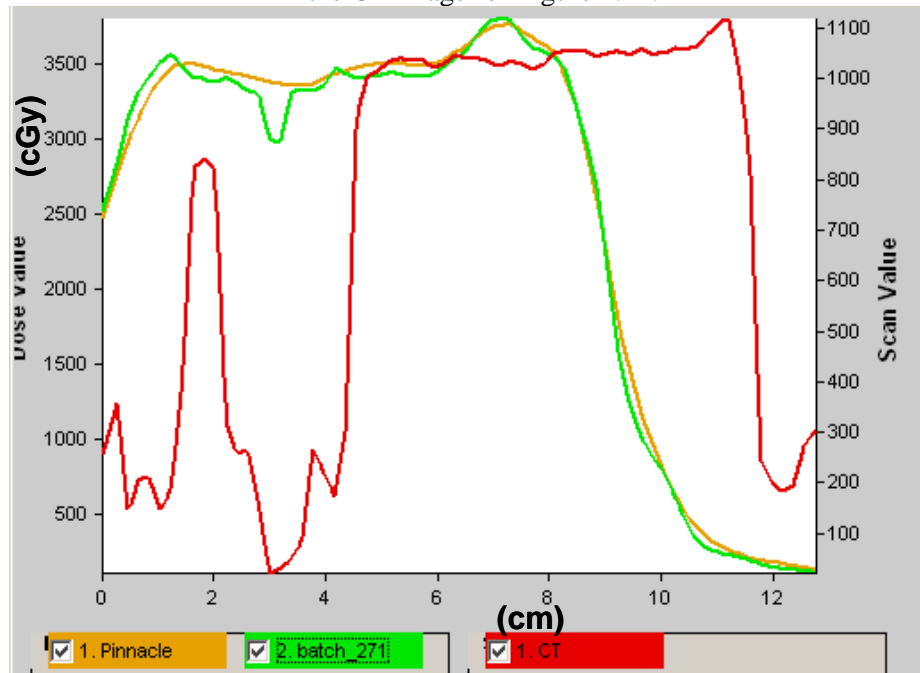


Figure 4.12 Dose (cGy) line profile comparing TPS and DPM calculations. Location of profile is shown in the CT image of Figure 4.11.

#### 4.3.2.5 6 MV IMRT head and neck phantom plan

In Figure 4.13, the DVHs from the TPS and DPM calculations of the 6 MV IMRT head and neck phantom benchmark are shown for the primary PTV, secondary PTV, and spinal cord critical structure (CS). Large differences were noted between the two calculations. For the primary target, the dose difference ranged from 4.8% at  $D_{50}$  to 6.7% at  $D_{95}$ . For the secondary

target, the dose difference ranged from 3.8% at  $D_{50}$  to 4.3% at  $D_{95}$ . The dose to the CS which was in close proximity to the primary target and in a dose gradient region was nearly the same for both calculations until approximately  $D_{50}$ . From  $D_{20}$  to  $D_{50}$  the TPS calculation overestimated the dose by about 18% in the critical structure.

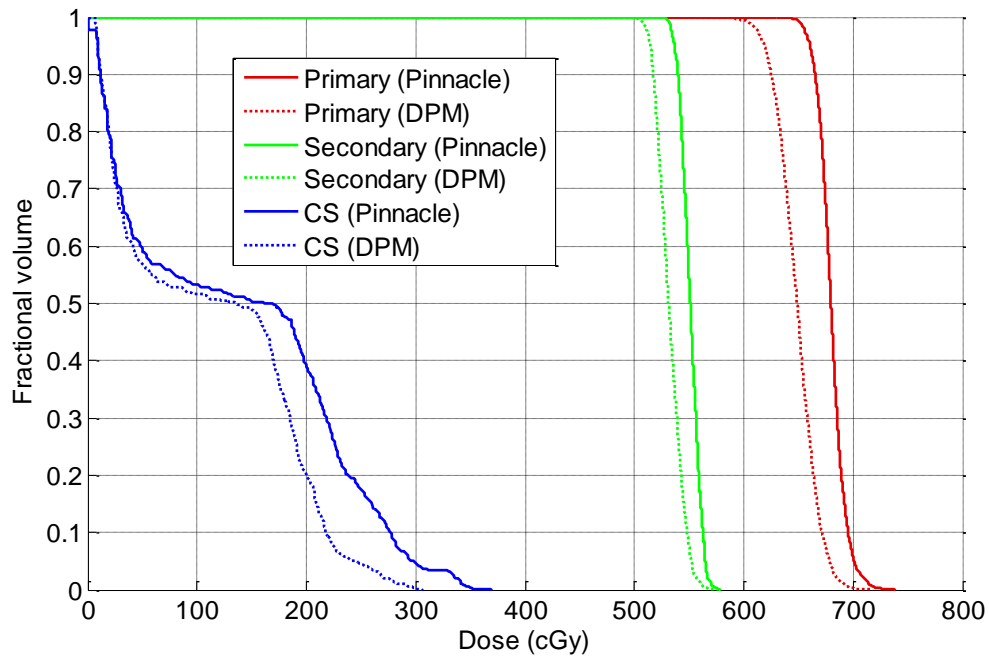


Figure 4.13 DVH of the 6 MV IMRT head and neck phantom plan for the primary, secondary, and the cord (CS).

Figure 4.14 shows the gamma map of the axial CT image in the center of the PTV for the head and neck phantom plan between the TPS and DPM calculations. The gamma map showed disagreement within the polystyrene insert which included the solid water targets and the acrylic critical structure (refer to Figure 2.4 (a)) as well as the build-up region of the phantom surface. The disagreement within the insert was beyond the 5%/3 mm criterion in the beam penumbra regions and in the primary target adjacent to the critical structure. This was expected based on the IMRT quality assurance results that were detailed in Section 4.3.1 by studying point dose information in the PTV. Table 21 and Table 22 showed the ratio between the TPS calculation and the DPM calculation in the center of the primary target was 1.049

(mean primary target ratio was 1.043). The dose profile in Figure 4.15 showed that the TPS calculation overestimated the dose in the plan across the primary and secondary targets in the range of 2% to 6%.

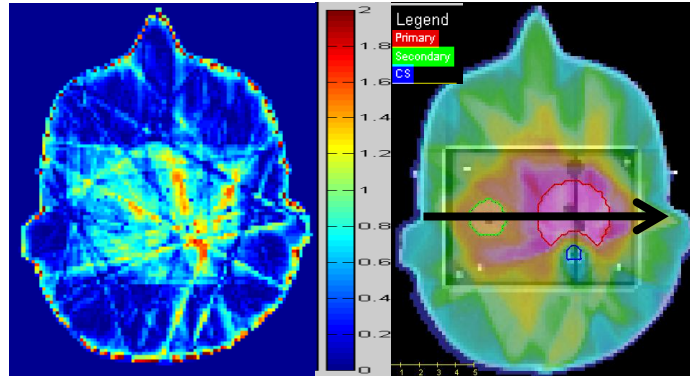


Figure 4.14 Gamma map (5%, 3mm) of the 6 MV IMRT head and neck phantom plan and associated axial CT image with DPM calculated dose distribution. The black arrow shows the dose line profile in the CT image for Figure 4.15.

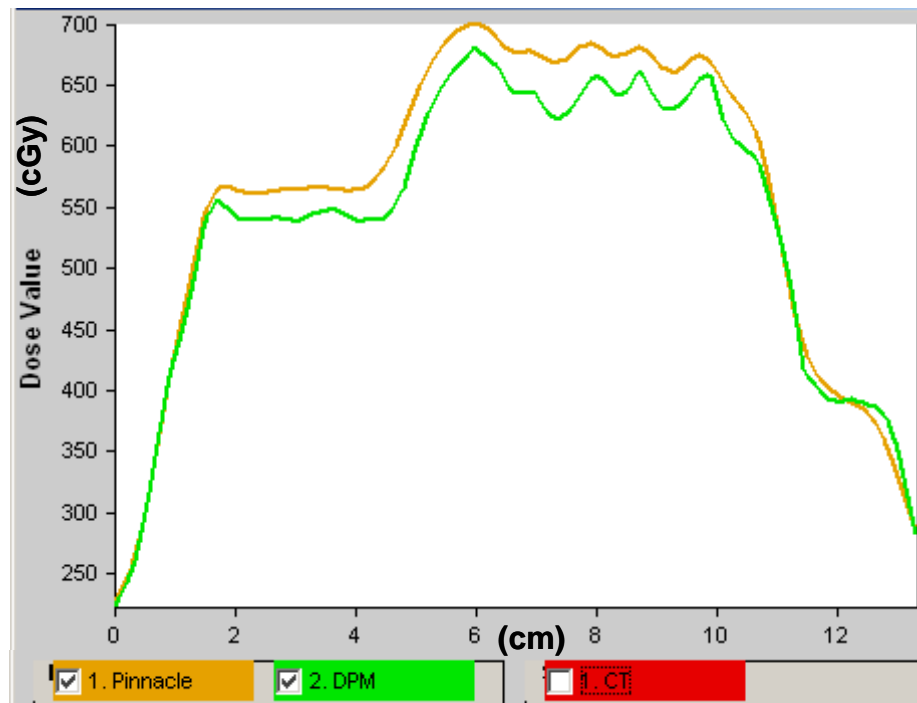


Figure 4.15 Dose (cGy) line profile comparing TPS and DPM calculations. Location of profile is shown in the CT image of Figure 4.14.

#### 4.3.2.6 6 MV SBRT lung phantom plan

In Figure 4.16, the DVHs from the TPS and DPM calculations of the 6 MV SBRT lung phantom benchmark are shown for the target, PTV, ipsilateral lung, and heart. While the target, lung, and heart DVHs between the two calculations were nearly identical, the TPS underestimated the dose in the PTV. The dose differences ranged from 2.6% to 3.8% for the  $D_{70}$  to  $D_{95}$  portions of the PTV, respectively. The behavior of the DVH for the PTV was the same for the SBRT patient case presented in Figure 4.4 above. Since the delivery was static using 9 coplanar beams equally spaced and conformed to simple shaped target, the difference can be attributed to a wider dose penumbra for the DPM calculation.

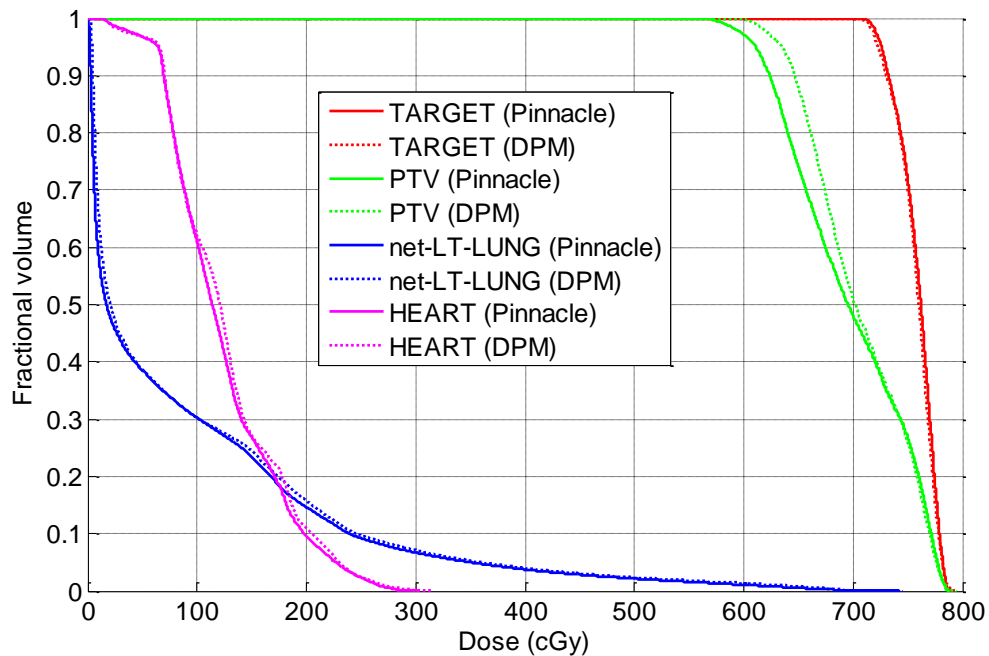


Figure 4.16 DVH of the 6 MV SBRT lung phantom plan for the target, PTV, left (LT) lung (net), and the heart.

Figure 4.17 shows the gamma map of the axial CT image in the center of the PTV for the lung phantom plan between the TPS and DPM calculations. Disagreement within the 5%/3



mm criteria occurred in some penumbra regions and at the skin surface. The dose profile in Figure 4.18 showed the DPM calculation predicted a slightly wider penumbra.

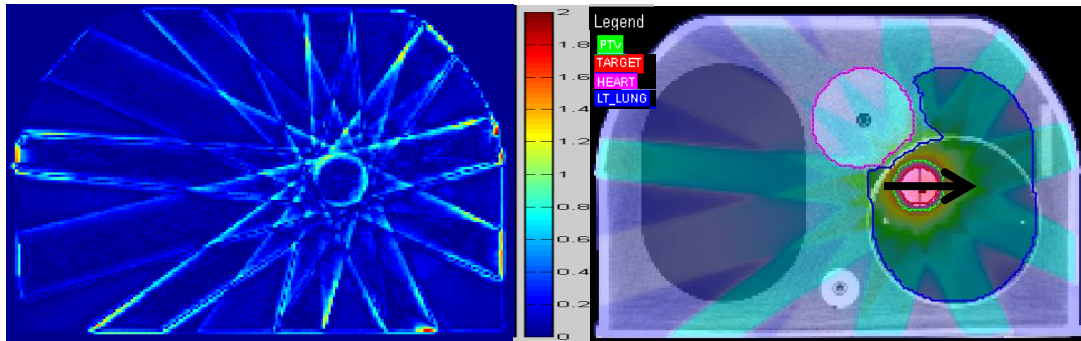


Figure 4.17 Gamma map (5%, 3mm) of the 6 MV SBRT lung phantom plan and associated axial CT image with DPM calculated dose distribution. The black arrow shows the dose line profile in the CT image for Figure 4.18.

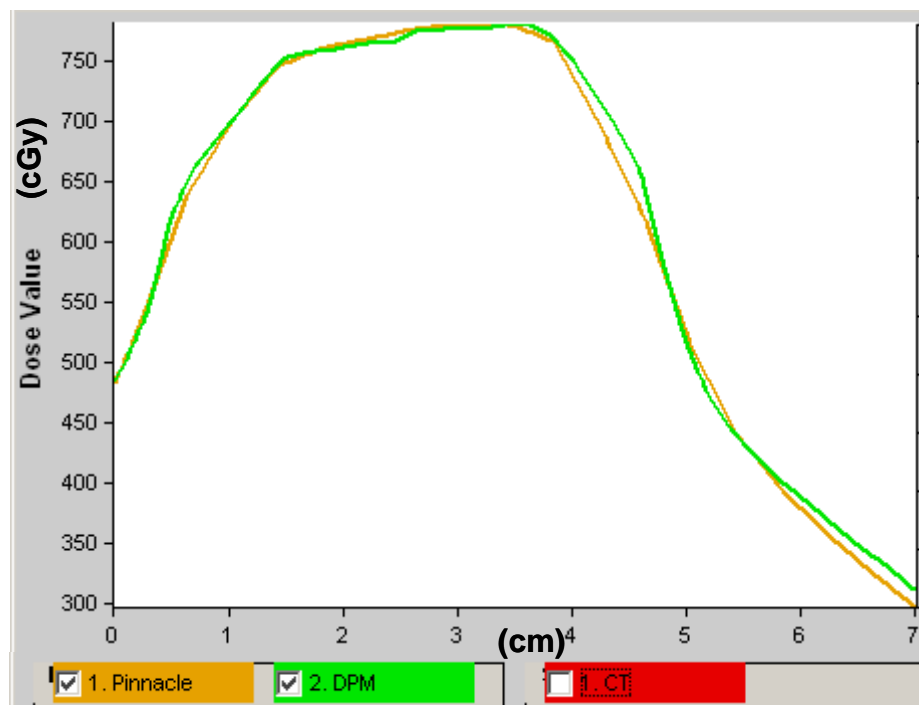


Figure 4.18 Dose (cGy) line profile comparing TPS and DPM calculations. Location of profile is shown in the CT image of Figure 4.17.

#### 4.3.2.7 6 MV IMRT lung phantom plan

In Figure 4.19, the DVHs from the TPS and DPM calculations of the 6 MV IMRT lung phantom benchmark are shown for the GTV, PTV, ipsilateral lung, and heart. For this plan, the TPS calculation tended to overestimate the dose to the target relative to the DPM calculation. Dose differences for the GTV were less than 2.4% and for the PTV less than 1.4%. Dose predictions for the critical structures were similar.

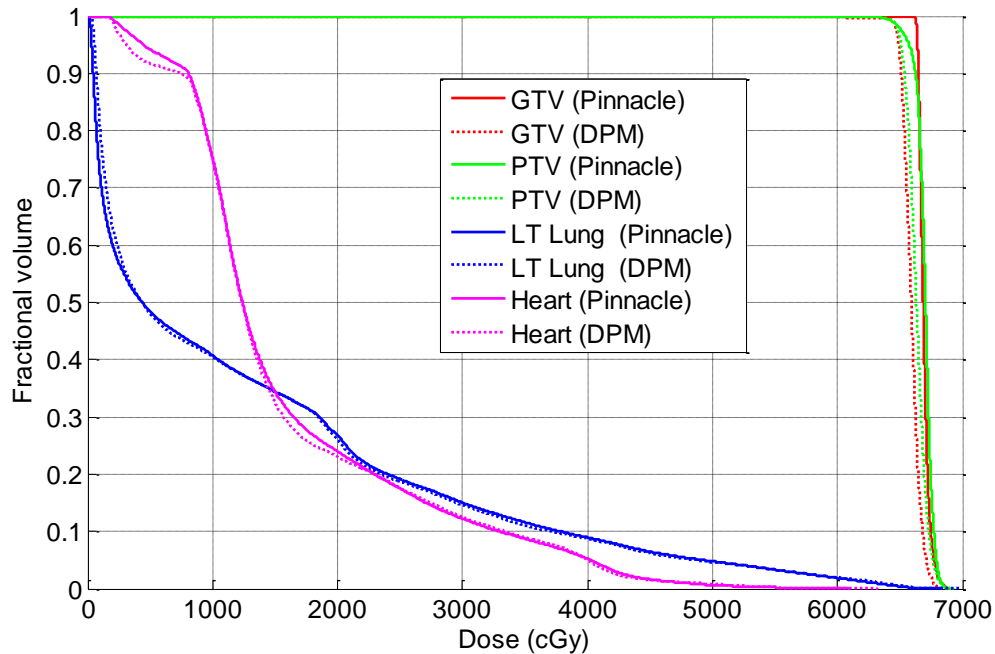


Figure 4.19 DVH of the 6 MV IMRT lung phantom plan for the GTV, PTV, left (LT) lung, and the heart.

Figure 4.20 shows the gamma map of the axial CT image in the center of the PTV for the lung phantom plan between the TPS and DPM calculations. Disagreement beyond the 5%/3 mm criteria occurred in some penumbra regions and at the skin surface. The dose profile in Figure 4.21 showed the DPM calculation predicted a slightly narrower penumbra in the low dose lung region. The TPS calculation for the IMRT lung plan did not show the same penumbra effect relative to the DPM calculation as was presented in the static SBRT lung plans

(4.3.2.2 and 4.3.2.6). This may have been an indication that the modulated IMRT treatment plan minimized inaccuracies in the TPS MLC model.

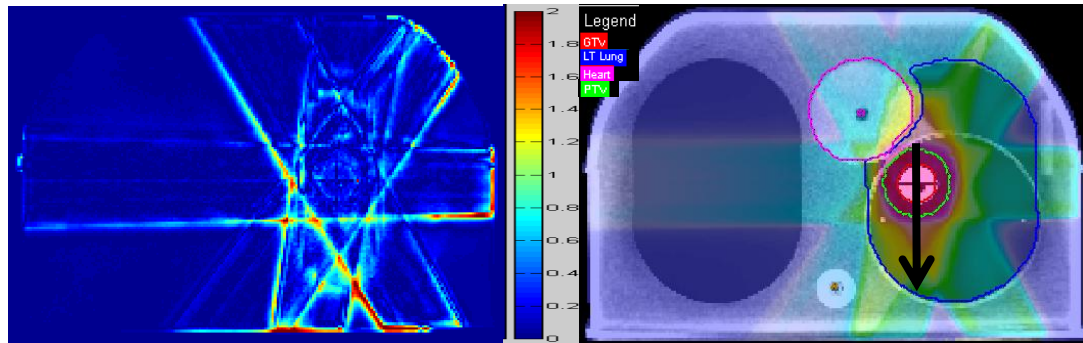


Figure 4.20 Gamma map (5%, 3mm) of the 6 MV IMRT lung phantom plan and associated axial CT image with DPM calculated dose distribution. The black arrow shows the dose line profile in the CT image for Figure 4.21.

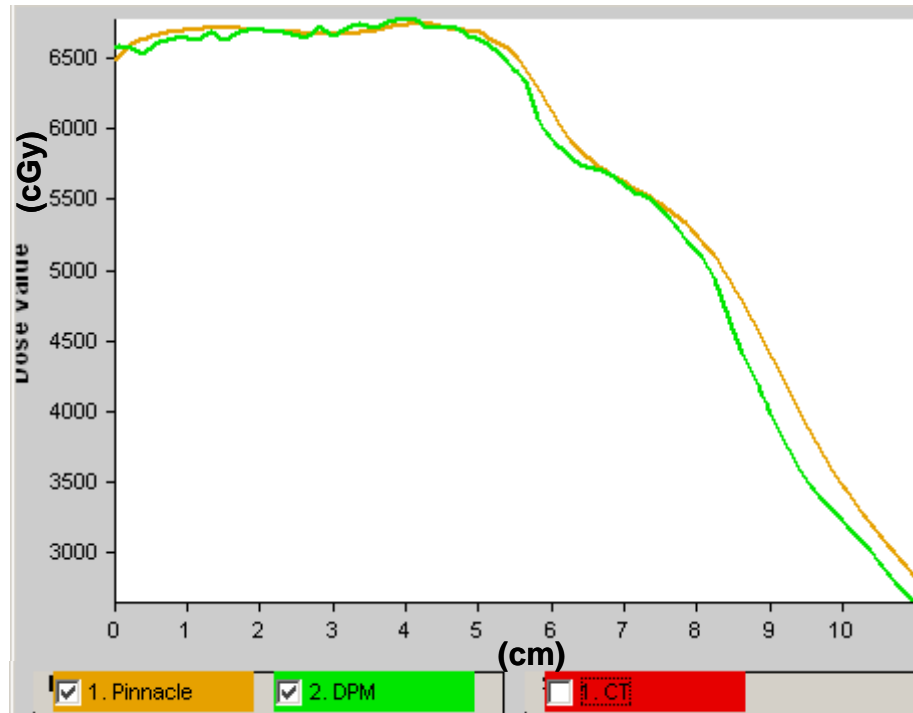


Figure 4.21 Dose (cGy) line profile comparing TPS and DPM calculations. Location of profile is shown in the CT image of Figure 4.20.

#### 4.3.2.8 10 MV IMRT head and neck phantom plan

In Figure 4.22, the DVHs from the TPS and DPM calculations of the 10 MV IMRT head and neck phantom benchmark are shown for the primary PTV, secondary PTV, and spinal

cord critical structure (CS). Similar to the 6 MV IMRT head and neck phantom DVH results, large differences were noted between the two calculations. For the primary target, the dose difference ranged from 2.0% at  $D_{50}$  to 5.5% at  $D_{95}$ . For the secondary target, the dose difference ranged from 3.4% at  $D_{50}$  to 5.8% at  $D_{95}$ . The dose to the CS was nearly the same for both calculations until approximately  $D_{40}$ . From  $D_{10}$  to  $D_{30}$  the TPS calculation overestimated the dose by about 25% in the critical structure, which was in a high dose gradient region in close proximity to the primary target.

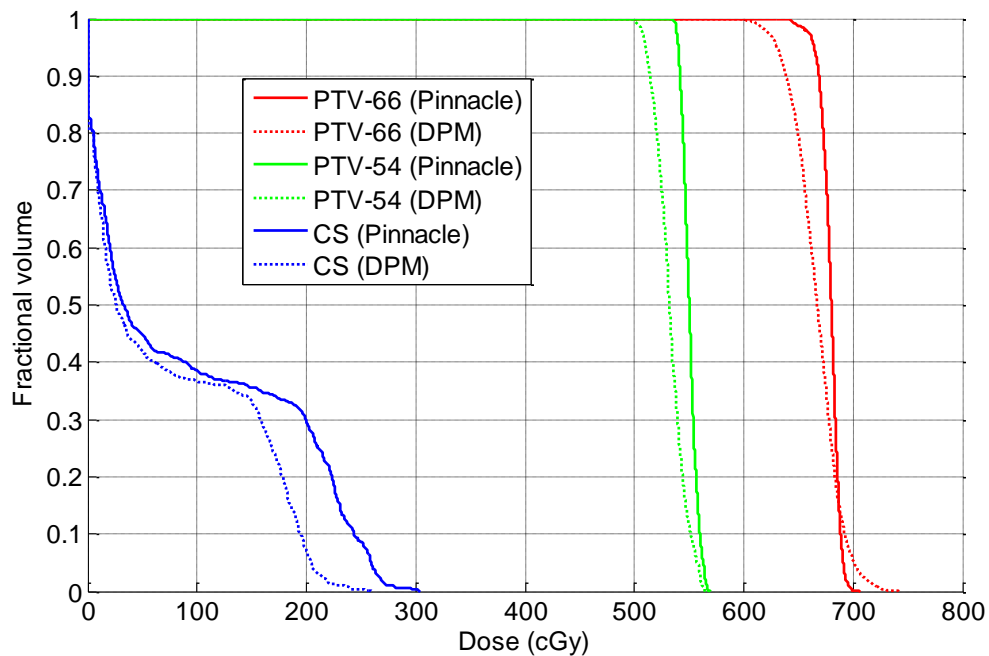


Figure 4.22 DVH of the 10 MV IMRT head and neck phantom plan for the primary (PTV-66), secondary (PTV-54), and the cord (CS).

Figure 4.23 shows the gamma map of the axial CT image in the center of the PTV for the head and neck phantom plan between the TPS and DPM calculations. The gamma map showed disagreement within the polystyrene insert which included the solid water targets and the acrylic critical structure (refer to Figure 2.4 (a)) as well as the build-up region of the phantom surface. Disagreement was within the 5%/3 mm criterion in the beam penumbra regions, except in the adjacent region between the primary target and critical structure where

the disagreement exceeded the criterion. Recall, Table 21 and Table 22 showed the ratio between the TPS calculation. Disagreement was also noted at the skin surface as this was a common result regardless of the plan evaluated. The dose profile in Figure 4.24 showed that the TPS calculation overestimated the dose and did not predict the small dose gradients that existed in both targets.

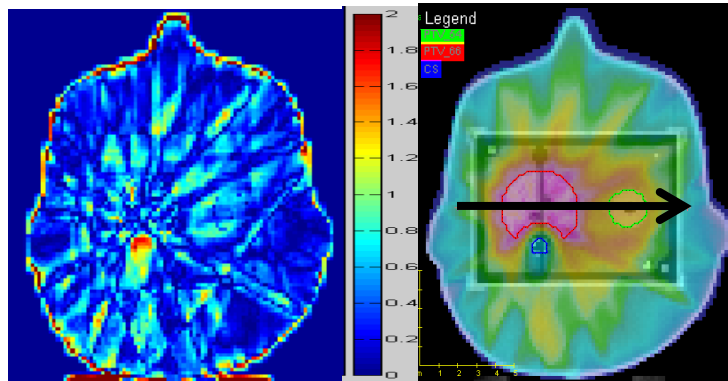


Figure 4.23 Gamma map (5%, 3mm) of the 10 MV IMRT head and neck phantom plan and associated axial CT image with DPM calculated dose distribution. The black arrow shows the dose line profile in the CT image for Figure 4.24.

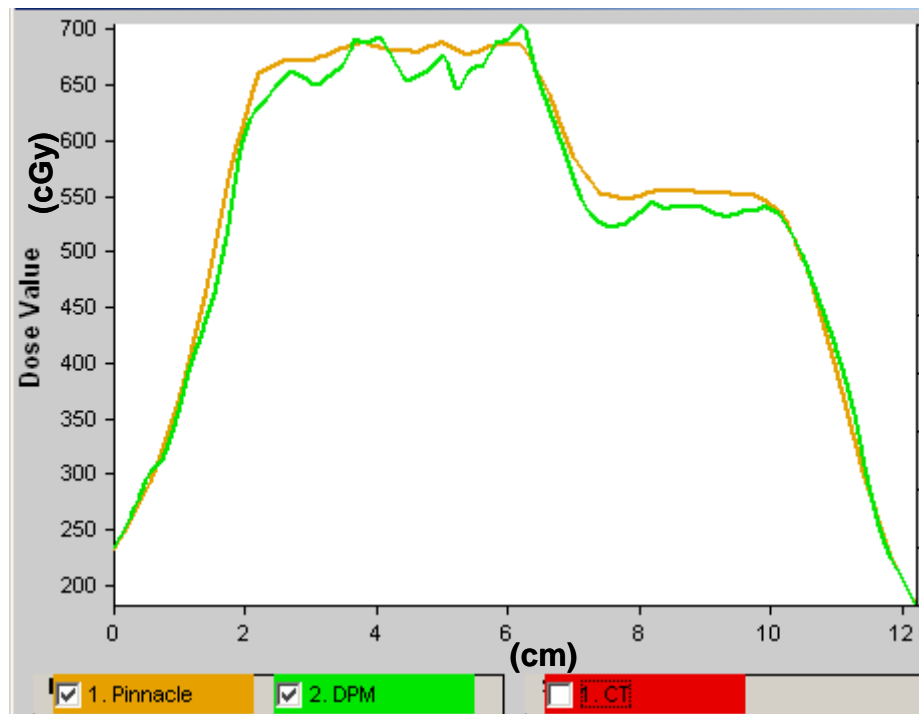


Figure 4.24 Dose (cGy) line profile comparing TPS and DPM calculations. Location of profile is shown in the CT image of Figure 4.23.

#### 4.3.2.9 10 MV SBRT lung phantom plan

In Figure 4.25, the DVHs from the TPS and DPM calculations of the 10 MV SBRT lung phantom benchmark are shown for the target, PTV, ipsilateral lung, and heart. While the target, lung, and heart DVHs between the two calculations were nearly identical, the TPS underestimated the dose in the PTV. The dose differences ranged from 3.7% to 6.8% for the  $D_{70}$  to  $D_{95}$  portions of the PTV, respectively. The DVH for the PTV showed a similar pattern to the 6 MV SBRT patient case presented in Figure 4.4 above. Since the delivery was static using 9 coplanar beams equally spaced and conformed to simple shaped target, the difference can be attributed to a wider dose penumbra for the DPM calculation.

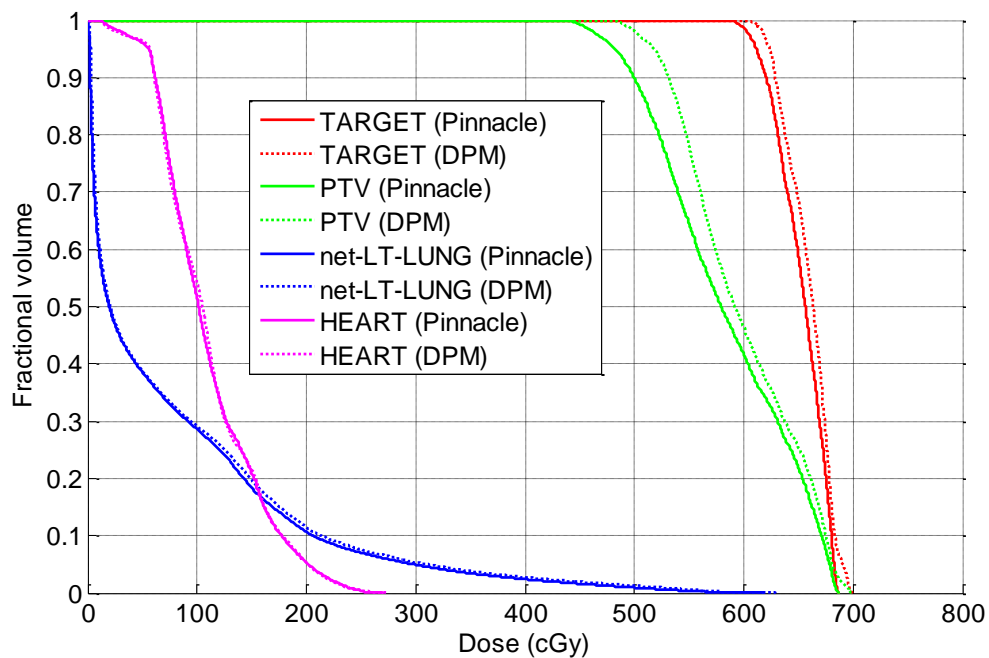


Figure 4.25 DVH of the 10 MV SBRT lung phantom plan for the target, PTV, left (LT) lung (net), and the heart.

Figure 4.26 shows the gamma map of the axial CT image in the center of the PTV for the lung phantom plan between the TPS and DPM calculations. Disagreement within the 5%/3 mm criteria occurred in some penumbra regions. The dose profile in Figure 4.27 showed the

DPM calculation predicted a slightly wider penumbra similar to the results of the 6MV SBRT lung phantom and patient plans.

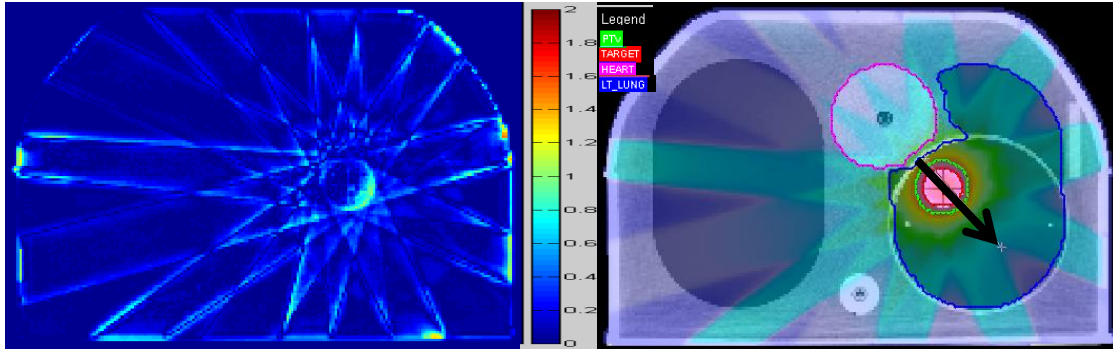


Figure 4.26 Gamma map (5%, 3mm) of the 10 MV SBRT lung phantom plan and associated axial CT image with DPM calculated dose distribution. The black arrow shows the dose line profile in the CT image for Figure 4.27.

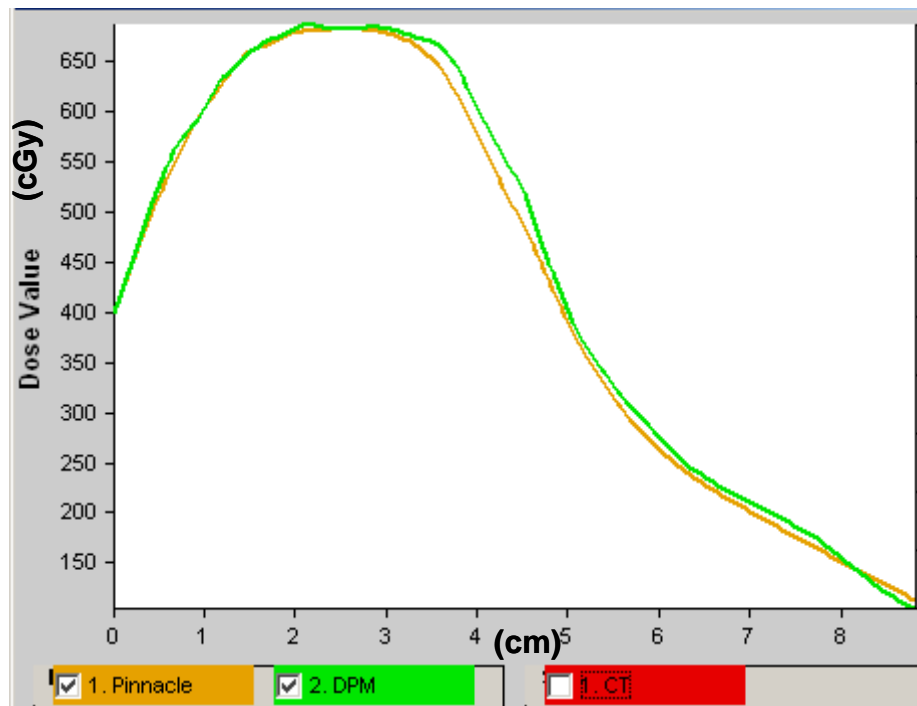


Figure 4.27 Dose (cGy) line profile comparing TPS and DPM calculations. Location of profile is shown in the CT image of Figure 4.26.

In Figure 4.28, the DVHs from the TPS and DPM calculations of the 10 MV IMRT lung phantom benchmark are shown for the target, PTV, ipsilateral lung, and heart. For this plan, the TPS calculation tended to overestimate the dose to the target by less than 1.7%

relative to the DPM calculation. However, the TPS calculation underestimated the dose in the PTV penumbra region by up to 2.7%. The DVH dose predictions for the critical structures for both dose calculations were similar.

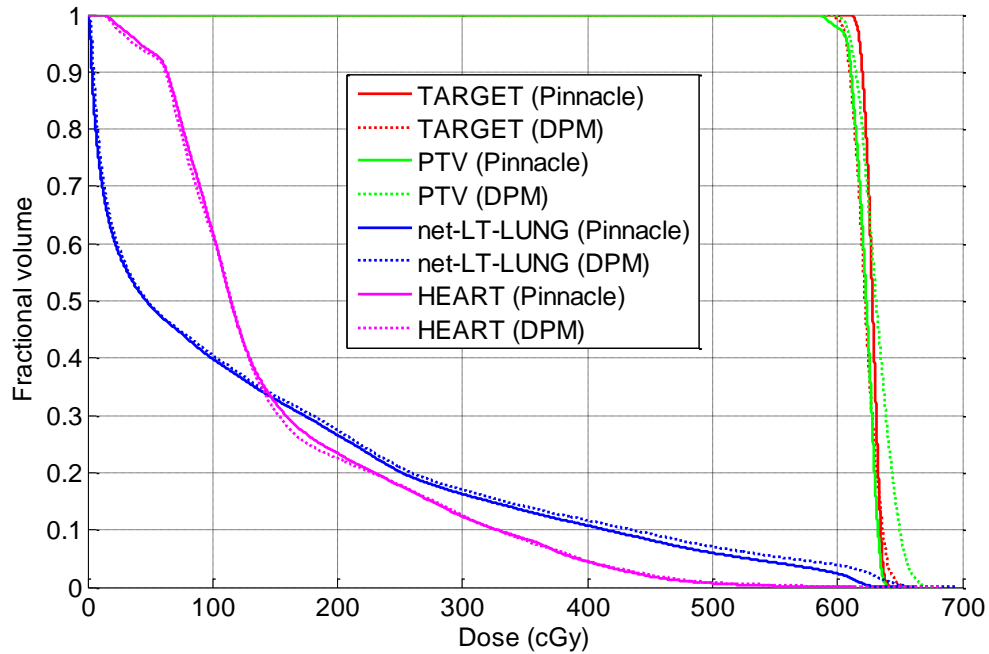


Figure 4.28 DVH of the 10 MV IMRT lung phantom plan for the target, PTV, left (LT) lung (net), and the heart

Figure 4.29 shows the gamma map of the axial CT image in the center of the PTV for the lung phantom plan between the TPS and DPM calculations. Some disagreement also occurred in the lung region adjacent to the target heterogeneity boundary. This effect may be attributed to the superior physics modeling inherent in the Monte Carlo code. The effect was not observed in the 6 MV SBRT and 6 MV IMRT phantom plans, but was noted in the lung patient plans and to a lesser extent in the 10 MV SBRT lung phantom plan. The dose profile in Figure 4.30 showed the DPM calculation predicted a wider penumbra and a high dose at the target/lung interface than the TPS calculation. The higher dose at the interface was observed in the measurement of the lateral dose profile (Figure 3.29).



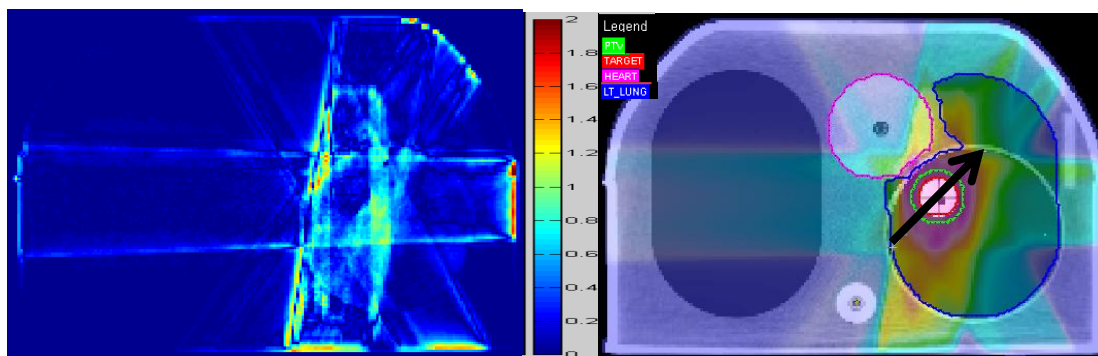


Figure 4.29 Gamma map (5%, 3mm) of the 10 MV IMRT lung phantom plan and associated axial CT image with DPM calculated dose distribution. The black arrow shows the dose line profile in the CT image for Figure 4.30.

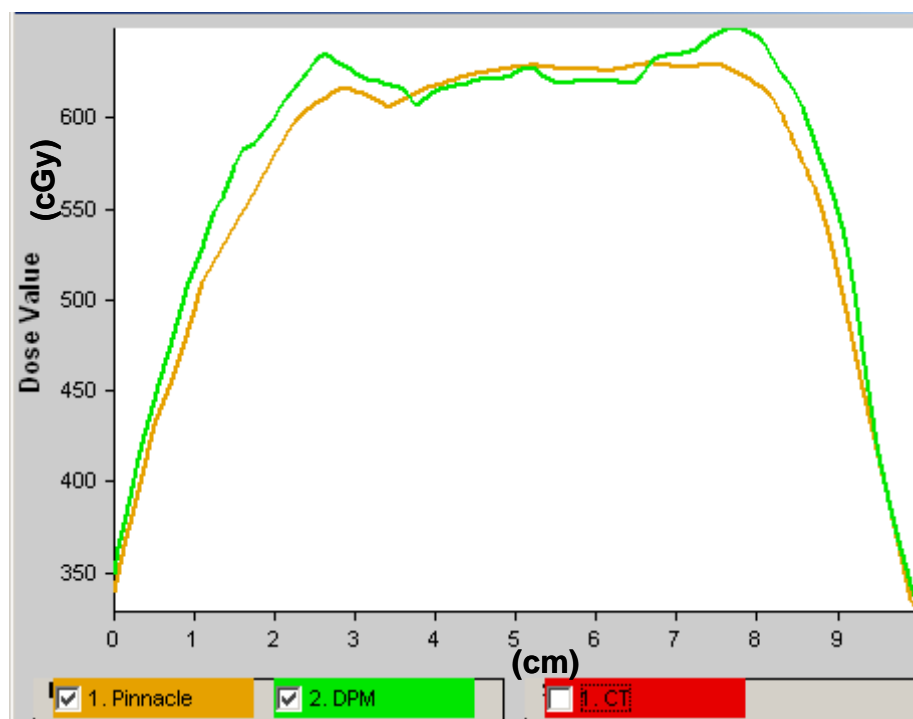


Figure 4.30 Dose (cGy) line profile comparing TPS and DPM calculations. Location of profile is shown in the CT image of Figure 4.29.

## **Chapter 5 Summary**

### **5.1 CHAPTER 2 AND CHAPTER 3 SUMMARY FOR VARIAN MACHINE MODELS**

The source model was developed for the Varian 6 MV (Chapter 2) and 10 MV (Chapter 3) linear accelerators. The models were validated against basic beam measurements. Percent depth dose curves and lateral beam profiles were calculated and compared to measurements for field sizes of 4 cm x 4 cm to 40 cm x 40 cm in water. The DPM Monte Carlo calculations agreed well with measurements tested to criteria of 2% of the maximum dose along the central axis and 2 mm distance to agreement. At least 95% of the data tested met the criteria. Additional testing compared local differences between the calculation and measurement. For the 6 MV and 10 MV source models, the average local percent difference along the central axis was no more than 2.0% and was less than 1.5% for field sizes below 20 cm x 20 cm. The average local percent differences of the off-axis doses (greater than or equal to 80% of the central axis dose) was no more than 1.3% for the field sizes tested.

The validated source model was benchmarked against a variety of treatment techniques using anthropomorphic phantoms. Point dose, dose profiles, and 2-D dose distributions were used to compare the DPM Monte Carlo calculation to TLD and radiochromic film measurements. The 2-D dose distributions from the calculation and measurement were tested to criteria of 3% of the target center dose and 2 mm distance to agreement. At least 85% of the data tested met the criteria.

## **5.2 CHAPTER 4 SUMMARY, PATIENT PLANS**

The validated source model with the DPM Monte Carlo code was applied to patient cases to establish a baseline of what might be expected from a retrospective calculation study as part of the clinical trial outcomes analysis. To perform this study, a commercial treatment planning system's (TPSs) dose calculation that was commissioned and used separately by two institutions was benchmarked against the DPM calculation. In a parallel effort, a proof of principle study was performed in a similar manner to the patient cases, but was performed on the same anthropomorphic phantom plans used in the benchmarking of the source model with DPM calculation presented in Chapter 2 and Chapter 3. In this way, the results between the DPM calculation and the TPS calculation were more interpretable since measurements were made.

In general, the TPS calculation and DPM calculation performed similarly. The mean dose to the GTV for the patient and phantoms cases were within 2% of one another, except for the 6 MV IMRT head and neck phantom plan which was nearly 5%. The IMRT QA for the head and neck phantom plan revealed consistency from the DPM calculation, however a discrepancy of about 3% existed between the plan and the QA TPS calculations. The results from this plan reinforced the superior physics inherent with the Monte Carlo code and suggested there are plans that the TPS calculation is not capable of providing accurate dose distribution predictions.

Although typically within the criteria of 5%/3 mm, the beam penumbra regions had the greatest differences between the TPS and DPM calculated doses. Dose changes at the heterogeneous boundaries were more prominent with the DPM calculation. The TPS calculation reported the dose in these transitions more smoothly. The Monte Carlo code was able to apply the material properties and associated material cross section data and therefore predicts the dose changes at the interfaces more accurately. In low density regions such as lung, the DPM calculation predicted a slightly wider penumbra than the TPS calculation.

Differences in the dose reported at the skin surface between the two calculations were common. Possible causes of this could be due to modeling of the build-up region at the surface and how the skin surface is defined within the source model for the DPM calculation.

### **5.3 EVALUATION OF THE HYPOTHESIS**

The hypothesis of this study was that a quality assurance tool based on the Monte Carlo Dose Planning Method (DPM) and coupled to a measurement-based source model could be developed to predict dose within 3%/2mm of measurement for IMRT and stereotactic treatments planned on the Varian linear accelerator at the photon energies of 6 MV and 10 MV.

To evaluate the hypothesis, the source model was first developed and validated for both energies with sufficient accuracy. This was accomplished in Specific Aim 1 where the model was commissioned by the standard set of basic beam data and performed to a criteria level within 2% or 2 mm for at least 95% of the data tested. The development and validation of the source model was detailed in Chapter 2 for the Varian 6 MV photon beam and in Chapter 3 for the 10 MV Varian photon beam.

The hypothesis was evaluated by benchmarking testing using the RPC anthropomorphic phantoms. The benchmark test plan was designed to increase the level of difficulty for the calculation based on the treatment technique and heterogeneity of the medium. The head and neck phantom was used to test the homogeneous condition with IMRT. The thorax phantom was used to test the low-density heterogeneous condition with SBRT and IMRT. Specific Aim 2 described the condition required to test the hypothesis. The requirement was that at least 85% of the data tested had to meet the stated criteria in order to prove the hypothesis true. As expected, the most difficult technique and treatment in terms of dose prediction was the IMRT lung plans where the minimum average percent of the data tested meeting the criteria was 85%. The IMRT treatment of the homogeneous medium and the SBRT treatment of the low-density heterogeneous medium yielded a range of the data

meeting criteria between 90% and 98%. The benchmark testing results proved that the hypothesis was true.

## **5.4 GENERAL CONCLUSIONS**

A custom-developed method for dose recalculation of patient plans entered into clinical trials was found to be accurate under a variety of conditions. The measurement-driven source model with analytical function parameters derived from a standard set of basic beam measurement data exceeded the objectives specified for agreement between the calculation and measurement for the common range of square fields at energies of 6 MV and 10 MV. The validated models also met or exceeded the objectives specified for agreement between the calculation and measurement for a variety of benchmark conditions using the RPC anthropomorphic phantoms and the common SBRT and IMRT treatment techniques. Confirmation of these results was demonstrated with patient cases where a commercial treatment planning system's (TPSs) dose calculation algorithm was benchmarked against the DPM method. The DPM method generated answers similar to the TPS system for IMRT and SBRT treatment plans. Differences were consistent with the superior physics modeling inherent in the Monte Carlo code. As a result, we believe the method will be useful for recalculating dose distributions for patients entered into clinical trials.

## **5.5 FUTURE WORK**

This project provided the proof of principle that an accurate independent dose calculation tool could be developed for use in the recalculation of patient plans entered into clinical trials. Currently, the custom-developed method is limited to the source models developed for the Varian 6 MV and 10 MV photon beams. While the Varian linear accelerators (linacs) comprise of a large percentage of the linacs listed by institutions participating in clinical trials (according to the RPC database, 93% of over 730 institutions have Varian linacs),

additional work is needed to develop source models for the Elekta and Siemens linacs. Equally important is the need to develop models for the 18 MV photon beams, as it is common to use this energy alone or along with other energies for certain treatments. Another helpful area for improvement lies in the speed of the calculation. It is estimated that the calculation time is more than 20 times slower than the typical commercially available dose calculation algorithm. While some graphical user interfaces currently exist (CERR and the rpcfilm tool), the actual dose calculation is executed using UNIX commands. Therefore, an effort to bring the dose calculation within the CERR platform would improve the ease of use. Finally, the approach to compensate for the assumption that the primary source is a point source by offsetting the MLC leaves by a fixed amount based on the source diameter could be improved. A better approach would be to modify the primary source and change it from a point source to a small Gaussian distributed source.

## Chapter 6 APPENDIX

### 6.1 VARIAN 6 MV: PERCENT DEPTH DOSE AND DOSE PROFILES

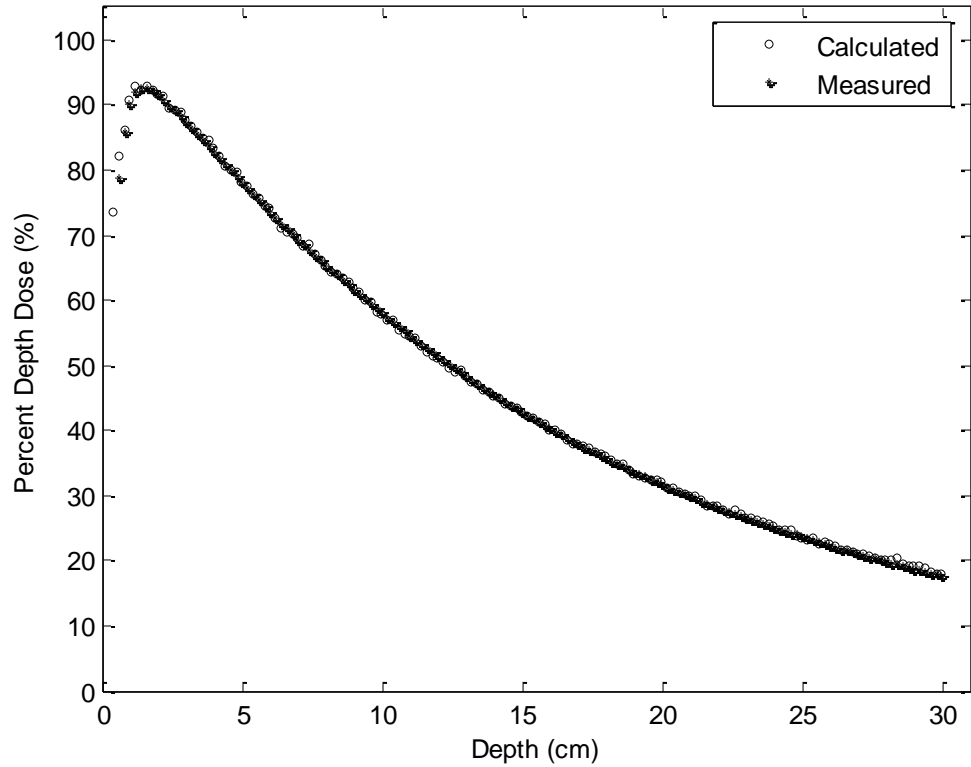


Figure 6.1 Calculated and measured percent depth dose curves at 6 MV from a 4 cm by 4 cm field.

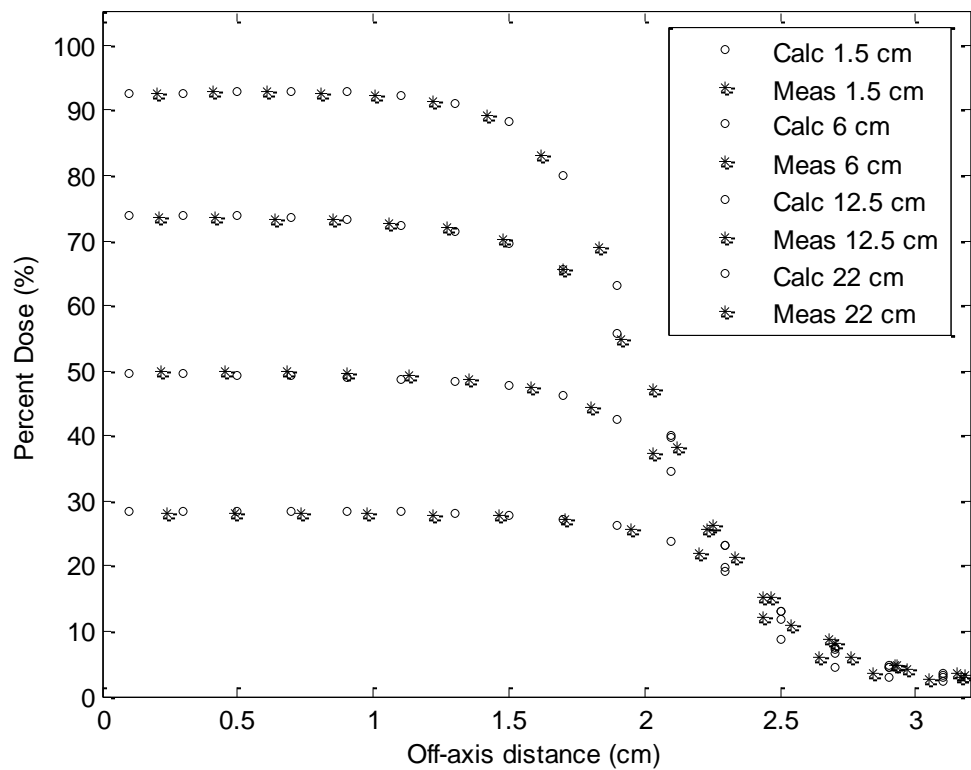


Figure 6.2 Calculated and measured dose profiles at 6 MV from a 4 cm by 4 cm field at depths of 1.5 cm, 6 cm, 12.5 cm, and 22 cm.

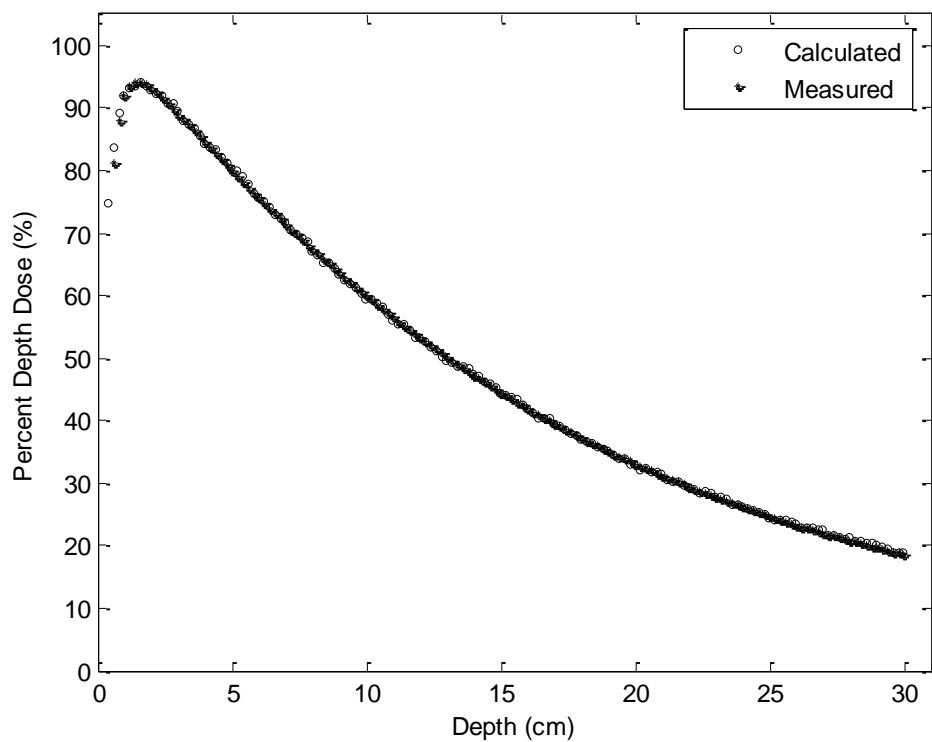


Figure 6.3 Calculated and measured percent depth dose curves at 6 MV from a 5 cm by 5 cm field.



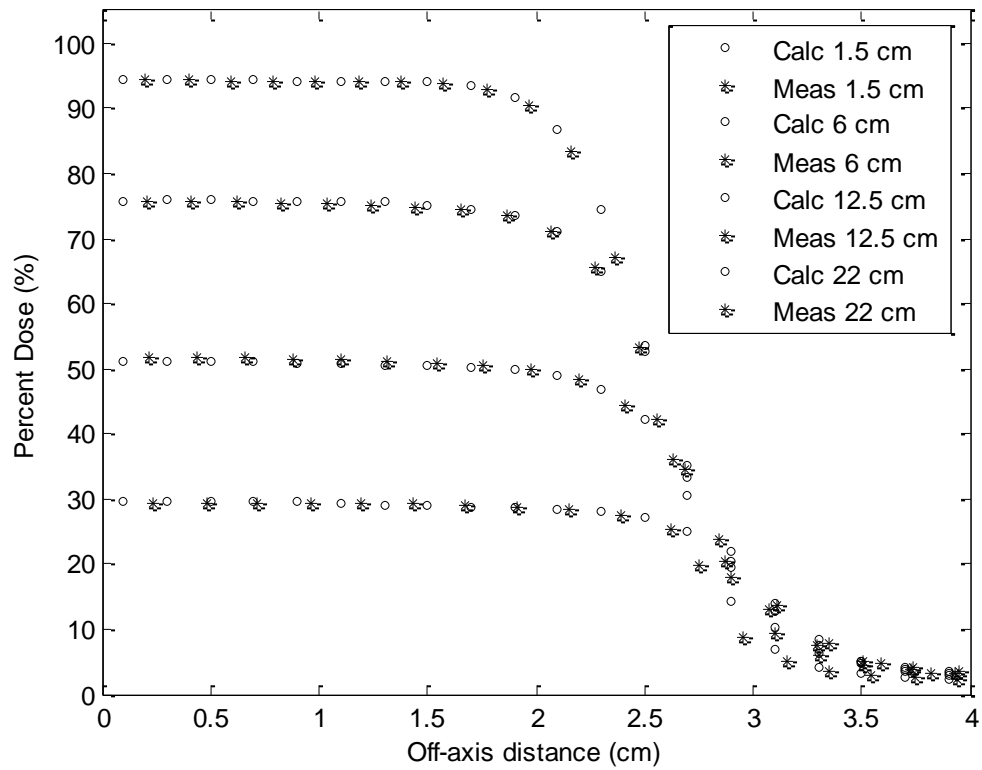


Figure 6.4 Calculated and measured dose profiles at 6 MV from a 5 cm by 5 cm field at depths of 1.5 cm, 6 cm, 12.5 cm, and 22 cm.

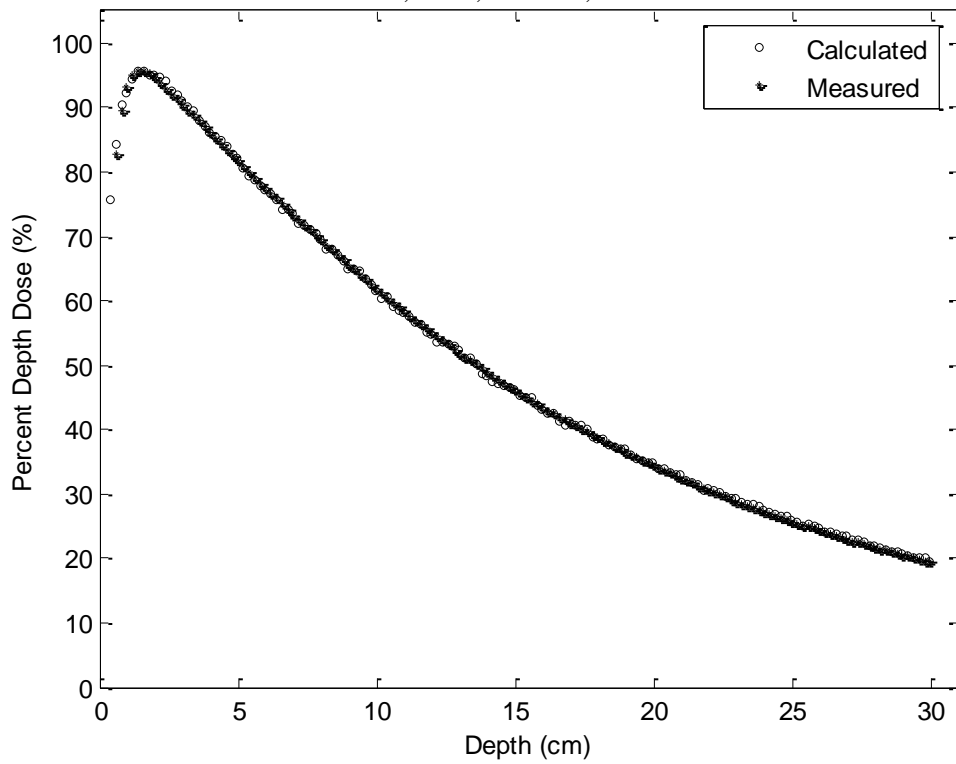


Figure 6.5 Calculated and measured percent depth dose curves at 6 MV from a 6 cm by 6 cm field.

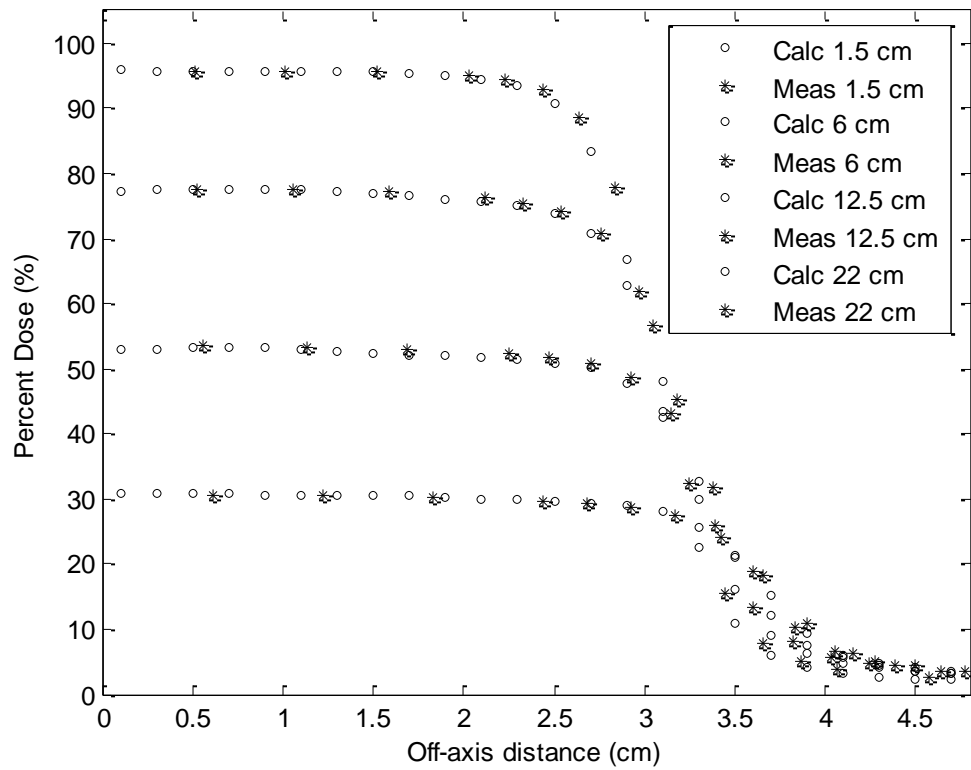


Figure 6.6 Calculated and measured dose profiles at 6 MV from a 6 cm by 6 cm field at depths of 1.5 cm, 6 cm, 12.5 cm, and 22 cm.

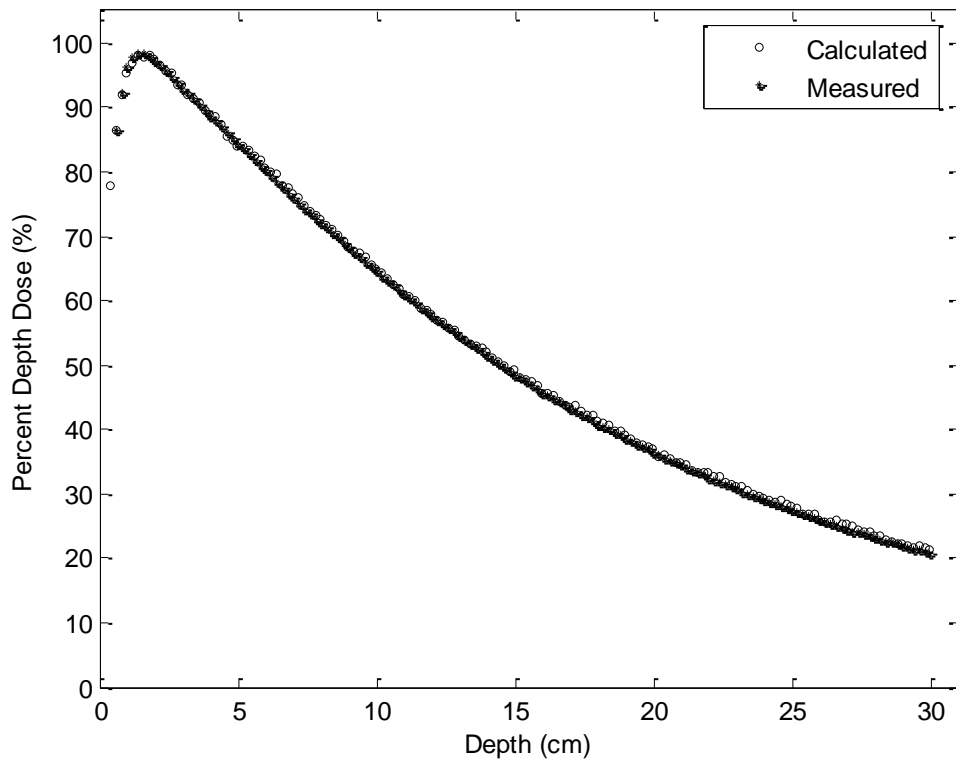


Figure 6.7 Calculated and measured percent depth dose curves at 6 MV from an 8 cm by 8 cm field.

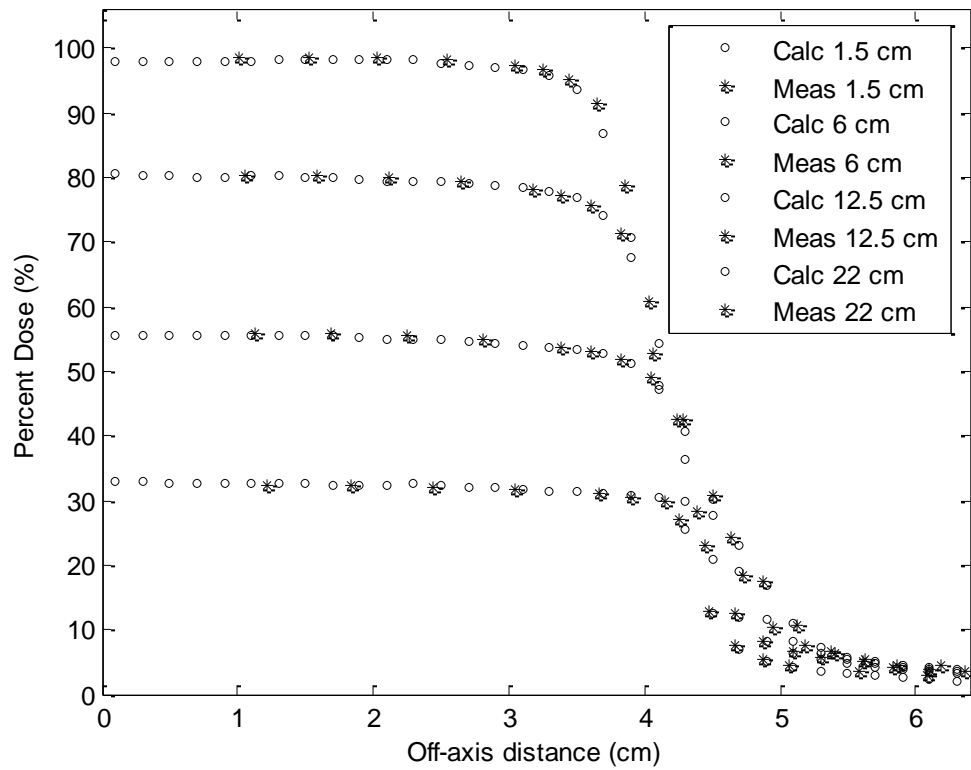


Figure 6.8 Calculated and measured dose profiles at 6 MV from a 8 cm by 8 cm field at depths of 1.5 cm, 6 cm, 12.5 cm, and 22 cm.

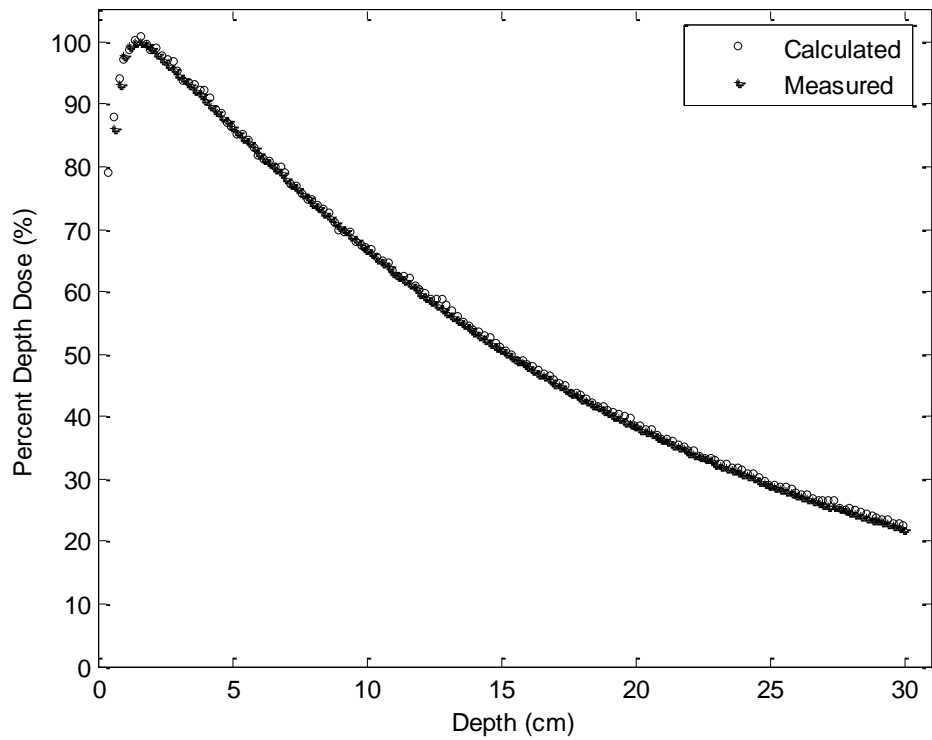


Figure 6.9 Calculated and measured percent depth dose curves at 6 MV from a 10 cm by 10 cm field.

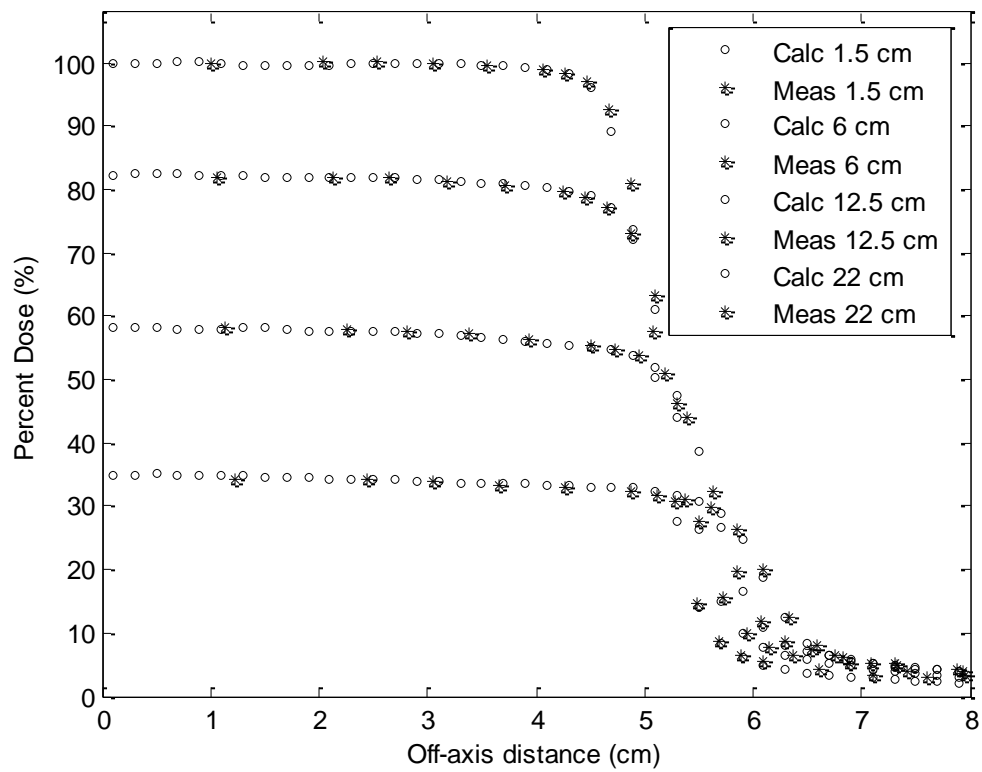


Figure 6.10 Calculated and measured dose profiles at 6 MV from a 10 cm by 10 cm field at depths of 1.5 cm, 6 cm, 12.5 cm, and 22 cm.

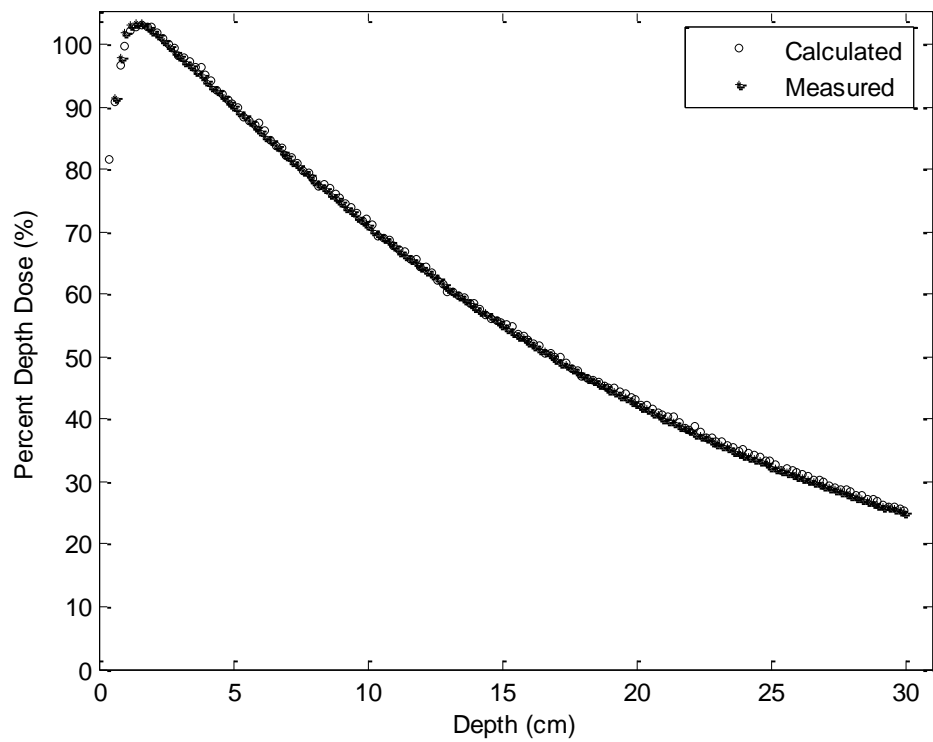


Figure 6.11 Calculated and measured percent depth dose curves at 6 MV from a 15 cm by 15 cm field.

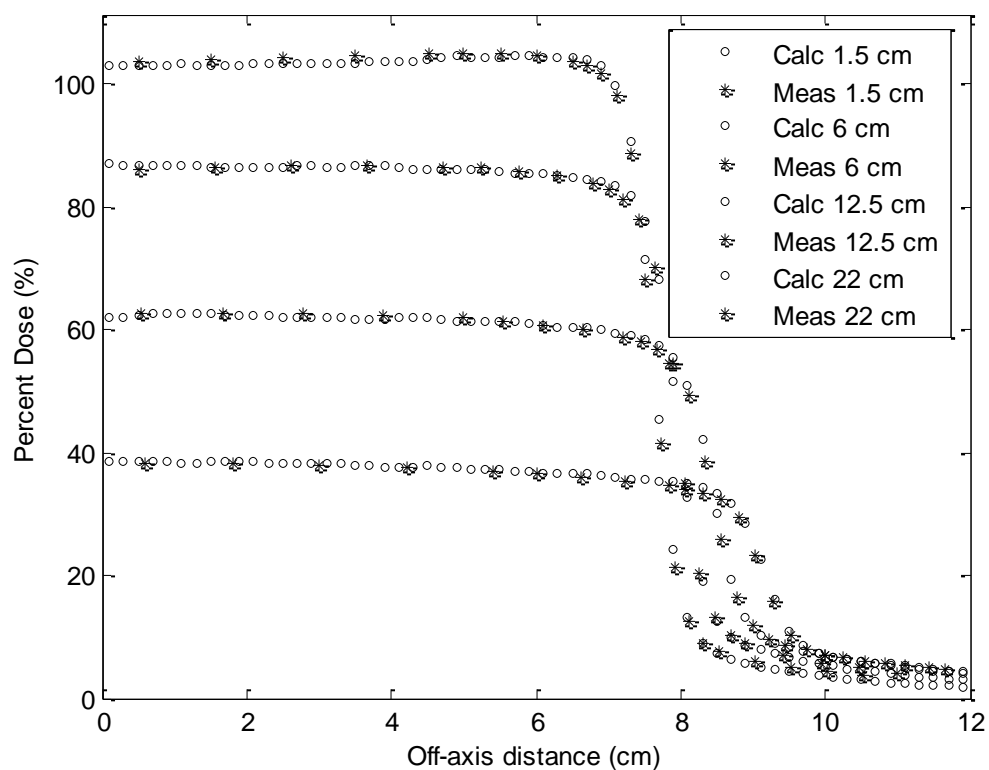


Figure 6.12 Calculated and measured dose profiles at 6 MV from a 15 cm by 15 cm field at depths of 1.5 cm, 6 cm, 12.5 cm, and 22 cm.

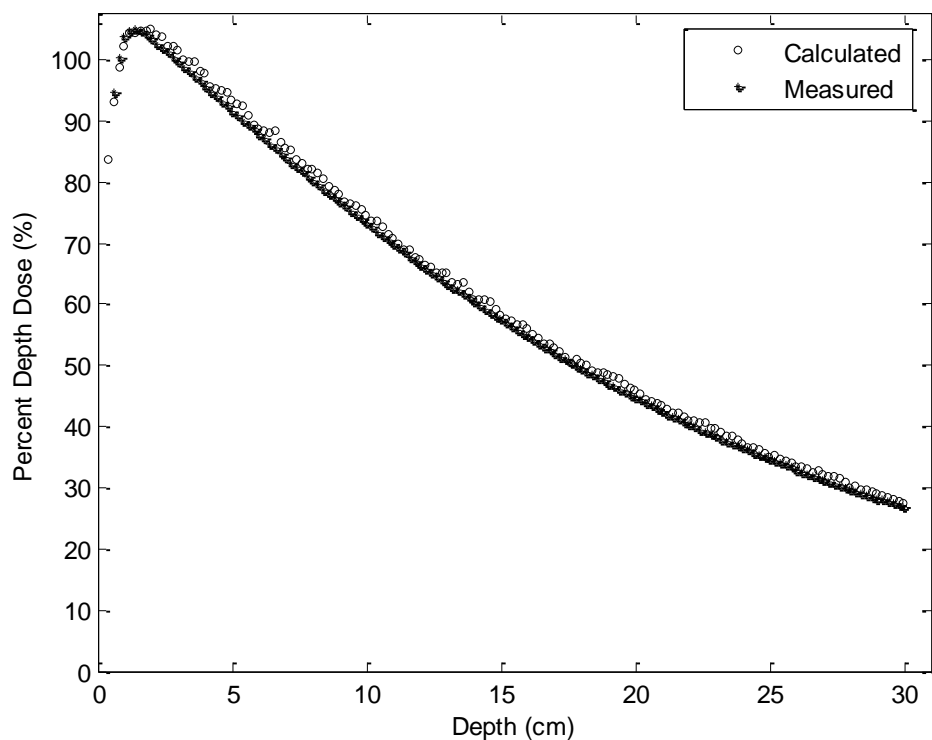


Figure 6.13 Calculated and measured percent depth dose curves at 6 MV from a 20 cm by 20 cm field.

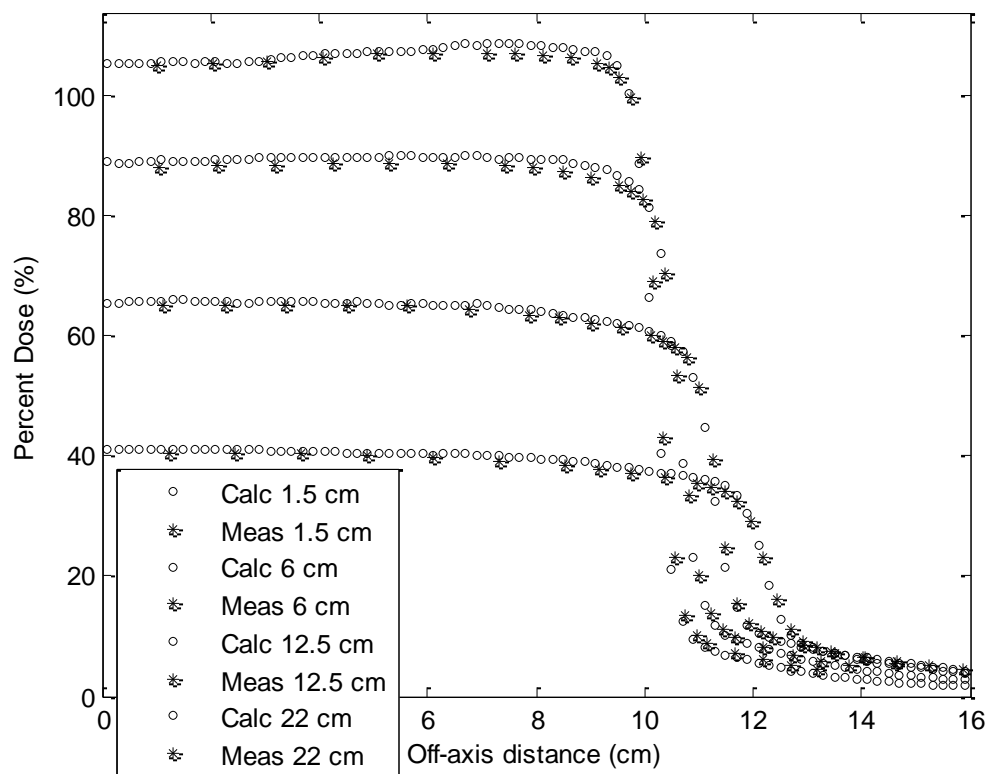


Figure 6.14 Calculated and measured dose profiles at 6 MV from a 20 cm by 20 cm field at depths of 1.5 cm, 6 cm, 12.5 cm, and 22 cm.

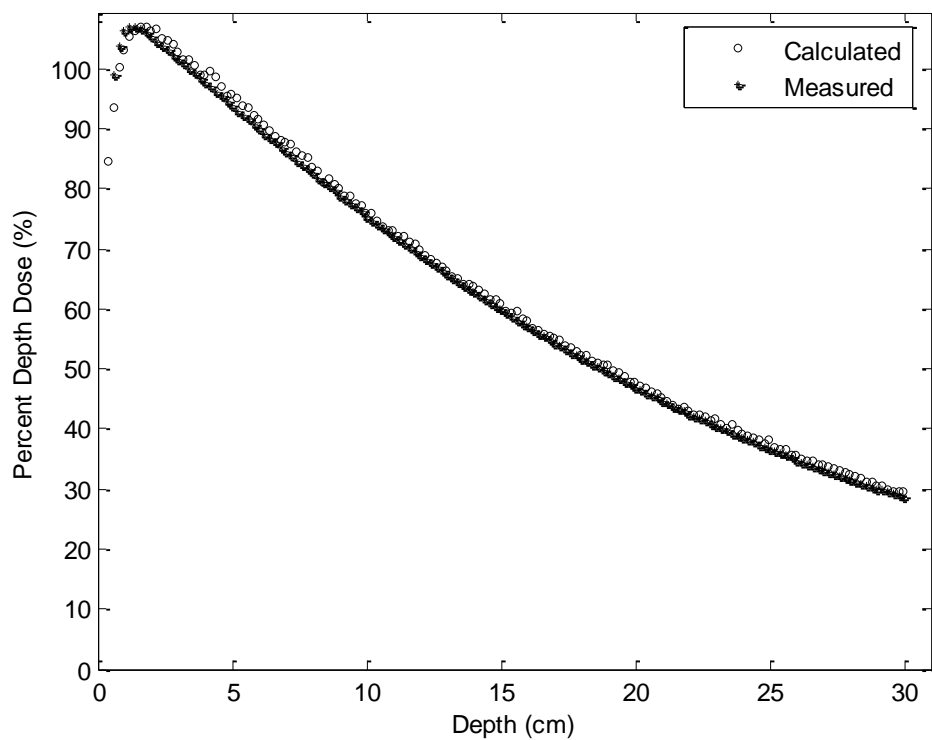


Figure 6.15 Calculated and measured percent depth dose curves at 6 MV from a 25 cm by 25 cm field.

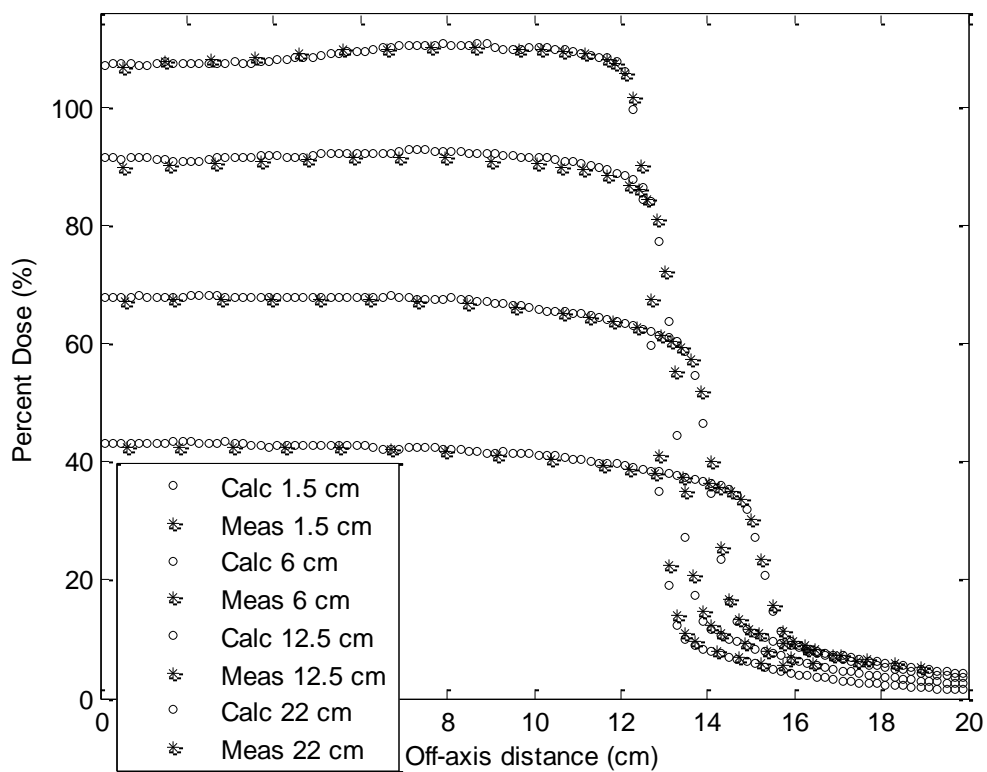


Figure 6.16 Calculated and measured dose profiles at 6 MV from a 25 cm by 25 cm field at depths of 1.5 cm, 6 cm, 12.5 cm, and 22 cm.

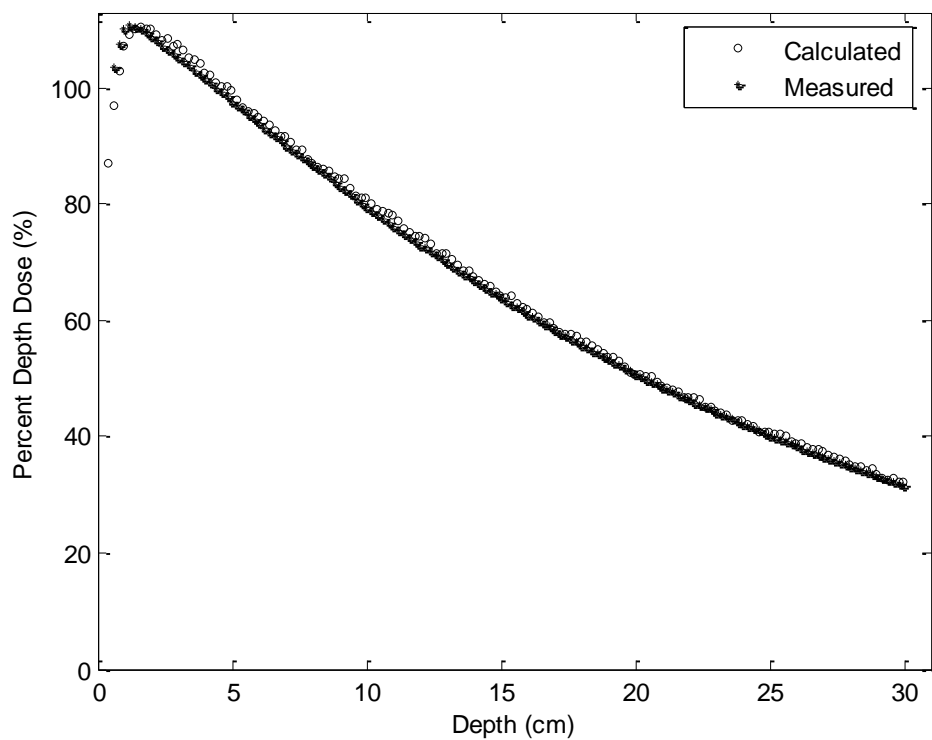


Figure 6.17 Calculated and measured percent depth dose curves at 6 MV from a 40 cm by 40 cm field.

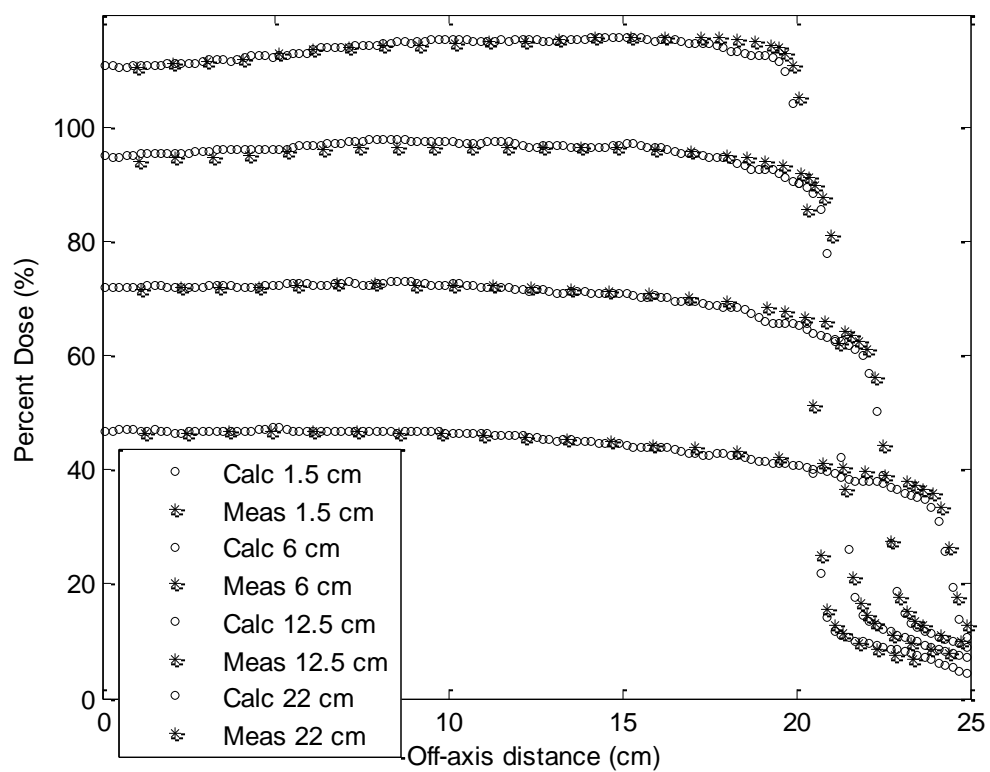


Figure 6.18 Calculated and measured dose profiles at 6 MV from a 40 cm by 40 cm field at depths of 1.5 cm, 6 cm, 12.5 cm, and 22 cm.



## 6.2 VARIAN 6 MV: GAMMA MAPS AND DOSE PROFILES

### 6.2.1 Varian 6 MV: Delivery for the IMRT head and neck plan

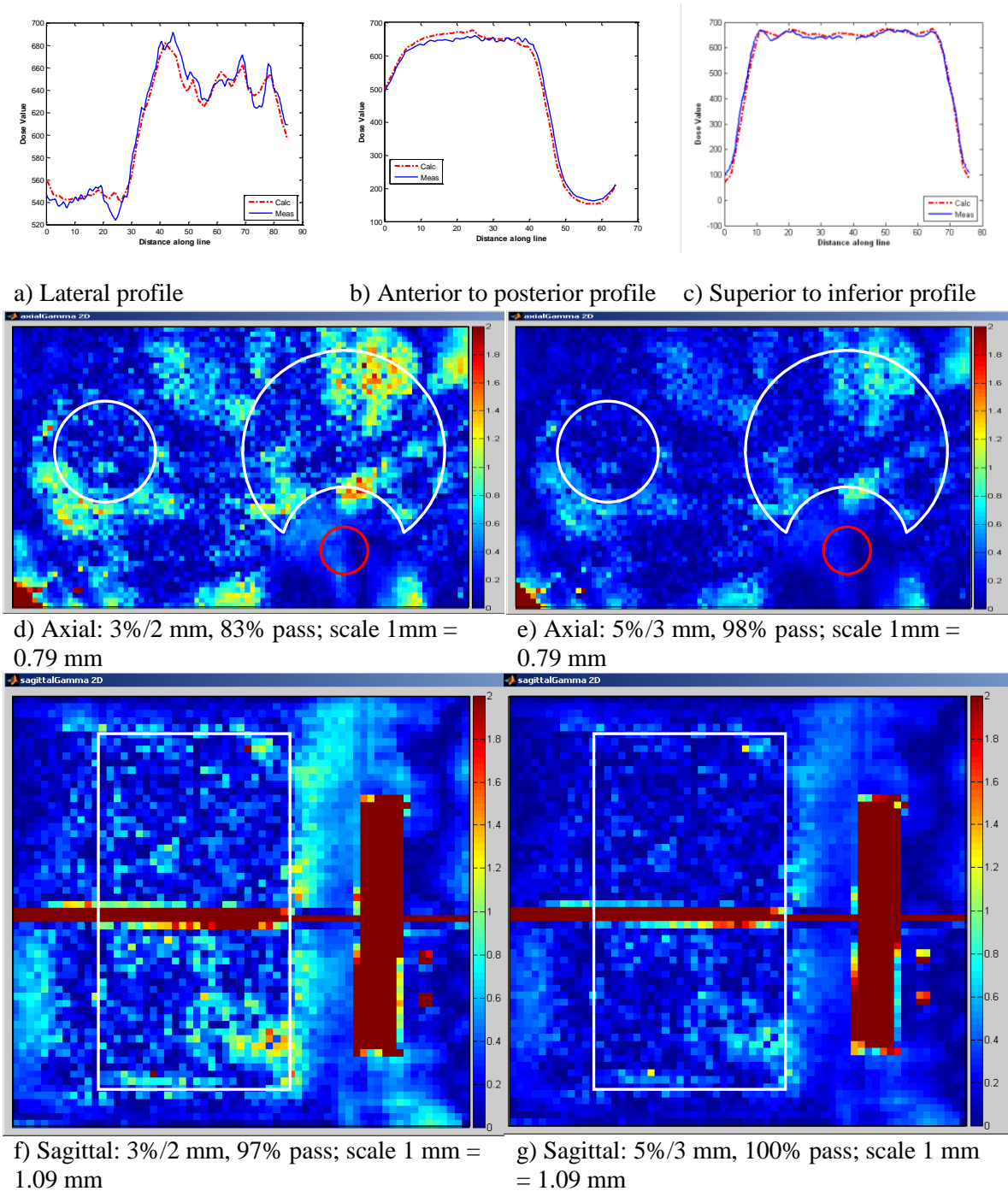
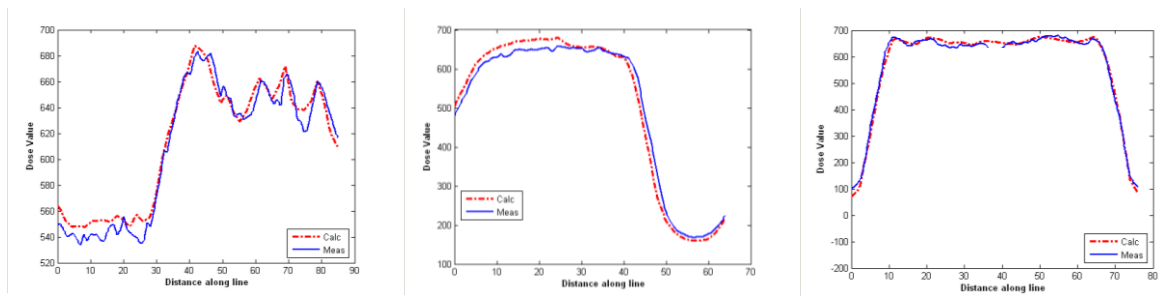


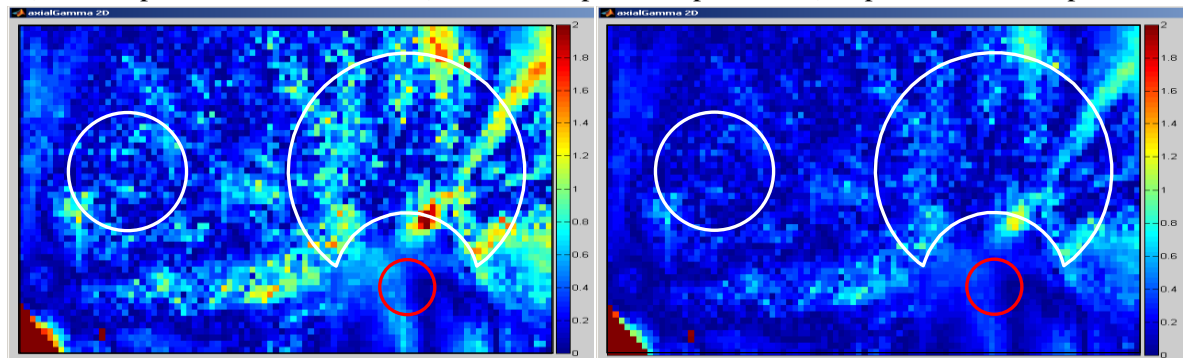
Figure 6.19 Varian 6 MV: IMRT H&N delivery single irradiation (number 1): Gamma maps and dose profiles.



a) Lateral profile

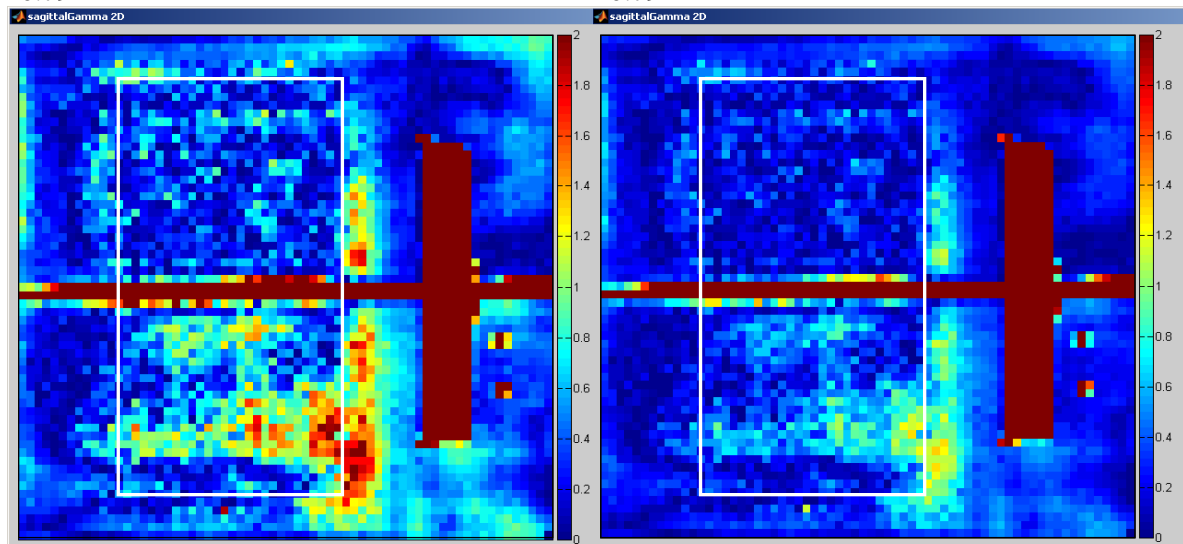
b) Anterior to posterior profile

c) Superior to inferior profile



d) Axial: 3%/2 mm, 93% pass; scale 1mm = 0.79 mm

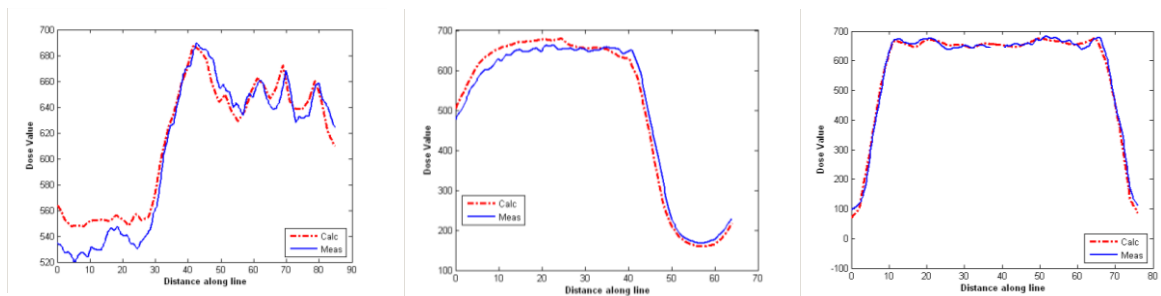
e) Axial: 5%/3 mm, 99% pass; scale 1mm = 0.79 mm



f) Sagittal: 3%/2 mm, 95% pass; scale 1 mm = 1.09 mm

g) Sagittal: 5%/3 mm, 99% pass; scale 1 mm = 1.09 mm

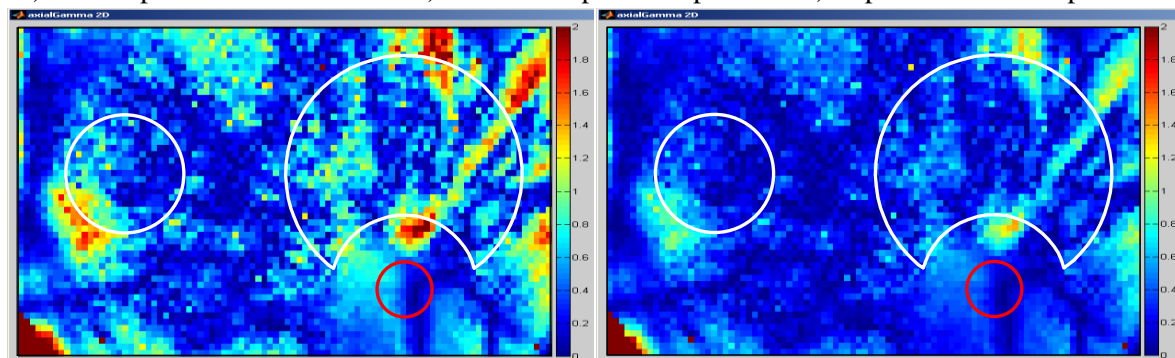
Figure 6.20 Varian 6 MV: IMRT H&N delivery single irradiation (number 2): Gamma maps and dose profiles.



a) Lateral profile

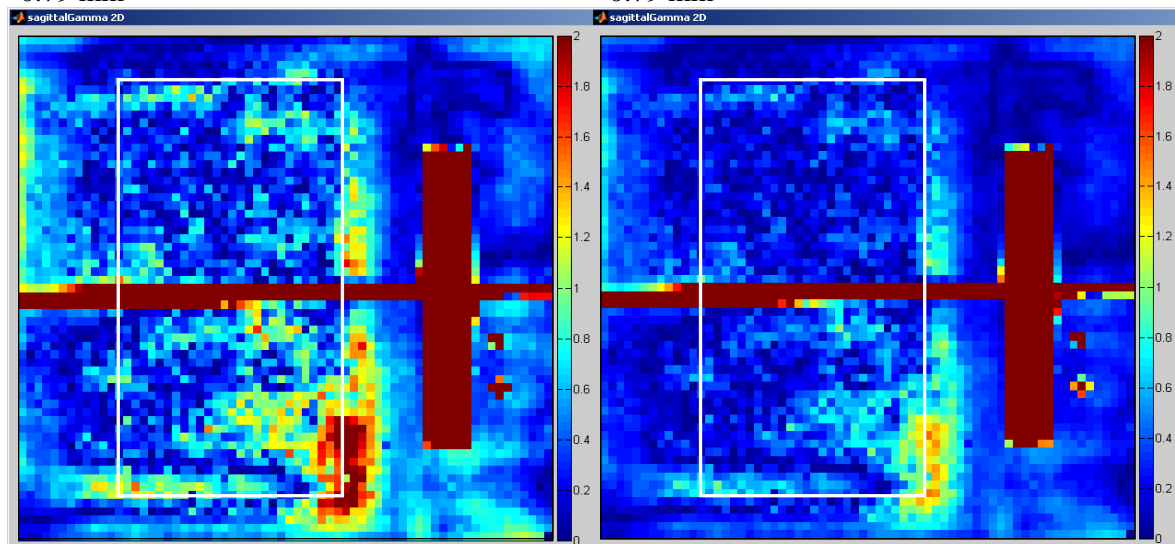
b) Anterior to posterior profile

c) Superior to inferior profile



d) Axial: 3%/2 mm, 80% pass; scale 1mm = 0.79 mm

e) Axial: 5%/3 mm, 97% pass; scale 1mm = 0.79 mm

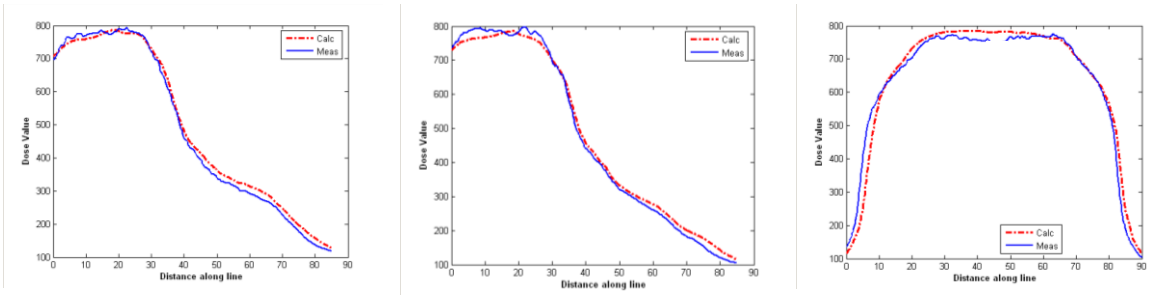


f) Sagittal: 3%/2 mm, 91% pass; scale 1 mm = 1.09 mm

g) Sagittal: 5%/3 mm, 99% pass; scale 1 mm = 1.09 mm

Figure 6.21 Varian 6 MV: IMRT H&N delivery single irradiation (number 3): Gamma maps and dose profiles.

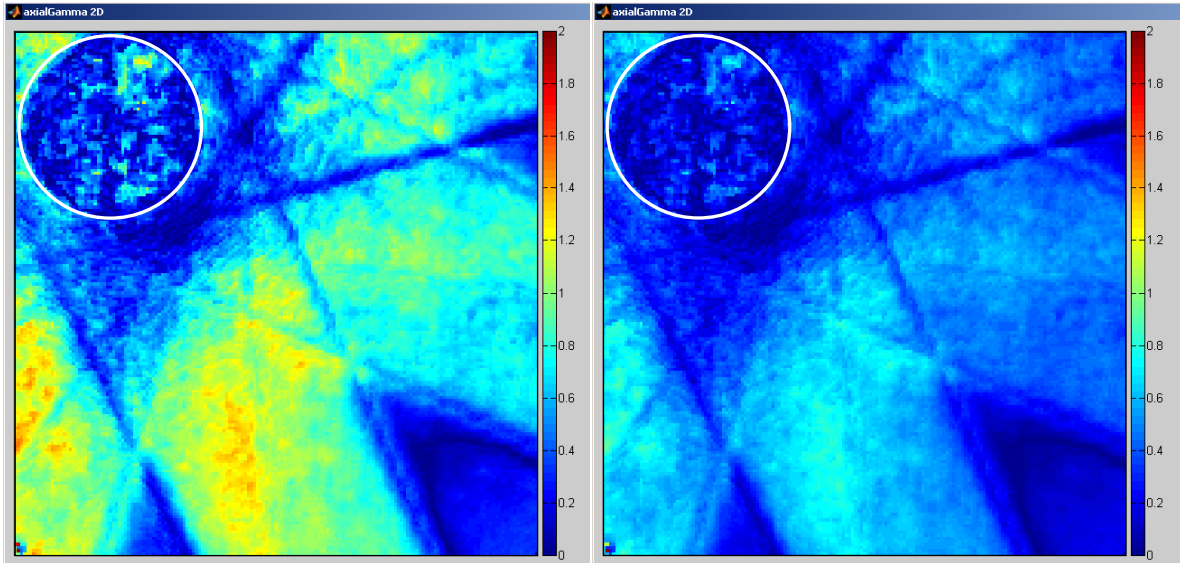
## 6.2.2 Varian 6 MV: Delivery for the SBRT lung plan



a) Lateral profile

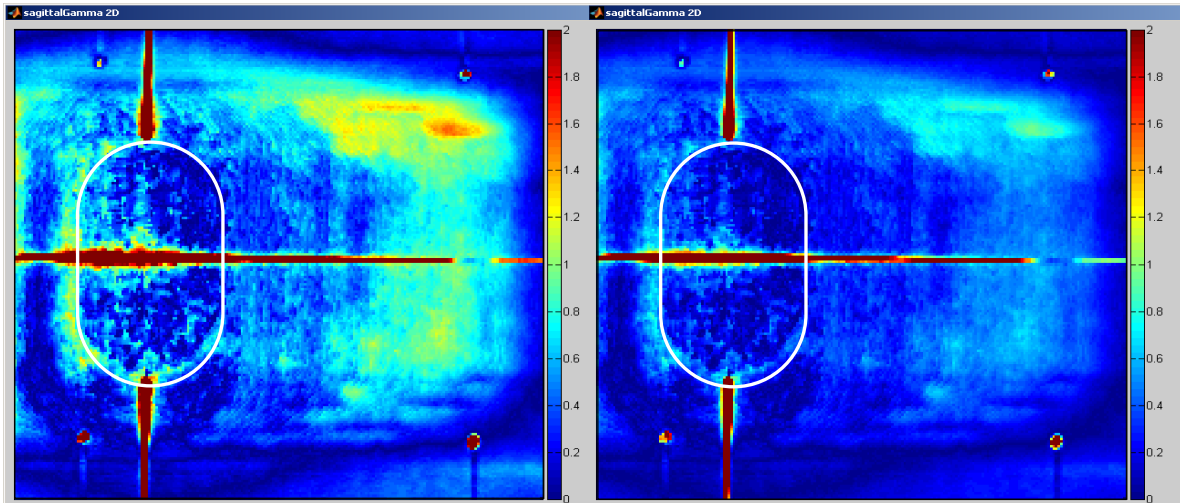
b) Anterior to posterior profile

c) Superior to inferior profile



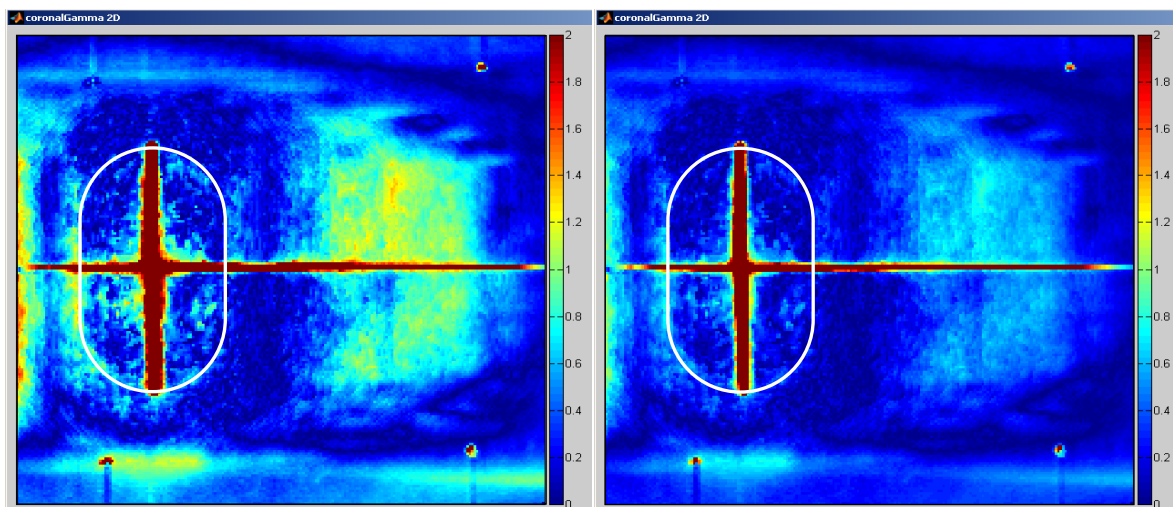
d) Axial: 3%/2 mm, 82% pass; scale 1mm = 0.82 mm

e) Axial: 5%/3 mm, 100% pass; scale 1mm = 0.82 mm



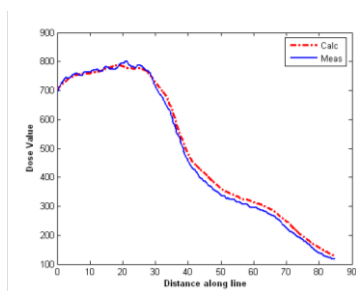
f) Sagittal: 3%/2 mm, 95% pass; scale 1 mm = 0.65 mm

g) Sagittal: 5%/3 mm, 100% pass; scale 1 mm = 0.65 mm

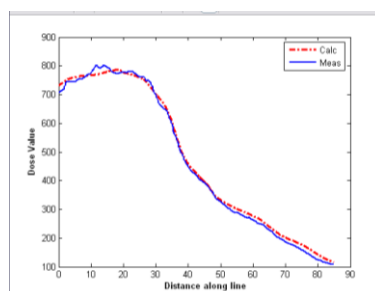


h) Coronal: 3%/2 mm, 93% pass; scale 1 mm = 0.65 mm      i) Coronal: 5%/3 mm, 99% pass; scale 1 mm = 0.65 mm

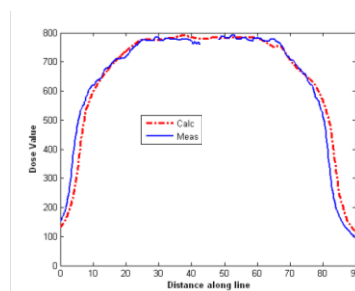
Figure 6.22 Varian 6 MV: SBRT lung delivery single irradiation (number 1): Gamma maps and dose profiles.



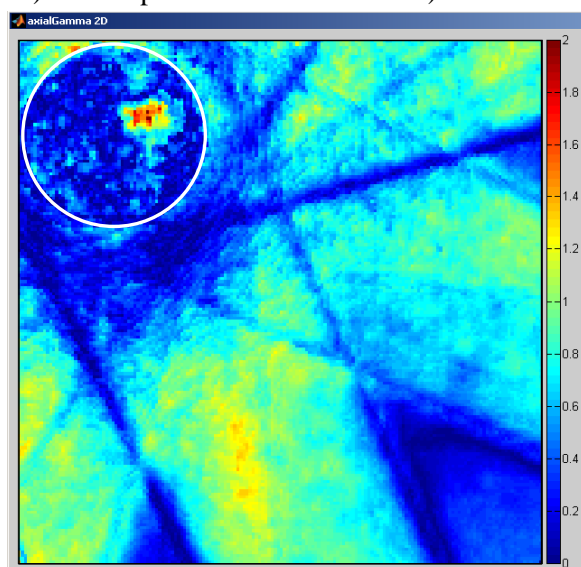
a) Lateral profile



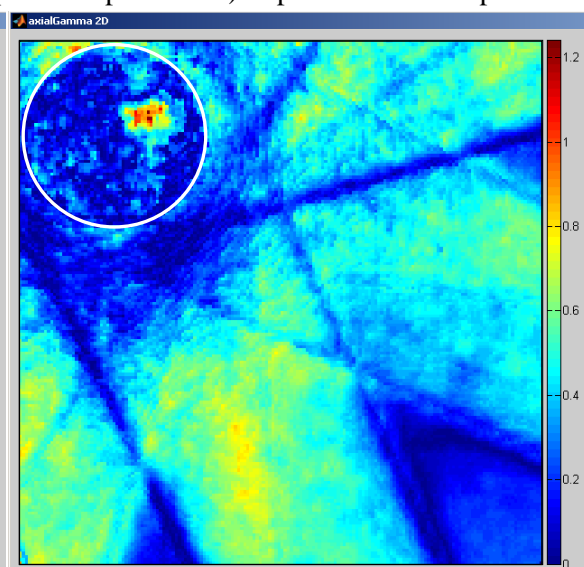
b) Anterior to posterior profile



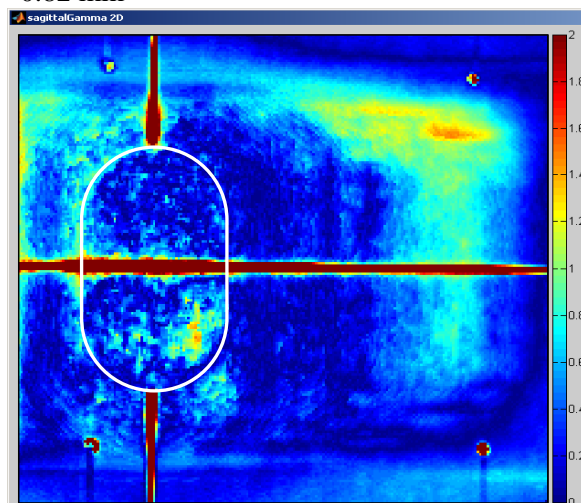
c) Superior to inferior profile



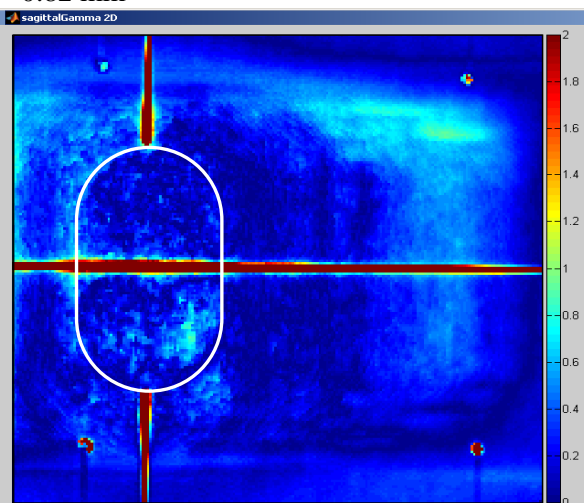
d) Axial: 3%/2 mm, 91% pass; scale 1mm = 0.82 mm



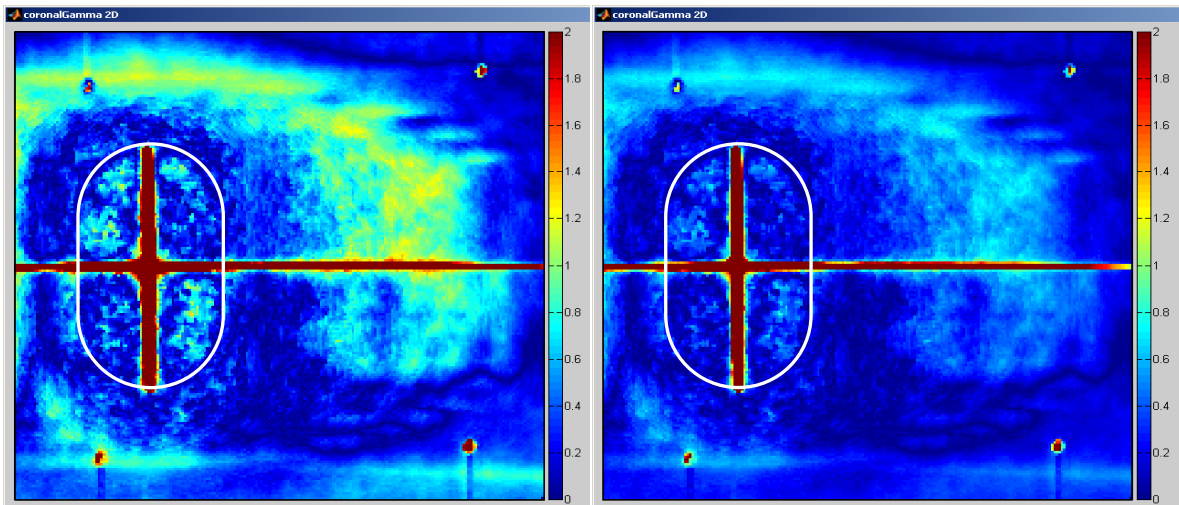
e) Axial: 5%/3 mm, 100% pass; scale 1mm = 0.82 mm



f) Sagittal: 3%/2 mm, 96% pass; scale 1 mm = 0.65 mm



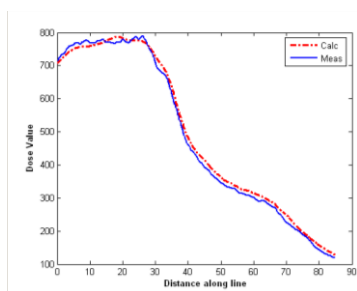
g) Sagittal: 5%/3 mm, 100% pass; scale 1 mm = 0.65 mm



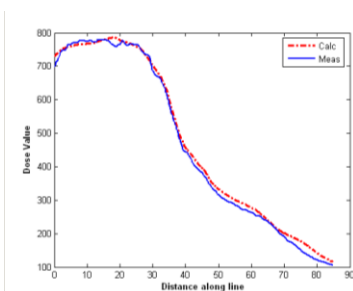
h) Coronal: 3%/2 mm, 94% pass; scale 1 mm = 0.65 mm      i) Coronal: 5%/3 mm, 99% pass; scale 1 mm = 0.65 mm

Figure 6.23 Varian 6 MV: SBRT lung delivery single irradiation (number 2): Gamma maps and dose profiles.

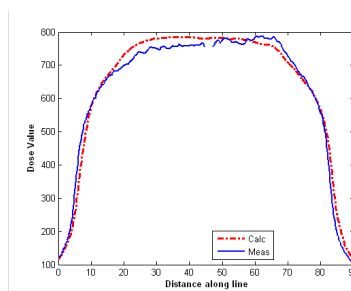




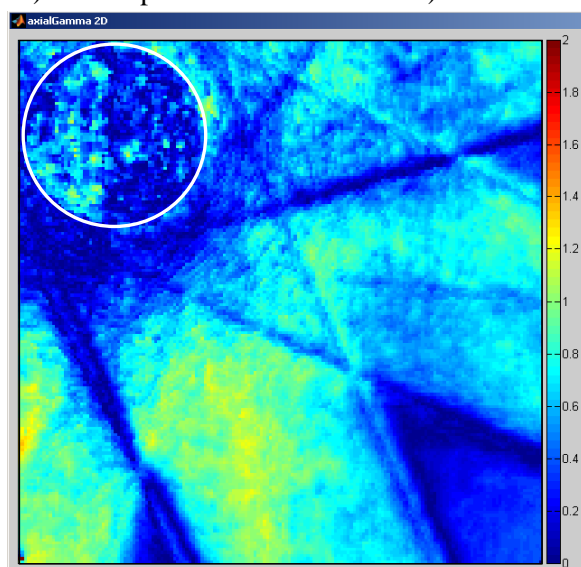
a) Lateral profile



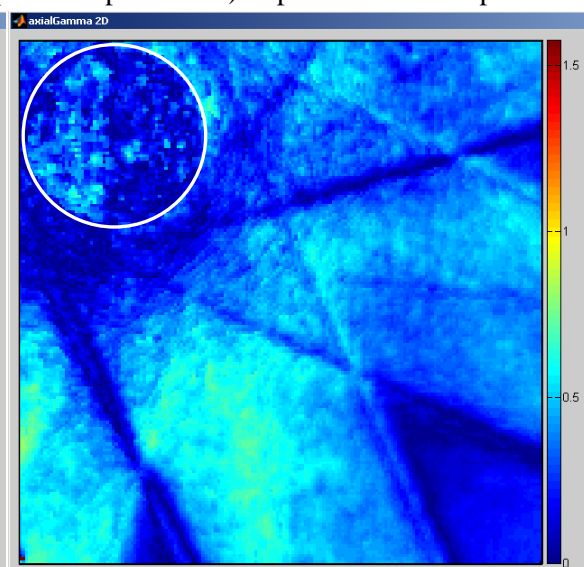
b) Anterior to posterior profile



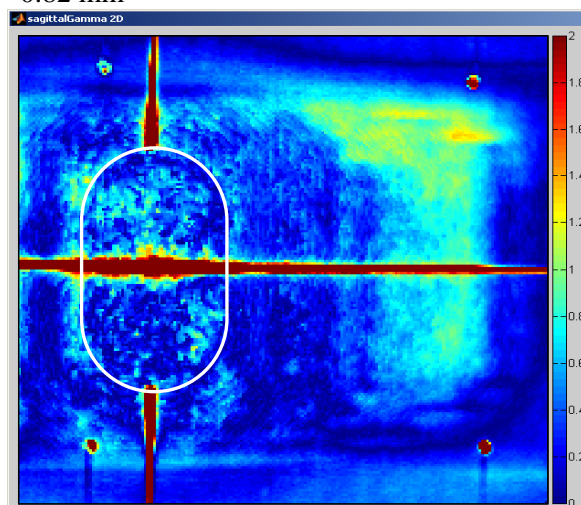
c) Superior to inferior profile



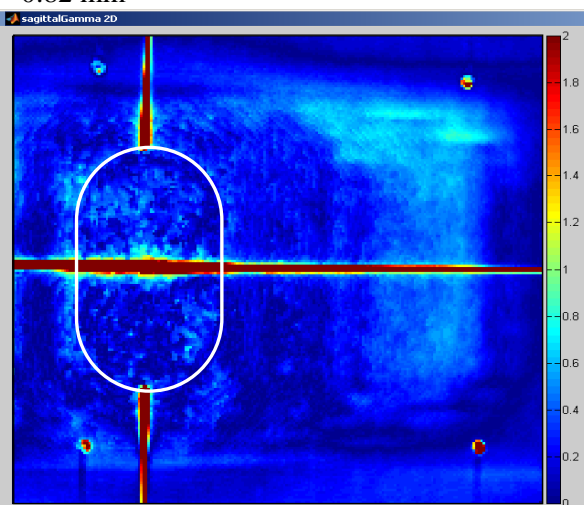
d) Axial: 3%/2 mm, 95% pass; scale 1mm = 0.82 mm



e) Axial: 5%/3 mm, 100% pass; scale 1mm = 0.82 mm

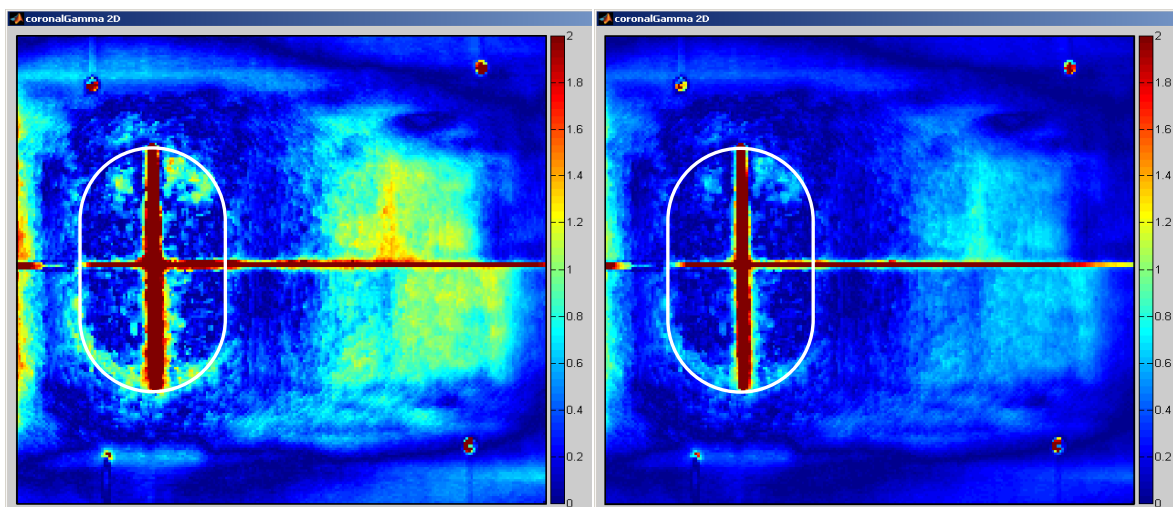


f) Sagittal: 3%/2 mm, 97% pass; scale 1 mm = 0.65 mm



g) Sagittal: 5%/3 mm, 100% pass; scale 1 mm = 0.65 mm

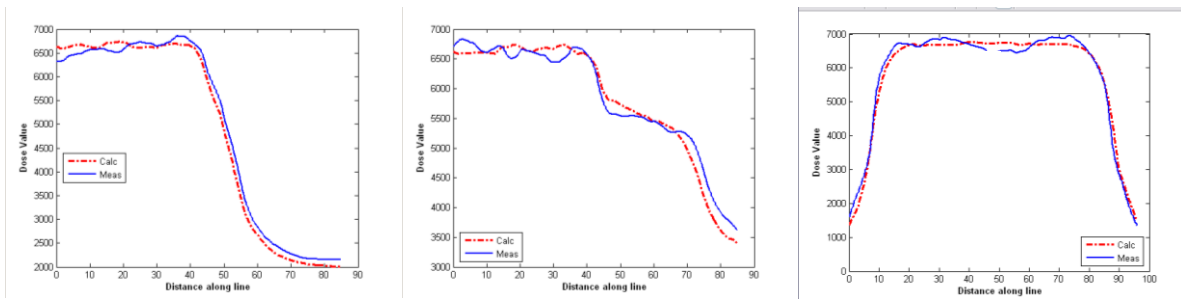




h) Coronal: 3%/2 mm, 93% pass; scale 1 mm = 0.65 mm      i) Coronal: 5%/3 mm, 100% pass; scale 1 mm = 0.65 mm

Figure 6.24 Varian 6 MV: SBRT lung delivery single irradiation (number 3): Gamma maps and dose profiles.

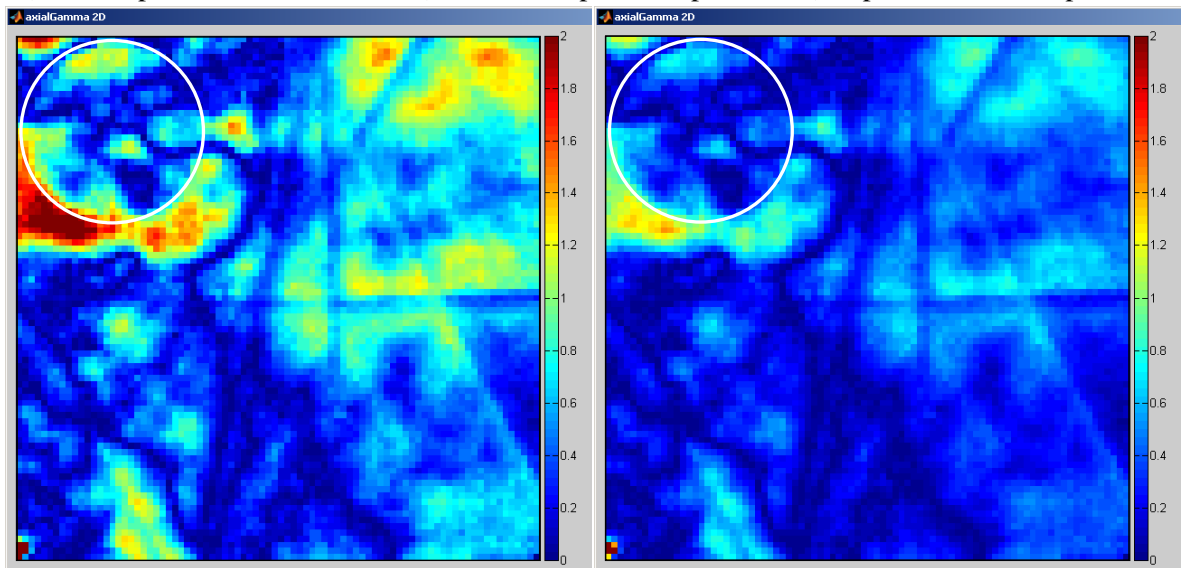
### 6.2.3 Varian 6 MV: Delivery for the IMRT lung plan



a) Lateral profile

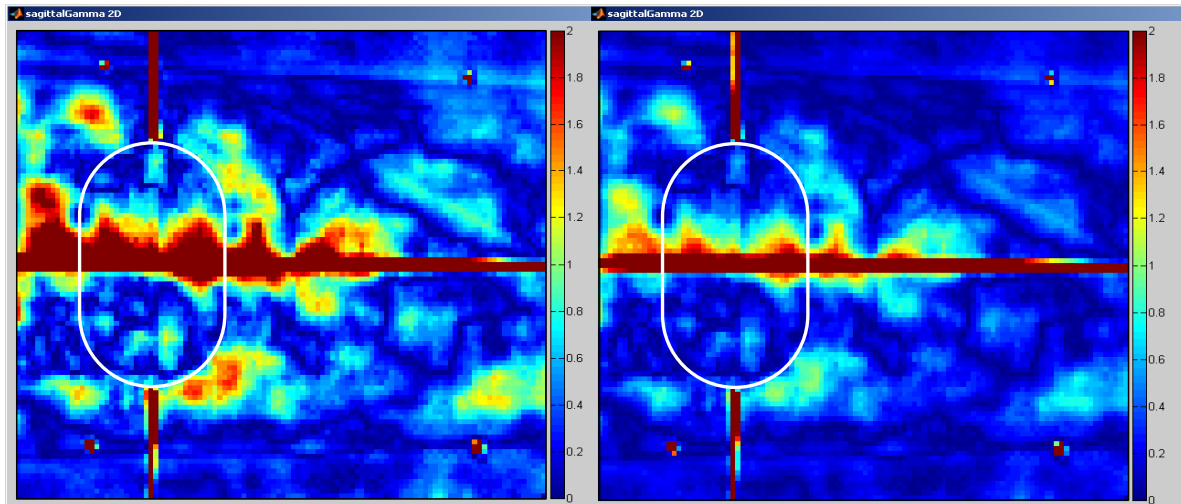
b) Anterior to posterior profile

c) Superior to inferior profile



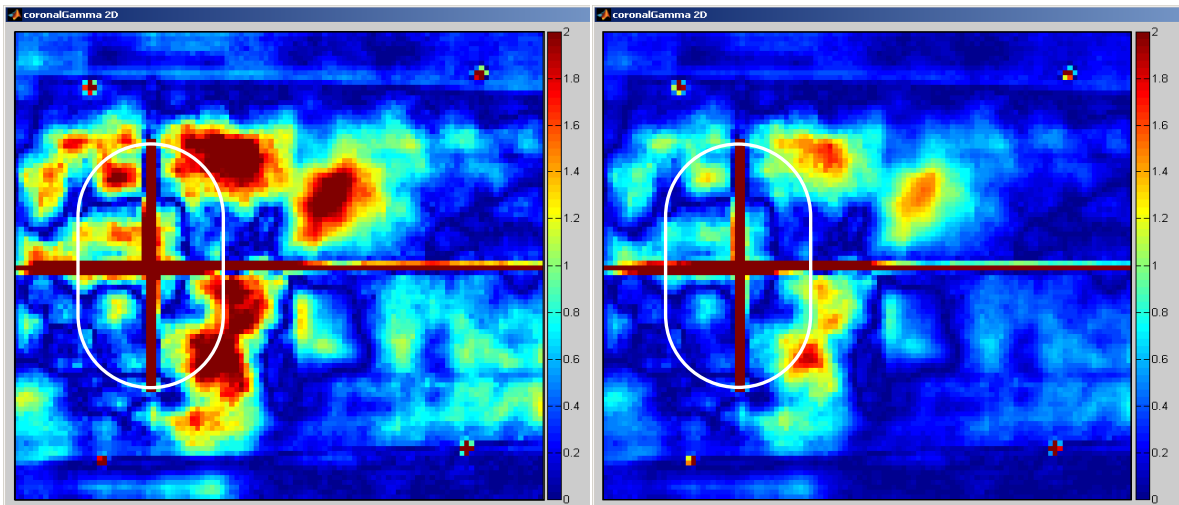
d) Axial: 3%/2 mm, 88% pass; scale 1mm = 0.82 mm

e) Axial: 5%/3 mm, 99% pass; scale 1mm = 0.82 mm



f) Sagittal: 3%/2 mm, 87% pass; scale 1 mm = 0.65 mm

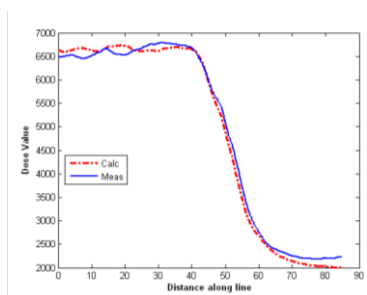
g) Sagittal: 5%/3 mm, 95% pass; scale 1 mm = 0.65 mm



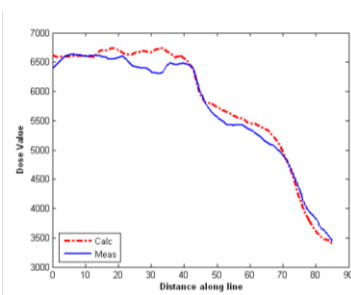
h) Coronal: 3%/2 mm, 82% pass; scale 1 mm = 0.65 mm

i) Coronal: 5%/3 mm, 94% pass; scale 1 mm = 0.65 mm

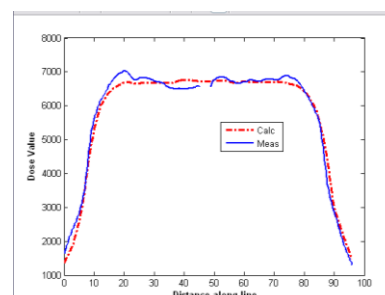
Figure 6.25 Varian 6 MV: IMRT lung delivery single irradiation (number 1): Gamma maps and dose profiles.



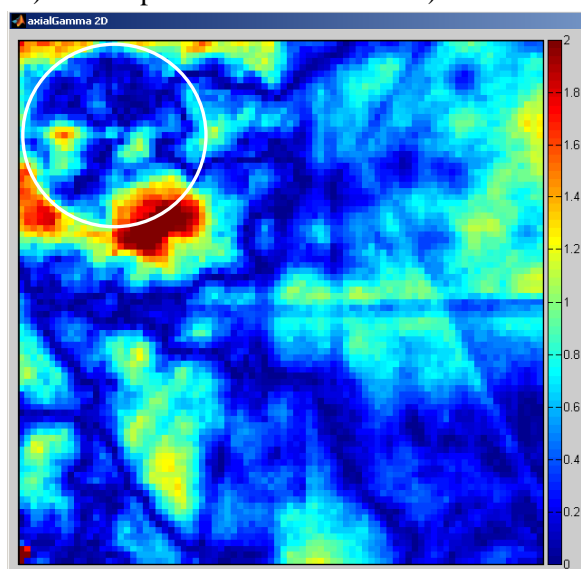
a) Lateral profile



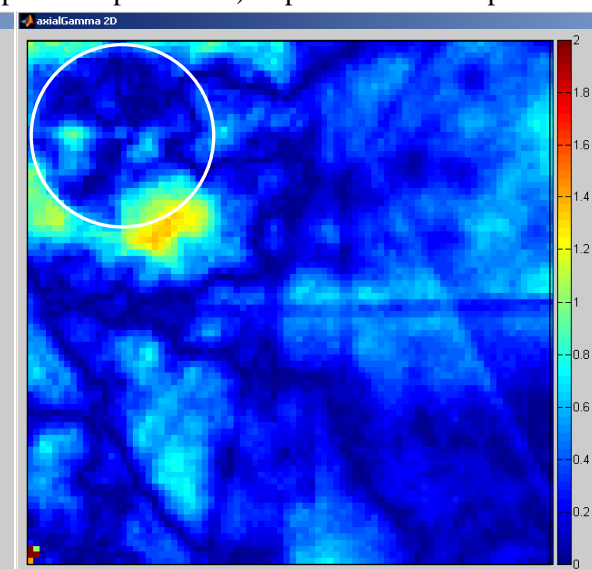
b) Anterior to posterior profile



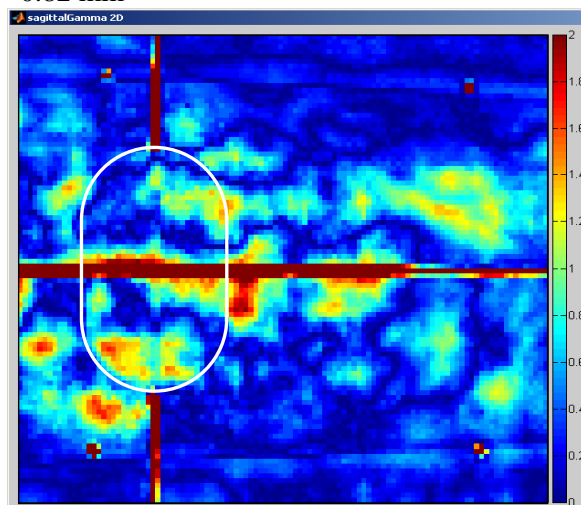
c) Superior to inferior profile



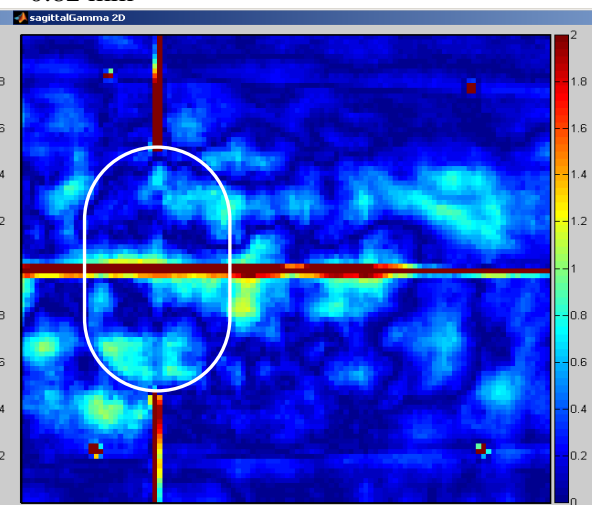
d) Axial: 3%/2 mm, 92% pass; scale 1mm = 0.82 mm



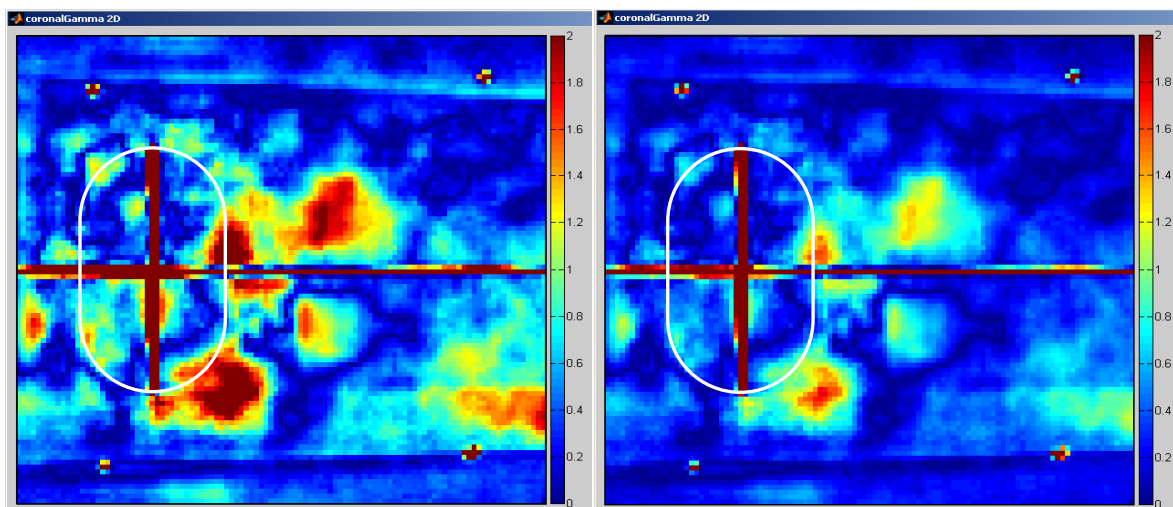
e) Axial: 5%/3 mm, 99% pass; scale 1mm = 0.82 mm



f) Sagittal: 3%/2 mm, 92% pass; scale 1 mm = 0.65 mm

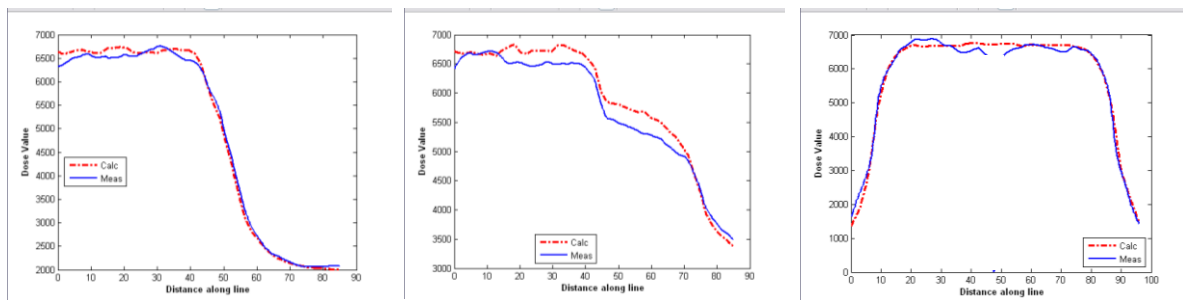


g) Sagittal: 5%/3 mm, 99% pass; scale 1 mm = 0.65 mm



h) Coronal: 3%/2 mm, 86% pass; scale 1 mm = 0.65 mm      i) Coronal: 5%/3 mm, 96% pass; scale 1 mm = 0.65 mm

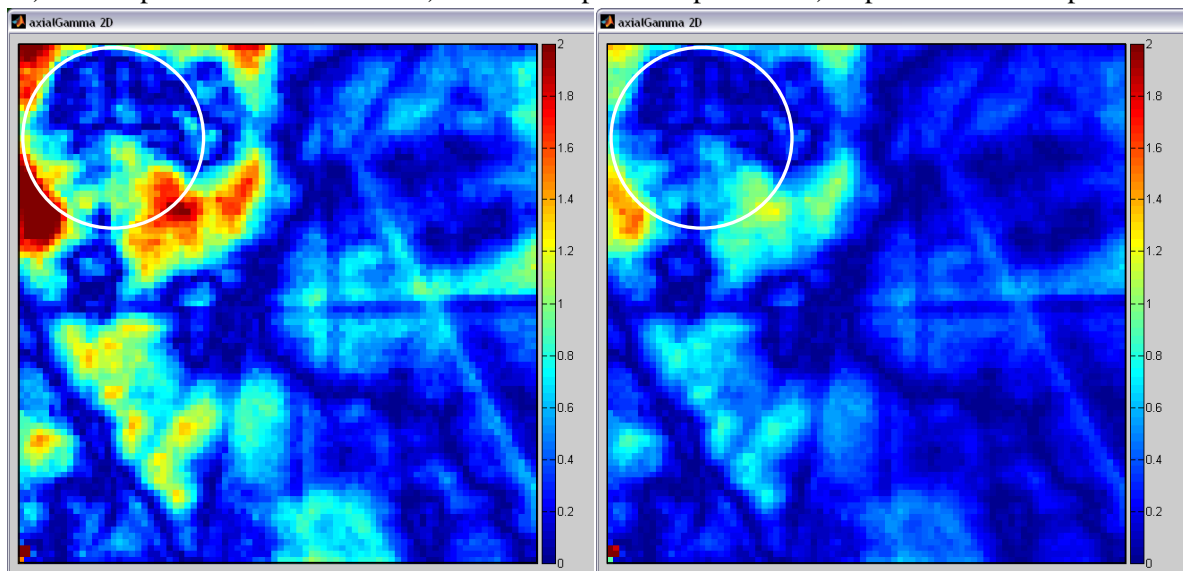
Figure 6.26 Varian 6 MV: IMRT lung delivery single irradiation (number 2): Gamma maps and dose profiles.



a) Lateral profile

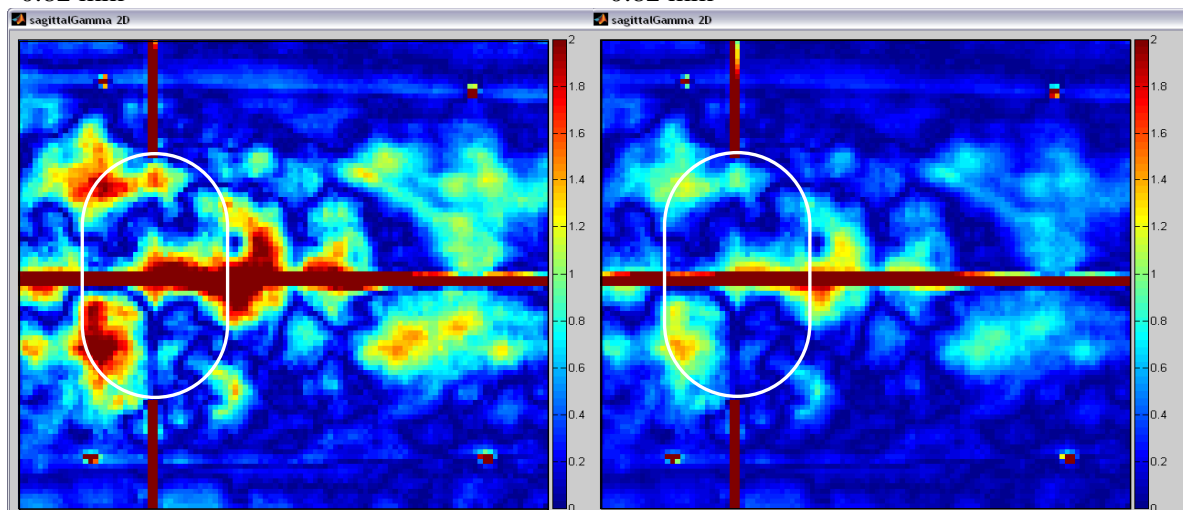
b) Anterior to posterior profile

c) Superior to inferior profile



d) Axial: 3%/2 mm, 89% pass; scale 1mm = 0.82 mm

e) Axial: 5%/3 mm, 98% pass; scale 1mm = 0.82 mm



f) Sagittal: 3%/2 mm, 87% pass; scale 1 mm = 0.65 mm

g) Sagittal: 5%/3 mm, 96% pass; scale 1 mm = 0.65 mm

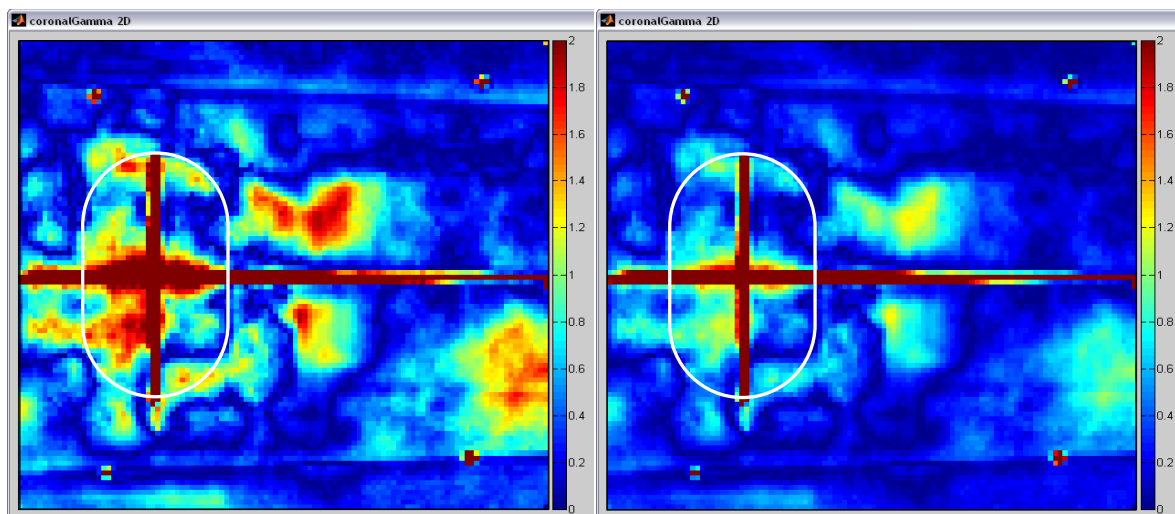
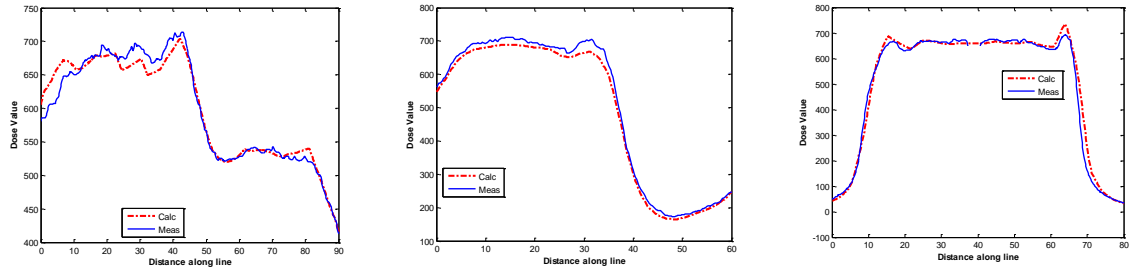


Figure 6.27 Varian 6 MV: IMRT lung delivery single irradiation (number 3): Gamma maps and dose profiles.

## 6.3 VARIAN 10 MV: GAMMA MAPS AND DOSE PROFILES

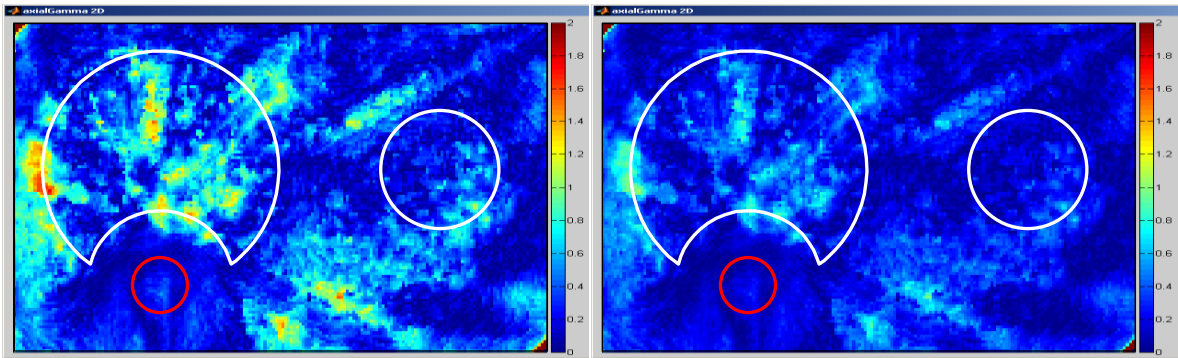
### 6.3.1 Varian 10 MV: Delivery for the IMRT head and neck plan



a) Lateral profile

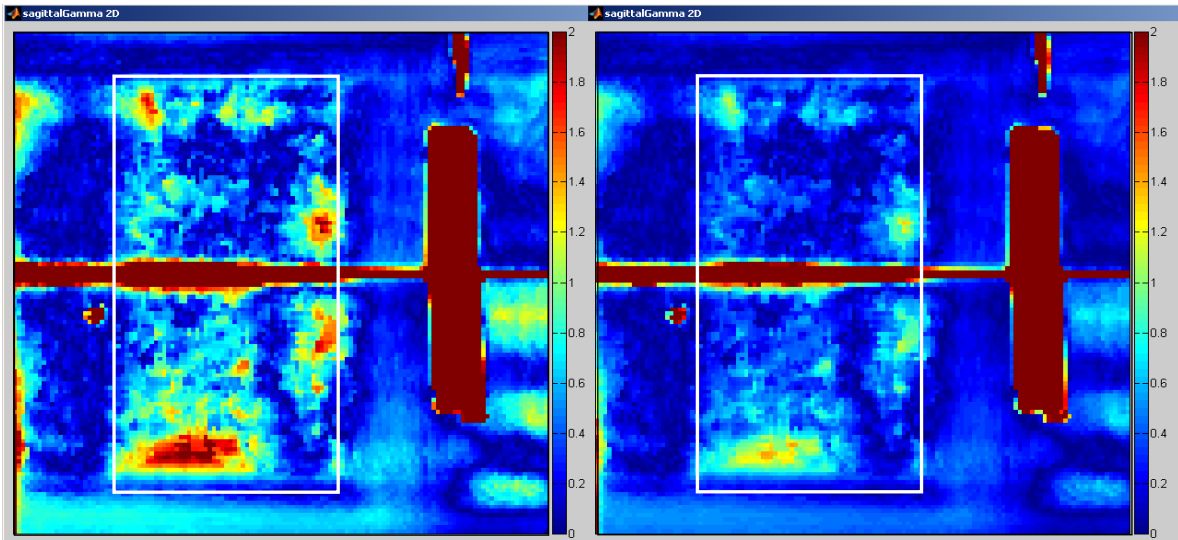
b) Anterior to posterior profile

c) Superior to inferior profile



d) Axial: 3%/2 mm, 97% pass; scale 1mm = 0.79 mm

e) Axial: 5%/3 mm, 100% pass; scale 1mm = 0.79 mm

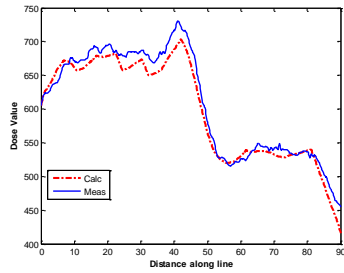


f) Sagittal: 3%/2 mm, 92% pass; scale 1 mm = 1.09 mm

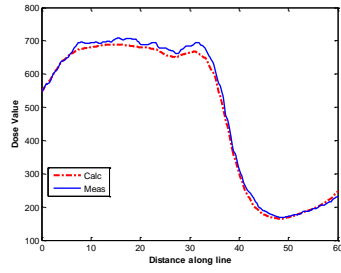
g) Sagittal: 5%/3 mm, 99% pass; scale 1 mm = 1.09 mm

Figure 6.28 Varian 10 MV: IMRT H&N delivery single irradiation (number 1): Gamma maps and dose profiles.

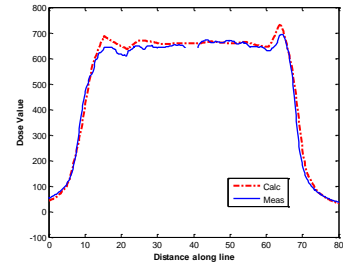




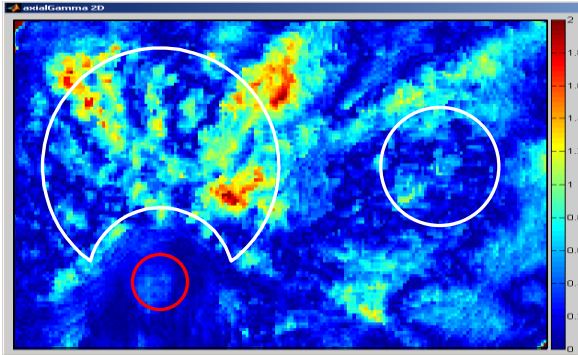
a) Lateral profile



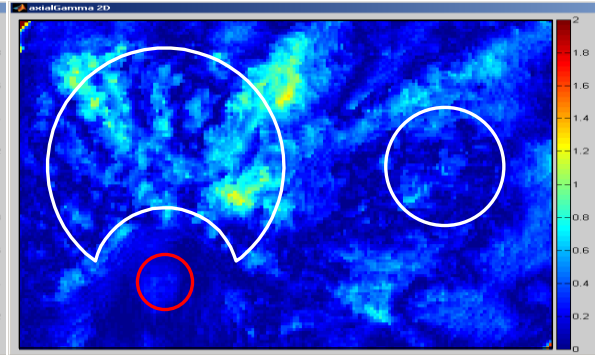
b) Anterior to posterior profile



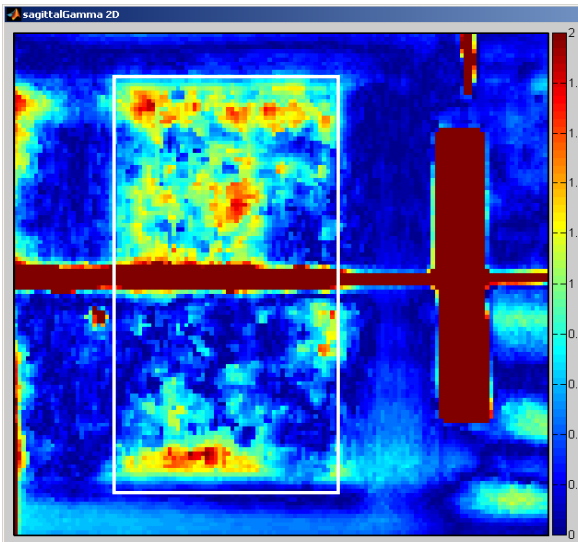
c) Superior to inferior profile



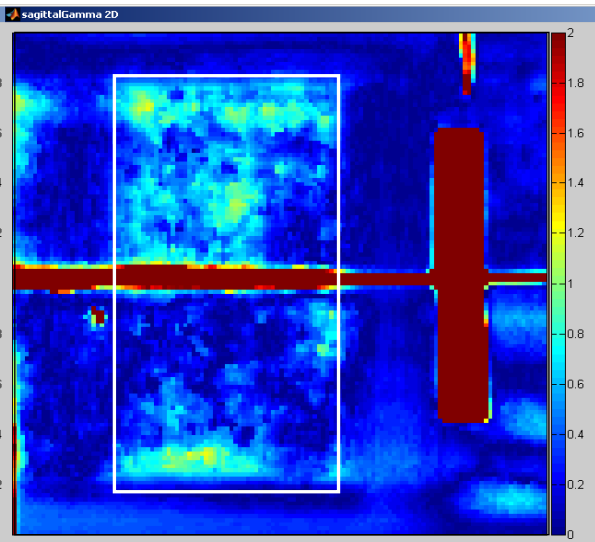
d) Axial: 3%/2 mm, 93% pass; scale 1mm = 0.79 mm



e) Axial: 5%/3 mm, 100% pass; scale 1mm = 0.79 mm

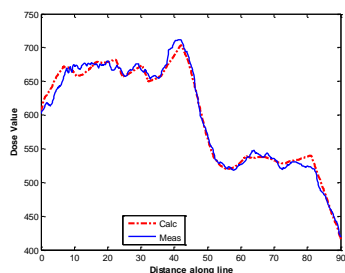


f) Sagittal: 3%/2 mm, 90% pass; scale 1 mm = 1.09 mm

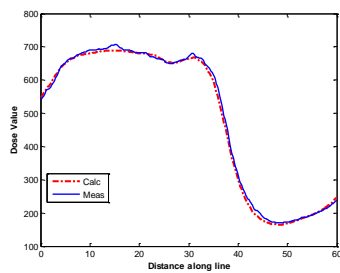


g) Sagittal: 5%/3 mm, 98% pass; scale 1 mm = 1.09 mm

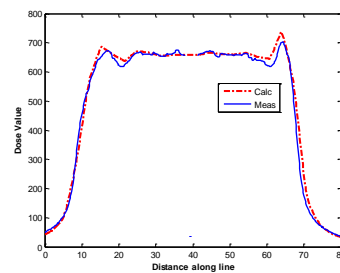
Figure 6.29 Varian 10 MV: IMRT H&N delivery single irradiation (number 2): Gamma maps and dose profiles.



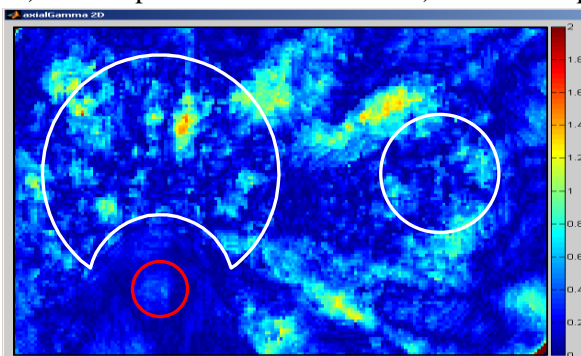
a) Lateral profile



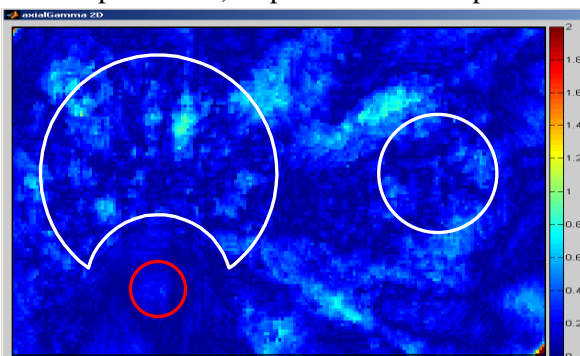
b) Anterior to posterior profile



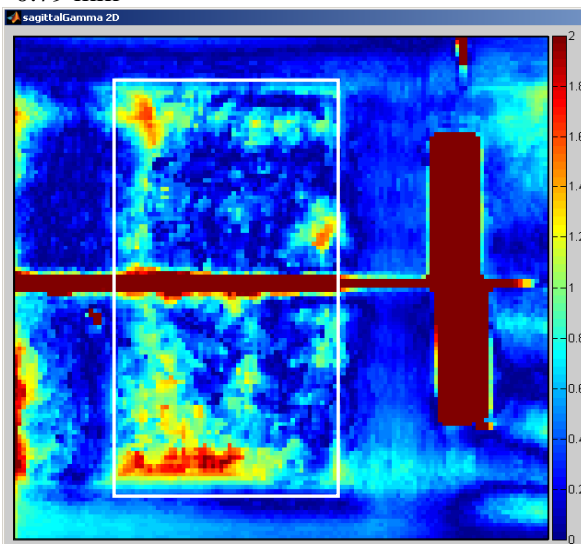
c) Superior to inferior profile



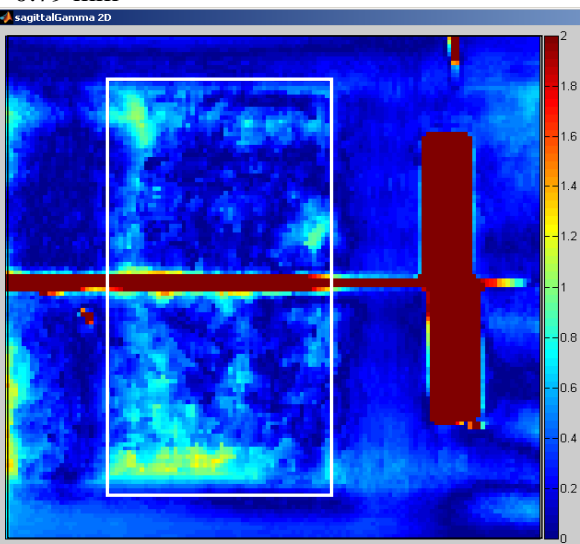
d) Axial: 3%/2 mm, 99% pass; scale 1mm = 0.79 mm



e) Axial: 5%/3 mm, 100% pass; scale 1mm = 0.79 mm



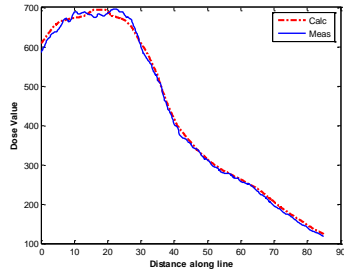
f) Sagittal: 3%/2 mm, 93% pass; scale 1 mm = 1.09 mm



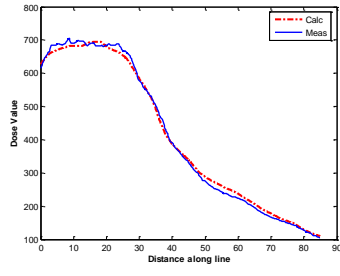
g) Sagittal: 5%/3 mm, 100% pass; scale 1 mm = 1.09 mm

Figure 6.30 Varian 10 MV: IMRT H&N delivery single irradiation (number 3): Gamma maps and dose profiles.

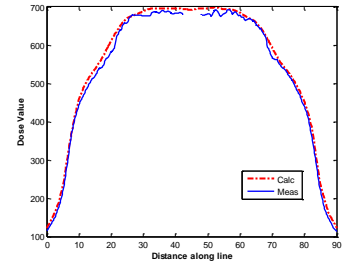
### 6.3.2 Varian 10 MV: Delivery for the SBRT lung plan



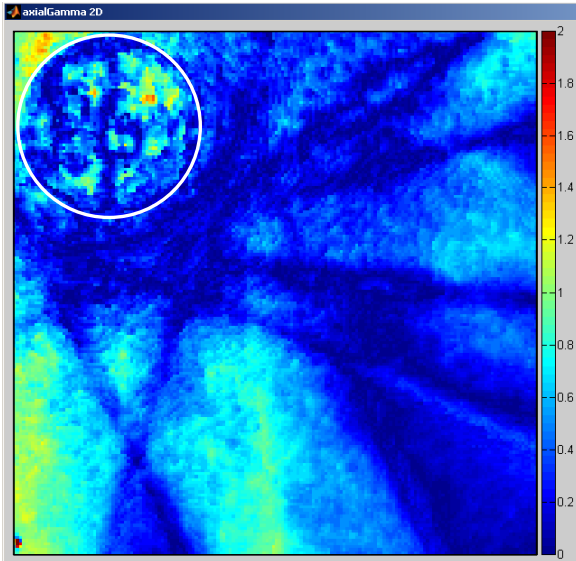
a) Lateral profile



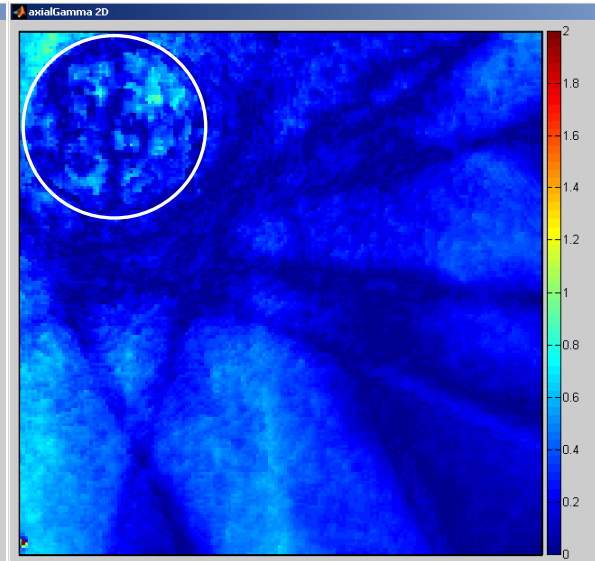
b) Anterior to posterior profile



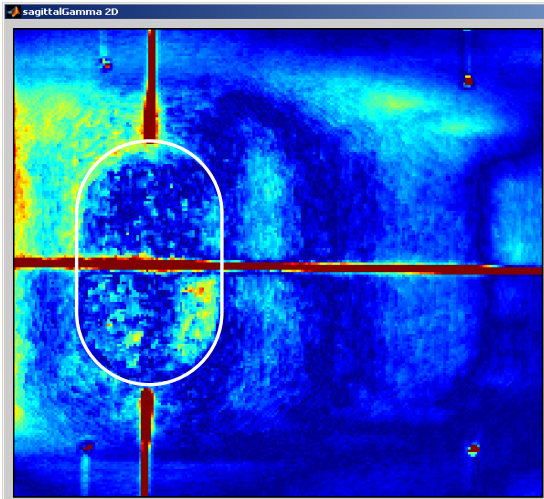
c) Superior to inferior profile



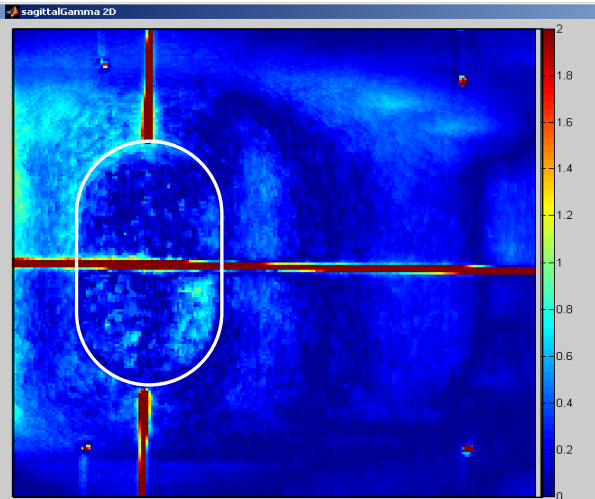
d) Axial: 3%/2 mm, 98% pass; scale 1mm = 0.82 mm



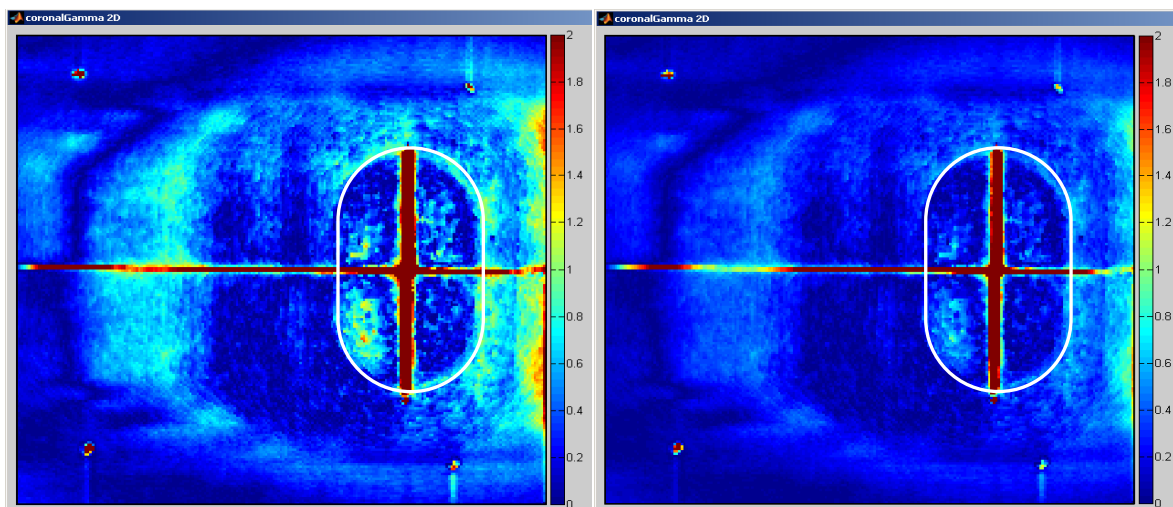
e) Axial: 5%/3 mm, 100% pass; scale 1mm = 0.82 mm



f) Sagittal: 3%/2 mm, 97% pass; scale 1 mm = 0.65 mm

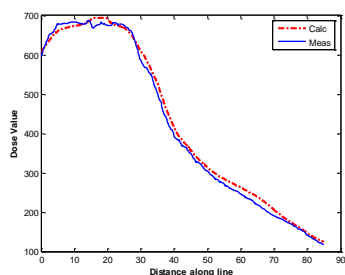


g) Sagittal: 5%/3 mm, 100% pass; scale 1 mm = 0.65 mm

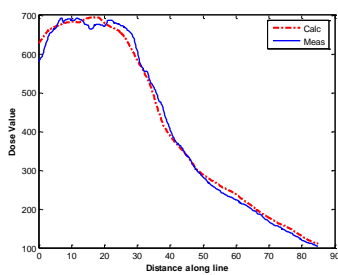


h) Coronal: 3%/2 mm, 98% pass; scale 1 mm = 0.65 mm      i) Coronal: 5%/3 mm, 100% pass; scale 1 mm = 0.65 mm

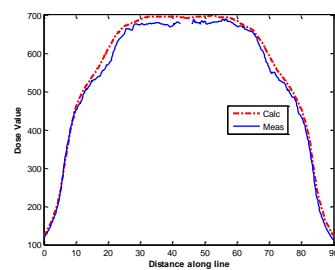
Figure 6.31 Varian 10 MV: SBRT lung delivery single irradiation (number 1): Gamma maps and dose profiles.



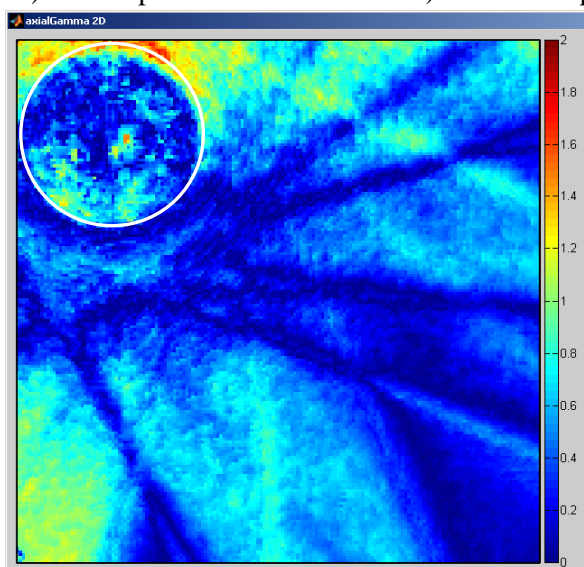
a) Lateral profile



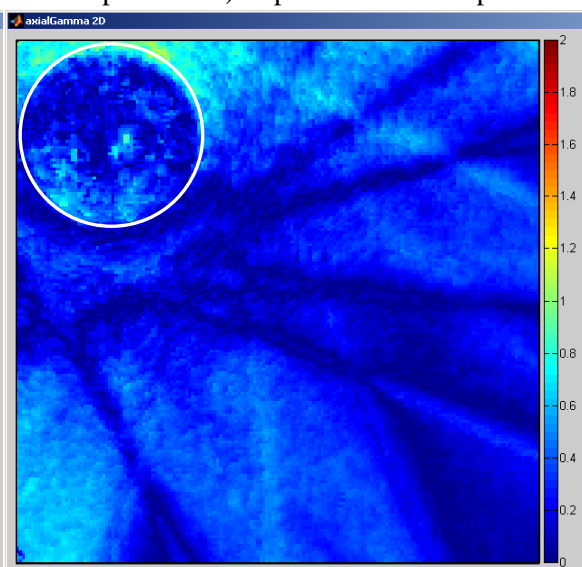
b) Anterior to posterior profile



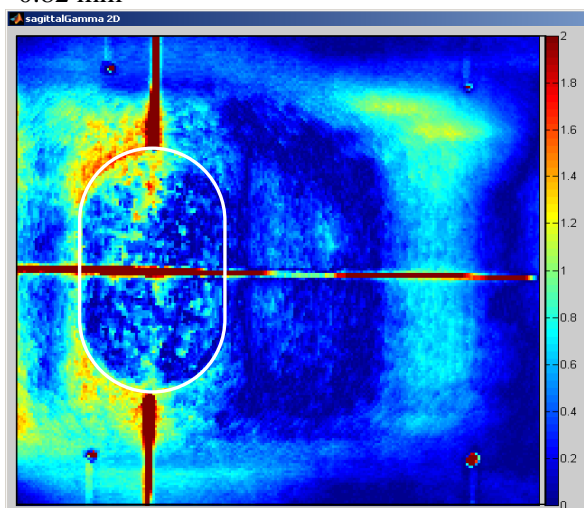
c) Superior to inferior profile



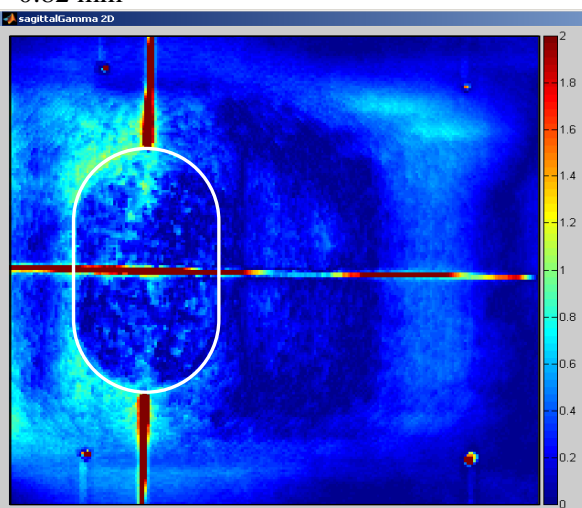
d) Axial: 3%/2 mm, 96% pass; scale 1mm = 0.82 mm



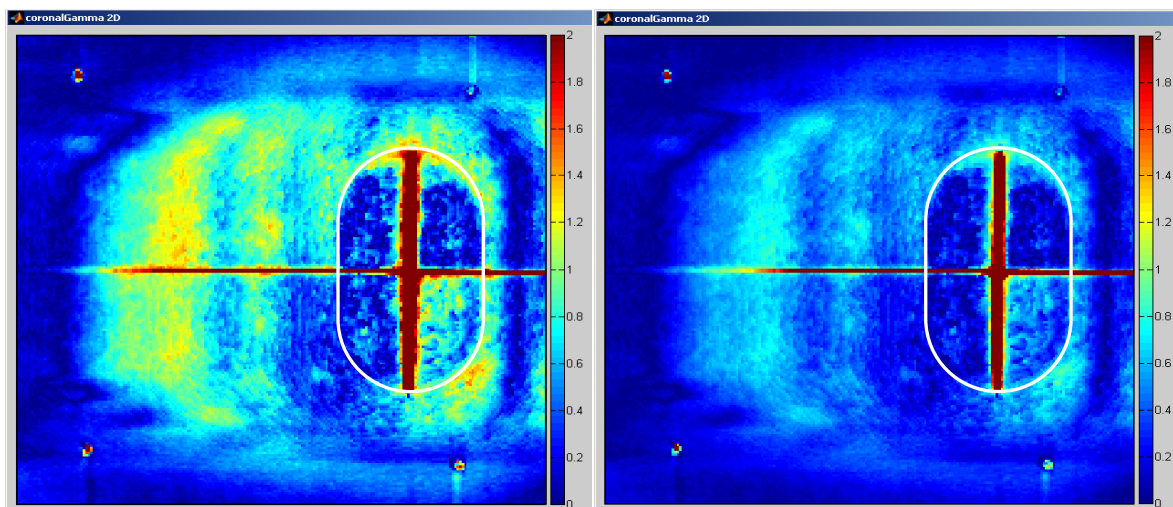
e) Axial: 5%/3 mm, 100% pass; scale 1mm = 0.82 mm



f) Sagittal: 3%/2 mm, 95% pass; scale 1 mm = 0.65 mm



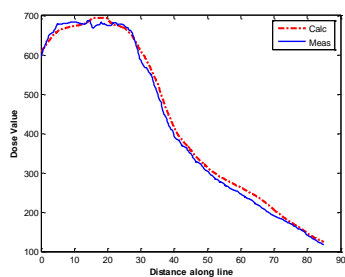
g) Sagittal: 5%/3 mm, 100% pass; scale 1 mm = 0.65 mm



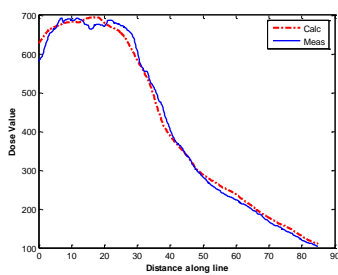
h) Coronal: 3%/2 mm, 91% pass; scale 1 mm = 0.65 mm      i) Coronal: 5%/3 mm, 100% pass; scale 1 mm = 0.65 mm

Figure 6.32 Varian 10 MV: SBRT lung delivery single irradiation (number 2): Gamma maps and dose profiles.

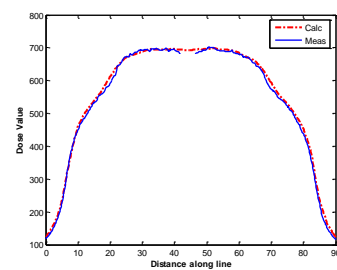




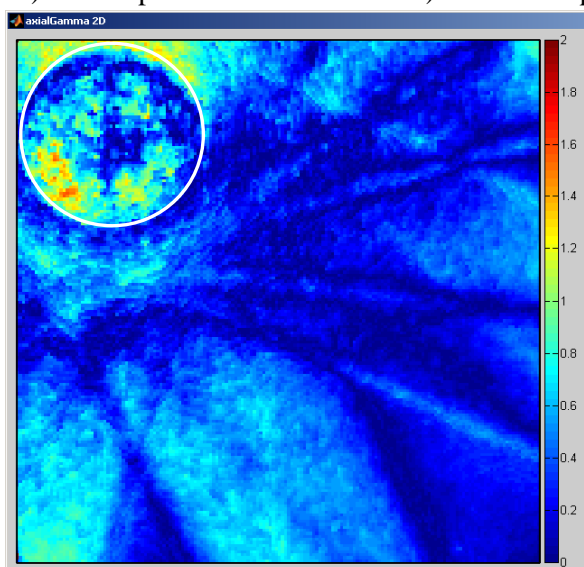
a) Lateral profile



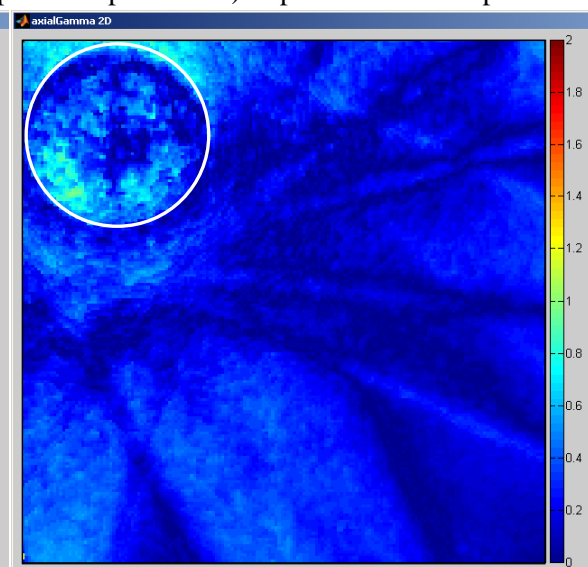
b) Anterior to posterior profile



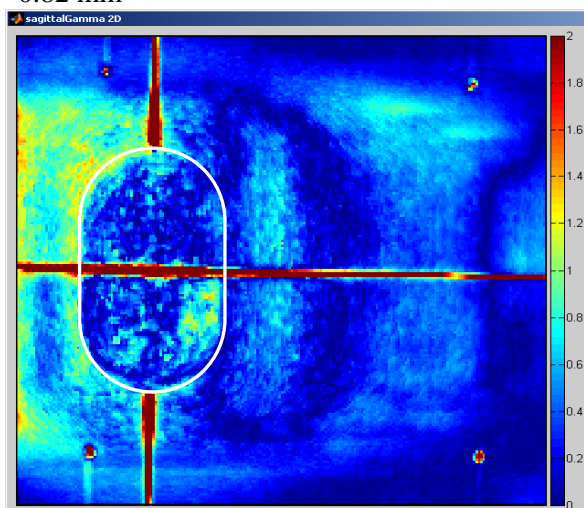
c) Superior to inferior profile



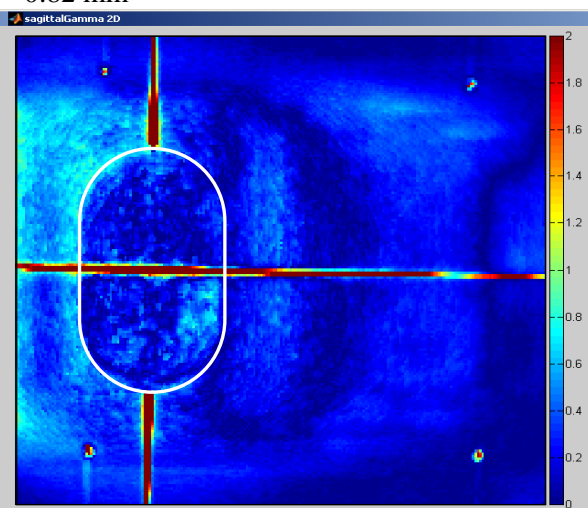
d) Axial: 3%/2 mm, 98% pass; scale 1mm = 0.82 mm



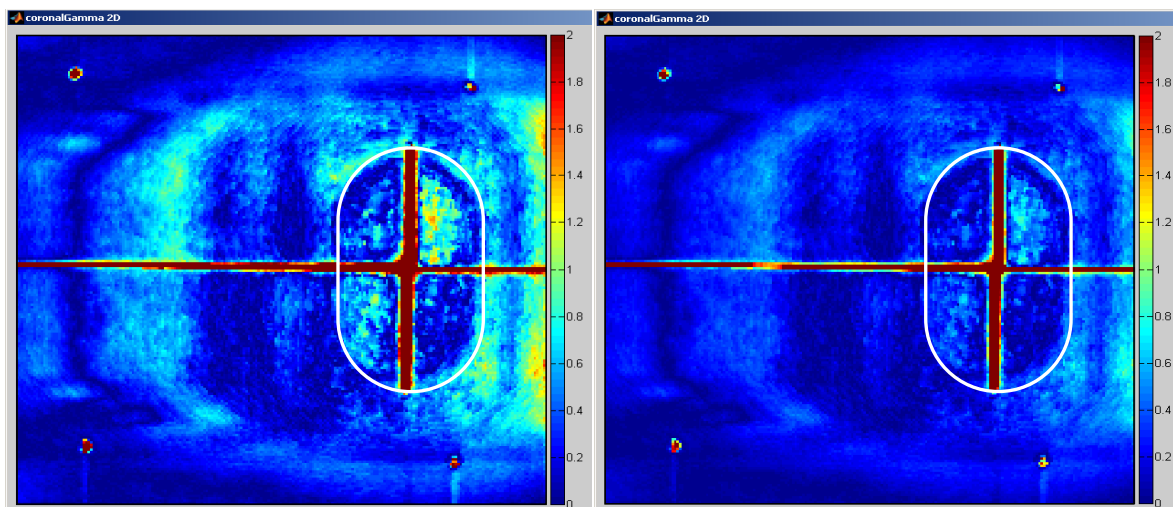
e) Axial: 5%/3 mm, 100% pass; scale 1mm = 0.82 mm



f) Sagittal: 3%/2 mm, 97% pass; scale 1 mm = 0.65 mm



g) Sagittal: 5%/3 mm, 100% pass; scale 1 mm = 0.65 mm

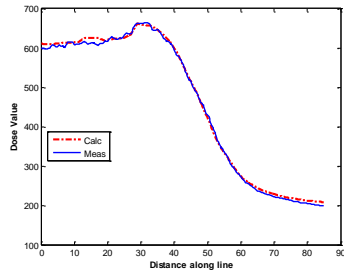


h) Coronal: 3%/2 mm, 98% pass; scale 1 mm = 0.65 mm      i) Coronal: 5%/3 mm, 100% pass; scale 1 mm = 0.65 mm

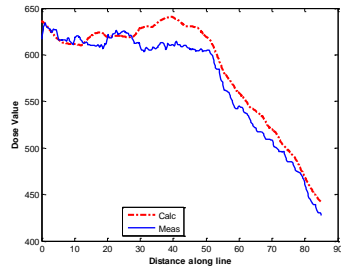
Figure 6.33 Varian 10 MV: SBRT lung delivery single irradiation (number 3): Gamma maps and dose profiles.



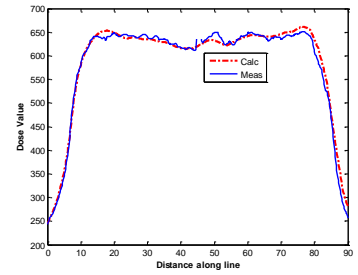
### 6.3.3 Varian 10 MV: Delivery for the IMRT lung plan



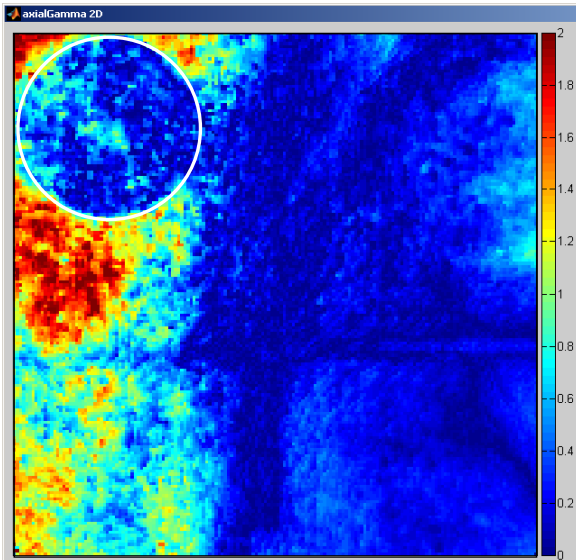
a) Lateral profile



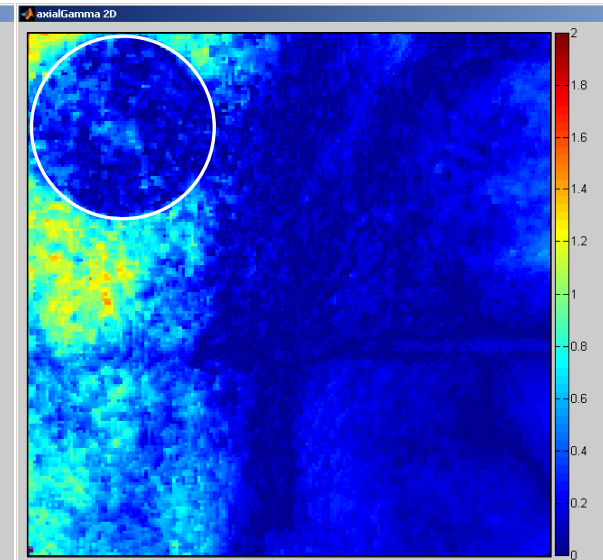
b) Anterior to posterior profile



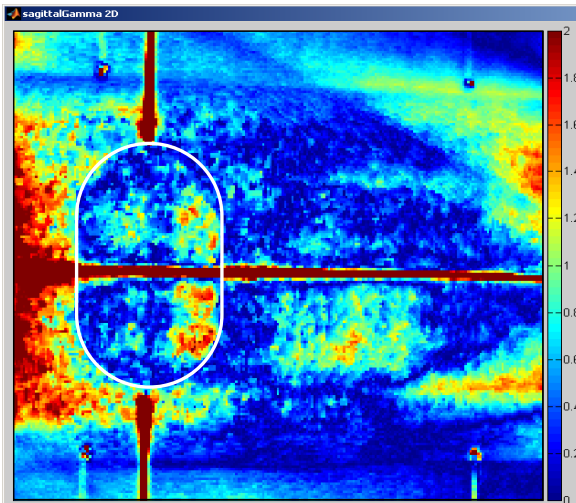
c) Superior to inferior profile



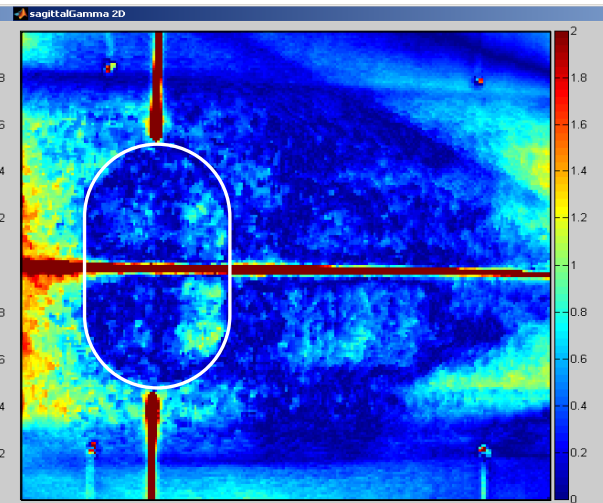
d) Axial: 3%/2 mm, 88% pass; scale 1mm = 0.82 mm



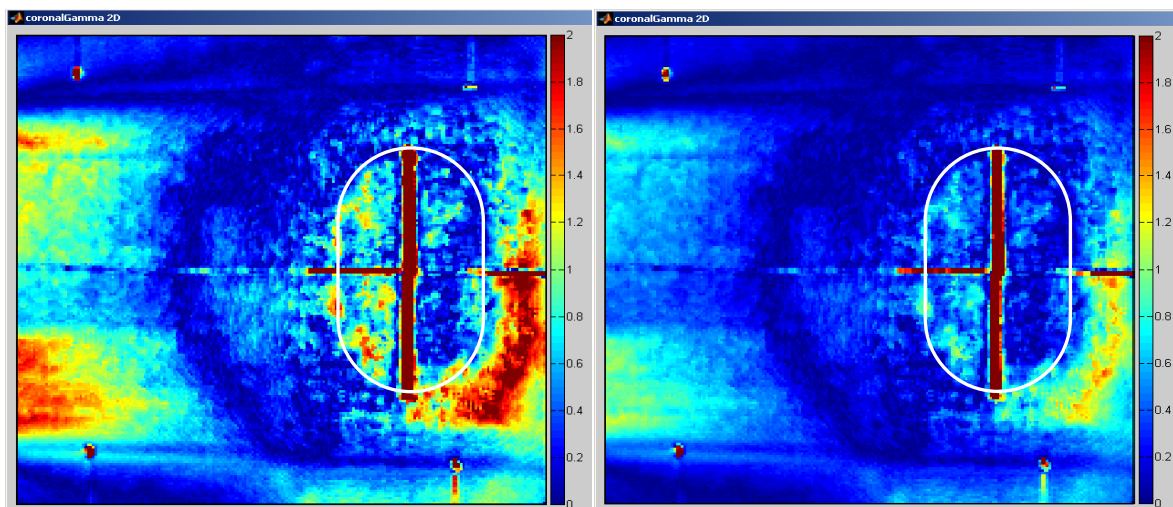
e) Axial: 5%/3 mm, 97% pass; scale 1mm = 0.82 mm



f) Sagittal: 3%/2 mm, 84% pass; scale 1 mm = 0.65 mm

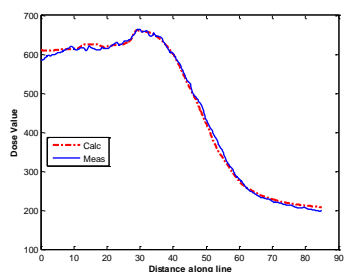


g) Sagittal: 5%/3 mm, 95% pass; scale 1 mm = 0.65 mm

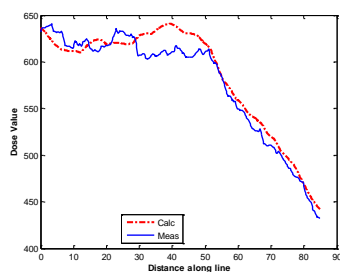


h) Coronal: 3%/2 mm, 86% pass; scale 1 mm = 0.65 mm      i) Coronal: 5%/3 mm, 98% pass; scale 1 mm = 0.65 mm

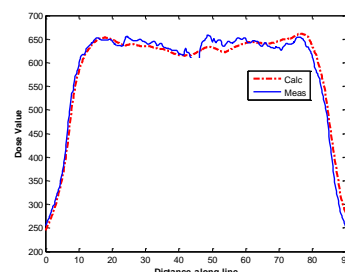
Figure 6.34 Varian 10 MV: IMRT lung delivery single irradiation (number 1): Gamma maps and dose profiles.



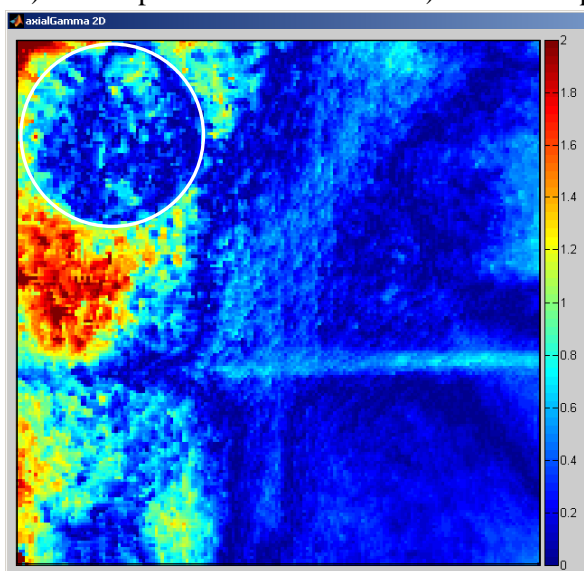
a) Lateral profile



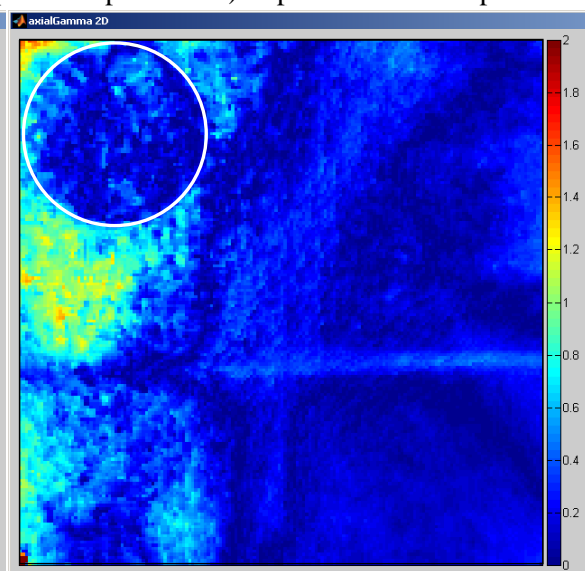
b) Anterior to posterior profile



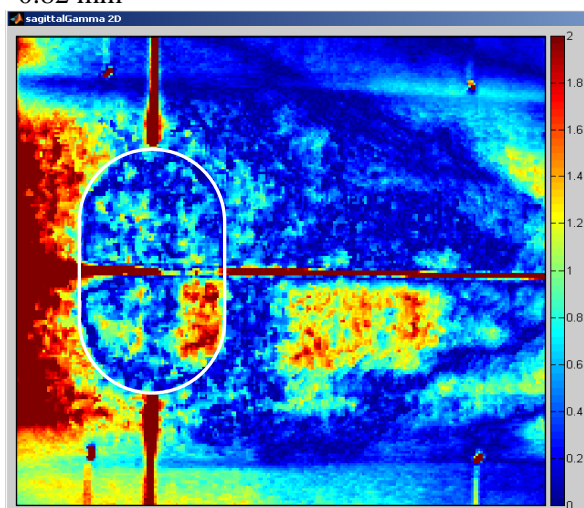
c) Superior to inferior profile



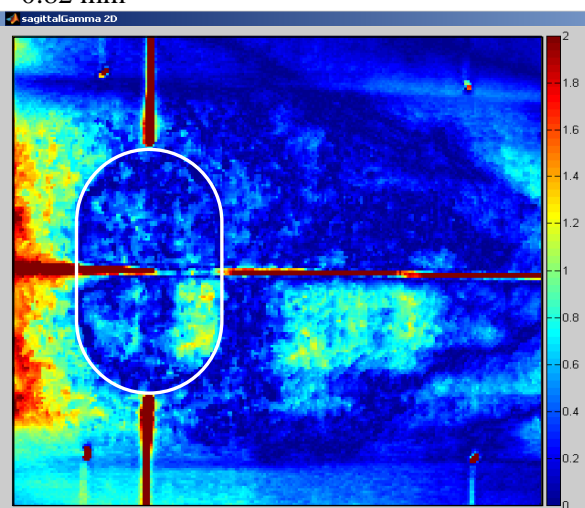
d) Axial: 3%/2 mm, 90% pass; scale 1mm = 0.82 mm



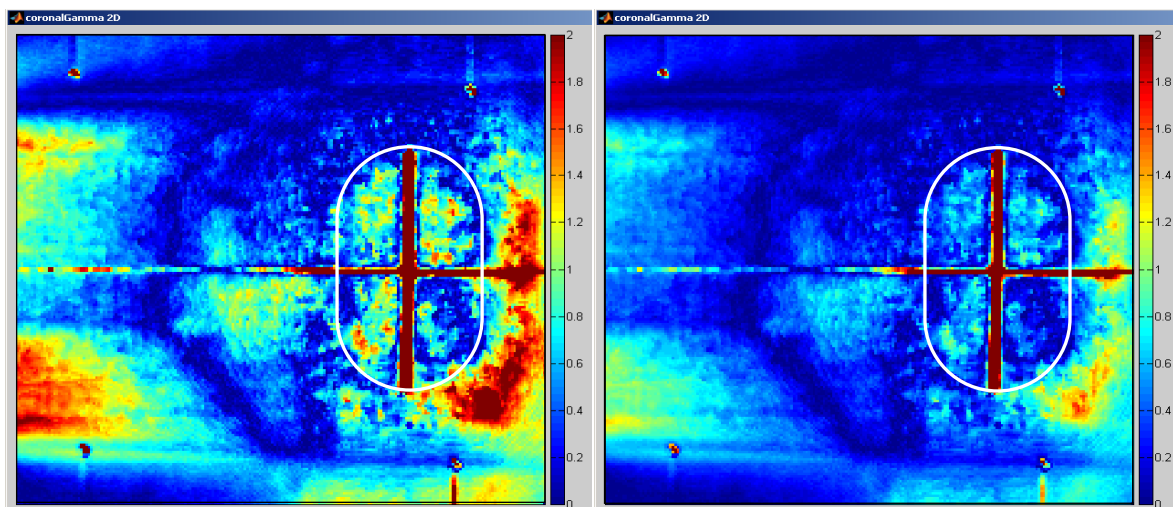
e) Axial: 5%/3 mm, 98% pass; scale 1mm = 0.82 mm



f) Sagittal: 3%/2 mm, 79% pass; scale 1 mm = 0.65 mm

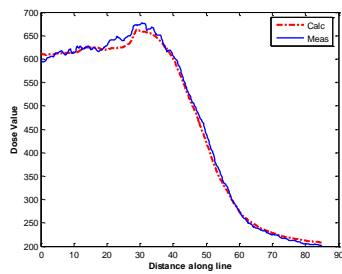


g) Sagittal: 5%/3 mm, 94% pass; scale 1 mm = 0.65 mm

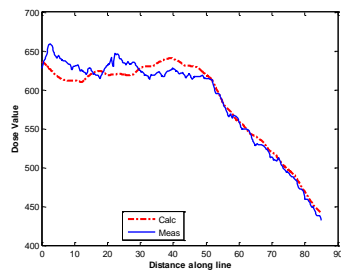


h) Coronal: 3%/2 mm, 83% pass; scale 1 mm = 0.65 mm      i) Coronal: 5%/3 mm, 98% pass; scale 1 mm = 0.65 mm

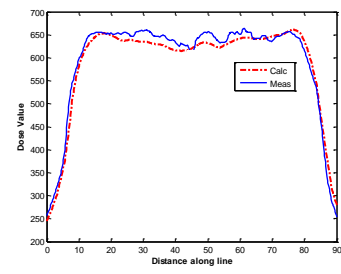
Figure 6.35 Varian 10 MV: IMRT lung delivery single irradiation (number 2): Gamma maps and dose profiles.



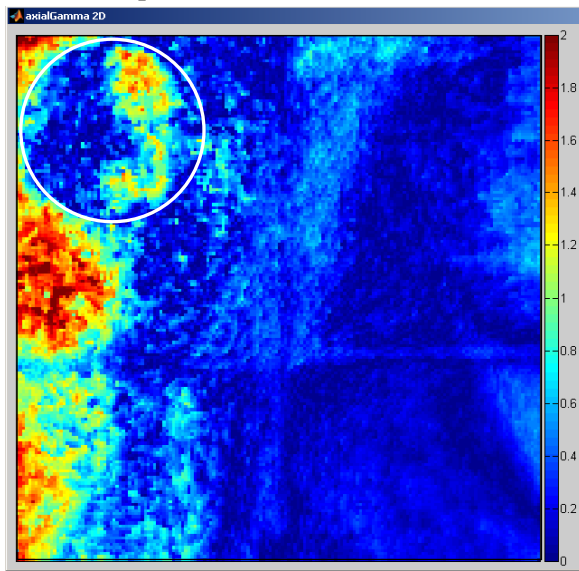
a) Lateral profile



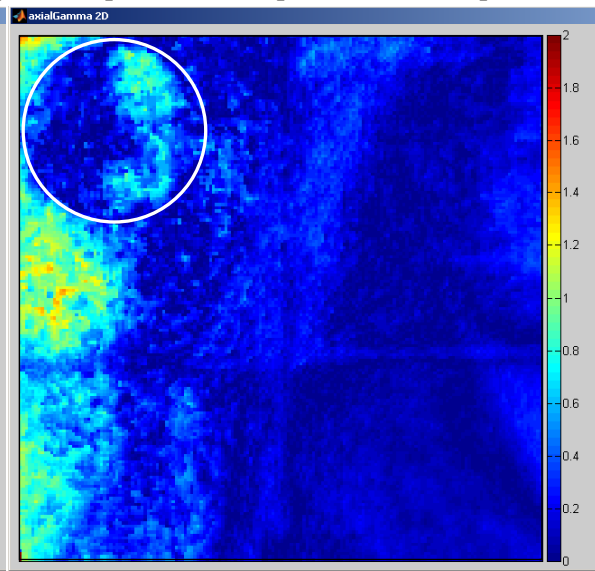
b) Anterior to posterior profile



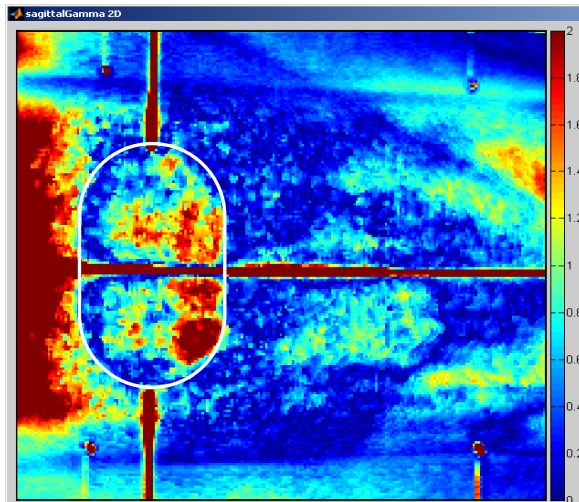
c) Superior to inferior profile



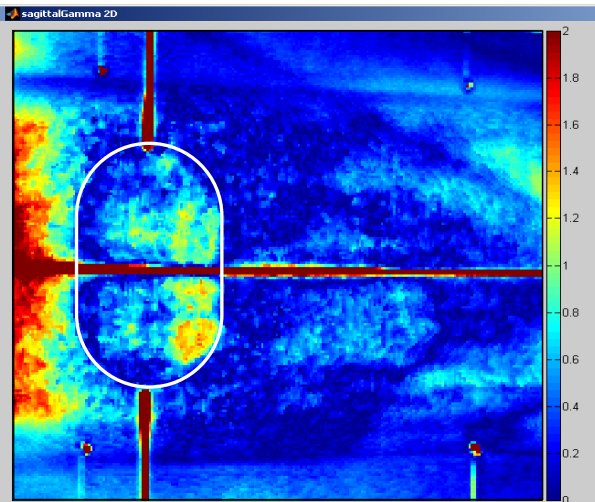
d) Axial: 3%/2 mm, 90% pass; scale 1mm = 0.82 mm



e) Axial: 5%/3 mm, 98% pass; scale 1mm = 0.82 mm

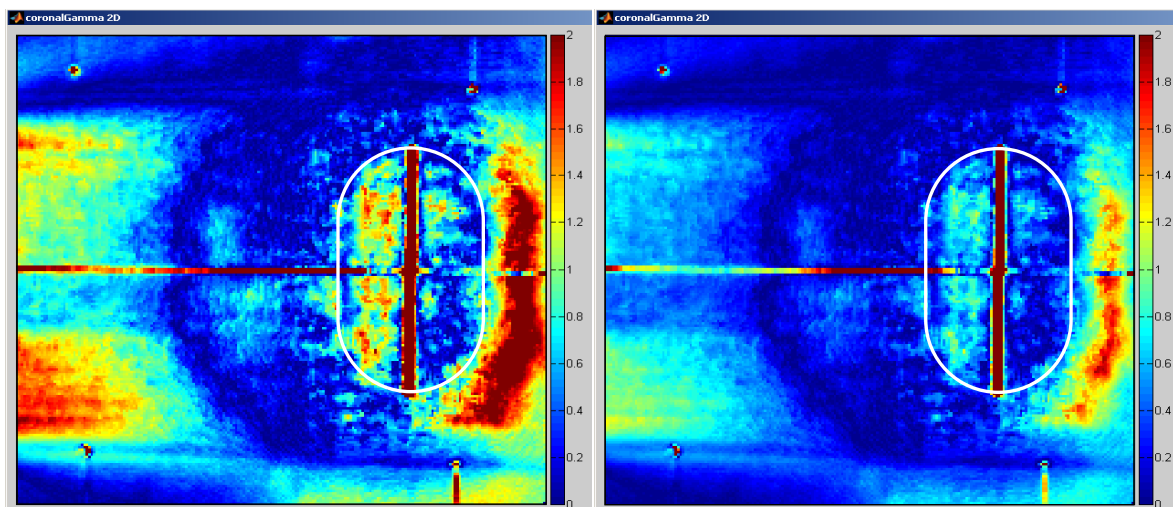


f) Sagittal: 3%/2 mm, 82% pass; scale 1 mm = 0.65 mm



g) Sagittal: 5%/3 mm, 93% pass; scale 1 mm = 0.65 mm





h) Coronal: 3%/2 mm, 80% pass; scale 1 mm = 0.65 mm      i) Coronal: 5%/3 mm, 96% pass; scale 1 mm = 0.65 mm

Figure 6.36 Varian 10 MV: IMRT lung delivery single irradiation (number 3): Gamma maps and dose profiles.

## **Chapter 7 Acknowledgement**

This work was supported by US Public Health Services grants CA010953, CA081647; and R01 grant CA85181 awarded by US National Cancer Institute, US Department of Human and Health Services.

## Chapter 8 References

- <sup>1</sup> GA Ezzell, JM Galvin, D Low, JR Palta, I Rosen, MB Sharpe, P Xia, Y Xiao, L Xing, and CX Yu, "Guidance document on delivery, treatment planning, and clinical implementation of IMRT: Report of the IMRT subcommittee of the AAPM radiation therapy committee," *Medical Physics* **30** (8), 2089-2115 (2003).
- <sup>2</sup> P Alvarez, A Molineu, N Hernandez, D Followill, and G Ibbott, "SU-FF-T-403: Evaluation of Doses Delivered by SBRT to the Lung of An Anthropomorphic Thorax Phantom," *Medical Physics* **32** (6), 2043-2044 (2005).
- <sup>3</sup> P Alvarez, A Molineu, N Hernandez, D Followill, and G Ibbott, "TU-E-224A-01: Evaluation of Heterogeneity Corrections Algorithms Through the Irradiation of a Lung Phantom," *Med Phys* **33** (6), 2214 (2006).
- <sup>4</sup> P Alvarez, A Molineu, N Hernandez, D Followill, and G Ibbott, "MO-D-AUD-04: A Comparison of Heterogeneity Correction Algorithms Within a Lung PTV," *Medical Physics* **34** (6), 2521 (2007).
- <sup>5</sup> A Molineu, N Hernandez, P Alvarez, D Followill, and G Ibbott, "SU-FF-T-148: IMRT Head and Neck Phantom Irradiations: Correlation of Results with Institution Size," *Medical Physics* **32** (6), 1983-1984 (2005).
- <sup>6</sup> D Followill, A Molineu, P Alvarez, and G Ibbott, "TH-D-224C-02: The State of Radiotherapy Physics Through The Eyes of a Quality Auditor," *Medical Physics* **33** (6), 2283 (2006).
- <sup>7</sup> AF Bielajew, H Hirayama, WR Nelson, and DWO Rogers, "History, overview and recent improvements of EGS4," National Research Council of Canada Report (1994).
- <sup>8</sup> J Briesmeister, Report No. LA-12625-M, 1993.



- <sup>9</sup> J Baro, J Sempau, J Fernandez-Varea, and F Salvat, "PENELOPE: an algorithm for Monte Carlo simulation of the penetration and energy loss of electrons and positrons in matter," Nucl. Instrum.Methods D **100**, 31-46 (1995).
- <sup>10</sup> IJ Chetty, B Curran, JE Cygler, JJ DeMarco, G Ezzell, BA Faddegon, I Kawrakow, PJ Keall, H Liu, CM Ma, DW Rogers, J Seuntjens, D Sheikh-Bagheri, and JV Siebers, "Report of the AAPM Task Group No. 105: issues associated with clinical implementation of Monte Carlo-based photon and electron external beam treatment planning," Med Phys **34** (12), 4818-4853 (2007).
- <sup>11</sup> C-M Ma, E Mok, A Kapur, T Pawlicki, D Findley, S Brain, K Forster, and AL Boyer, "Clinical implementation of a Monte Carlo treatment planning system," Medical Physics **26** (10), 2133-2143 (1999).
- <sup>12</sup> M Miften, M Wiesmeyer, A Kapur, and CM Ma, "Comparison of RTP dose distributions in heterogeneous phantoms with the BEAM Monte Carlo simulation system," Journal of Applied Clinical Medical Physics **2** (1), 21-31 (2001).
- <sup>13</sup> FC du Plessis, CA Willemse, MG Lotter, and L Goedhals, "Comparison of the Batho, ETAR and Monte Carlo dose calculation methods in CT based patient models," Medical Physics **28** (4), 582-589 (2001).
- <sup>14</sup> L Wang, E Yorke, and CS Chui, "Monte Carlo evaluation of 6 MV intensity modulated radiotherapy plans for head and neck and lung treatments," Medical Physics **29** (11), 2705-2717 (2002).
- <sup>15</sup> L Wang, E Yorke, G Desobry, and CS Chui, "Dosimetric advantage of using 6 MV over 15 MV photons in conformal therapy of lung cancer: Monte Carlo studies in patient geometries.[see comment]," Journal of Applied Clinical Medical Physics **3** (1), 51-59 (2002).

- <sup>16</sup> PN McDermott, T He, and A DeYoung, "Dose calculation accuracy of lung planning with a commercial IMRT treatment planning system," *Journal of Applied Clinical Medical Physics* **4** (4), 341-351 (2003).
- <sup>17</sup> R Jeraj, PJ Keall, and JV Siebers, "The effect of dose calculation accuracy on inverse treatment planning," *Phys Med Biol* **47** (3), 391-407 (2002).
- <sup>18</sup> PJ Keall, J Siebers, and R Mohan, presented at the Proceedings of the 13th ICCR, Heidelberg, GE, 425-427 (2000)
- <sup>19</sup> MR Arnfield, CH Siantar, J Siebers, P Garmon, L Cox, and R Mohan, "The impact of electron transport on the accuracy of computed dose," *Medical Physics* **27** (6), 1266-1274 (2000).
- <sup>20</sup> TD Solberg, JJ DeMarco, FE Holly, JB Smathers, and AA DeSalles, "Monte Carlo treatment planning for stereotactic radiosurgery," *Radiother Oncol* **49** (1), 73-84 (1998).
- <sup>21</sup> SN Rustgi, AK Rustgi, SB Jiang, and KM Ayyangar, "Dose perturbation caused by high-density inhomogeneities in small beams in stereotactic radiosurgery," *Phys Med Biol* **43** (12), 3509-3518 (1998).
- <sup>22</sup> J Sempau, SJ Wilderman, and AF Bielajew, "DPM, a fast, accurate Monte Carlo code optimized for photon and electron radiotherapy treatment planning dose calculations," *Phys Med Biol* **45** (8), 2263-2291 (2000).
- <sup>23</sup> MJ Berger, "Monte Carlo calculation of the penetration and diffusion of fast charged particles," *Methods Comput. Phys.* **1**, 135-215 (1963).
- <sup>24</sup> IJ Chetty, PM Charland, N Tyagi, DL McShan, BA Fraass, and AF Bielajew, "Photon beam relative dose validation of the DPM Monte Carlo code in lung-equivalent media," *Medical physics.* **30** (4), 563-573 (2003).

- 25 M Fragoso, S Pillai, TD Solberg, and IJ Chetty, "Experimental verification and clinical  
implementation of a commercial Monte Carlo electron beam dose calculation  
algorithm," *Medical Physics* **35** (3), 1028-1038 (2008).
- 26 S Davidson, J Cui, G Ibbott, D Followill, and J Deasy, "A flexible Monte Carlo tool for  
patient or phantom specific calculations: comparison with preliminary validation  
measurements," *Journal of Physics: Conference Series* (2008).
- 27 RC Taylor, VM Tello, CB Schroy, M Vossler, and WF Hanson, "A generic off-axis  
energy correction for linac photon beam dosimetry," *Medical Physics* **25** (5), 662-667  
(1998).
- 28 Fatigue-function, <http://www.itl.nist.gov/div898/handbook/eda/section3/eda366a.htm>.
- 29 D Sheikh-Bagheri and DWO Rogers, "Monte Carlo calculation of nine megavoltage  
photon beam spectra using the BEAM code," *Medical Physics* **29** (3), 391-402 (2002).
- 30 HH Liu, TR Mackie, and EC McCullough, "A dual source photon beam model used in  
convolution/superposition dose calculations for clinical megavoltage x-ray beams,"  
*Medical Physics* **24** (12), 1960-1974 (1997).
- 31 M Fippel, F Haryanto, O Dohm, F Nusslin, and S Kriesen, "A virtual photon energy  
fluence model for Monte Carlo dose calculation," *Medical Physics* **30** (3), 301-311  
(2003).
- 32 B Libby, J Siebers, and R Mohan, "Validation of Monte Carlo generated phase-space  
descriptions of medical linear accelerators," *Med Phys* **26** (8), 1476-1483 (1999).
- 33 MR Arnfield, K Otto, VR Aroumougame, and RD Alkins, "The use of film dosimetry  
of the penumbra region to improve the accuracy of intensity modulated radiotherapy,"  
*Med Phys* **32** (1), 12-18 (2005).
- 34 JO Deasy, AI Blanco, and VH Clark, "CERR: a computational environment for  
radiotherapy research," *Med Phys* **30** (5), 979-985 (2003).

35 D Rogers, B Faddegon, G Ding, C Ma, J We, and T Mackie, "BEAM: a Monte Carlo  
code to simulate radiotherapy treatment units," *Med Phys* **22** (5), 503-524 (1995).

36 I Kawrakow, presented at the Proceedings of the Monte Carlo 2000 Conference, Lisbon  
(2000)

37 CLH Siantar, RS Walling, TP Daly, B Faddegon, N Albright, P Bergstrom, AF  
Bielajew, C Chuang, D Garrett, RK House, D Knapp, DJ Wieczorek, and LJ Verhey,  
"Description and dosimetric verification of the [small-caps PEREGRINE] Monte Carlo  
dose calculation system for photon beams incident on a water phantom," *Medical  
Physics* **28** (7), 1322-1337 (2001).

38 H Neuenschwander and EJ Born, "A macro Monte Carlo method for electron beam  
dose calculations," *Physics in Medicine and Biology* (1), 107 (1992).

39 DA Jaffray, JJ Battista, A Fenster, and P Munro, "X-ray sources of medical linear  
accelerators: Focal and extra-focal radiation," *Medical Physics* **20** (5), 1417-1427  
(1993).

40 PJ Keall, JV Siebers, B Libby, and R Mohan, "Determining the incident electron  
fluence for Monte Carlo-based photon treatment planning using a standard measured  
data set," *Medical Physics* **30** (4), 574-582 (2003).

41 B Parker, University of Texas, 2004.

42 SH Cho, ON Vassiliev, S Lee, HH Liu, GS Ibbott, and R Mohan, "Reference photon  
dosimetry data and reference phase space data for the 6 MV photon beam from Varian  
Clinac 2100 series linear accelerators," *Medical Physics* **32** (1), 137-148 (2005).

43 RA Horn, "Computer programs for output and depth dose from hyperbolic equations,"  
*Medical Physics* **8** (1), 108-110 (1981).

44 in *Pinnacle3 Physics Reference Guide* (2005), pp. 3-35.

45 D Followill, D Radford-Evans, C Cherry, A Molineu, G Fisher, W Hanson, and G  
Ibbott, "Design, Development, and Implementation of the Radiological Physics

Center's Pelvis and Thorax Anthropomorphic Quality Assurance Phantoms," Med. Phys. (2007).

- 46 A Molineu, DS Followill, PA Balter, WF Hanson, MT Gillin, MS Huq, A Eisbruch, and GS Ibbott, "Design and implementation of an anthropomorphic quality assurance phantom for intensity-modulated radiation therapy for the Radiation Therapy Oncology Group," International Journal of Radiation Oncology\*Biology\*Physics **63** (2), 577-583 (2005).
- 47 WB Harms, Sr., DA Low, JW Wong, and JA Purdy, "A software tool for the quantitative evaluation of 3D dose calculation algorithms," Med Phys **25** (10), 1830-1836 (1998).
- 48 DA Low, WB Harms, S Mutic, and JA Purdy, "A technique for the quantitative evaluation of dose distributions," Med Phys **25** (5), 656-661 (1998).
- 49 MS Huq, H Song, P Andreo, and CJ Houser, "Reference dosimetry in clinical high-energy electron beams: Comparison of the AAPM TG-51 and AAPM TG-21 dosimetry protocols," Medical Physics **28** (10), 2077-2087 (2001).
- 50 N Tyagi, JM Moran, DW Litzenberg, AF Bielajew, BA Fraass, and IJ Chetty, "Experimental verification of a Monte Carlo-based MLC simulation model for IMRT dose calculation," Medical Physics **34** (2), 651-663 (2007).
- 51 SE Davidson, RA Popple, GS Ibbott, and DS Followill, "Technical note: Heterogeneity dose calculation accuracy in IMRT: study of five commercial treatment planning systems using an anthropomorphic thorax phantom," Med Phys **35** (12), 5434-5439 (2008).
- 52 TH Kirby, WF Hanson, and DA Johnston, "Uncertainty analysis of absorbed dose calculations from thermoluminescence dosimeters," Medical physics. **19** (6), 1427-1433 (1992).

- 53 S Devic, J Seuntjens, G Hegyi, EB Podgorsak, CG Soares, AS Kirov, I Ali, JF  
Williamson, and A Elizondo, "Dosimetric properties of improved GafChromic films for  
seven different digitizers," *Medical Physics* **31** (9), 2392-2401 (2004).
- 54 A Rangel and P Dunscombe, "Tolerances on MLC leaf position accuracy for IMRT  
delivery with a dynamic MLC," *Med Phys* **36** (7), 3304-3309 (2009).
- 55 PA Jursinic, "Clinical implementation of a two-component x-ray source model for  
calculation of head-scatter factors," *Med Phys* **24** (12), 2001-2007 (1997).
- 56 A Ahnesjo, T Knoos, and A Montelius, "Application of the convolution method for  
calculation of output factors for therapy photon beams," *Medical Physics* **19** (2), 295-  
301 (1992).
- 57 PB Dunscombe and JM Nieminen, "On the field-size dependence of relative output  
from a linear accelerator," *Med Phys* **19** (6), 1441-1444 (1992).
- 58 MB Sharpe, DA Jaffray, JJ Battista, and P Munro, "Extrafocal radiation: a unified  
approach to the prediction of beam penumbra and output factors for megavoltage x-ray  
beams," *Med Phys* **22** (12), 2065-2074 (1995).
- 59 MK Yu and R Sloboda, "Analytical representation of head scatter factors for shaped  
photon beams using a two-component x-ray source model," *Med Phys* **22** (12), 2045-  
2055 (1995).
- 60 A Ahnesjo, "Analytic modeling of photon scatter from flattening filters in photon  
therapy beams," *Medical Physics* **21** (8), 1227-1235 (1994).
- 61 KE Sixel and EB Podgorsak, "Buildup region and depth of dose maximum of  
megavoltage x-ray beams," *Medical Physics* **21** (3), 411-416 (1994).
- 62 GM Mora, A Maio, and DWO Rogers, "Monte Carlo simulation of a typical [sup  
60]Co therapy source," *Medical Physics* **26** (11), 2494-2502 (1999).

- <sup>63</sup> AB Jani, LW Davis, and TH Fox, "Integration of Databases for Radiotherapy Outcomes Analyses," *Journal of the American College of Radiology* **4** (11), 825-831 (2007).
- <sup>64</sup> D Liu, M Ajlouni, J-Y Jin, S Ryu, F Siddiqui, A Patel, B Movsas, and IJ Chetty, "Analysis of outcomes in radiation oncology: An integrated computational platform," *Medical Physics* **36** (5), 1680-1689 (2009).

## Chapter 9 Vita

Scott Eric Davidson was born in St. Louis, Missouri on December 10<sup>th</sup>, 1964, the son of Bobby and Lucille Davidson. He attended the University of Missouri – Columbia as a co-op student where he earned the degree of Bachelor of Science in Electrical Engineering in 1989. After graduation, he held various engineering positions in the electronics industry where he published one paper and was awarded three US patents. In August of 2003, he entered The University of Texas Health Science Center at Houston Graduate School of Biomedical Sciences. In May of 2006 he received the degree of Masters of Science in Medical Physics.

Permanent address:  
16611 McCormick Drive  
Houston, TX 77095